

Springer Series in Measurement Science and Technology

Songling Huang
Shen Wang

New Technologies in Electromagnetic Non-destructive Testing



 Springer

Springer Series in Measurement Science and Technology

Series editors

Markys G. Cain, Surrey, UK

Giovanni Battista Rossi, Genoa, Italy

Jiří Tesař, Prague, Czech Republic

Marijn van Veghel, JA Delft, The Netherlands

The Springer Series in Measurement Science and Technology comprehensively covers the science and technology of measurement, addressing all aspects of the subject from the fundamental physical principles through to the state-of-the-art in applied and industrial metrology. Volumes published in the series cover theoretical developments, experimental techniques and measurement best practice, devices and technology, data analysis, uncertainty, and standards, with application to physics, chemistry, materials science, engineering and the life sciences.

The series includes textbooks for advanced students and research monographs for established researchers needing to stay up to date with the latest developments in the field.

More information about this series at <http://www.springer.com/series/13337>

Songling Huang · Shen Wang

New Technologies in Electromagnetic Non-destructive Testing



Songling Huang
Department of Electrical Engineering
Tsinghua University
Beijing
China

Shen Wang
Department of Electrical Engineering
Tsinghua University
Beijing
China

ISSN 2198-7807 ISSN 2198-7815 (electronic)
Springer Series in Measurement Science and Technology
ISBN 978-981-10-0577-0 ISBN 978-981-10-0578-7 (eBook)
DOI 10.1007/978-981-10-0578-7

Jointly published with Tsinghua University Press

Library of Congress Control Number: 2016931194

© Tsinghua University Press and Springer Science+Business Media Singapore 2016

Original Chinese edition published by Tsinghua University Press, Beijing, 2013

This work is subject to copyright. All rights are reserved by the Publishers, whether the whole or part of the material is concerned, specifically the rights of translation, reprinting, reuse of illustrations, recitation, broadcasting, reproduction on microfilms or in any other physical way, and transmission or information storage and retrieval, electronic adaptation, computer software, or by similar or dissimilar methodology now known or hereafter developed.

The use of general descriptive names, registered names, trademarks, service marks, etc. in this publication does not imply, even in the absence of a specific statement, that such names are exempt from the relevant protective laws and regulations and therefore free for general use.

The publishers, the authors and the editors are safe to assume that the advice and information in this book are believed to be true and accurate at the date of publication. Neither the publishers nor the authors or the editors give a warranty, express or implied, with respect to the material contained herein or for any errors or omissions that may have been made.

Printed on acid-free paper

This Springer imprint is published by SpringerNature

The registered company is Springer Science+Business Media Singapore Pte Ltd.

Preface

Electromagnetic nondestructive testing technologies have developed rapidly in recent years, and there have been some new methods or new applications. For example, the magnetic memory testing method for stress concentration of in-service pressure vessels is one kind of nondestructive testing technique emerging in the late twentieth century; the pulsed magnetic flux leakage testing technique for detection of corrosion defects in the pipeline with insulation or anti-corrosion layers is a new development of the original technology. In recent years, the theories and applications of electromagnetic ultrasonic guided wave testing, remote field eddy current testing, defect quantification in magnetic flux leakage testing, and pulsed eddy current testing have achieved rapid development, and these techniques are widely used in the online defect detection of oil and gas pipeline, rail track, pressure vessel, and so on.

This book introduces new methods and technologies in the electromagnetic nondestructive testing field, mainly including the electromagnetic ultrasonic guided wave testing technology, the pulsed eddy current testing technology, the remote field eddy current testing technology, the low frequency eddy current testing technology, the magnetic memory testing technology, and some key techniques in magnetic flux leakage testing. The theoretical models, methods of numerical simulations and designs, analysis of the influencing factors, implementation of the testing device, and some typical engineering application examples are given for each of these electromagnetic testing methods.

During the past more than 10 years, the authors have been conducting continuous research and practical applications in electromagnetic nondestructive testing, and much of the content of this book comes from the doctor and master theses guided by the authors. These students include Shen Wang, Wei Cui, Kuansheng Hao, Chaofeng Ye, Yun Tong, Yongsheng Zhang, Peng Li, Junjun Xin, Zhiyi Su, Yuhang Su, Xinyi Wu, etc. This book also references the latest research results by the relevant counterparts in this field. In the implementations of related technologies, we obtained considerable support and assistance from the leaders and

engineers of Sinopec, PetroChina, and CNOOC to ensure continuous improvement of the related technologies in practice. The author thanks those people sincerely!

Chapters 1–3 were written by Shen Wang, Chaps. 4–6 were written by Songling Huang.

With the growth in demand for nondestructive testing, research in electromagnetic nondestructive testing is drawing more attention, and the industrial applications even more widely. The authors hope that the publication of the book can provide references for the research and development staff, for students and teachers in universities, and engineers and technicians. If any error is found in the book, criticism and correctness from the readers are welcomed.

Beijing, China

Songling Huang
Shen Wang

Contents

1	The Electromagnetic Ultrasonic Guided Wave Testing	1
1.1	Outline	1
1.2	Influencing Factors of EMAT	4
1.2.1	Influence of Wire Spacing of the Coil on the Performance of EMAT	4
1.2.2	The Influence of the Number of Foldings on the Performance of EMAT	5
1.2.3	The Influence of Coil Liftoff on the Performance of EMAT	5
1.3	EMATs for the Generation of Guided Waves Along the Axial Direction of the Pipe	6
1.3.1	The Modes of Axial Guided Waves and Frequency Dispersion	6
1.3.2	The Structure of Axial Guided Wave EMAT and Its Transduction Principle	7
1.4	The Dispersion Characteristics of the Guided Waves	9
1.4.1	The Dispersion Characteristics of the Lamb Waves in the Plate	9
1.4.2	The Dispersion Characteristics of the SH Guided Waves in the Plate	10
1.5	The Electromagnetic Ultrasonic Guided Wave Testing Technique	11
1.5.1	Thickness Measurement Based on Electromagnetic Ultrasound	11
1.5.2	Electromagnetic Ultrasonic Guided Wave Testing Along the Axial Direction of the Pipeline	18
1.5.3	Electromagnetic Ultrasonic Guided Wave Testing for Cracks in the Natural Gas Pipeline	35
	References	39

2	The Pulsed Eddy Current Testing	41
2.1	Basic Principle of Electromagnetism	42
2.1.1	The Penetration Depth and the Skin Effect	43
2.1.2	Principle of Probe Design	45
2.1.3	Principle of the Pulsed Eddy Current Testing	46
2.2	The Coil Sensors in the Pulsed Eddy Current Testing	48
2.2.1	Classifications of the Testing Coils	49
2.2.2	Working Modes of the Testing Coils	49
2.2.3	Probes of the Pulsed Eddy Current Testing	50
2.2.4	The Reciprocity Rule in Probe Design	72
2.3	Circuits of the Pulsed Eddy Current Testing	72
2.3.1	The Power Supply Module	73
2.3.2	The Excitation Source	75
2.3.3	The Analog Signal Processing Module	76
2.3.4	The Microcontroller Subsystem	77
	References	79
3	The Remote-Field Eddy Current Testing	81
3.1	Outline	81
3.2	The Mathematical Model of the RFEC in the Pipeline	84
3.2.1	Basic Equations	84
3.2.2	The Propagation of the AC Magnetic Field in the Ferromagnetic Pipe Wall	88
3.2.3	The Voltage Signal of the Receiving Coil	90
3.3	The FEM Modeling of the RFEC in the Pipeline	91
3.3.1	Introduction to the FEM and ANSYS	91
3.3.2	Building the Remote-Field Eddy Current Model	95
3.4	2D FEM Simulation of RFEC in Pipeline	105
3.4.1	Electromagnetic Decomposition Analysis	109
3.4.2	The Evaluation Model of the Magnetic Field at the Inner Pipeline Surface	112
3.4.3	Analysis of the Full Circumferential Defect	114
3.4.4	Relation of the Defect Signal with the Dimensions of the Defect	118
3.5	3D FEM Simulation of the RFEC in the Pipeline	121
3.5.1	Signal of the Groove Defect	121
3.5.2	Relationship Between Axial Defect Signal and Defect Size	128
	References	135

- 4 Low-Frequency Eddy Current Testing** 137
 - 4.1 Introduction 137
 - 4.2 Finite Element Simulation of Eddy Current Coils. 138
 - 4.2.1 The Finite Element Modal of Coils 138
 - 4.2.2 Result of Probe Coil Finite Element Simulation. 140
 - 4.2.3 Theoretical Analysis of Probe Coil Model 150
 - 4.3 Pipe Deformation Detecting System Based on Low-Frequency Eddy Current 160
 - 4.3.1 Systematic Design 160
 - 4.3.2 Digital Alternating Current Bridge Measuring Circuit. 161
 - 4.3.3 Signal Processing and Display Module. 165
 - References 167
- 5 Metal Magnetic Memory Testing** 169
 - 5.1 Introduction 169
 - 5.2 The Relationship Between Metal Magnetic Memory and Geomagnetic Field. 170
 - 5.2.1 The Influence of Geomagnetic Field to Metal Magnetic Memory Testing 170
 - 5.2.2 The Influence of Geomagnetic Field to Metal Magnetic Memory Generation. 175
 - 5.2.3 Stress Distribution Detection by Metal Magnetic Memory Testing Method. 179
 - References 183
- 6 Magnetic Flux Leakage Testing** 185
 - 6.1 Introduction 185
 - 6.2 Magnetic Flux Leakage Testing Principle 187
 - 6.3 The Influence Factors of Magnetic Flux Leakage Testing 189
 - 6.3.1 The Thickness of Material 190
 - 6.3.2 The Component of Material 190
 - 6.3.3 The Coupling Loop 190
 - 6.3.4 The Space Between Magnetic Poles. 190
 - 6.3.5 The Speed of Inspector 191
 - 6.3.6 The Remanence 192
 - 6.3.7 The Internal Stress. 193
 - 6.3.8 The Lift off of Probe 193

- 6.4 Defect Quantification Method of Magnetic Flux Leakage Testing 196
 - 6.4.1 Defect Quantification Method Based on Statistical Identification. 197
 - 6.4.2 Defect Quantification Method Based on Radial Basis Function Neural Network (RBFNN) 202
 - 6.4.3 Defect Quantification Method Based on Three-Dimensional Finite Element Neural Network 208
- References 221

Chapter 1

The Electromagnetic Ultrasonic Guided Wave Testing

1.1 Outline

As an important branch of the nondestructive testing field, ultrasonic testing is widely used in the steel, electric power, petroleum, transportation, and medical and other industries. In the process of ultrasonic testing, the ultrasonic transducer is the core component of excitation and reception of ultrasonic waves, mainly including the piezoelectric ultrasonic transducer and the electromagnetic acoustic transducer (EMAT). Compared with the piezoelectric ultrasonic transducer, EMAT has many advantages, such as being non-contact, without the need for the coupling medium, and easy to produce the shear horizontal (SH) wave. In particular, it can be applied under a high-temperature environment, or there is an isolation layer, and other special situations [1]. It is of great value and a wide range of applications.

In 1939, Rnadall [2] did the first experiment of generating acoustic elastic vibration by the Lorentz force. In 1955, Aksneov and Vkin [3] reported that they found the phenomenon that the resonance effect of nuclear magnetic resonance coil in a magnetic field is interfered, which is considered the earliest report about EMAT. In the mid- and late-1970s of the twentieth century, studies of EMAT began to develop rapidly. Researchers from the UK, the USA, Russia, Germany, Japan, and other countries conducted theoretical and experimental researches of EMAT, significantly expanding the scope of technological innovation and application of EMAT. After nearly 50 years of continuous improvement, EMAT technology has entered the stage of industrial application, and its application fields have gradually evolved from the testing of metal plates and train wheel, and high-temperature metal sample thickness measurement to inspections of metal welds, steel bars, steel pipes, rail tracks, composite materials, and so on [4–13].

The limitation of EMAT is the poor energy efficiency compared with the piezoelectric transducer, which then leads to a low signal-to-noise ratio of the ultrasonic signal generated from the EMAT. The most important and difficult problems of the research field of EMAT are as follows: improving the energy

conversion efficiency and the signal-to-noise ratio, generating and receiving ultrasonic waves with purer modes, and reducing the interference of other ultrasonic signals with different modes. Early studies of the EMAT were based mostly on experimental ways, which is time-consuming and inefficient. Later, by exploring the establishment of mathematical EMAT model, people tried to carry out further research on the physical mechanism of EMAT by theoretical analysis and numerical simulation. Up to now, the mathematical models of EMAT based on the Lorentz force mechanism and the magnetostrictive mechanism have been established. Some related numerical methods and analytical methods have already been put forward [1].

However, the theoretical analysis of EMAT involves the static magnetic field, pulsed electromagnetic field, ultrasonic field, and so on, that is, this is a multifield coupling problem. The analysis is also related closely to the material characteristics of the tested sample. The numerical simulation and calculation of the transducer can be very complex, especially for the problem of EMAT based on the magnetostrictive mechanism. When it is used to test the ferromagnetic specimen, its complete energy transduction process is related to the magnet material's mechanical properties, magnetostrictive properties, inverse magnetostrictive properties, and so on, and it can be more difficult to do numerical simulation analysis. In order to have a deeper understanding of the energy transduction mechanism of EMAT, grasping the physical properties of EMAT comprehensively, and then making an optimal design for it, it has great theoretical and practical significance in solving the problems of theory and the method existing in the numerical simulations. Furthermore, with the application of new materials and the improvement of the EMAT manufacturing, the coil with a more complex structure is being used in EMAT; thus, it is very important to introduce some new analyzing methods for EMAT with new structures.

EMAT consists of three parts—the magnet that provides a biased magnetic field; the coils that produce a pulsed magnetic field; and the test sample in which the ultrasonic wave is generated and propagated. A variety of types and patterns of ultrasonic waves can be generated by the different combinations of coils and magnets. For example, Lamb wave, Rayleigh wave, SH wave, and body wave can be generated in the platelike specimen and L-mode and T-mode guided waves with pipe axial direction can be generated in the tubelike specimen. EMAT not only can work in pulse-echo mode, in which only one probe is needed, but also can be used in through-transmission mode, in which two probes are needed to play the roles of generating and reception. Generally, the structures of the transmitting probe and the receiving probe are similar to each other.

In the plate and pipe circumferential testing, where the dimension of plate specimen or diameter of pipe-shaped specimen is considerably larger than the dimension of EMAT itself, the coils of EMAT are all of a flat type. On the other hand, the magnet that provides the bias magnetic field is usually a permanent magnet. The widely used structures of EMAT include meander coil, spiral coil, and racetrack coil; the structures of the magnet include square type, horseshoe type, and periodic permanent magnet. These are shown in Figs. 1.1 and 1.2.

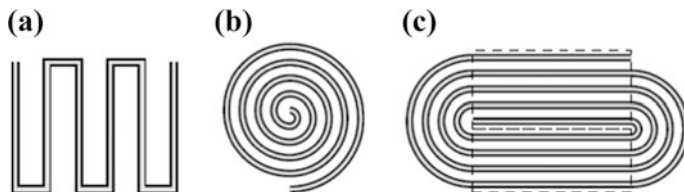


Fig. 1.1 The structure of the coil of EMAT. **a** Meander coil, **b** spiral coil, and **c** racetrack coil

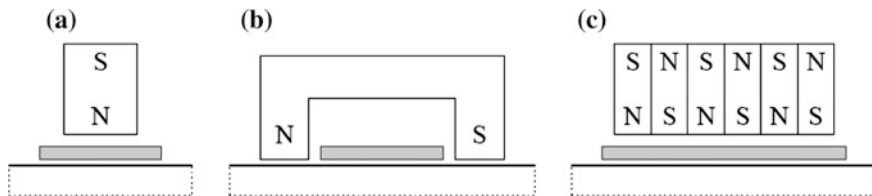


Fig. 1.2 The structure of the magnet of EMAT. **a** Vertical bias, **b** horizontal bias, and **c** periodical bias

The different types of ultrasonic waves or modes that have different applications can be generated inside the specimen by the various combinations of coils, magnet, and specimen. With the combination of meander coil and square magnet, Lamb wave and Rayleigh wave can be generated in the non-ferromagnetic specimen [14–20]. The specific type of ultrasonic wave is related to the coils’ dimension and the frequency of the excitation signal. It is also possible to generate guided wave of SH mode in the ferromagnetic sample [21]. The spiral coil and the racetrack coil are mainly used to generate body waves in the ferromagnetic specimen and the thickness measurement of the sample under test. They can generate transverse wave when combined with the square magnet [22, 23], or combined with the horseshoe permanent magnet in the circumstance for the generation of longitudinal wave [24]. With the combination of racetrack-shaped coil and periodic permanent magnet, the SH wave can be generated and received in the ferromagnetic and non-ferromagnetic material [25].

The types, strength, frequency, propagation direction, and some other parameters of the ultrasonic waves can be controlled by changing the scale and orientation of the bias magnetic field, or the scale and frequency of a high-frequency current, as well as the shape and size of the coils of the EMAT with different structures. In the meantime, the bandwidth of the received ultrasonic waves and some other parameters can also be changed in the same way.

For the formation of a strong bias magnetic field in the surface or near the surface, the magnet should be made by using magnetic materials with high field intensity, and specifically, the materials can be a permanent magnet or electromagnet. The advantage of using electromagnets is that the strength of the magnetic field can be adjusted easily. There is a certain level of skin effect in the magnetic field when the electromagnets are used in AC magnetization, in the circumstance of which the intensity of the bias magnetic field can be enhanced. The advantage of

using a permanent magnet is the small size of the magnet, which can make the structure more compact. However, it is important to note that although the structure of EMAT can become more compact using the permanent magnet, it can be restricted by the temperature and the magnetic field intensity. In order to generate stronger magnetic field and get the right direction of the magnetic field, the magnet needed by EMAT should be well designed.

The coils used by EMAT mainly include spiral type, racetrack type, and meander type. The improvement of the EMAT coils has undergone the flat cable, thin film, wire, printed circuit, and so on [1, 14].

1.2 Influencing Factors of EMAT

The driving force of ultrasound generation in the test sample comes from the Lorentz force and the magnetostrictive force. In the Lorentz force mechanism EMAT, the Lorentz force of the test sample is proportional to the bias magnetic field and the eddy current within the sample. In the magnetostrictive mechanism EMAT, the magnetostrictive force of the sample is proportional to the piezomagnetic coefficients and derivative of the dynamic magnetic field to the coordinates. Both the magnitudes and directions of the forces are related to the magnitudes and directions of the static and dynamic magnetic fields. For the meander line EMAT, the direction of the force determines the mode of the ultrasonic waves in the test sample. The magnitude of the force determines the value of the amplitude of the ultrasonic waves.

1.2.1 Influence of Wire Spacing of the Coil on the Performance of EMAT

In the design of the meander line coil, generally the matching criteria between the wavelength of the guided wave and the coil structure should be satisfied, that is,

$$D = (2n + 1)\lambda, \quad n = 0, 1, 2, \dots \quad (1.1)$$

in which D is the spatial period of the meander coil and λ is the wavelength of the guided wave. Generally, $n = 0$, that is, $D = \lambda$. The purpose of the design is to enhance the desired ultrasonic wave mode and weaken other ultrasonic wave modes through superposition or cancelation of the ultrasonic waves, according to the spatial periodical characteristic of the meander coil.

The wavelength of the guided wave and the frequency should satisfy the relation

$$D = \lambda = c/f \quad (1.2)$$

in which c is the phase velocity of the selected ultrasonic wave mode.

By changing the spacing between adjacent wires of the coils, the influence of the spacing on the performance of the EMAT is studied. Assuming that the excitation frequency is 310 kHz, and A0 mode Lamb wave is generated, the corresponding spatial period of the meander coil is $D = 6.5$ mm. By changing the spatial periods of the excitation and receiving coils, the change of the signal in the receiving coil is observed. When increasing or decreasing the spatial period of the receiving coil, amplitude of the received signal is reduced, and the signal waveform will change. Obviously, changing the spatial periods of the exciting coil and receiving coil have the same effect on the received signal.

Therefore, when designing the meander coil, by ensuring the exciting coil and receiver coil have the same spatial period, and the period matches the wavelength of the desired ultrasonic wave mode, maximum efficiency can be realized for the excitation and reception of this mode of ultrasonic wave.

1.2.2 The Influence of the Number of Foldings on the Performance of EMAT

The multifolding structure of the meander coil can enhance the signal of the desired ultrasonic wave mode and weaken the signals of other ultrasonic wave modes. While fixing the excitation current of the coil and changing the numbers of foldings of the exciting coil and receiving coil, the change of the received signal is observed.

When the number of foldings of the exciting coil is increased, due to the tuning of folding structure of the coil, amplitude of the received guided wave signal is increased, and the width of the signal wave pack is also enlarged. So, when selecting the number of foldings for the meander coil, it is necessary to consider the influence of the change of the number of foldings. When larger signal amplitude and smaller interference of other modes are required to improve testing sensitivity and there is no need to consider width of the signal wave pack, the number of foldings of the meander coil can be increased; when narrower signal wave pack is required to improve the resolution of the received signal, the number of foldings of the meander coil can be decreased. Generally, the two aspects need to be taken into account to design the number of foldings of the meander coil, depending on the practical application.

1.2.3 The Influence of Coil Liftoff on the Performance of EMAT

Coil liftoff is an important factor influencing the performance of EMAT. As the coil liftoff increases, the amplitude of the received signal decays exponentially, so in the design of EMAT, the liftoff of the coil should be reduced as much as possible.

If analyzing these results, the influences of the number of foldings and wire spacing on the performance of EMAT can be interpreted by the analysis of mechanical field, and the best design is realized by enhancing the particle vibration of the desired ultrasonic wave mode. By suitable wire spacing design and increasing the number of foldings of the coil, this purpose can be achieved.

In order to further enhance the amplitude and signal-to-noise ratio of the received signal, under the condition of satisfying the number of foldings and the wire spacing, the meander coil can be designed as a multilayer and multisplit structure. The multilayer and multisplit structure increased the ampere-turns of the exciting coil and number of inductive conductors of the receiving coil, thereby increasing the amplitude of the signal.

1.3 EMATs for the Generation of Guided Waves Along the Axial Direction of the Pipe

For the meander coils, the distance between adjacent wires and the excitation frequency must satisfy the specific matching relation, and this makes the design of the coil structure simpler, and the types and modes of the excited ultrasonic waves can be better controlled. At the same time, the amplitude and time width of the pulse in the ultrasonic signal can be adjusted through the number of turns of the coil and the dimensions of the wire conductor. If such coil structure is applied to the detection of defects in the pipelines made from ferromagnetic material, the drawbacks of the single-belt coil structure can be effectively overcome.

1.3.1 The Modes of Axial Guided Waves and Frequency Dispersion

In the case of the pipes, the axial guided waves are dispersive. The phase velocity and group velocity dispersion curves of axial guided waves in pipes are shown in Figs. 1.3 and 1.4. As shown in the figures, there are four different modes, $L(0,1)$,

Fig. 1.3 Phase velocity dispersion curves of a pipe

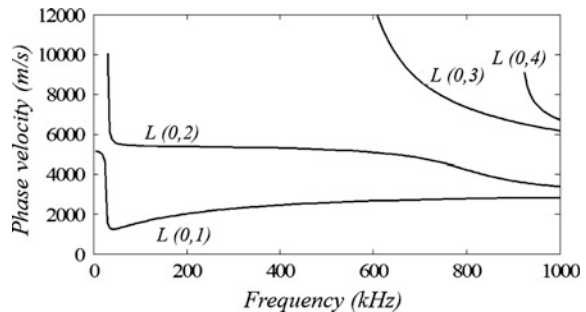
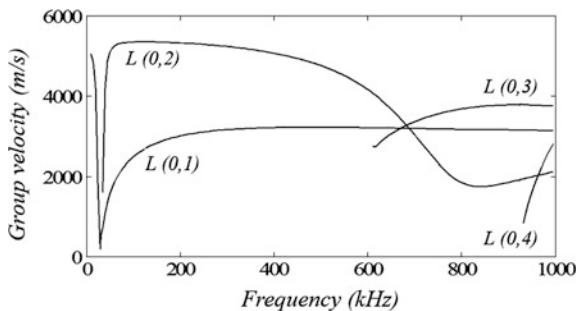


Fig. 1.4 Group velocity dispersion curves of a pipe

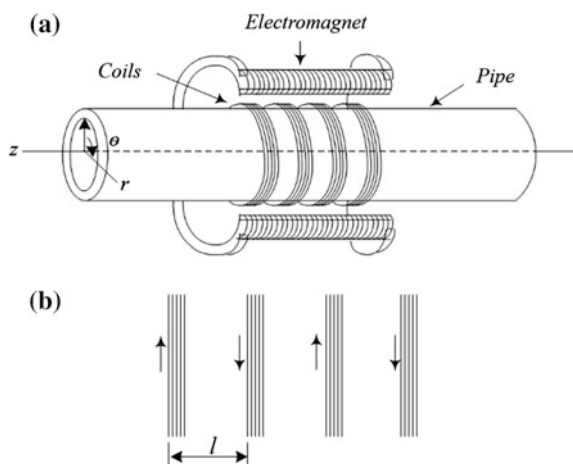


$L(0,2)$, $L(0,3)$, and $L(0,4)$. The range of operating frequency of a typical axial guided wave EMAT is from tens of kHz to several hundreds of kHz, and in this frequency range, $L(0,1)$ and $L(0,2)$ wave modes are generally used. However, the $L(0,1)$ mode and $L(0,2)$ mode coexist in a large frequency range, so under one frequency, both $L(0,1)$ and $L(0,2)$ wave modes could be excited simultaneously. The generation of one specific mode is closely related to the structure of the coils.

1.3.2 The Structure of Axial Guided Wave EMAT and Its Transduction Principle

The schematic diagram of the new multibelt EMAT structure is shown in Fig. 1.5a. To keep the bias magnetic field to be homogeneously distributed around the circumference of the pipe, a solenoid electromagnet is used instead of a U-shaped magnet. The multibelt coil, which can be built by wound enameled wires or flexible

Fig. 1.5 The structure of the multibelt EMAT. **a** The structure of the transducer and **b** the structure of the coil



printed circuit (FPC) technology, is used to provide a periodic dynamic bias field. The transmitting coil and receiving coil have the same structure.

In Fig. 1.5b is the structure of the coil, in which the multibelt coil is unfolded around the circumference and the details of end connection of the coil are neglected. The applied electric currents in the adjacent wires have opposite directions to generate opposite dynamic magnetic fields. According to the structure and principle of the meander coils of the EMATs used for plate inspection, the distance l of the adjacent belts should be half of the wavelength of the generated axial guided waves. Therefore, the frequency of the ultrasonic waves could be expressed as (1.3)

$$f_L = \frac{c_L}{\lambda} = \frac{2c_L}{l} \quad (1.3)$$

In the above equation, f_L is the frequency of axial guided wave; c_L is the phase velocity; λ is the wavelength; and l is half of the wavelength. If c_L is fixed, f_L is solely determined by l .

During the operation of the transducer, the electromagnet will generate the static bias magnetic field H_s and the multibelt coil will generate dynamic magnetic field H_d , and their directions are both along the axis of the pipe. The superposition of the static and the dynamic magnetic fields generates the combined dynamic magnetic field H_c , as shown in Fig. 1.6. The application of H_c causes the movement of the magnetic domains in the pipe wall and leads to the generation of the ultrasonic waves. The magnetostrictive force leading to the oscillation of particles can be described as (1.4)

$$F_{ms} = -\frac{1}{2}(3\tau + 2\mu)(1 - 2\nu) \frac{\partial \zeta}{\partial M_0} \frac{\partial m_z}{\partial z} \quad (1.4)$$

The process of receiving ultrasonic waves is the inverse of the process of generating ultrasonic waves. When the ultrasonic waves propagate to the position of the receiving coil, the oscillation of particles in the pipe wall causes the variation of the magnetic field, and then, electrical potential is induced in the receiving coil.

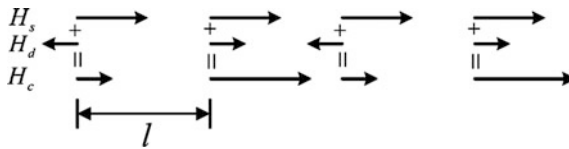


Fig. 1.6 Superposition of the dynamic magnetic field and the static magnetic field

1.4 The Dispersion Characteristics of the Guided Waves

1.4.1 The Dispersion Characteristics of the Lamb Waves in the Plate

Generally, the propagation of the guided waves is associated with the dispersion phenomenon, which means that the propagation velocity of the guided waves depends not only on the material properties, but also on the geometrical structure of the waveguide. The velocity of the guided waves is the function of the frequency, and there exist multiple mode curves for different wave modes simultaneously. The relation between the propagation velocity and the frequency for the steady-state guided waves is recorded in the phase velocity dispersion curves, while the group velocity dispersion curves are used to describe the propagation velocity of a pulse train or a wave packet. Since in practical guided wave testing, a pulse train with limited time duration is generally used as the excitation, the actual propagation velocity of the guided waves as recorded in the received signal is the group velocity.

The phase velocity dispersion curves of Lamb wave propagating in a steel plate with 1 mm thickness are shown in Fig. 1.7a, where S_n represents the symmetric modes, A_n represents the antisymmetric modes, and $n = 0, 1, 2, \dots$

As discussed above, the phase velocity dispersion curves correspond to the situation of a steady-state excitation. In practical testing, a pulse train with limited time duration is used as the excitation, and its propagation velocity is the group velocity. The group velocity can be obtained from the phase velocity. The group velocity dispersion curves corresponding to Fig. 1.7a are given in Fig. 1.7b.

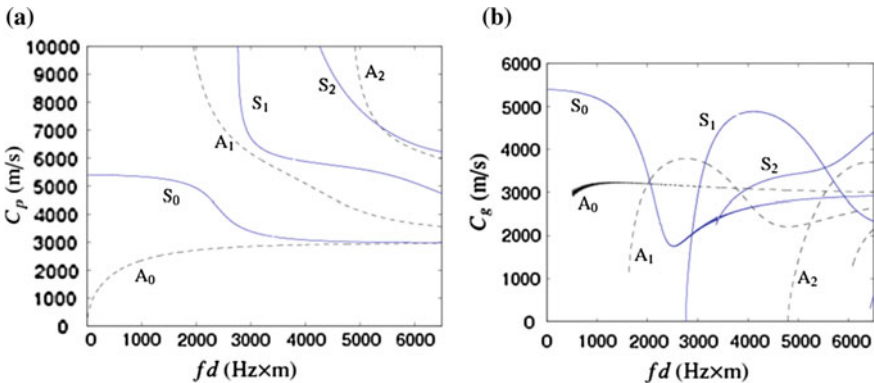


Fig. 1.7 The frequency dispersion curves of Lamb wave in the 1-mm-thickness steel plate. **a** Phase velocity dispersion curves and **b** group velocity dispersion curves

1.4.2 The Dispersion Characteristics of the SH Guided Waves in the Plate

For the shear horizontal (SH) guided waves in a plate, the direction of the displacement is parallel with the upper and lower boundaries of the plate waveguide, so the interaction of the SH guided waves with the defects perpendicular to the cross section is simple, and this kind of guided waves is promising in applications. Plate Lamb waves could be seen as a superposition of longitudinal waves and shear vertical (SV) waves, and the SH guided waves could be seen as a superposition of SH bulk waves reflected continuously in the plate.

The mode of vibration of SH guided wave in a plate is relatively simple, so the method of potential function decomposition is not needed to solve the dispersion equation. There exists an analytical solution for the dispersion equation of the SH guided waves; thus, it is not necessary to obtain the solutions numerically. An analytical expression also exists for the group velocity. The dispersion curves of the SH guided wave in a steel plate with 1 mm thickness are shown in Fig. 1.8. It can be seen from Fig. 1.8 that there is no dispersion for the SH_0 mode, which means that neither the phase velocity nor the group velocity changes with the excitation frequency. This non-dispersive characteristic makes the SH_0 mode frequently selected for defect detection. In the “ SH_n ” labels in Fig. 1.8, an even n corresponds to a symmetric mode and an odd n corresponds to an antisymmetric mode.

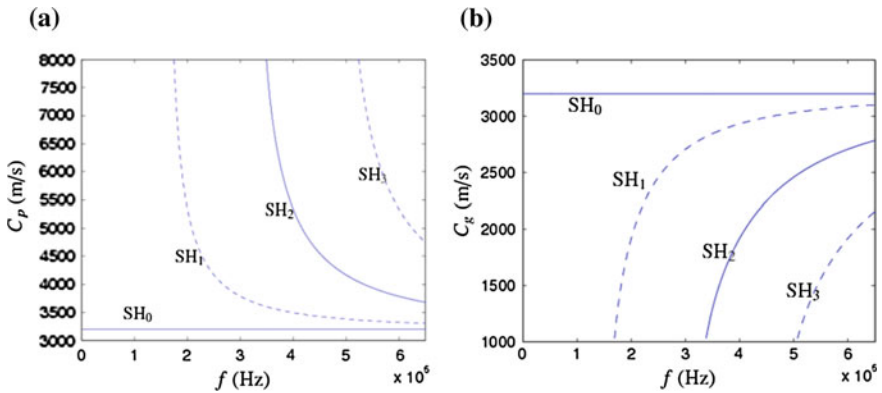


Fig. 1.8 The dispersion curves of the SH guided waves in a plate. **a** Phase velocity dispersion curves and **b** group velocity dispersion curves

1.5 The Electromagnetic Ultrasonic Guided Wave Testing Technique

1.5.1 Thickness Measurement Based on Electromagnetic Ultrasound

There exist two mechanisms for the thickness measurement using electromagnetic ultrasound: One is based on Lorentz force, and the other is based on the magnetostrictive force, which is applicable to the ferromagnetic conductive materials. During the thickness measurement of structures made from the ferromagnetic conductive materials, there often exist the two effects at the same time.

Normal incidence pulse-echo method could be used in the thickness measurement with the EMA technique. When rapid scan and high-resolution inspection are required, or the tested material is very thin, oblique incidence under pitch and catch mode could also be adopted.

During the propagation of the ultrasonic waves, the reflection and transmission phenomena could take place at the interface between the two media. When the normal incident waves travel back and forth between the top and bottom surfaces of the structure, reflection and transmission occur at the top and bottom interfaces between the structure and the air. If the acoustic impedances of the structure (made of metal material) and the air are Z_1 and Z_2 , respectively, for the case of normal incidence, the reflection coefficient R and the transmission coefficient T are

$$R = \left(\frac{Z_1 - Z_2}{Z_1 + Z_2} \right)^2 \times 100 \% \quad (1.5)$$

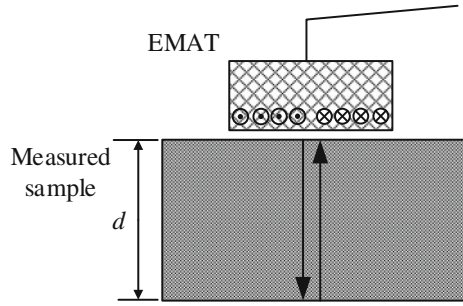
$$T = \frac{4Z_1Z_2}{(Z_1 + Z_2)^2} \times 100 \%$$

Because the acoustic impedance Z_2 of the air is far less than the acoustic impedance Z_1 of the structure, R is close to 1 and T is close to 0. Basically, total reflection takes place at the interface, and the waves could propagate back and forth between the top and bottom surfaces many times, and then, the thickness of the structure could be calculated as

$$d = \frac{CT_n}{2} \quad (1.6)$$

in which d is the thickness of the structure and T_n is the time difference between two peaks in the recorded ultrasonic wave signal, i.e., the time of propagation of the waves between the top and bottom surfaces of the structure under inspection. C is the sound speed of the electromagnetic ultrasonic waves. The principle of thickness measurement is as in Fig. 1.9. Because under different temperatures the propagation velocities of the ultrasonic waves will be different, sometimes temperature compensation is needed.

Fig. 1.9 Thickness measurement with electromagnetic ultrasonic waves



The electromagnetic ultrasonic thickness measurement system is mainly composed of the following parts: the EMAT, the matching circuit, the ultrasound excitation circuit, the receiving and amplification circuit for the wave signal, and the data acquisition and processing circuit. The permanent magnet could supply a constant bias magnetic field as large as 1 T. The matching circuit increases the transduction efficiency of the transducer. The measured sample is made of ferromagnetic or conductive material. The ultrasound generation circuit comprises a power amplifier, an impulse excitation circuit, and a frequency regulator. The power amplifier charges the impulse excitation circuit, and the frequency regulator could be used to tune the pulse width and the frequency of the sinusoidal waveform. The core electronic part is the FPGA, which could be used to tune a waveform of arbitrary frequency. The reflected wave signal is received by an EMAT, amplified, filtered, and acquired into a PC. With a further digital filtering process, the value of the thickness could be calculated. The waveform after the amplification and filtering could also be observed by an oscilloscope. The structure of the system is as in Fig. 1.10.

In an EMA thickness measurement device, the receiving and amplification are the key processes, which are directly related to the measuring accuracy. The ultrasonic signal received by the EMAT is amplified and filtered, as in Fig. 1.11.

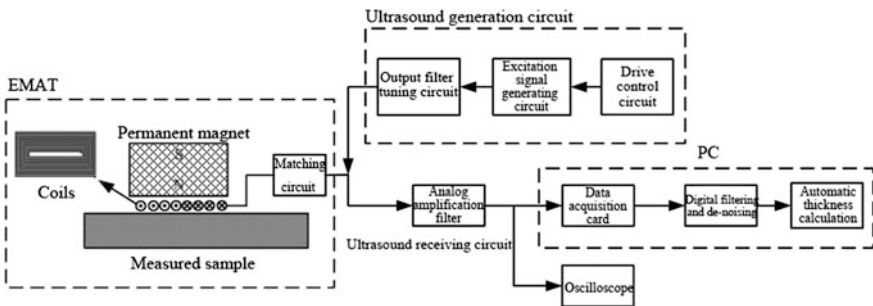


Fig. 1.10 The structure of the EMA thickness measurement system

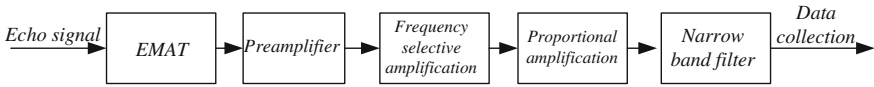


Fig. 1.11 The receiving and processing of the ultrasonic signal from EMA thickness measurement

The EMAT receives the echo ultrasonic waves, and its output goes to the filtering and amplification circuit. The preamplifier is generally broadband and low gain device and could amplify the ultrasonic signal linearly in the whole range of signal amplitude.

If the signal is increased to the voltage level high enough to overcome the noises of the subsequent amplification and filtering stages, the signal-to-noise ratio could be maximized. The amplifier increases the amplitude of the ultrasonic echo signal to the degree to make the signal processing circuit work normally. The filter is narrow-banded, so unnecessary frequency responses of the EMAT are eliminated, and the interference from the power supply is reduced. Frequency characteristic of the signal is decided by the band-pass filter, and controlling the frequency band of the amplified signal helps to improve the signal-to-noise ratio. The amplified and filtered signal then enters the DAQ system for data collection.

Usually, even when good matching is achieved for the circuit and the peak-to-peak value of the current in the transmitter coil is 50 A, the voltage on the receiver coil is only tens of microvolts. At the same time, the high power transmission circuit can produce strong electromagnetic interference when operating, causing much noise for the EMAT system. Therefore, in order to get higher SNR for the received signal, the EMAT receiving circuit must have the ability to detect weak signal in a strong background noise. In order to reduce the interference, the wiring of the receiving circuit adopts coaxial cable and BNC connectors with good shielding performance. In addition, the possible damage of the excitation high voltage interference to the receiving circuit should be avoided. Figure 1.12 shows the diagram of the protection and frequency selective amplification hardware for the amplification circuit.

The coil excitation needs a high-voltage and high-power excitation circuit, and the excitation circuit should generate a high-frequency sinusoidal signal or pulse

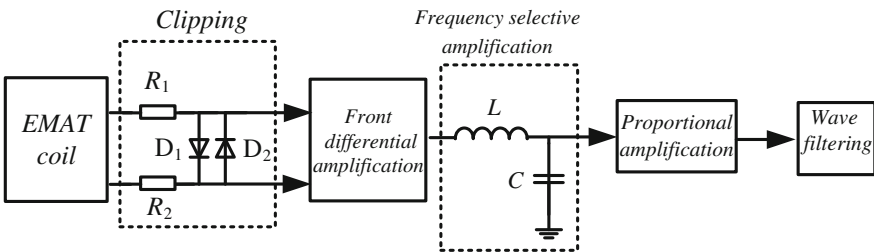


Fig. 1.12 The clipping and amplification stages of the receiving circuit

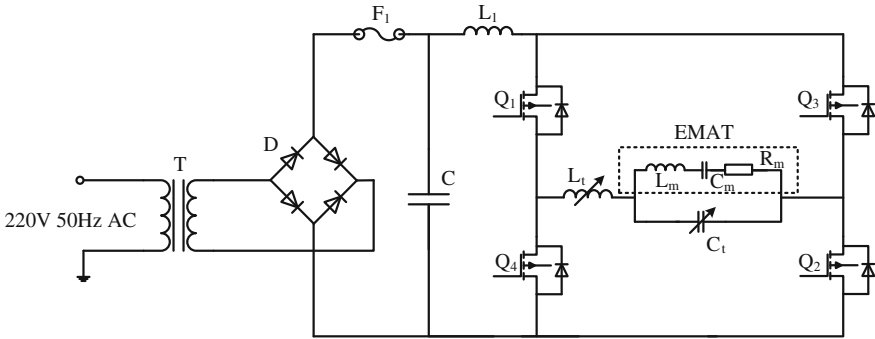


Fig. 1.13 The principle of the full-bridge inversion of the excitation circuit

signal. According to current technology and the request of the electromagnetic ultrasonic thickness measurement, a full-bridge inverter power amplifier circuit is used to generate the sine waves. A single switch transistor is used for the charge–discharge of the capacitance to generate the high-voltage narrow pulse.

The principle of the full-bridge inverter power amplifier excitation circuit is shown in Fig. 1.13. A 220V AC power is connected to a rectifier bridge through an adjustable transformer. The AC is transferred into the DC through the full-bridge rectifier, providing the input voltage for the inverter circuit. At the end of the AC input, the alternating voltage is transferred into the direct voltage through the full-bridge rectifier composed of four diodes. The maximum value of the voltage can reach 400 V. The peak value of the output voltage by the full-bridge inverter circuit is close to the DC voltage at the input terminal, but the peak value of the output voltage by the half-bridge circuit is only half of the DC voltage after the front-end rectification. Compared to the half-bridge inverter circuit, the full-bridge circuit has a higher efficiency. The inductance L_1 is the filtering section after rectification, in which the high-frequency spike pulses generated from the rectifying process can be filtered. The capacitance at the back-end is the high-voltage charging capacitance with a large capacity, which can help to form a stable DC voltage at the input terminal. F_1 is the fuse used to control the electric current in the switching transistor, so that the average current in the switching transistor can be restricted. The full-bridge inverter mainly includes the driving module, inverting module, and tunable filtering module. The driving capability of the pulse signal produced by the signal generation module is limited, so the signal should be amplified by the driving module before entering the power switch transistor. For the inverter module, a switch transistor with high frequency, high voltage, and high power is selected. Through controlling on/off of the switch transistor, the symmetric square pulse is output. Finally, with the tuning module, the signal is tuned into approximate sinusoidal pulse. The buffering circuit is used to absorb the sharp pulses and noises generated in the turning on/off process of the switch transistor.

Thickness measurement based on the electromagnetic ultrasound shares the same idea as the approach with the traditional piezoelectric ultrasound, where the

impulse reflection process is used. The ultrasonic wave is reflected back and forth in the tested sample, and the recorded waveform has strict repeatability. The characteristics of the waveform are obvious. The time differences corresponding to these peak values are used to calculate the thickness. Since pulsed energy is mostly used as the excitation of the thickness measurement, if the pulse is used to modulate the sine wave with the resulted signal as the excitation signal of the transducer, the echo signal is amplitude-modulated with the same frequency as that of the excitation pulse. The echoed signal of EMAT is usually highly contaminated by noises, and the signal-to-noise ratio is relatively low. The superposition of the noise makes the output signal non-stationary, and the amplitudes and phases of the sinusoidal components with various frequencies are time-varying parameters. However, the analog filtering circuit has an insufficient ability to handle the random noise of the non-stationary signal; thus, it is necessary to carry out some digital filtering and processing of the signal.

Using the time-domain analysis to extract the time-varying sine signal submerged in the noises can improve the quality of EMAT signal. In the averaging technique, the random characteristic of the noise is used, and in the time domain, the echoed signal is sampled multiple times and the average is obtained to improve the signal-to-noise ratio. Now, it has been a general method for dealing with the signal received by EMAT. For the recurring signal received by EMAT, within the error range the waveforms are basically the same, but the noise of the signal is random. After several acquisitions of the signal, through the summing and averaging the corresponding sampling points, the noise level of the useful signal can be significantly reduced, and the echoed signal is strengthened.

In Fig. 1.14 is the ultrasonic echo signal excited by the sinusoidal burst signal with a center frequency of 2 MHz and a number of periods of 12 in the aluminum plate with a thickness of 29.2 mm. The subfigure (a) is the original signal, and the subfigure (b) is the waveform after averaging 128 times. It can be seen from the

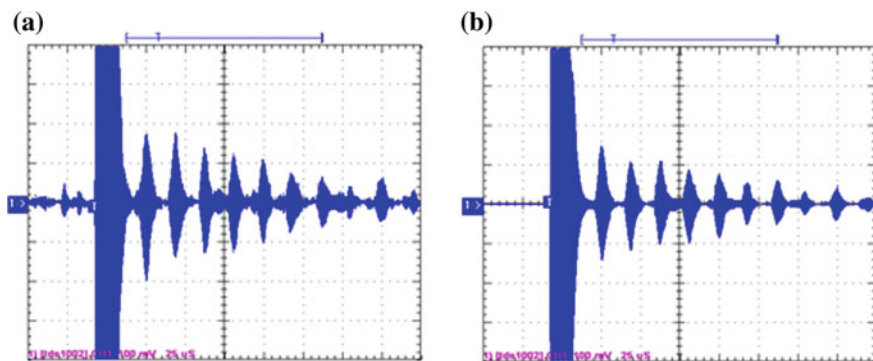


Fig. 1.14 The averaging process of the echoed signal. **a** The original signal and **b** the averaged signal

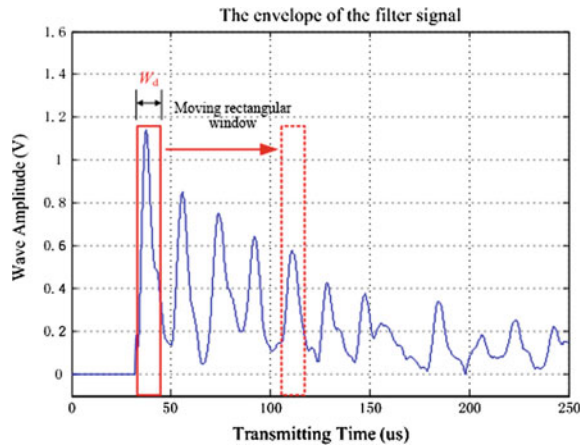
figure that the random noise is suppressed effectively, and there is no obvious attenuation of the useful signal. The signal-to-noise ratio is also improved.

In order to measure the time difference of the echoed signal to obtain the thickness of the tested specimen, the envelope of the testing signal should be obtained first. The envelopes are the top and bottom lines wrapping the signal, generated by connecting the maximum and minimum points of the signal sequentially.

Common methods used to extract the signal envelope are listed as follows: the complex modulation method, the full-wave rectification method, the detection/filtering method, and the Hilbert transform method. Those demodulation methods are generally required to work with the filter, to be effectively applied in practice. The Hilbert transform method is simple and effective and is used widely in the engineering field.

After the extraction of the envelope of the ultrasonic echo signal, in order to implement the automatic thickness measurement, the time difference between the two adjacent peaks of the echo signal should be solved. The thickness of the specimen is calculated from the corresponding thickness calculation equation. However, the difficulty of the method is how to solve the locations of the two waveform peaks. In order to perform further analysis and processing of the ultrasonic echo signal, two functions reflecting the characteristics of the echo signal are defined: The energy distribution function represents the energy distribution of the echo signal, and the comparability distribution function represents the level of similarity between the n th reflected waveform and the 1st reflected waveform of the ultrasonic signal. Firstly, the burst signal in the envelope is removed, and a rectangular window with a width of W_d is constructed as shown in Fig. 1.15. Moving the rectangular window along the time axis, the rank two norm of the vector, composed of all the data points within the scope of the rectangular window, is the value of the energy distribution function corresponding to the central point of the rectangular window. Its waveform is shown in Fig. 1.16a. The x coordinate corresponding to the maximum value of the energy distribution function is the time

Fig. 1.15 The characteristic function for establishing the ultrasonic echo signal envelope



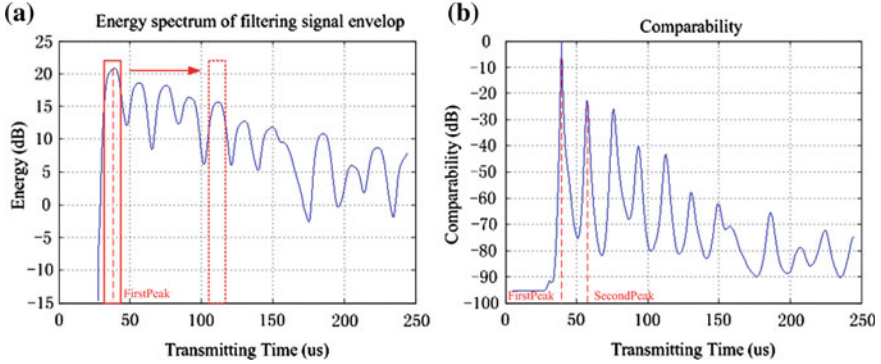


Fig. 1.16 The characteristic function of the ultrasonic echo signal envelope. **a** Energy distribution function and **b** waveform similarity function

instant FirstPeak corresponding to the peak of the first echo waveform. Setting this time instant as the center position of the rectangular window, at this time the vector composed of the values of the energy distribution function within this rectangular window is $P_1(W_d)$. Moving the rectangular window along the time axis on the waveform of the energy distribution function, when it reaches any position, the vector composed by the values of the energy distribution function within the rectangular window is $P_n(W_d)$. Then, the comparability distribution function can be expressed by

$$f(n) = \exp\left[-\|P_1(W_d) - P_n(W_d)\|^2\right] \quad (1.7)$$

in which $\|P_1(W_d) - P_n(W_d)\|^2$ represents the rank two norm of the two vectors, then the waveform of the time instant FirstPeak corresponding to the peak of the first echo is the most similar to itself, and the corresponding $f(n)$ value is the maximum. It is followed, in similarity, by the waveform of the time instant SecondPeak corresponding to the peak of the second echo and then by the waveform corresponding to the peak of the n th echo. The waveform of this function is as in Fig. 1.16b. From the instant FirstPeak, the x coordinate corresponding to the maximum value of the function $f(n)$ is the instant SecondPeak corresponding to the peak of the second echo. The time difference between these two time instants is the propagation time T_n of the ultrasonic wave bouncing back and forth once inside the specimen. If the propagation velocity C of the ultrasonic wave in the specimen is already known, then the thickness of the tested specimen can be obtained by the electromagnetic ultrasonic thickness calculation Eq. (1.6).

The energy distribution function represents the energy distribution of the echo signal. Compared with the method that through comparing the amplitude of the echo signal, the time of the first waveform peak is obtained directly from the echo signal envelope, the time of the first echo peak obtained from the energy distribution function is more accurate and reliable. With the energy distribution function,

the misjudgment caused by the singular values contained in the echo signal envelope and the high-frequency noises can be eliminated. The width of the rectangular window depends on the frequency of the ultrasonic wave signal, the data sampling rate, and the shape of peak of the echo signal, so the width of the rectangular window should be selected according to the different circumstances.

1.5.2 Electromagnetic Ultrasonic Guided Wave Testing Along the Axial Direction of the Pipeline

1.5.2.1 Hardware of System of the Electromagnetic Ultrasonic Guided Wave Testing Along the Axial Direction of the Pipeline

The structure of the longitudinal mode guided wave EMAT for the pipeline is shown in Fig. 1.17. Two schemes of single cluster coil and multiple cluster coil are shown, respectively. Enamelled wire is used to wind the coil of the electromagnet. After the DC is input, a static bias magnetic field will be generated along the axial direction of the pipeline. The EMAT coil is wound along the circumference of the pipeline. If high-frequency alternating current is loaded in the coil, a dynamic magnetic field will be generated. The direction of the dynamic magnetic field is parallel to that of the static bias magnetic field.

From the phase velocity and group velocity dispersion curves of the longitudinal mode, within a frequency range of 0–1 MHz, there are four guided wave modes from $L(0,1)$ to $L(0,4)$. Since the $L(0,2)$ guided wave mode is not dispersive, this mode is selected for the test.

In the design of the multiple cluster coil, the space D between adjacent clusters is half the wavelength of the longitudinal guided wave mode

$$D = \frac{\lambda}{2} = \frac{c_p}{2f} \quad (1.8)$$

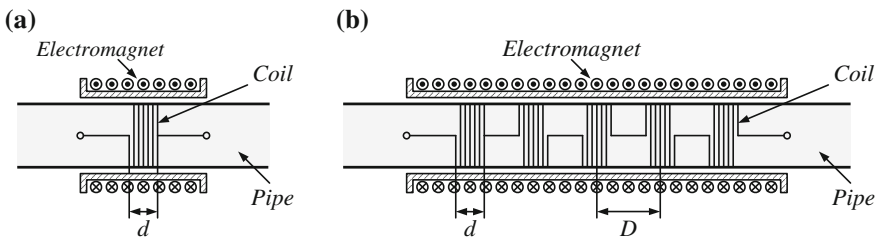


Fig. 1.17 The structure diagram of the longitudinal mode guided wave EMAT. **a** Single cluster coil and **b** multiple cluster coil

In the above equation, λ is the wavelength of the longitudinal guided wave mode; c_p is the phase velocity of the guided wave, and f is the frequency.

Thus, the space between adjacent clusters corresponds to the selected guided wave frequency. At the same time, adjacent clusters are wound along the clockwise and anticlockwise directions, respectively, making the directions of the currents in adjacent clusters opposite to each other to generate a dynamic magnetic field with opposite directions. Based on this design, when the particle vibration caused by a cluster propagates to the distance of $\lambda/2$ (the position of the adjacent cluster) with a phase velocity of c_p , it will produce constructive interference with the particle vibration in the same direction caused by the adjacent cluster, which will enhance the vibration intensity. For the guided waves of other modes, the phase velocity, frequency, and designed distance between adjacent clusters do not satisfy the relationship expressed in (1.8), and the particle vibrations caused by the adjacent clusters cannot generate the constructive interference and may even cancel out each other. Thus, if multiple cluster coil is used, the vibration intensity of the desired guided wave mode can be improved, and the generation of other guided wave modes can be restrained.

The design parameters of the EMAT multiple cluster coil that can excite the $L(0,2)$ guided wave mode are given in Table 1.1. From the phase velocity dispersion curve of the longitudinal guided waves in the pipe, at the 250 kHz frequency point, the phase velocity of the $L(0,1)$ mode is 2169 m/s and the wavelength is 8.68 mm, while the phase velocity of the $L(0,2)$ mode is 5364 m/s and the wavelength is 21.46 mm. In this way, when the spacing between adjacent cluster coil is designed as 10.73 mm, that is, half of the wavelength of the $L(0,2)$ mode, the $L(0,2)$ mode can be excited, while at the same time, the generation of the $L(0,1)$ mode guided wave is restrained.

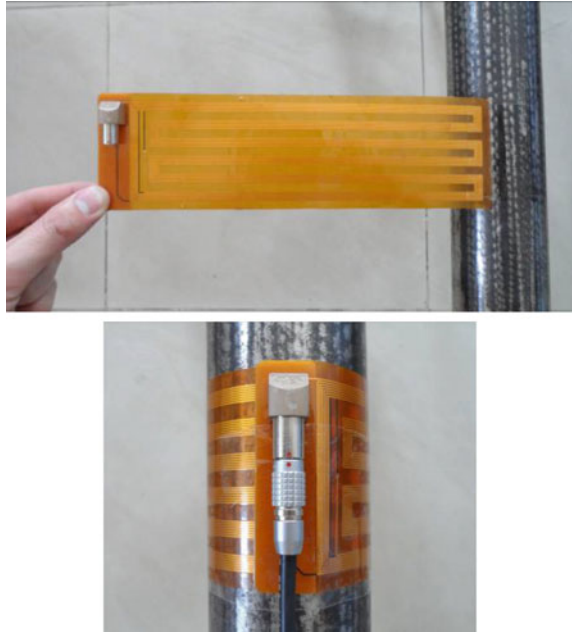
The width d of the single cluster coil should be smaller than or equal to half the wavelength of the desired guided wave mode; otherwise, the vibrations caused by the wire at the ends of the coil will cancel out each other, reducing the vibration intensity of the desired guided wave mode. When designing multiple cluster coil, the width of each cluster also needs to meet this requirement. Although the principle of interferometry cannot be used to enhance the vibration intensity of the desired guided wave mode when the single cluster coil is used, the longitudinal guided wave of different frequencies can be generated by adjusting the coil width, with great flexibility.

In the above design, the electromagnet and coil are both wound with enameled wire, so it is easy to adjust the intensity of the static bias magnetic field, the working

Table 1.1 The design parameters of the $L(0,2)$ mode guided wave EMAT with multiple cluster coil

Parameter	Value			
Guided wave frequency f (kHz)	100	150	200	250
Guided wave phase velocity c_p (m/s)	5412	5392	5378	5364
Distance between adjacent clusters D (mm)	27.06	17.97	13.45	10.73

Fig. 1.18 Coil made of the flexible printed circuit board



frequency of EMAT, the thickness and number of turns of the coil wire, and so on, which is convenient for use in the laboratory. However, multiple cluster coil used in practical engineering is often made of a flexible printed circuit board, while the magnet is made of the neodymium–iron–boron permanent magnet, as shown in Figs. 1.18 and 1.19.

A printed circuit board is used to make the EMAT coil. The width of the wire in the coil and the spacing between the adjacent clusters can be controlled with high accuracy, which benefits the miniaturization of the EMAT and improves its energy conversion efficiency. The magnets can be divided into four groups. Each group of

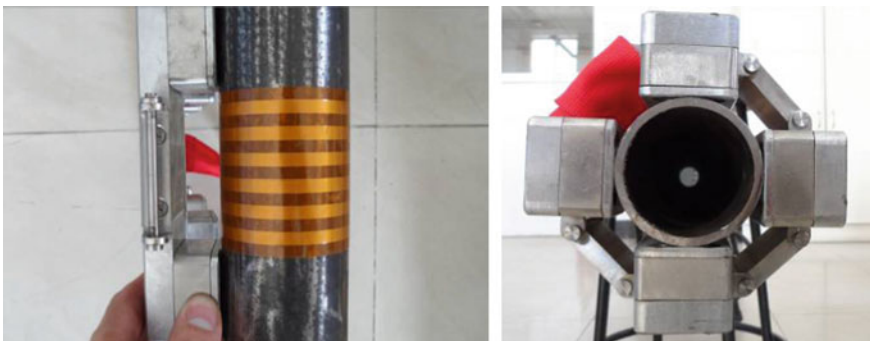


Fig. 1.19 A magnet made of the neodymium–iron–boron permanent magnet

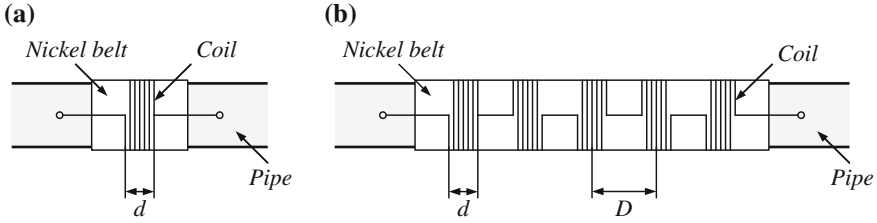


Fig. 1.20 The structure diagram of the torsional mode guided wave EMAT. **a** Single cluster coil and **b** multiple cluster coil

magnets is composed of two neodymium–iron–boron permanent magnets and an iron yoke. The different magnet groups are connected by a hinge. When they are used, the magnets can be placed on the outer surface of the pipeline axisymmetrically in order to provide a static bias magnetic field along the axial direction of the pipeline for the coils.

The structure of the torsional mode guided wave EMAT is shown in Fig. 1.20. The single cluster coil and multiple cluster coil are used. A premagnetized nickel belt is wrapped around the outer surface of the pipeline to generate the static bias magnetic field along the circumferential direction of the pipeline. The coil is wrapped along the circumferential direction of the pipeline to generate the dynamic magnetic field, the direction of which is perpendicular to the static bias magnetic field. Similar to the longitudinal guided wave EMAT, the single cluster coil width, distance between the adjacent clusters, etc., should meet the matching relationship of the selected guided wave mode.

The design parameters of the EMAT multiple cluster coil that can excite the $T(0,1)$ mode guided wave are given in Table 1.2. From the phase velocity dispersion curve of the torsional mode in the pipe, at the 190 kHz frequency point, the phase velocity of the $T(0,1)$ guided wave mode is 3200 m/s and the wavelength is 16.84 mm. In this situation, when the spacing between adjacent clusters is designed as 8.42 mm, that is, half the wavelength of the $T(0,1)$ mode, the $T(0,1)$ guided wave mode can be excited.

The premagnetized nickel strap can be fixed on the pipeline surface using either epoxy resin glue or a mechanical clamping ring, and the coil can be made of the enameled wire or the flexible printed circuit board. Since the EMAT with this kind of structure will first generate vibration inside the ferromagnetic nickel strap and

Table 1.2 The design parameters of the $T(0,1)$ mode guided wave EMAT multiple cluster coil

Parameter	Value		
Guided wave frequency f (kHz)	100	150	190
Guided wave phase velocity c_p (m/s)	3200	3200	3200
Distance between adjacent clusters D (mm)	16.00	10.67	8.42

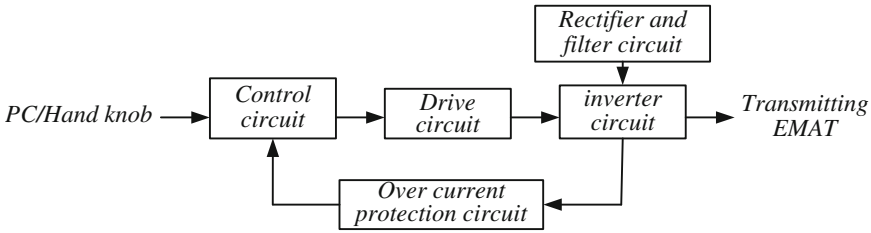


Fig. 1.21 A structure diagram of the electromagnetic ultrasonic guided wave excitation source

then couple the vibration into the tested pipeline, it can also be used to test a pipeline made of non-conducting or non-ferromagnetic material.

The circumferential electromagnetic ultrasonic excitation source is mainly composed of a control circuit, a drive circuit, a rectifier and filter circuit, an inverter circuit, and an overcurrent protection circuit. Its principle structure is shown in Fig. 1.21. Initially, the control circuit generates a control signal, either through the computer or using the parameter set by the hand knob. Then, the control signal is amplified by the driving circuit and drives the power MOSFET in the inverter circuit. Finally, the inverter circuit converts the DC voltage generated by the rectifier and filter circuit into the high-power pulse signal and outputs it to the excitation EMAT. At the same time, the output current of the inverter circuit is measured by the overcurrent protection circuit composed of a Hall sensor and an analog–digital converter, and it is fed back to the control circuit to realize the overcurrent protection.

The hardware programming language VHDL is used to write the control circuit program. It mainly includes modules such as the clock divider, the trigger, the control signal generation, and overcurrent protection. Its structure diagram is shown in Fig. 1.22. The clock divider module is based on the phase-locked loop in the FPGA.

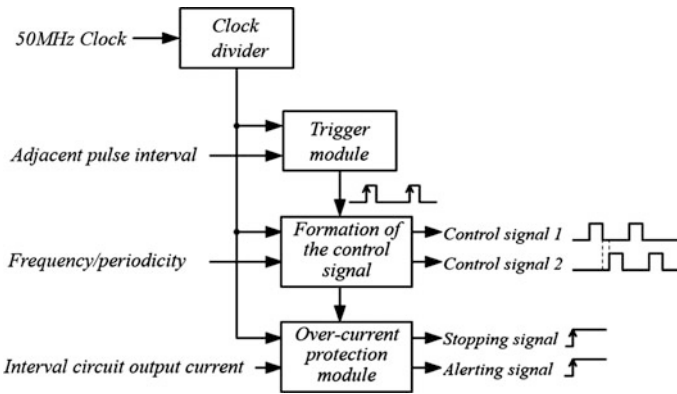


Fig. 1.22 A structure diagram of the control circuit program



Fig. 1.23 A structure diagram of the axial electromagnetic ultrasonic filtering amplifier

By frequency multiplication, the 50 MHz clock of the external active crystal oscillator is changed into a global clock with a frequency of 200 MHz. All signals in the FPGA are generated through edge-triggered counting of this global clock. In the trigger module, the counter X is defined. When the value of X is accumulated to the number of the global clock corresponding to the time interval of adjacent pulses, the trigger module will output a trigger signal, the time width of which is a global clock cycle. Then, the counter X is reset and the counting restarts. The rising edge of the trigger signal prompts the counters Y and Z in the control signal generation module to begin counting, while at the same time, a case structure is used to judge the numerical range of Y and Z . Double-channel control signal is generated according to the set excitation signal frequency and number of cycles and is used to control the switching element in the inverter circuit. The output current of the inverter circuit is monitored by the overcurrent protection module through the overcurrent protection circuit of the excitation source. If the peak value of the output current exceeds the established threshold value, the alerting signal and stopping signal are set from a low level to a high level by the overcurrent protection module, which will cause a buzzer to raise alarm. At the same time, the output of the excitation signal is stopped to make sure the whole excitation source is working within the safety range.

For the axial direction electromagnetic ultrasonic guided wave testing device, the filtering amplifier is mainly composed of a preamplifier, a band-pass filter circuit, and the main amplifying circuit. Its structure is shown in Fig. 1.23. Initially, the voltage signal detected by the receiving EMAT is amplified preliminarily; then, the band-pass filtering is made by the band-pass filter circuit, in which the guided wave frequency used in the actual application is taken as the center frequency; then, the signal after filtering is amplified further with the main amplification circuit. Finally, an oscilloscope or a computer is used to acquire and display the signal.

1.5.2.2 Experiment of the Axial Electromagnetic Ultrasonic Guided Wave Testing and the Influencing Factors

Firstly, longitudinal mode and torsional mode ultrasonic guided waves are generated by EMAT and the correctness of the excitation is verified through the measured wave velocity. Then, the influences of the number of cycles of the excitation signal, the static bias magnetic field, and the dynamic magnetic field on the guided wave signal amplitude are studied. Finally, for the artificial defect on the outer wall of the pipeline, the experiment of the axial electromagnetic ultrasonic guided wave is conducted.

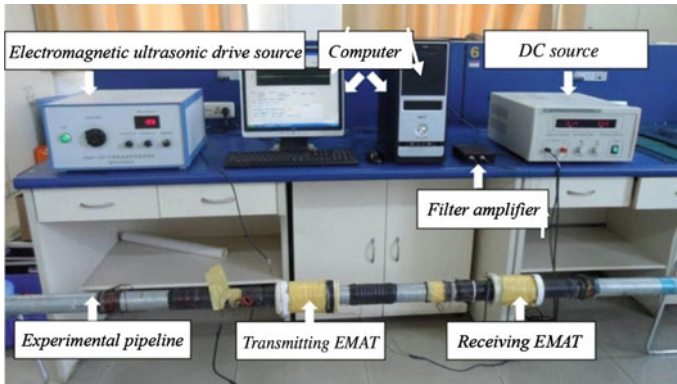


Fig. 1.24 The experimental system of the axial electromagnetic ultrasonic guided wave excitation and defect detection

The experimental system of the pipeline axial electromagnetic ultrasonic guided wave excitation and defect detection is shown in Fig. 1.24. It is mainly composed of the electromagnetic ultrasonic excitation source, the transmitting EMAT, the receiving EMAT, the filtering amplifier, the computer, direct current source, and the experimental pipeline. In the experiment, the high-power pulse excitation signal is generated by the electromagnetic ultrasonic excitation source and output to the excitation EMAT. The excitation EMAT is based on the magnetostrictive effect, and the ultrasonic guided wave propagating along the axial direction of the pipeline is generated in the pipe wall. The receiving EMAT is based on the inverse magnetostriction effect. The ultrasonic guided wave in the pipe wall is converted into a voltage signal. The voltage signal detected by the receiving EMAT is amplified and filtered by the filtering amplifier and then acquired and processed by the computer. The direct current inside the electromagnet of the EMAT is provided by the direct current source to generate the static bias magnetic field. For the tested pipeline, the external diameter is 59 mm, the inner diameter is 53 mm, and the length of pipeline is 3 m.

A PCI-9812 data acquisition card is installed in the computer in the experimental system to acquire the ultrasonic guided wave signal and convert it into a digital signal. The data acquisition card has four independent A/D channels, a 12-bit A/D resolution, and a synchronous sampling rate of up to 20 MS/s, which is good enough to meet the requirements of the acquisition and conversion of the ultrasonic guided wave signal. The PCI-9812 data acquisition card is very flexible in that the ultrasonic guided wave signal itself could be used as the trigger signal, and the external digital signal is also supported as the trigger signal. An EMAT data acquisition and analysis software is also installed in the computer. Its main interface is shown in Fig. 1.25. Using this software, we can set the trigger type, trigger level, sampling rate, and number of sampling points, and the acquired data can also be processed and analyzed by the software. The processing includes band-pass filtering, averaging of multiple acquisitions, and envelope calculation.

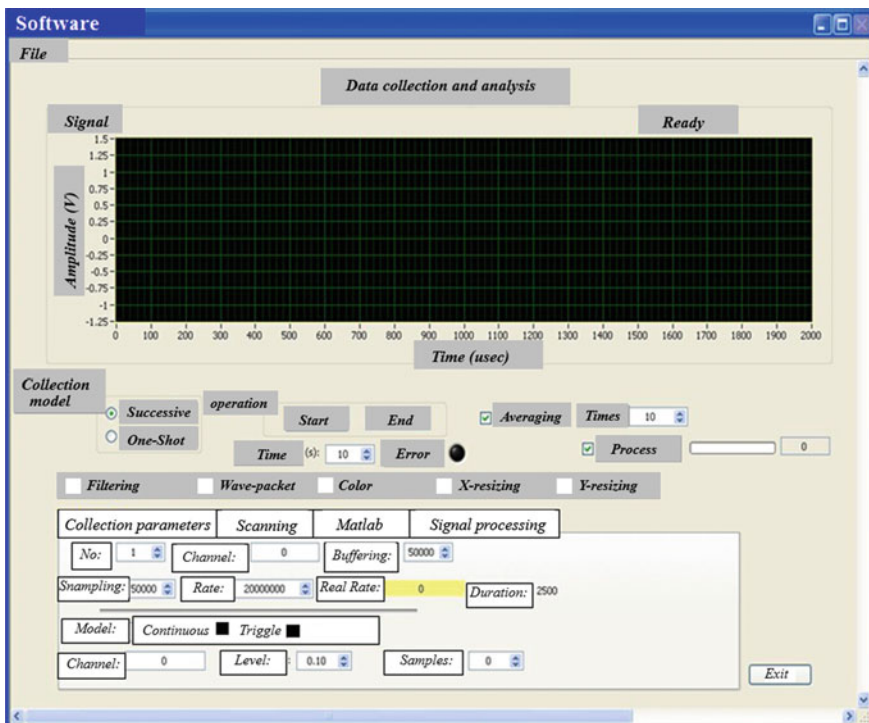


Fig. 1.25 The main interface of the EMAT data acquisition and analysis software

The ultrasonic guided wave has multimode characteristics. Multiple modes can exist at a certain frequency point. It is the basic precondition of pipeline testing to verify the correctness of the guided wave mode excitation. In practice, comparison of the measured wave velocity and the theoretical wave velocity is usually used to verify the excited guided wave mode is the desired mode.

When verifying the longitudinal guided wave mode, the experimental setup of the transmitting and receiving EMATs as shown in Fig. 1.26 is used. The distance

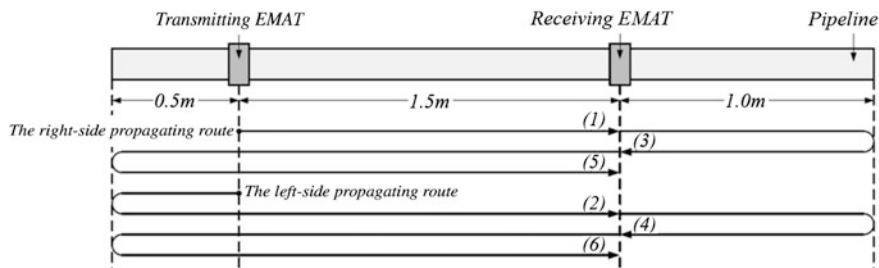


Fig. 1.26 The experimental setup for the longitudinal guided wave mode verification

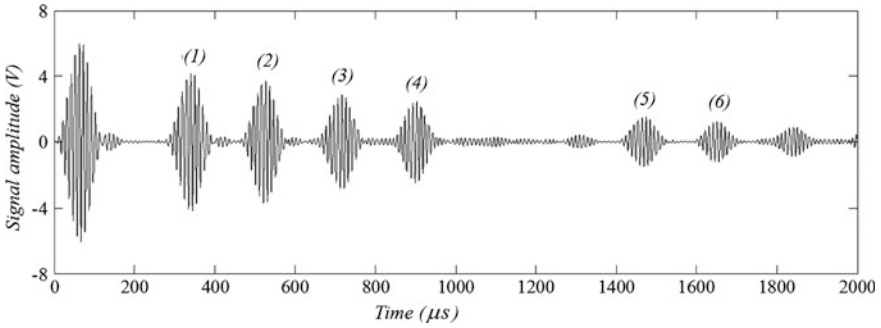


Fig. 1.27 The longitudinal guided wave mode signal

between the central position of the excitation EMAT and the left margin of the pipeline is 0.5 m. The coil is wound with copper enameled wire with a diameter of 1 mm into two layers, and each layer has 25 turns, with a total width of 25 mm. The distance between the central position of the receiving EMAT and the left margin of the pipeline is 2.0 m. The coil is wound with copper enameled wire with a diameter of 0.31 mm into four layers, and each layer has 70 turns, with a total width of 21.7 mm.

The amplitude of the excitation voltage of the transmitting EMAT is set at 50 V, the excitation frequency is 100 kHz, the number of cycles is 6, and the magnetizing current of the electromagnet is 6 A. A computer is used to acquire and filter the voltage signal detected by the receiving EMAT, and the obtained longitudinal guided wave signal is as shown in Fig. 1.27.

After the excitation signal is loaded into the transmitting EMAT, the longitudinal guided waves excited by the EMAT will propagate to the left and right directions. The guided wave propagation path is shown in Fig. 1.26, and the temporal relation of the signal features is shown in Fig. 1.27. It could be known that signal (1), signal (3), and signal (5) are the signal of directly arriving wave propagating to the right side, the signal of the wave reflected from the right margin, and the signal of the wave reflected from the left margin, respectively. Signal (2), signal (4), and signal (6) are the signal of the first wave propagating to the left side and reflected from the left margin, the signal of the reflected wave from the right margin, and the signal of the second wave reflected from the left margin, respectively. The unnumbered signal on the left side of signal (1) in Fig. 1.27 is the initial excitation signal sensed by the receiving EMAT through the space coupling, when the excitation signal is applied on the transmitting EMAT and is not the signal of the ultrasonic wave propagating in the pipe wall.

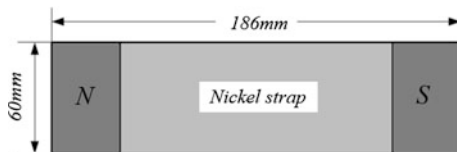
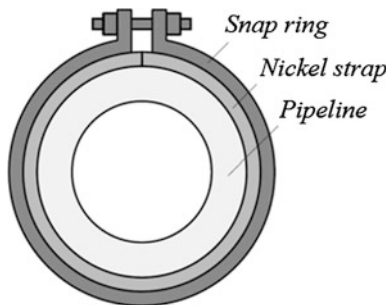
If signal (1) is taken as the reference, the difference in propagation distance between other signals and signal (1) can be obtained from Fig. 1.26. The delays of each signal compared with signal (1) can be obtained from Fig. 1.27, and then, the propagation velocity of the excited longitudinal guided wave can be calculated, with the results shown in Table 1.3.

Table 1.3 Experimental results of the longitudinal guided wave propagation velocity

Number	Propagation distance (m)	Propagation time (μ s)	Propagation velocity (m/s)
(2)	1.0	183	5464
(3)	2.0	375	5333
(4)	3.0	559	5366
(5)	6.0	1128	5319
(6)	7.0	1310	5344

From the group velocity dispersion curves of the longitudinal guided waves in the pipeline, at the frequency of 100 kHz, the theoretical value of the group velocity of the $L(0,2)$ guided wave mode is 5349 m/s. As shown in Table 1.3, the average value of the longitudinal guided wave propagation velocity is 5365 m/s. The error between the theoretical value and the experimental value of the $L(0,2)$ mode guided wave group velocity is 0.3 %. It can therefore be verified that the excited longitudinal guided wave is the $L(0,2)$ mode.

For the torsional mode guided wave EMAT, the nickel strap should be pre-magnetized first to generate the static magnetic field along the length direction of the EMAT. The method is shown in Fig. 1.28. The length of the nickel strap is 186 mm, its width is 60 mm, and its thickness is 0.2 mm. N and S represent two permanent magnets with opposite polarity. After the pre-magnetization, the nickel strap is wrapped around the outside surface of the pipeline along the circumferential direction and fixed in place by a snap ring, so it has tight contact with the pipeline surface. The method is shown in Fig. 1.29.

**Fig. 1.28** The pre-magnetization of the nickel strap**Fig. 1.29** The installation and fixation of the nickel strap

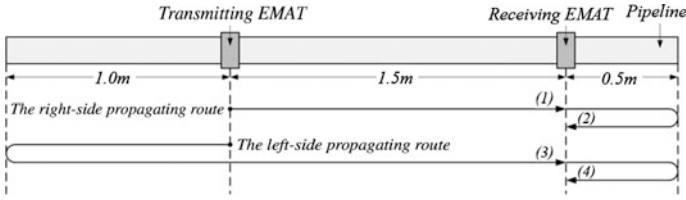


Fig. 1.30 The experimental setup for the verification of the torsional mode guided wave

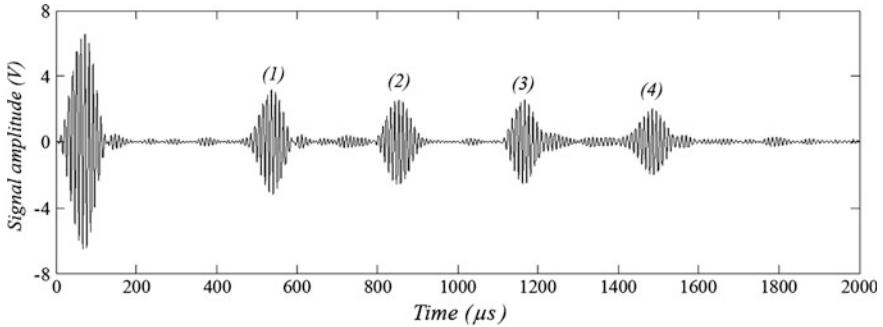


Fig. 1.31 The torsional mode guided wave signal

The setup of the transmitting EMAT and receiving EMAT for the verification of the torsional mode guided wave is shown in Fig. 1.30. The distance between the central position of the transmitting EMAT and the left margin of the pipeline is 1.0 m. The coil is wound with copper enameled wire with a diameter of 1 mm into four layers, and each layer has 12 turns, with a total width of 12.5 mm. The distance between the central position of the receiving EMAT and the left margin of the pipeline is 2.5 m. The coil is wound with copper enameled wire with a diameter of 0.31 mm into four layers, and each layer has 35 turns, with a total width of 12.4 mm.

It is assumed that the amplitude of excitation voltage of the transmitting EMAT is 50 V, the excitation frequency is 100 kHz, and the number of cycles is 6. A computer is used to acquire and filter the voltage signal detected by the receiving EMAT. The torsional mode signal is shown in Fig. 1.31.

After the excitation signal is applied to the transmitting EMAT, the torsional mode guided waves generated by the EMAT are propagating to the left and right sides, respectively. The guided wave propagation path is shown in Fig. 1.29, and the temporal relation of the signal features is shown in Fig. 1.30. It could be known that signal (1) and signal (2) are the signal of directly arriving wave propagating to the right side and the signal of the wave reflected from the right margin, respectively. Signal (3) and signal (4) are the signal of wave propagating to the left side and reflected by the left margin and the signal of the wave reflected from the right margin, respectively.

Table 1.4 Experimental results of the torsional guided wave propagation velocity

Number	Propagation distance (m)	Propagation time (μ s)	Propagation velocity (m/s)
(2)	1.0	314	3185
(3)	2.0	627	3190
(4)	3.0	947	3168

If signal (1) is taken as the reference, the difference in propagation distance between other signals and signal (1) can be obtained from Fig. 1.29. The delays of each signal compared with signal (1) can be obtained from Fig. 1.30, and then, the propagation velocity of the excited torsional guided wave can be calculated, with the results shown in Table 1.4.

From the group velocity dispersion curves of the torsional guided waves in the pipeline, at the frequency of 100 kHz, the theoretical value of the group velocity of the $T(0,1)$ guided wave mode is 3200 m/s. As shown in Table 1.4, the average value of the torsional guided wave propagation velocity is 3181 m/s. The error between the theoretical value and the experimental value of the $T(0,1)$ mode guided wave group velocity is 0.6 %. It can therefore be verified that the excited torsional guided wave is the $T(0,1)$ mode.

When the electromagnetic ultrasonic technology is used to test the pipeline, the excitation signal applied to the EMAT is usually the pulse containing several cycles of high-frequency signal. If the amplitude and frequency of the high-frequency signal remain unchanged, its number of cycles decides the energy from the excitation source to the EMAT and further decides energy of mechanical vibration of the ultrasonic waves inside the pipeline.

With the single cluster coil longitudinal guided wave EMAT, the amplitude of the excitation voltage of the transmitting EMAT is set at 20 V, the excitation frequency is 100 kHz, the magnetizing current of the electromagnet is 5 A, and the number of cycles N is tuned for the experiment. With the multiple cluster coil longitudinal guided wave EMAT, the coil of the transmitting EMAT is wound with copper enameled wire with a diameter of 1 mm into four clusters, each cluster having two layers and each layer having 7 turns of wire. The spacing between two adjacent clusters is 27 mm. The coil of the receiving EMAT is wound with copper enameled wire with a diameter of 0.31 mm into four clusters, each cluster having two layers and each layer having 15 turns of wire. The spacing between two adjacent clusters is 27 mm.

The amplitude of the excitation current of the transmitting EMAT is set at 16 A, the excitation frequency is 100 kHz, the magnetizing current of the electromagnet is 7 A, and the number of cycles N is tuned for the experiment.

When the number of periods of the excitation signal is 4, the amplitude of the direct arrival signal is taken as the denominator and the amplitudes of the direct arrival signals under the excitation signals with other numbers of periods are taken as the numerator. Then, we obtain the curve of variations of the relative value of the

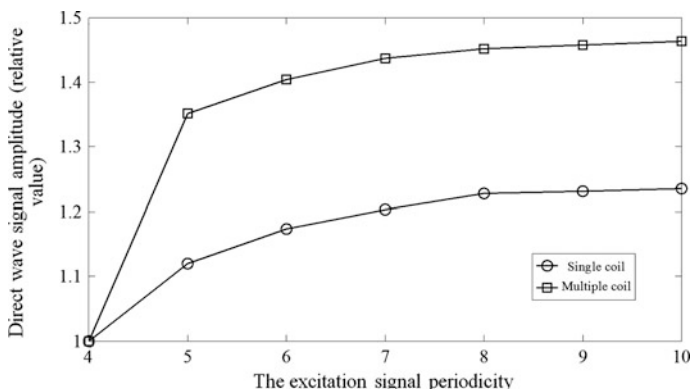


Fig. 1.32 Curve of variations of the relative value of the direct signal amplitude with the numbers of periods of the excitation signal

direct signal amplitude with the numbers of periods of the excitation signal, as shown in Fig. 1.32.

It can be seen that whether the single cluster coil EMAT or the multiple cluster coil EMAT is used, the amplitude of the guided wave signal will be improved with increase in the number of cycles of the excitation signal, but there is a saturation effect. When the number of periods of the excitation signal changes in the range from 4 to 8, with the increase of the number of periods of the excitation signal, the amplitude of the guided wave signal increases greatly. When the number of periods of the excitation signal is bigger than 8, the effect of increasing the signal amplitude through increasing the number of periods of the excitation signal is weakened. The distance between the adjacent coil clusters in the multiple cluster coil has a matching relationship with the wavelength of the excited guided wave, which means that the particle vibrations of the adjacent clusters have constructive interference, while there is no corresponding relationship between the single cluster coil structure and the wavelength of the excited guided wave. The effect of increasing the signal amplitude through increasing the number of periods of the excitation signal is not as obvious as in the case for the multiple cluster coil structure.

In addition, with the increase of the number of periods of the excitation signal, the time width of the guided wave signal will also increase accordingly and the spatial resolution of defect detection will decrease. So, when we select the number of periods of the excitation signal, its influence on the guided wave signal amplitude and spatial resolution of defect detection should be considered comprehensively to achieve a good testing effect.

The intensity of the bias magnetic field can also affect the received signal. The peak of the excitation current of the transmitting EMAT coil is set at 8 and 14 A, adjusting the magnetizing current of the electromagnet. The data of the signal detected by the receiving EMAT are shown in Fig. 1.33.

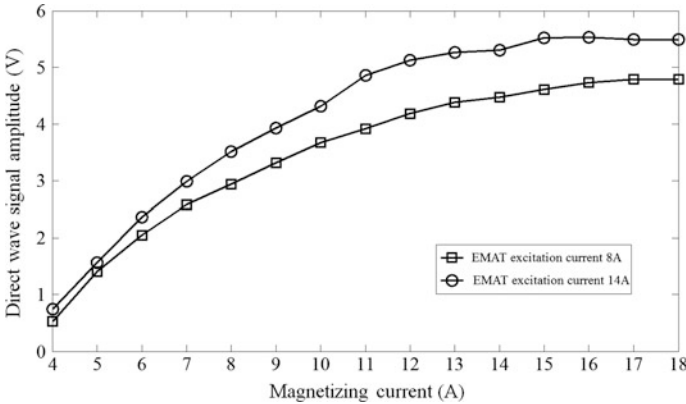


Fig. 1.33 Variation of the direct arrival wave signal amplitude with magnetizing current of the electromagnet

It can be seen that when the magnetizing current of the electromagnet is lower than 15 A, the direct arrival signal amplitude will increase linearly with the increasing magnetizing current of the electromagnet. When the magnetizing current of the electromagnet is higher than 15 A, the direct arrival signal amplitude will tend to a stable value and does not change with increasing magnetizing current of the electromagnet. The finite element simulation shows that when the magnetizing current of the electromagnet is 15 A, the magnetic induction intensity in the pipe wall is in the range of 1.6–2.0 T. At this time, the tested pipeline has already entered the saturation state. Thus, in practice, the EMAT DC bias magnetic field should be set such that the pipe wall is close to the saturation state, so that higher conversion efficiency between the electric energy and acoustic energy can be achieved.

In order to verify the testing ability of EMAT along the pipeline axial direction, an artificial defect is machined on the outer wall of the tested pipeline, and its shape is as shown in Fig. 1.34. The length of the artificial defect along the pipeline circumferential direction is 40 mm, and its width along the pipeline axial direction is 4 mm. Its maximum depth along the pipeline radial direction is 2 mm.

When the $L(0,2)$ guided wave mode is used to detect the defect in the pipe, the arrangement of the transmitting EMAT and receiving EMAT is as shown in Fig. 1.35. The distance from the center position of the transmitting EMAT to the left margin of the pipe is 1.745 m. The coil is wound with copper enameled wire



Fig. 1.34 A sketch of the artificial defect in the outer wall of the experimental pipeline

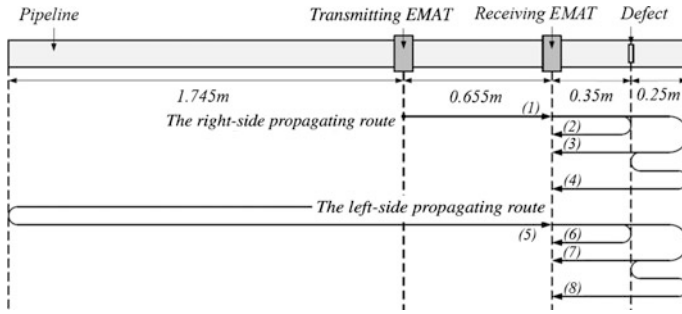


Fig. 1.35 The experimental setup of the defect detection in the pipe by the $L(0,2)$ guided wave mode

with a diameter of 1 mm into eight clusters, each cluster having two layers and each layer having 3 turns of wire. The spacing between two adjacent clusters is 10.8 mm. The distance from the center position of the receiving EMAT to the left margin of the pipe is 2.4 m. The coil is wound with copper enameled wire with a diameter of 0.31 mm into eight clusters, each cluster having two layers and each layer having 10 turns of wire. The spacing between two adjacent clusters is 10.8 mm. The distance from the center position of the artificial defect to the left margin of the pipe is 2.75 m.

The amplitude of the excitation voltage of the transmitting EMAT is set at 350 V, the excitation frequency is 250 kHz, the number of cycles is 12, and the magnetizing current of the electromagnet is 15 A. The $L(0,2)$ mode guided wave signal detected by the receiving EMAT is shown in Fig. 1.36.

After the excitation signal is applied to the transmitting EMAT, the $L(0,2)$ mode guided waves generated by the EMAT are propagating to the left and right sides. The guided wave propagation path is shown in Fig. 1.35, and the temporal relation

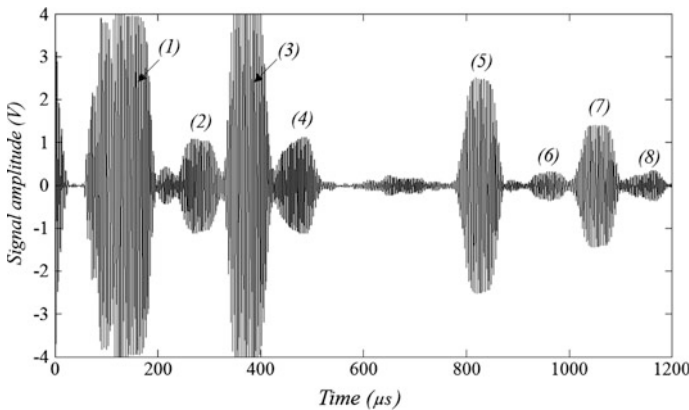


Fig. 1.36 The $L(0,2)$ mode guided wave signal in the pipeline with defect

Table 1.5 The results of the $L(0,2)$ guided wave mode propagation velocity

Number	Propagation distance (m)	Propagation time (μs)	Propagation velocity (m/s)
(3)	1.20	230	5217
(5)	3.49	670	5209
(7)	4.69	900	5211

of the signal features is shown in Fig. 1.36. It could be known that signal (1), signal (2), signal (3), and signal (4) are the signal of directly arriving wave propagating to the right side, the signal of the wave reflected from the defect, the signal of first reflection from the right margin, and the signal of second reflection from the right margin, respectively. Signal (5), signal (6), signal (7), and signal (8) are the signal of wave propagating to the left side and reflected by the left margin, the signal of the wave reflected from the defect, the signal of first reflection from the right margin, and the signal of second reflection from the right margin, respectively. It must be noted that since the artificial defect is a non-axisymmetric defect, when the $L(0,2)$ mode guided wave is reflected at the artificial defect, the $L(0,1)$ guided wave mode and torsion mode of the guided wave can also be generated.

If signal (1) is taken as the reference, the difference in propagation distance between other signals and signal (1) can be obtained from Fig. 1.35. The delays of each signal compared with signal (1) can be obtained from Fig. 1.36, and then, the propagation velocity of the excited $L(0,2)$ mode guided wave can be calculated, with the results shown in Table 1.5.

As shown in Table 1.5, the average value of the $L(0,2)$ mode guided wave propagation velocity is 5212 m/s. It can be obtained from Fig. 1.35 that the delayed time of the reflection wave signal (2) relative to the direct arrival signal (1) is 135 μs . The difference in propagation distance between the defect echo signal (2) and direct arrival signal (1) is

$$L = 5212 \times 135 \times 10^{-6} = 0.704 \text{ m} \quad (1.9)$$

Therefore, the distance between the defect and the receiving EMAT is

$$d = \frac{L}{2} = 0.352 \text{ m} \quad (1.10)$$

The actual distance between the artificial defect and the receiving EMAT is 0.35 m. Using the $L(0,2)$ mode, the detected distance from the defect to the receiving EMAT is 0.352 m and the relative error is 0.6 %. It can be seen that the artificial defect on the outside surface of the pipeline can be detected effectively using the $L(0,2)$ guided wave mode, and with this mode, a higher accuracy of defect locating could be achieved.

When the $T(0,1)$ guided wave mode is used to detect the defect in the pipe, the arrangement of the transmitting EMAT and receiving EMAT is as shown in Fig. 1.37. The distance from the center position of the transmitting EMAT to the left

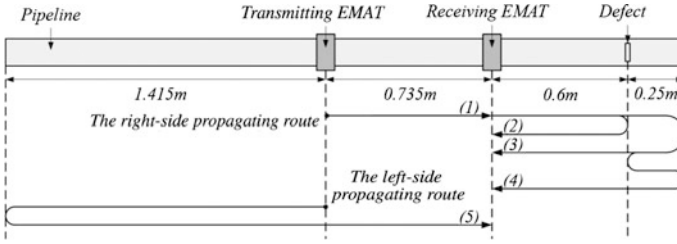


Fig. 1.37 The experimental setup for defect detection in the pipe by the $T(0,1)$ mode

margin of the pipe is 1.415 m. The coil is wound with copper enameled wire with a diameter of 1 mm into six clusters, each cluster having two layers and each layer having 3 turns of wire. The spacing between two adjacent clusters is 8.4 mm. The distance from the center position of the receiving EMAT to the left margin of the pipe is 2.15 m. The coil is wound with copper enameled wire with a diameter of 0.31 mm into six clusters, each cluster having two layers and each layer having 8 turns of wire. The spacing between two adjacent clusters is 8.4 mm. The distance from the center position of the artificial defect to the left margin of the pipe is 2.75 m.

The amplitude of the excitation voltage of the transmitting EMAT is set at 350 V, the excitation frequency is 190 kHz, and the number of periods is 10. The $T(0,1)$ mode guided wave detected by the receiving EMAT is shown in Fig. 1.38.

After the excitation signal is applied to the transmitting EMAT, the $T(0,1)$ mode guided waves generated by the EMAT are propagating to the left and right sides. The guided wave propagation path is shown in Fig. 1.37, and the temporal relation of the signal features is shown in Fig. 1.38. It could be known that signal (1), signal (2), signal (3), and signal (4) are the signal of directly arriving wave propagating to the right side, the signal of the wave reflected from the defect, the signal of first reflection from the right margin, and the signal of second reflection from the right

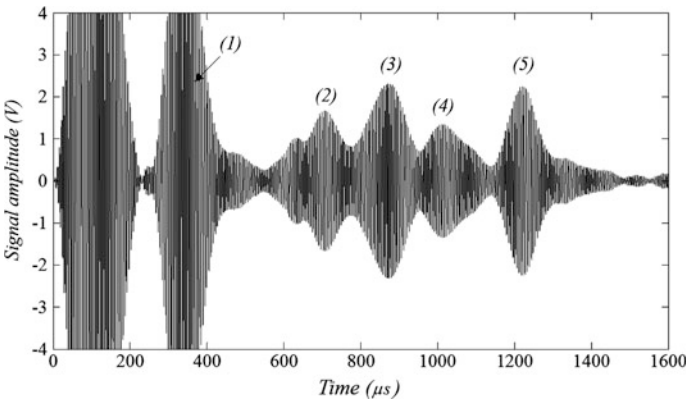


Fig. 1.38 The $T(0,1)$ mode guided wave signal in the pipeline with defect

Table 1.6 The results of the $T(0,1)$ guided wave mode propagation velocity

Number	Propagation distance (m)	Propagation time (μ s)	Propagation velocity (m/s)
(3)	1.70	536	3172
(5)	2.83	885	3198

margin, respectively. Signal (5) is the signal of wave propagating to the left side and reflected by the left margin. Similar to the $L(0,2)$ guided wave mode, when the $T(0,1)$ mode guided wave is reflected at the non-axisymmetric artificial defect, it can also generate the torsional mode.

If signal (1) is taken as the reference, the difference in propagation distance between other signals and signal (1) can be obtained from Fig. 1.36. The delays of each signal compared with signal (1) can be obtained from Fig. 1.37, and then, the propagation velocity of the excited $T(0,1)$ mode guided wave can be calculated, with the results shown in Table 1.6.

As shown in Table 1.6, the average value of the $T(0,1)$ mode guided wave propagation velocity is 3185 m/s. It can be obtained from Fig. 1.37 that the delayed time of the reflection wave signal (2) relative to the direct arrival signal (1) is 370 μ s. The difference in propagation distance between the defect echo signal (2) and direct arrival signal (1) is

$$L = 3185 \times 370 \times 10^{-6} = 1.178 \text{ m} \quad (1.11)$$

Therefore, the distance between the defect and the receiving EMAT is

$$d = \frac{L}{2} = 0.589 \text{ m} \quad (1.12)$$

The actual distance between the artificial defect and the receiving EMAT is 0.6 m. Using the $T(0,1)$ mode, the detected distance from the defect to the receiving EMAT is 0.589 m and the relative error is 1.8 %. It can be seen that the artificial defect on the outside surface of the pipeline can be detected effectively using the $T(0,1)$ guided wave mode, and with this mode, a higher accuracy of defect locating could be achieved.

1.5.3 Electromagnetic Ultrasonic Guided Wave Testing for Cracks in the Natural Gas Pipeline

The inspector includes three sections, with each section containing three groups of testing probes arranged evenly along the circumferential direction of the pipeline. The testing probes of two adjacent sections are arranged with a staggered angle of 30°, as in Fig. 1.39. Each group of testing probes contains one transducer from each of the three different types of EMATs. The circumferential guided wave



Fig. 1.39 A structure diagram of the electromagnetic ultrasonic inspector for crack detection

electromagnetic ultrasonic probe is used to detect stress corrosion cracks; the surface wave electromagnetic ultrasonic probe is used to detect inner surface cracks and distinguish between cracks on the inside and outside wall of the pipeline; the vertical incident wave electromagnetic ultrasonic probe is used to check pipe wall thickness and identify the circumferential weld for the accurate location and quantification of the defect. The first section of the inspector is equipped with two seal cups and six supporting wheels; the second section is equipped with two supporting cups, and the internal sealed cabin contains a battery; the third section is equipped with two supporting cups, and the internal sealed cabin contains an electronic data recorder. These three sections are connected by a universal joint, as shown in Fig. 1.39.

In order to avoid cross talk between channels and improve the excitation power of the electromagnetic ultrasonic probe, an independent physical channel is used in the excitation circuit and signal detection circuit of the 27 probes of the inspector, each probe having a dual role of exciting and receiving of the ultrasonic signals.

The pulse signal is output by the signal-generating unit and excites the transmitting coil of the excitation probe after the power amplification. Under the excitation of the pulsed current, the ultrasonic wave is excited by the transmitting coil. The electromagnetic ultrasonic signal is recorded by the receiving coil and then saved to the electronic hard disk after amplification, filtering, data acquisition, and data compression. After the testing project, the saved test data are transferred onto a computer and the results are analyzed using dedicated data analysis software.

The pulsed power supply is composed of a signal-generating unit and a power amplification unit. The phase-shift full-bridge control chip UCC2895 is used in the signal-generating unit. Its characteristics are as follows: The output open time delay and self-adaption time delay can be set through programming; it can be used either in voltage mode or in current mode; it has a soft close function; its maximum operating frequency is 1 MHz; and the complementary square wave signal is output from two pins OUTA and OUTB, the duty cycle being adjustable from 0 to 100 %. Because the working frequency range of the EMAT is usually from 100 kHz to 1 MHz, the UCC2895 can meet the requirements of the probe on the pulsed power supply.

The circuit connection diagram of the signal-generating unit is shown in Fig. 1.40.

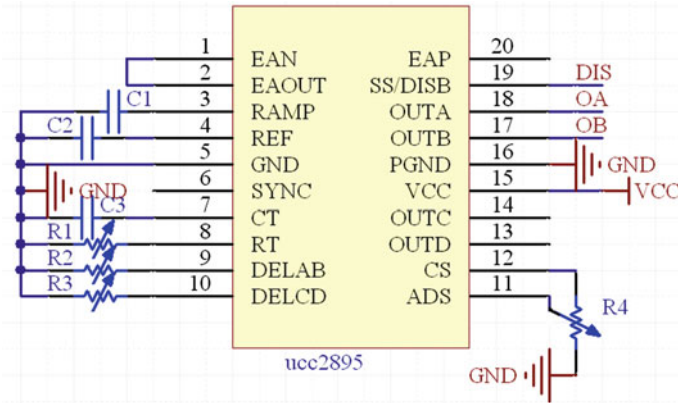


Fig. 1.40 The circuit connection diagram of UCC2895

The signal cycle is determined by the capacitance $C3$ and the resistance $R1$. The cycle satisfies

$$t_{osc} = \frac{5 \times R1 \times C3}{48} + 120 \text{ ns} \tag{1.13}$$

The duty cycle of the square signal is determined by the resistances $R2$, $R3$, and $R4$. In order to generate a group of pulse signals, the UCC2895 should be controlled. The chip has the control pin SS/DISB. As long as the pin is set to a low level, the OUTA and OUTB will output low-level voltage. A microcontroller is used to output the high- to low-level voltage regularly to the SS/DISB so that the UCC2895 chip can be controlled to output the square wave pulse periodically. The pulsed square wave is amplified by the power amplification unit and becomes a large current pulse. In the power amplification unit, the MOSFET is used as the power device, and a full-bridge circuit structure is designed. MOSFET works in the switching state; the consumed power of its own is small, which improves the efficiency of the pulsed power supply.

In order to improve the energy conversion efficiency of the electromagnetic ultrasonic probe, the receiving coil is matched with capacitors in parallel so that the signal amplitude can be improved. Because the received signal is at a microvolt level, a perfect shielding and ground connection are needed, and a weak signal amplifier with high precision and low noise also needs to be designed.

AD797 has the characteristics of ultralow noise and low distortion. The bandwidth can reach up to 110 MHz and the response speed is 20 V/μs, which is suitable for preamplification. A LT1568 chip is used in the design of the band-pass filter to remove the noise signal. Through the amplification of the main amplifier, the gain can reach up to 80 dB.

The 27-channel parallel ADC is used to complete the parallel sampling of each channel. FPGA is used as the controlling core of the acquisition system, in charge

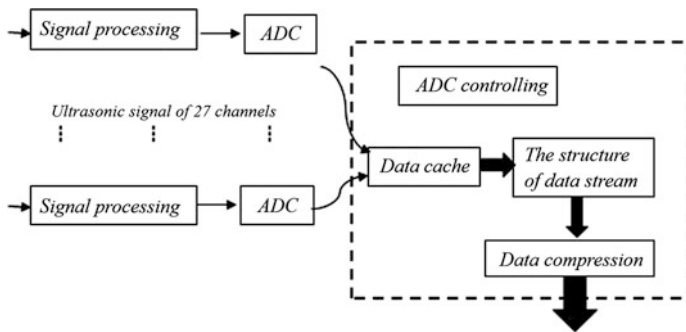


Fig. 1.41 The functional block diagram of the data acquisition, compression, and storage

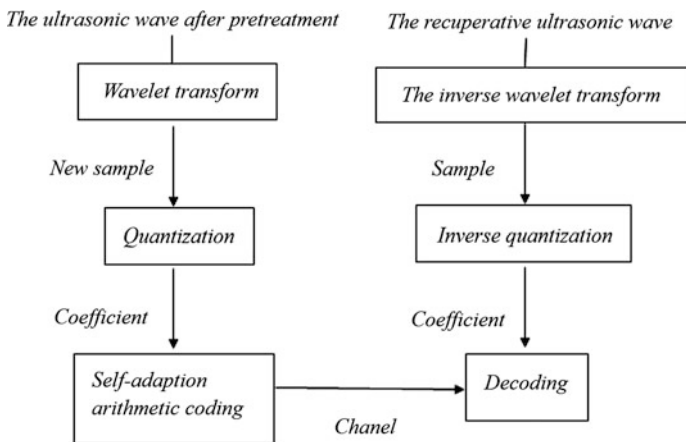


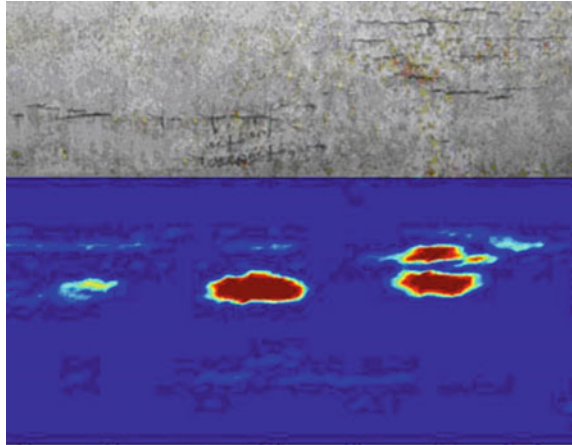
Fig. 1.42 The functional block diagram of the data compression

of controlling the parallel sampling of the ADC, organizing the data flow, and compressing and storing the data. Its functional block diagram is shown in Fig. 1.41.

The compression mainly contains two parts: the wavelet transform and the self-adaptation arithmetic coding. Its functional block diagram is shown in Fig. 1.42. Both the wavelet transform and self-adaptation arithmetic coding can be realized through FPGA, with the main modules established using the VHDL language.

A hybrid programming method using Visual C and LabVIEW is adopted to develop the data analysis software. The software has a friendly user interface and has a strong ability for data analysis and processing. The functions that can be achieved using this software are as follows: the automatic importing of the test data into the database, displaying the image (C-S scan) of the planar scanning of the pipeline conditions and the ultrasonic waveform plot of the crack defect, identifying the pipe welds automatically, and quantifying and locating the crack defect, etc. For

Fig. 1.43 Result comparison of magnetic particle inspection and electromagnetic ultrasonic testing of cracks in the pipeline



the test data, the switch display between the spatial domain and time domain can be conducted conveniently. It also has functions such as filtering, spectral analysis, automatic capture, and measure of the local peak value. A comparing display window is available in this software, with local plot zooming function. According to the needs, the user can select to display one or all of the following: the original signal, the envelope of the original signal, and the filtered signal.

The experiment of electromagnetic ultrasonic crack detection is conducted on the natural gas pipeline that has stress corrosion cracks. It shows that the crack with a minimum length of 20 mm and minimum depth of 1 mm can be detected effectively, and it has a resolving ability for crack clusters. The experimental result is shown in Fig. 1.43.

The highest testing speed is 2 m/s and the longest testing distance is 100 km, and it can pass through a 1.5D bend of the natural gas pipeline. Based on the development of the natural gas pipeline, higher pressure and higher throughput of the pipe will be the future trend. If we can improve the testing speed and single run distance of the inspector, the electromagnetic ultrasonic crack detector will have better adaptability. With the development of electronic techniques and computer technology, the testing speed can be improved significantly if rapid acquisition and storage technology for large volumes of data are introduced in electromagnetic ultrasonic inspectors for natural gas pipelines in the near future.

References

1. Masahiko, H., Hirotsugu, O.: EMATs for science and industry non-contacting ultrasonic measurements. Kluwer Academic publishers, Boston (2003)
2. Randall, R.H., Rose, F.C., Zener, C.: Intercrystalline thermal currents as a source of internal friction. *Phys. Rev.* **56**, 343 (1939)

3. Akseno, S.I., Vkin, B.P., Vladimirskii, K.V.: The excitation of ultrasonic vibrations by ponderomotive forces. *J. Exper. Theoret. Phys. USSR* **128**, p. 762 (1955)
4. Alers, G., Mclauchlan, D., Maiseri, H., et al.: Development of a prototype EMAT system for inspection of rails. United States Federal Railroad Administration, Report. (FRA/RD-80/45): 71 (1980)
5. Thompson, R.B., Elsley, R.K.: A prototype EMAT system for inspection of steam generator tubing. Electric Power Research Institute (Report) EPRI NP (1983)
6. Maxfield, B.W., Kuramoto, A., Hulbert, J.K.: Using EMATs for High Temperature Ultrasonics. Int Committee on Nondestructive Testing, Columbus (1985)
7. Alers, G.A.: EMATS as Noncontact Transducers for Tube Inspection. Cincinnati, OH, USA. Iron & Steel Soc of AIME, Warrendale (1991)
8. Hirao, M., Ogi, H., Fukuoka, H.: Advanced ultrasonic method for measuring rail axial stresses with electromagnetic acoustic transducer. *Res. Nondestr. Eval.* **5**(3), 211–223 (1994)
9. Fujisawa, K., Murayama, R., Yonehara, S., et al.: Measuring equipment of residual stress in railroad wheel by EMAT. *NDT E Int.* **27**(2), 113 (1994)
10. Gori, M., Giamboni, S., D'Alessio, E., et al.: Guided waves by EMAT transducers for rapid defect location on heat exchanger and boiler tubes. *Ultrason.* **34**(2–5), 311–314 (1996)
11. Sebko, V.P., Suchkov, G.M., Malakhov, A.V.: Ultrasonic testing of rail heads with EMA (electromagnetic-acoustic) method. *Defektoskopiya* **7**, 17–25 (2004)
12. Ho, K.S., Billson, D.R., Hutchins, D.A.: Inspection of drinks cans use non-contact electromagnetic acoustic transducers. *J. Food Eng.* **80**(2), 431–444 (2007)
13. Vasiljevic, M., Kundu, T., Grill, W., et al.: Pipe wall damage detection by electromagnetic acoustic transducer generated guided waves in absence of defect signals. *J. Acoust. Soc. Am.* **123**(5), 2591–2597 (2008)
14. Maxfield, B.W., Kuramoto, A., Hulbert, J.K.: Evaluating EMAT designs for selected applications. *Mater. Eval.* **45**(10), 1166–1183 (1987)
15. Komarov, V.A., Pakhomov, P.A.: A quasi-steady electromagnetic acoustic transducer of null modes of lamb waves in plates (generation of waves). *Russ. J. Nondestr. Test.* **28**(7), 392–399 (1992)
16. He, F., Rokhlin, S.I., Adler, L.: Application of SH and Lamb wave EMAT's for evaluation of adhesive joint in thin plate. *Rev. Prog. Quant. Nondestr. Eval.* **7B**, 911–918 (1988)
17. Yamasaki, T., Hirao, M., Fukuoka, H.: Generation of S₀ mode lamb wave using electromagnetic acoustic transducers. *Nippon Kikai Gakkai Ronbunshu, Hen Trans. Jan. Soc. Mech. Eng. Part A* **61**(585), 1136–1142 (1995)
18. Murayama, R.: Driving mechanism on magnetostrictive type electromagnetic acoustic transducer for symmetrical vertical-mode Lamb wave and for shear horizontal-mode plate wave. *Ultrasonics* **34**(7), 729–736 (1996)
19. Voltmer, F.W., White, R.M., Turner, C.W.: Magnetostrictive generation of surface elastic waves. *Appl. Phys. Lett.* **15**(5), 153–154 (1969)
20. Sethares, J.C., Frost, H.M., Szabo, T.L.: Fields of flat conductor electromagnetic surface acoustic wave transducers. *IEEE Trans. Son. Ultrason.* **SU-24**(2), 88–94 (1977)
21. Edwards, R.S., Dixon, S., Jian, X.: Enhancement of the Rayleigh wave signal at surface defects. *J. Phys. D Appl. Phys.* **37**(16), 2291–2297 (2004)
22. Thompson, R.B.: New configurations for the electromagnetic generation sh waves in ferromagnetic materials. In: *Proceedings of the Symposium on Ultrasonics*, pp. 374–378 (1978)
23. Igarashi, B., Alers, G.A.: Excitation of bulk shear waves in steel by magnetostrictive coupling. In: *Proceedings of the IEEE Ultrasonics Symposium*, vol. 1, 893–896 (1998)
24. Hobbis, A., Aruleswaran, A.: Non-contact thickness gauging of aluminium strip using EMAT technology. *Nondestr. Test. Eval.* **20**(4), 211–220 (2005)
25. Vasile, C.F., Thompson, R.B.: Periodic magnet non-contact electromagnetic acoustic wave transducer-theory and application. In: *Proceedings of the Symposium on Ultrasonics*, pp. 84–88 (1977)

Chapter 2

The Pulsed Eddy Current Testing

As one kind of eddy current testing technology, the pulsed eddy current testing technology is based on the principle of electromagnetic induction and is used to detect the defects in conductive materials. The principle of pulsed eddy current testing is basically the same as that of traditional eddy current testing, and differences are the means of excitation and the signal analysis method.

In the early 1970s of the twentieth century, Witting et al. proposed the pulsed eddy current method. With this method, the rectangle pulse is applied to the exciting coil, and time-domain analysis is conducted to the voltage pulse received by the testing coil [1]. In recent years, in order to overcome the shortcomings of the conventional eddy current testing method, the Iowa State University and the US Federal Aviation Administration have jointly commissioned a study of the pulsed eddy current method and developed a corresponding testing device. At the 2002 ATA NDT Forum held in Houston, the pulsed eddy current method was universally recognized by the aviation industry.

Due to the jumps of the excitation pulse at the rising and falling edges, eddy currents will be induced in the specimen. Compared to the conventional eddy current testing using single frequency sinusoidal excitation, frequency spectrum of the excitation signal of the pulsed eddy current testing has richer contents, and with it, the response will contain multiple frequency components. In view of the relationship between the eddy current penetration depth and the frequency of excitation source, from one single pulse excitation, all the defect information within a certain depth is obtained.

Basic principle of the pulsed eddy current testing is conducting transient analysis for the magnetic field generated by the eddy current signal sensed by the testing coil and studying the defects through detecting the peak value of the voltage induced by the magnetic field and its corresponding time instant. The smaller is the depth of the defect, the stronger is the magnetic field generated by the eddy current, and the

higher is the peak value of the induced voltage, the sooner is the time instant that this peak value appears. On the other hand, with the same depth, the bigger is the defect, the higher is the peak value of the induced voltage.

In conventional eddy current testing device, different sensors and signals of different frequencies must be configured to detect defects at different depths of the tested object. While with the pulsed eddy current testing, it is not necessary to replace the sensor and change the frequency of the excitation signal according to the testing depth, because with one test, defects of different depths in the sample can be detected [2].

In the pulsed eddy current testing, another advantage of the wideband signal is better noise suppression. Based on the principle of the multifrequency eddy current, response of each frequency can cancel out an interfering factor. In the response of the pulsed eddy current testing, more frequency components are included, so noises from different sources can be suppressed. The pulsed eddy current testing also has other advantages. The operation is simple, the testing speed is high, the structure is simple [3], and the excitation signal is stable and so on.

The analysis of the data of the pulsed eddy current testing is mainly conducted in the time domain, for example, at the Iowa State University, and the defects in the aircraft structure were evaluated using the peak value and the corresponding time instant [4]. With only the time-domain analysis, the rich information about the defects contained within the wideband pulse excitation is not fully exploited. At Newcastle University, a principal component analysis (PCA) method was used to extract the “time rising point,” the extracted features were used to classify the surface, subsurface, and corrosion cracks, and the performance was better than that with the classification according to the time-domain features [5, 6].

In recent years, the pulsed eddy current testing method is applied in stress evaluation [7]. It is also used to heat the tested object to conduct a fast and large area thermography testing [8].

2.1 Basic Principle of Electromagnetism

When the detection coil loaded with alternating current is placed near the object to be tested, because of the effect of the exciting magnetic field, eddy currents will be induced in the tested object. The amplitude, phase, and path of the eddy current are under the influence of the properties of the object to be tested, and the magnetic field generated by the eddy current in the tested object will induce a voltage in the coil. Thus, by observing the changes of induced voltage on the coil, we can determine whether the tested object is flawed.

Because the magnetic field generated by the alternating excitation current is also alternating, the eddy current in the tested object is alternating. Then, the magnetic field in the testing coil is a combination of the excitation magnetic field and the magnetic field of the eddy current.

Assuming that the excitation signal does not change, and the distance between the coil and the tested object remains unchanged, then the intensity and distribution

of the eddy current and the generated magnetic field are determined by the nature of the metal being tested. Therefore, from the synthetic magnetic field, whether the properties of the tested object change could be told, the change could be transformed by the magnetic sensor into electrical signal outputs. The pulsed eddy current testing is based on the theory of electromagnetic induction, so Maxwell's equations become the necessary analysis tools.

2.1.1 The Penetration Depth and the Skin Effect

As a theoretical basis for analysis of eddy current testing, Maxwell's equations are as follows:

$$\begin{cases} \nabla \times H = J + \frac{\partial D}{\partial t} \\ \nabla \times E = -\frac{\partial H}{\partial t} \\ \nabla \cdot D = \rho \\ \nabla \cdot B = 0 \end{cases} \quad (2.1)$$

in which $B = \mu H$, $D = \varepsilon E$, $J = \sigma E$, σ is the electric conductivity, μ is the magnetic permeability, ε is the electric permittivity, J is the electric current density, E is the electric field strength, H is the magnetic field strength, B is the magnetic induction strength, D is the electric flux density, and ρ is the free charge density.

For the traditional sinusoidal excitation, $H = H_m e^{j\omega t}$, and H_m is the peak value of the sinusoidal magnetic field, and then, from Eq. (2.1), $\nabla^2 H = j\omega\sigma\mu H - \omega^2\mu\varepsilon H$. Let $k^2 = j\omega\sigma\mu - \omega^2\mu\varepsilon$, then,

$$\nabla^2 H - k^2 H = 0 \quad (2.2)$$

When testing, the coil is placed at the surface of the object being tested. The axial direction of the coil is selected as the z -axis, and one tangent of the coil is the y -axis. Another tangent of the coil that is perpendicular to the z -axis and the y -axis simultaneously is the x -axis. Because the magnetic field strength along the y -axis and z -axis is not decaying, we have $\nabla = d/dx$, and Eq. (2.2) could be expressed as follows:

$$d^2 H_z / dx^2 - k^2 H_z = 0 \quad (2.3)$$

Solving the PDE (2.3),

$$H_z = c_1 e^{-kx} + c_2 e^{kx} \quad (2.4)$$

in which the boundary restriction coefficients c_1, c_2 are constant.

During inspection, if the area of the tested object under the coil is assumed to be infinite, then H_z is not restricted in the x direction, so $c_2 = 0$, $H_z = c_1 e^{-k_1 x}$, in which $k_1 = \sqrt{j\omega\mu(\sigma + j\omega\varepsilon)}$. Since $\omega\varepsilon \ll \sigma$, we have

$$H_z = c_1 e^{-x(1+j)\sqrt{\omega\mu\sigma/2}} \quad (2.5)$$

When $x = 0$, $H_z = H_{z0}$, so $c_1 = H_{z0}$, i.e.

$$H_z = H_{z0} e^{-x(1+j)\sqrt{\omega\mu\sigma/2}} \quad (2.6)$$

and because $dH_z/dx = -J_x$, the eddy current density in the tested object is as follows:

$$J_x = (1+j)\sqrt{\omega\mu\sigma/2} H_{z0} e^{-x(1+j)\sqrt{\omega\mu\sigma/2}} \quad (2.7)$$

Equation (2.7) indicates that the eddy current density in the tested object decreases exponentially with the increasing distance from the coil, while the phase difference of the eddy current increases proportionally with the increasing depth. Equation (2.7) is rewritten as follows:

$$J_y = J_0 e^{-x\sqrt{\pi f \sigma \mu}} \quad (2.8)$$

where J_0 is the eddy current at the surface of the object, x is the distance to the defect surface, J_x is the eddy current density at the depth of x in the tested object, and f is the frequency of the excitation signal. This phenomenon is the skin depth effect.

Generally, the depth where the eddy current is $1/e$ of that of the surface is called the standard penetration depth, expressed with δ . Because the phase difference increases proportionally with the increasing depth, when the depth is the standard penetration depth, the phase of the eddy current lags 1 rad.

$$J_y/J_0 = e^{-x\sqrt{\pi f \sigma \mu}} = 1/e \quad (2.9)$$

So $\delta = 1/\sqrt{\pi\sigma\mu f}$. It shows the range of depth for the eddy current testing, and the maximum depth of the eddy current testing is around 3 times of δ , but the eddy current density at this position is only 5 % of that at the surface, so the testing sensitivity is relatively low. Normally, the excitation frequency, electric conductivity, and magnetic permeability parameters should be selected such that the calculated standard penetration depth δ is bigger than $1/3$ of the testing depth to realize effective inspection. If it is required to detect defects deep under the surface of the tested object, the excitation frequency must be reduced. The testing depth of the eddy current not only depends on the frequency, but also is associated with the diameter of the probe. When the probe is at the surface of the tested object,

the penetration depth, into the tested object, of the excitation magnetic field produced by the probe is about 1/4 of the probe diameter. However, although with large-diameter probes, deeper testing depth can be obtained, and the range of distribution of the eddy current in the tested object also increases with the probe diameter, making the defects relatively smaller compared with the cross section of the eddy current flow, resulting in decreased sensitivity of the probe, so we should design the probe properly, according to the actual situation, and considering the experimental results.

2.1.2 Principle of Probe Design

In eddy current testing, coils are often used as the probes, and their shapes and sizes are related to the sensitivity of the probes and testing range. In order to improve the performance of pulsed eddy current testing probes, we always hope for a larger testing range and higher sensitivity. To obtain a larger range, axial distribution of the excitation magnetic field must be increased, and to gain a high sensitivity, the amount of change of the eddy current loss power when moving the probe should be relatively large. According to Biot–Savart law, with the same excitation current, current-loading coil with a smaller radius will generate a larger magnetic induction strength near the coil, but the magnetic field attenuates more fast along the axial direction; for the current-loading coil with a bigger radius, although the magnetic induction strength near the coil is smaller than that of the coil with a smaller radius, the magnetic induction strength at a farther position is bigger than that of the coil with a smaller radius, i.e., the testing range of a coil with a bigger radius is larger. However, because the axial magnetic field of the small radius coil changes faster, the testing sensitivity of a small diameter coil is higher. A coil could be seen as being composed of several single-turn coils, so its magnetic field can be considered as a superposition of the magnetic fields of the corresponding single-turn coils.

Theoretical calculation and experimental validation show that the bigger is the outer diameter of the coil, the deeper is the testing depth, but the sensitivity decreases; for the small outer diameter, the linear range will be smaller, but the sensitivity is increased. The smaller is the difference between the inner and outer diameters of the coil, i.e., the thinner is the coil, the higher is the sensitivity of the probe. Therefore, when designing a probe, to ensure that a probe with a fixed outer diameter has a large testing range and sensitivity as high as possible, it is required that the coil thickness is as thin as possible. For probes requiring large testing range, the outer diameter should be big; if the testing range is small and the sensitivity is required to be high, the outer diameter of the probe should be small.

Designs of the probes are based on the above conclusions and implemented by a model test method. As for the mathematical models of conventional eddy current probes, the target function of optimized design is generally related to the inner and outer diameters of the exciting coil, the length of the axis, inductance, resistance, number of turns, wire diameter, wire strands, fill factor, excitation frequency, the

geometry of the object to be tested, electric conductivity, and magnetic permeability. For the pulsed eddy current testing, because the excitation signal contains multiple frequencies, it is difficult to obtain a clearly expressed objective function, especially the optimization design between multiple frequencies is difficult to achieve. However, design methods applied in traditional single frequency eddy current probe design are still applicable for the pulsed eddy current probe design, except for the influence of the frequency.

In the practical design of pulsed eddy current testing probe, according to the needs, typically, there is a scale range for the diameter of the coil. In a given range, one should try to reduce the outer diameter of the coil to increase the sensitivity of testing; meanwhile, a probe with small outer diameter is easy to use, i.e., inclination of the probe causes less impact. When the geometrical dimensions of the coil are fixed, for a certain amount of inductance, the number of turns of the coil can be determined. However, note that corresponding to different frequencies, the inductance of the coil will vary; therefore, corresponding to the different frequency components in the signal, the equivalent inductance of the coil is also different. In the actual design, it is only required to be in a range. Based on the magnitude of the excitation current and the maximum allowable current density in the wire, the diameter of wire could be calculated. Sometimes, when the current is large while the wire is fine, multiple strands of wire could be used, and according to given wire parameters and the geometry of the coil, the resistance of the coil could be obtained.

2.1.3 Principle of the Pulsed Eddy Current Testing

Using the pulse signal as the excitation, according to the Fourier transform, solving the Fourier transform of a time-domain function is just to compute the spectrum of this time function; that is, a pulse can be expressed as the sum of an infinite number of harmonic components.

If $\Phi_n(x)$ is the family of standard orthogonal functions, then

$$C_n = \int_a^b f(x)\Phi_n(x)dx \quad (n = 1, 2, 3, \dots) \quad (2.10)$$

A pulse signal $f(t)$ could be expanded as the generalized Fourier series of the family of standard orthogonal functions $\Phi_k(t)$,

$$f(t) = \sum_{n=1}^{\infty} C_k \Phi_k(t) \quad (2.11)$$

In the above equation, the Fourier coefficients C_k could be calculated with (2.12),

$$C_k = \int_0^{\infty} f(t)\Phi_k(t)dt \tag{2.12}$$

Thus, in theory, a pulse can be expanded into an infinite number of harmonic components. The pulsed eddy current testing is different from the conventional eddy current testing, in that in the traditional eddy current testing, the coil impedance is investigated to determine whether a defect exists, while in the pulsed eddy current testing, the transient variation of the induced voltage is tested. For the pulsed eddy current testing, when the probe is moved past a defect, the probe output waveform is as shown in Fig. 2.1.

Therefore, the surface and subsurface defects have more influence on the first half section of the transient signal, while less influence on the latter half section of the signal. By contrast, the situation is just the reverse for the deep defects. Often in the pulsed eddy current, the two features of the peak value of the signal and the corresponding time are used to quantify the defects. Among them, the signal peak value is related to the size of the defect. The bigger is the defect, the higher is the signal peak value. Meanwhile, the peak value also depends on the depth where the defect resides. The time corresponding field, that is, the defect location. While the penetration path of the magnetic field is not linear with the time corresponding to the peak value. However, the deeper is the defect location, the later is the time corresponding to the peak value of the transient signal, and from this, the depth of the defect location could be analyzed qualitatively.

Figure 2.2 shows the transient signal waveforms corresponding to the same flaw at different depths. In the experiments, defects are manufactured on the surface of a metal sample, and metal plates of the same material and different thicknesses are placed above it, and the two are pressed together, to simulate the internal defects at different depths in the testing. Figure 2.2 shows that the deeper is the defect, the

Fig. 2.1 The transient waveform of the pulsed eddy current testing

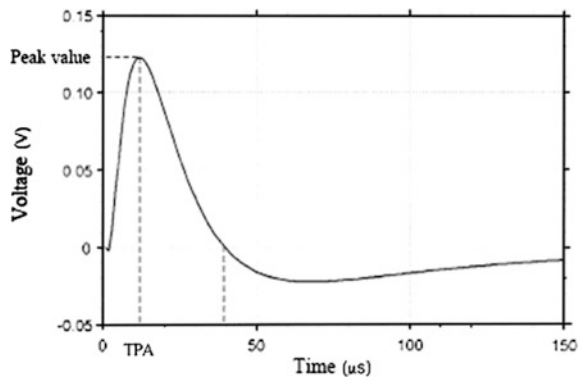
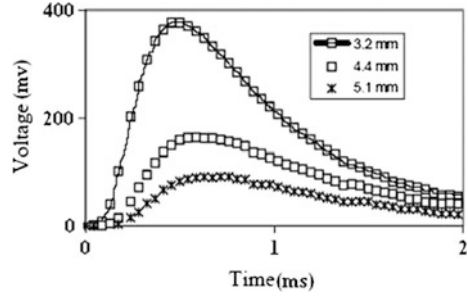


Fig. 2.2 The probe output waveforms corresponding to defects with different depths



lower is the peak value of the sensor output signal, and the longer is the time required for the signal to rise to the peak value.

Influenced by the skin effect, the conventional eddy current testing is mainly used to detect surface defects. Because pulsed eddy current contains low-frequency components, it can also detect deeper defects. The structure of the pulsed eddy current testing device is simple, and the cost is low. The device also has strong anti-interference ability. At present, air core and ferrite core coil probes are applied to the pulsed eddy current testing. With ferrite cores, the magnetic field is better gathered, thus improving the signal-to-noise ratio of the sensor, but introduction of ferrite makes the analysis more complex. Some researchers have conducted experimental analysis and theoretical study of the air core and ferrite core coil probes, comparing air core coil and ferrite core coil with the same geometrical shape, and assuming there are no other differences for the two coils except for the ferrite core. Experiments showed that the signal waveforms of the two probes are similar proportionally with a scaling factor as the difference.

In practice, pulsed eddy current has been used to detect the defects in the conductive multilayer connection parts and decide their locations, especially in the testing of the aircraft components. Pulsed eddy current testing device used for this purpose can differentiate effectively the internal defects of the connection parts, surface warping, dents, change of surface protection layer thickness of the tested object, bolts, and other geometrical deformations.

2.2 The Coil Sensors in the Pulsed Eddy Current Testing

In the pulsed eddy current testing, to meet the testing requirements of the workpieces with different shapes and sizes, it is necessary to design different testing probes or coils.

2.2.1 Classifications of the Testing Coils

According to the mutual positional relationship between the coil and the tested object, the testing coils could be classified into three categories,

(a) Through coil

For the through coil, the tested object is put inside the coil and moved through the coil. It can be used to test tubes, rods, and wires that can pass through the inside of the coil. With the through coil, it is easy to implement in eddy current testing high speed and automatic mass production. Therefore, it is widely used in quality inspection of tubes, rods, and wires and in addition also can be used to detect skew and eccentric rods.

(b) Inner passing coil

When testing the inner wall of the pipe, the coil must be placed in the inside of the pipe; this type of coil inserted inside the tested object is known as inner passing coil, also known as the internal coil; it is currently mainly used for the in-line inspection of the condenser.

(c) Placed coil

It is also known as the probe coil. During testing, the coil is placed at the surface of the tested object. The coil is usually small, with an internal magnetic core, which could gather the magnetic field, so its sensitivity is high. The placed coil is suitable for surface inspection of all kinds of sheet, strip, and large-diameter pipes and rods and also suitable for local testing of parts with complex shapes.

2.2.2 Working Modes of the Testing Coils

In the testing, a coil or multiple separate coils can be used, but according to testing purpose, the coils must be connected into a certain form, called working modes of the coils in this chapter. The working mode where only one coil is used is called the absolute mode, while the mode that two coils are connected reversely is called a differential mode. According to the position with relevance to the tested object, the differential probes could be further classified into the standard and the self-comparison modes.

With the absolute coil, the output voltage of the coil is directly measured and the magnitude and phase of this voltage are used to determine whether defects exist in the object to be tested. The general testing process includes first testing the standard specimen with the coil, the corresponding output voltage is used as a reference, and then, the tested object is put into the coil. If the output voltage exceeds the previously established reference, then it is regarded that there exist flaws. The absolute working mode can also be used for the sorting and the thickness measurement of

the material, and the output voltage when testing a standard specimen is generally adjusted to 0; then, if there is no output, it is indicated that the tested object has the same parameters as the standard part.

The working mode of standard comparison is the typical differential testing, and specifically, the two coils are reversely connected to obtain a differential form. A standard workpiece is placed in a coil, and the other coil is used to check the tested object. Because the two coils are connected as a differential form, when the object to be tested is different from the standard workpiece, there is signal output in the coil, so the testing is achieved.

The self-comparison mode is one special case of the standard comparison mode, and its name is derived from that the different parts of the same tested object are used as the references of comparison. When two adjacent coils are used to check the adjacent parts of the tested object, the differences of the physical and geometrical parameters of the two tested locations are generally small, and the influence on the coil output voltage is relatively weak. When the defect exists, output voltage signal with an abrupt change is generated in the coil close to the defect, and output of the other coil is still essentially the same without any defect. Therefore, there will be an abrupt change in the differential output, and from this signal, the existence of the defect could be judged.

In addition, the coils can be connected into various forms of bridge circuits. In the bridge mode of connection, a probe composed of two coils is commonly used to detect small impedance variations caused by the defects. Two coils are set at the adjacent bridge arms; if one coil serves as a testing coil, and another is used as a reference coil, then the probe is known as an absolute probe; if both coils are used to test the object simultaneously, then it is a differential probe.

In the pulsed eddy current testing, the absolute probe could reflect the material properties including the electric conductivity, magnetic permeability, the geometry of the object being tested, and the various changes of the defects, while the comparison signal of the adjacent parts of the tested object is the output of the differential probe. In this chapter, mainly the placed probe is used to test the surface and subsurface defects of the object under investigation. The absolute coil is prone to drift when the temperature is instable and its anti-interference ability is inferior to that of the differential probe.

2.2.3 Probes of the Pulsed Eddy Current Testing

Probe, also known as sensor, is an important part of the pulsed eddy current testing device. In the pulsed eddy current testing, the defect in the tested object could be reflected by the change of the output voltage of the pulsed eddy current testing probe. Magnetic sensing devices such as coil, Hall sensor, magnetic sensing diode, and the magnetoresistance can all be used to develop pulsed eddy current probe. In the conventional eddy current testing, a testing coil is generally applied, but in the pulsed eddy current testing, sometimes in order to detect the low-frequency signal,

Hall element is often accepted. Experiments show that magnetic field of about 10^{-8} T could be detected in the testing coil, while with a Hall sensor, only 10^{-6} T magnetic field could be measured, so the testing coil has higher resolution. Secondly, the Hall element detects the magnetic field strength, while a coil could detect changes in the magnetic field. During steady-state operation, the Hall element outputs a voltage and the voltage is much larger than the voltage generated by the defect. If the voltage is seen as the background noise, then the probe's signal-to-noise ratio is relatively low.

According to the principle of pulsed eddy current testing, first in the probe there must be the exciting coil fed with repeated pulse sequence to generate the exciting magnetic field in its surrounding and within the tested object, while in order to detect defects in the object to be tested, a testing coil is needed. The probe should have three functions: first, generating eddy current in the tested object and second, testing and obtaining signal reflecting the situation of the tested object and doing the analysis and evaluation. Then, the pulsed eddy current probe is required to have the ability to suppress noises; for example, in defect detection, interferences from the probe tilt, liftoff, temperature, humidity, and the electromagnetic interference from the outside world should be suppressed.

2.2.3.1 Requirements of the Working Conditions of the Pulsed Eddy Current Testing

In the pulsed eddy current testing, the surface of the tested object is often covered with non-conductive protective materials, or dirt, grease, and so on. Therefore, in the testing when the sensor is moved at the surface of the tested object, the distance between the probe and the tested object will change inevitably because of jitter or changes in the surface conditions of the tested object. The eddy current in the tested object induced by the probe will also change with this distance. The greater is the distance, the smaller is the magnitude of the eddy current induced in the tested object. Therefore, when the probe departs from the position close to the surface of the tested object, the testing sensitivity will decrease, and this phenomenon is called the liftoff effect.

According to Lenz's law, the magnetic field of the eddy current in the tested object is in the opposite direction of the exciting magnetic field. In the testing, when the probe approaches to the tested object, due to the magnetic field generated by the eddy current, a part of the induced voltage in the coil from the exciting magnetic field will be canceled out. When the probe is lifted from the tested object, i.e., the distance between the tested object and the probe increases, the voltage in the coil induced by the exciting magnetic field is essentially the same. While because the distance increases, in the tested object, the strength of the exciting magnetic field of the probe decreases, so the eddy current produced in the tested object gets smaller. Similarly, because the distance between the probe and the tested object gets larger, the voltage in the testing coil of the probe induced by the magnetic field of the eddy current will be smaller. Therefore, when liftoff exists, in the testing coil, the

counter-reaction of the magnetic field generated by the eddy current to the excitation magnetic field gets weaker, so the resulting amplitude of the induced voltage of the probe gets larger. This phenomenon can also be seen as that a noise is superimposed on the induced voltage signal, thus making the induced voltage larger, so this superposition is also called the liftoff noise. The liftoff noise can sometimes cover up the voltage changes of the minor defects. If the alarm threshold of the testing device is unreasonable or the liftoff noise is excessive, the testing device may generate false alarms, which will affect the inspection.

Another issue of the pulsed eddy current inspection is how to effectively detect cracks in all directions in the tested object. Taking the example of the surface fatigue crack, its extension may be in any direction on the 2D plane. According to the testing principle, when the flowing direction of the eddy current in the tested object is perpendicular to the defect direction, the alteration of the magnetic field of the eddy current exerted by the defect is maximized; when the two are parallel, the influence of the defect on the eddy current distribution is minimized. Therefore, how to design the probe, so that it can effectively detect the flaws in all directions, is also one of the main problems of the pulsed eddy current testing to be solved.

2.2.3.2 Selection of the Material of the Probe Magnetic Core

The properties of the magnetic core material directly determine the value of the coil inductance and will affect the testing performance of the probe. Commonly used core materials are the pure iron, ferrite, and amorphous alloy.

Even though the pure iron has high magnetic permeability, its high-frequency response characteristic is poor. When using the pure iron as the core, there will be large amount of eddy current in the iron, which consumes the energy of the excitation source, also makes the temperature of the probe increase, and causes a temperature drift. In addition, compared with materials such as ferrite and amorphous alloys, the magnetic permeability of the pure iron is relatively low.

Amorphous alloy is a new kind of high magnetic permeability material developed after the 1970s of the twentieth century; it has the advantage of high efficiency, low loss, and high magnetic permeability. Compared with traditional metal magnetic materials, atoms of the amorphous alloy are not in order, and crystal anisotropy does not exist, so in applications, this alloy has high permeability and low loss and can be used in place of silicon steel, permalloy, ferrite, and other traditional materials. Using amorphous alloy as the probe core, the sensitivity of the probe could be improved effectively, and the volume of the probe is reduced, the weight is decreased, and the energy loss is lowered. However, amorphous alloy cores are usually thin, and this kind of material is brittle and easily broken. When hand winding the coil, it is necessary to stack several pieces of amorphous alloy together as the magnetic core, which makes winding more difficult to operate. So when hand winding the coil, amorphous alloy core is not recommended.

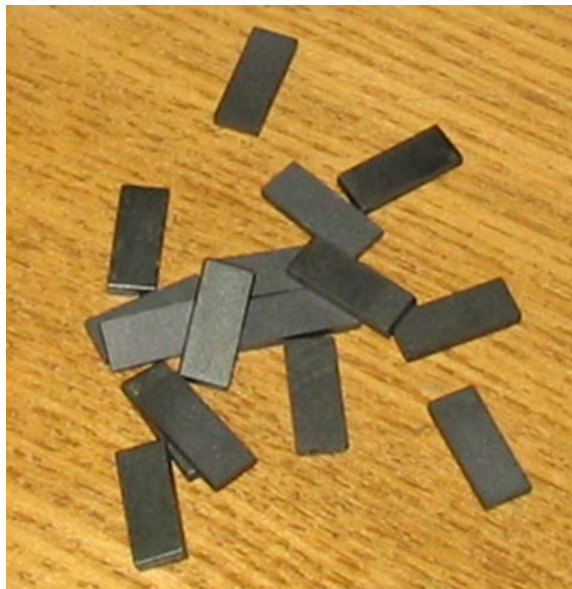
Ferrite is often used as the magnetic core material in actual testing; it can increase the inductance of the coil, improve the quality factor of the coil, and enhance the testing sensitivity of the probe.

For the ferrite strips in Fig. 2.3, the parameters are as follows:

Initial magnetic permeability	$\mu_0 = 2500 \pm 25 \%$
Amplitude permeability	3200
Saturation magnetic flux density (25 °C)	510 mT
Magnetic remanence (25 °C)	110 mT
Magnetic coercive force (25 °C)	$H_c = 12 \text{ A/m}$
Curie temperature	220 °C
Density	4800 kg/m ³
Dimensions	12.5 mm × 5 mm × 1.2 mm

This model of ferrite has high initial permeability and Curie temperature, and when used as cores for pulsed eddy current probes, they can meet the testing needs well. Tests show that in the above three materials, the ferrite is the most appropriate. The magnetic permeability of the pure iron is relatively low, and large amount of excitation energy will be consumed because of the iron loss when used as the core material. In addition, the density of the pure iron is big, and this increases the weight of the probe, so it is not appropriate as probe core material; If the amorphous alloy is used as the magnetic core material, the difficulty in building a probe is increased; meanwhile, the sensitivity of the probe is too high, and the probe is prone to the interferences, so the useful signal might be buried in the noises, which

Fig. 2.3 Ferrite magnetic cores



apparently is not helpful to detect the defects; the ferrite cores are easy to make, and the density is moderate. During the development of the probes, u-shaped and cup-shaped ferrite magnetic cores are used to gather the magnetic field and improve the sensitivity of the probe.

2.2.3.3 Winding of the Probe Coil

When the temperature changes, the probe will have performance shift. In order to reduce the effect of the change of temperature on the sensor performance, in addition to the previously mentioned differential connection method, the relationship between the probe wire and the temperature drift should be considered. When high-frequency large current excitation is used, the probe temperature will rise greatly and even gets hot; therefore, for the wire of the probe, material with low resistance coefficient and low temperature coefficient should be selected. Made of metal and insulating varnish, the wires should have good quality, and when the probe temperature rises, the internal metal and external insulating varnish of the wire will expand when heated. When the temperature is high, the large expansion may cause the shedding of insulating varnish, and the exposure of the wire will result in a short circuit inside the coil, reducing the inductance of the coil. When temperature rises, the wire resistance will also increase, and the impedance characteristics of the probe will be changed.

The thermal expansion coefficient and resistivity of copper wires are both low, and they are suitable as coil wires. In order to reduce the resistance of the coil, the number of turns of the wounded coils in this work is between 100 and 150, and the diameter of the wire is 0.1 mm. If the wires are too thin, on the one hand, the coil resistance is large, and on the other hand, in the process of probe making, the wire is easy to break. If the wires are too thick, the thickness of the coil will be affected. For the multilayer winding, this also causes uneven distribution of the coil. Meanwhile, the skin effect of current distribution in the coil will be more obvious; i.e., when the frequency of the excitation signal is high, the current density at the surface of the wire is far greater than that at the center of the wire. Because the effective current-loading area becomes smaller, the equivalent resistance of the probe becomes bigger, and the skin effect of the current also changes the equivalent inductance. The increase of the wire diameter also increases the instability of the inductance; so in the design, all the factors should be considered integrally, and diameter of core wire should be selected reasonably.

In order to reduce the interference to the signal transmitted from the probe to the testing device, shielded signal cable can be used as the signal transmission line. The signal cable has shielding net woven with fine copper wires and can effectively reduce the interference of electromagnetic environment on the transmission line. The shielding layer of the signal cable is connected to the ground at the ground point of the circuit board of the testing device.

2.2.3.4 Suppression of the Liftoff Effect of the Probe

In the pulsed eddy current testing, the liftoff effect can be seen as the consequence of the change of the interaction of the magnetic fields caused by the change of the distance of the probe and tested object. If not controlled, the liftoff noise can cover up the testing signal. In particular, for the absolute probe, the liftoff effect is a major problem influencing its normal operation. The liftoff effect is not linear with the lift distance. The closer is the probe to the tested object, the greater the liftoff will influence the probe output voltage. In order to improve the sensitivity of the probe, the probe should be placed as close as possible to the tested object, which requires that when testing the object closely, the liftoff effect of probe caused by jitter should be suppressed.

When using the probe that the exciting coil and the testing coil are separated, at the same time that the excitation magnetic field induces eddy current in the tested object, voltage u_1 is induced in the testing coil, and the induced voltage u_e in the testing coil by the eddy current is in the opposite direction of u_1 , and the closer is the probe to the tested object, i.e., the closer to the eddy current, the stronger is the magnetic field generated by the eddy current and sensed by the testing coil. Therefore, the larger is u_e , the smaller is the output voltage $u = u_1 - u_e$. With liftoff of the probe, u_e gets smaller, and because the relative position of the exciting coil with respect to the testing coil makes no change, u_1 can be considered approximately constant, so the probe output u increases. When choosing the peak value of the probe output voltage as the basis of judging whether a defect exists, the increase of the output signal resulted from the liftoff sometimes will surpass the change of voltage caused by the tiny defects in the tested object, which will lead to that the defects could not be detected effectively by the device.

In view of the above problem, the solution is to remove the voltage induced by the original exciting magnetic field in the testing coil and only measuring the change of voltage Δu caused by the defect. When there is no defect, the probe output is 0. When there is a defect, as the liftoff distance increases, the output signal of the probe decreases. Then, when voltage is used as the basis of judging, there will be no false alarms due to the change of the liftoff distance.

The liftoff effect originates from the change of the eddy current in the tested object caused by the change of distance between the exciting coil and the tested object, and the change of the strength of the magnetic field in the testing coil generated by the eddy current. For the probe design, the liftoff noise should be reduced as much as possible or even removed. An implementation is using the self-comparison probe. The two coils of the differential probe are placed closely side-by-side; when the probe is at a certain liftoff height, the distances of the two coils from the surface of the tested object are kept the same, so the liftoff noises of the two coils are the same. With the differential connection, the liftoff noises in the two coils are canceled out, and the background noises, temperature drift, and interference of the earth magnetic field are also removed. Of the differential probes, the electric differential probe is the most typical.

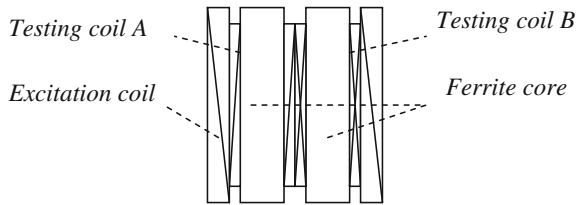


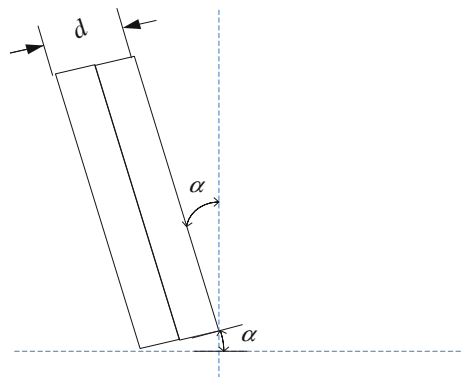
Fig. 2.4 The electric differential probe

The structure of the electric differential probe is as shown in Fig. 2.4. This probe is composed of two testing coils and an exciting coil. The two testing coils are connected in a differential form. During operation, the induced voltages of the two testing coils are subtracted, so the probe is called an electronic differential probe.

The testing coils A and B have the same structure and are made of the same material with the same manufacture process. In theory, the two coils have the same parameters, such as induction and resistance. When they are located in the same exciting magnetic field, the same voltages will be induced in the coils A and B. Connecting the two coils at the dotted terminals and measuring the voltages at the other two ends, then the net output voltage after subtraction will be 0. For the electric differential probe, the same interferences confronted by the two coils, such as temperature, humidity, external electromagnetic interference and earth magnetic field, can be effectively suppressed through a differential design. When the two testing coils are placed closely and perpendicular to the surface of the tested object, the two testing coils have the same liftoff height. Using the differential design, theoretically the liftoff effect can be canceled out. But in the actual testing, the probe moves at the surface of the tested object, and it is difficult to ensure that the probe movement is always perpendicular to the surface of the tested object; i.e., the probe may deviate from the vertical direction at an angle of α , as shown in Fig. 2.5.

In the differential probe design, the thickness of the probe d should be minimized, so that the difference between the liftoff distances of the two coils (difference

Fig. 2.5 The diagram of tilting of the differential probe



of heights from the centers of the two coils), $\Delta h = 0.5d \cdot \sin \alpha$, is small. When winding the probe, coils are wound on the two cores, respectively, and then, the two coils are fixed closely side-by-side. If the coil is thin, it will be helpful to ensure uniform geometry of the coil, to avoid concentrating the coil in a region. If the geometry of the coil is not uniform, for example, there is a hump, then the two coils cannot be placed closely side-by-side; on the one hand, increasing the thickness of the probe and, on the other hand, making it difficult to guarantee the two coils are on the same horizontal position. If the two coils cannot be placed side-by-side on the same level, even if the probe is perpendicular to the surface of the tested object, the liftoff heights of the two coils are not the same; that is, in this case, it would be difficult to effectively suppress the liftoff noises.

The structure of the magnetic differential probe is as shown in Fig. 2.6. In testing, the two exciting coils with the same number of turns and the same structure are connected reversely and fed with the same excitation current, so the excitation magnetic fields of the same magnitude and opposite directions are generated by the two exciting coils.

As shown in Fig. 2.6, two exciting coils are wound on the ferrite cores, respectively, and then connected in the differential mode. Winding testing coil at the outside of the two exciting coils, when the magnetic differential probe is placed at a point without any defect at the tested object, the magnetic fields generated by the two exciting coils in the testing coil are canceled out, and then, the coil output is 0, indicating there is no defect in the tested object. When one of the two exciting coils is close to a defect, the magnetic field generated by the exciting coil will change due to interference of the defect, resulting in that the magnetic fields generated by the two exciting coils cannot cancel each other out, and the testing coil will output a voltage value reflecting the defect. In the course of the probe passing by the defect, according to the differential subtraction relation, when the two exciting coils pass by the defect, respectively, the magnetic fields in the testing coils are in the opposite direction. While when the defect is between the two coils, the instant synthetical magnetic field is 0; therefore, induction voltages of the testing coils are alternating. If judging the existence of the defect from the signal amplitude, there will be two abrupt voltage changes when the magnetic differential probe passes by the same defect. Compared with the absolute probe, the number of missed defects can be effectively reduced.

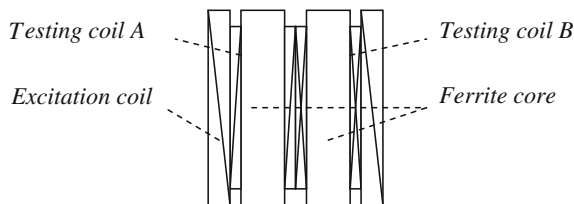


Fig. 2.6 The magnetic differential probe

In the absence of defects, the output of the magnetic differential probe is 0. When there is a defect, the output is the voltage change caused by the defect. When the magnetic differential probe is lifted to a certain height, as what is detected by the testing coil is only the voltage induced by the change of the magnetic field of the eddy current caused by the defect, with the magnetic differential probe, the liftoff noises can be effectively suppressed.

Observing the structures of the magnetic differential probe and electronic differential probe, it is not difficult to see, both structures are exactly the same, only the functions of the exciting coil and the testing coil are interchanged, and thus, testing probes with similar functions can be constructed. This idea will be described in detail later. In this book, it is called the reciprocity rule of probe design.

2.2.3.5 Sensors with Closed Magnetic Circuits

Learned from the preceding analysis, the liftoff noise is in fact not from a separate source and superimposed on the signal, but due to the decrease of the signal caused by that a testing coil is moved away from the magnetic field. With probes that can suppress the liftoff effect, the increase of the output voltage of the probe with the increasing liftoff height has been suppressed, and the expected results are achieved; that is, the probe output gets smaller when the liftoff is increased. In actual testing, under the most circumstances, it is required to implement a non-contact testing; that is, there should be a distance between the probe and the tested object. Meanwhile, in actual testing, the probe will inevitably be affected by the interference of the noise; if the signal is too weak, it is difficult to extract it from the noise and analyze it. Therefore, a certain degree of sensitivity should be maintained when the probe is at some liftoff height.

Therefore, for the probe design, it is necessary to slow down the trend that the output voltage decreases with the increasing liftoff height, and make sure a high signal-to-noise ratio is achieved. This on the one hand means increasing the amplitude of the signal, ensuring that when the probe is at a certain liftoff height, it still maintains a high output; on the other hand, it is required to reduce the noise and suppress the interference.

To suppress the phenomenon of the decrease of the probe output signal caused by the liftoff, it is necessary to reduce the trend that the magnetic field generated by the eddy current decreases with the increasing distance, so as to make the magnetic field generated by the eddy current in a certain liftoff range maintain a certain intensity in the testing coil. On the one hand, this requires that the strength of the excitation magnetic field in the tested object be enhanced, making the magnetic field strength changes gradually in a certain liftoff range; on the other hand, this means reducing the change of the magnetic field generated by the eddy current in the coil when the liftoff changes.

According to the concept of effective magnetic permeability of the magnetic circuit, when there is an air gap in the magnetic circuit, the magnetic permeability of the whole magnetic circuit is as follows

$$\mu_e = \frac{\mu_i}{1 + g\mu_i/l_e} \quad (2.13)$$

in which μ_i is the initial magnetic permeability, g is the length of the air gap, and l_e is the length of the effective magnetic circuit. Equation (2.13) is an approximate calculation of the effective magnetic permeability of the magnetic circuit in case of a small air gap. When the air gap is large, part of the magnetic flux will pass through the outer part of the gap, and its effective magnetic permeability is slightly larger than the result of calculation in accordance with Eq. (2.13).

Viewing the liftoff distance as the air gap of the magnetic circuit, the effective magnetic permeability could be used to analyze the magnetic field when the probe is lifted. The higher is the effective permeability of the whole magnetic circuit, the more will the magnetic force lines concentrate, and the larger is the strength of the magnetic field in the magnetic circuit. In order to ensure enough magnetic field strength, it is required to design a probe making the effective magnetic permeability of the magnetic circuit high. The idea of design is to try to make the probe core and the tested object form a closed magnetic circuit, so that it has a high effective magnetic permeability.

In order to enhance the excitation magnetic field based on the differential design and closed loop, a U-shaped magnetic core probe could be used, and its structure is shown in Fig. 2.7.

The two testing coils of A and B of the u-shaped magnetic core probe are wound respectively around the two yokes of the u-shaped ferrite core, and the exciting coil position is as in Fig. 2.7; i.e., the two testing coils share a common magnetic circuit, in the same exciting magnetic field.

Because the magnetic flux of the u-shaped magnetic core probe is not leaking, so under the same excitation intensity, the excitation magnetic field strength of the u-shaped core probe is about twice of that of the three-core probe.

2.2.3.6 The Two-Level Differential Probe

The purpose of using the two-level differential probe is to better suppress the noise and keep the consistency of the coils on the two cores. The structure of the designed two-level differential probe is as shown in Fig. 2.8.

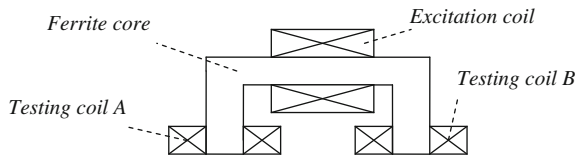
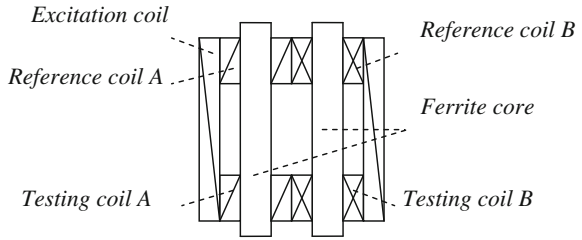


Fig. 2.7 The U-shaped magnetic core probe

Fig. 2.8 The structure of the two-level differential probe



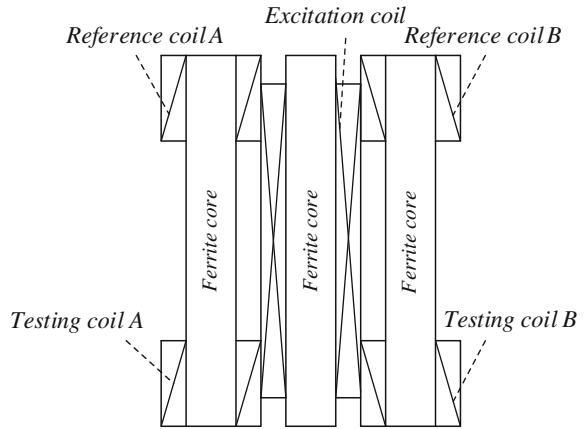
In Fig. 2.8, the structures of the reference coil A and B and the testing coil A and B are the same. The so-called two-level differential probe is connecting first the two coils on the same core differentially; that is, the dotted terminal of reference coil A is connected to the dotted terminal of the testing coil A; the reference coil B and the testing coil B are also connected into the differential form. At this point, the reference coil of the first-level differential is equivalent to a testing coil placed on top of a non-conductive material under the same excitation magnetic field. In the design of a differential probe, the coil used as the reference could be the coil placed at a point of the tested object without any defect, or the coil placed on top of the non-conductive material.

The purpose of adopting the design in Fig. 2.8 is to better ensure the consistency of the two coils with magnetic cores. When winding the electrical differential probe, often the output voltage is not 0 because inductances of the two testing coils are different. When winding the coil, first the upper part of the core is wounded N turns in one direction, and then, the bottom half of the core is wounded N turns in the reverse direction. The reference coil should be as close as possible to the top of the core, while the testing coil should be as close as possible to the bottom of the coil. When not testing, the overall inductance of the coils on each core is 0, but when the probe is placed on the surface of the conductor to be tested, the testing coil is closer to the eddy current than the reference coil, and the magnetic field strength is larger, so the differential output of the coils on one single core is not 0. Then, the coils on the two cores are connected into the differential form, so after subtracting the induced voltages of the two coils on the same core, subtraction is then conducted for voltages of different cores, in order to better suppress the liftoff noise.

When designing two-level differential probes, the design idea of the aforementioned closed magnetic circuit could be introduced, increasing the magnetic field strength by increasing the effective permeability of the magnetic circuit, particularly making the magnetic field strength generated by the defects small, and improving the phenomenon that the magnetic field decreases rapidly with the increase of the liftoff distance. Based on the three-core probe structure, the two-level differential probe structure is shown in Fig. 2.9.

In the winding of the coils shown in Fig. 2.9, we should ensure that the four coils, i.e., the testing coils A and B, and the reference coils A and B, have the same structure. However, when using the three-core two-level differential probe, there is the problem that the excitation magnetic fields of the two magnetic circuits may

Fig. 2.9 Three-core two-level differential probe



have difference; meanwhile, its exciting magnetic field strength is only half of that of the U-core probe. Therefore, in this book, a two-level differential probe with u core is also given, as shown in Fig. 2.10.

In Fig. 2.10, in the magnetic circuit composed of ferrite cores, the tested object, and the liftoff air gap, the reference coil A and the testing coil A are connected differentially into a new coil. The reference coil B and the testing coil B are also connected differentially. Then, in the second level of differential, outputs of the coils on the two yokes of the U-shaped probe are subtracted.

Another probe with a closed magnetic circuit is the double U-type two-level differential probe, as shown in Fig. 2.11. Experimental results showed that, although sharing the same exciting coil, because the reluctance of the lower part of the magnetic circuit is small, most of the flux distribution is in the U-shaped magnetic circuit of the lower part of the probe. Because the excitation magnetic field sensed by the reference coil is different from that of the testing coil, the noise reduction, especially the liftoff noise suppression, is no better than the two-level differential probe shown in Fig. 2.10, but better than the probe without a two-level differential design.

Fig. 2.10 Two-level differential probe with U core

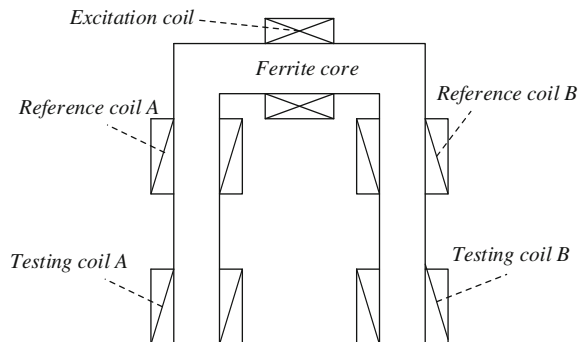
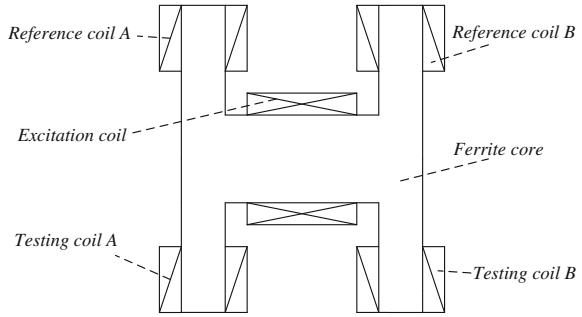


Fig. 2.11 The two-level differential probe with different excitation magnetic field



In the two-level differential, the first-level difference is used to eliminate the voltage in the coil induced by the exciting magnetic field, and the second-level differential is used to remove the eddy current at the position without any defect, or induced voltage of the eddy current without amplitude and phase changes caused by the defects. After the two-level differential, the output of the probe is the voltage induced by the magnetic field generated by the eddy current changed by the defect.

The thing to note is, for the electrical differential probes and the three-core probes, in coil winding, two identical coils with magnetic cores could be wound with the same winding direction and then connecting the lower terminals. However, magnetic fluxes on both yokes of the probe with the U-shaped magnetic cores are in the opposite direction, so attention should be paid to the coil winding, avoiding sequential connection.

2.2.3.7 Rotating Magnetic Field Probe

The pulsed eddy current is mainly used for detection of defects on the surface of the tested object, especially the fatigue cracks, so the extensions of the defects may be in any direction on the 2D plane; i.e., the directions of the defects are in different angles with the scan direction of the probe; therefore, it is needed to ensure the probe can produce an appropriate response signal to the defects in any direction.

With the differential probes, for long cracks, when the extension of the crack and the probe movement are in the same direction, there are only alarm outputs at the beginning and end of the crack. When the two coils are located on the same long crack, the probe's output will be 0, so the long crack will be mistaken recognized as two separate small cracks.

According to the principle of the eddy current testing, it is desired to detect the change of the magnetic field resulting from the changes of the magnitude and phase of the eddy current caused by defects. When the defect is perpendicular to the flow of the eddy current in the tested object, the defect can change the eddy current distribution on the maximum; therefore, the signal detected by the probe reaches the maximum and vice versa when the defect is parallel to the eddy current flow; because the change of the eddy current is very small, the slight change of the signal

caused by the defect is difficult to detect. When designing the probes, we should take into account the relationship between the extension direction of the defect and the probe output signal. By designing the cooperation between the excitation and testing subsystems properly, defects along different directions can be detected.

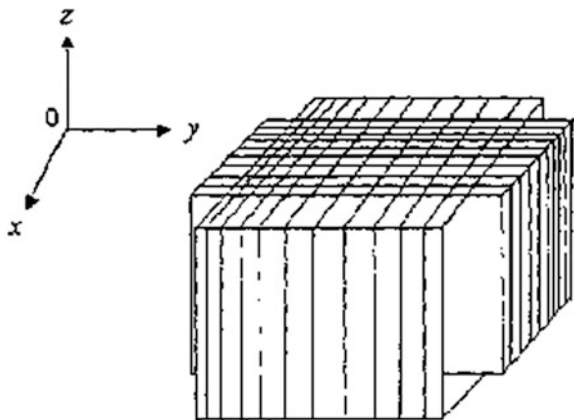
In the absolute coil often used in the conventional eddy current testing, the eddy currents produced in the tested object are several eddy current rings below the coil, while the coil itself is a symmetrical cylinder, so the probe has no directional differences. Where there are no defects, the generated eddy currents are concentric rings. The absolute coil has poor anti-interference performance and especially is sensitive to liftoff. In testing, when there is liftoff between the probe and the tested object, the reverse voltage caused by the defect becomes small rapidly, introducing the liftoff noise while at the same time also reducing the sensitivity of the probe itself. Absolute coil has no directional differences, but is limited by its poor anti-interference ability and lack of testing sensitivity and is rarely used in actual testing.

With the rotating magnetic field eddy current testing probe, cracks in all directions can be detected. The probe produces a periodically rotating exciting magnetic field, so the eddy current on the tested object is also periodically rotating. Fig. 2.12 shows the structure diagram of the composite coil used to generate the rotating exciting magnetic field.

The excitation coil in Fig. 2.12 is composed of two orthogonal excitation coils wound on a cubic magnetic core. Sinusoidal signals with a phase difference of 90° are loaded, respectively, into the two coils. According to the principle of electromagnetic induction, the eddy current induced by the coil in the tested object is parallel to the direction of the excitation current.

Because the two excitation signals are sinusoidal signals with a phase difference of 90° , the generated eddy currents also have approximately sinusoidal waveforms. If the eddy current induced by the excitation coil in the tested object is represented as follows:

Fig. 2.12 Structure diagram of the composite exciting coil used to generate the rotating exciting magnetic field



$$I_x = I_0 \sin(\omega t + \varphi) \quad (2.14)$$

then the eddy current induced by the other excitation coil in the tested object is as follows:

$$I_y = I_0 \sin(\omega t + \varphi + \pi/2) = I_0 \cos(\omega t + \varphi) \quad (2.15)$$

in which $\omega = 2\pi f$, with f as the frequency of the excitation signal and φ as the initial phase of the eddy current.

When the excitation coil is wounded upright, each exciting coil only generates magnetic field along the axis; accordingly, only eddy currents parallel to the excitation currents are produced in the tested object. The two eddy currents are perpendicular to each other, so below the probe in the tested object, the amplitude of the combined eddy currents is as follows:

$$I = \sqrt{I_x^2 + I_y^2} = I_0 \sqrt{\sin^2(\omega t + \varphi) + \cos^2(\omega t + \varphi)} = I_0 \quad (2.16)$$

The phase angle of the combined eddy current is as follows:

$$\theta = \arctan\left(\frac{I_y}{I_x}\right) = \arctan\left(\frac{\cos(\omega t + \varphi)}{\sin(\omega t + \varphi)}\right) = -(\omega t + \varphi) \quad (2.17)$$

Therefore, for the exciting coil as shown in Fig. 2.12, when using two sinusoidal signals with a phase difference of 90° as the excitation signals of the two orthogonal coils, in the tested object, eddy current with a constant amplitude and a rotating frequency the same as the excitation signal frequency will be generated. The direction of the eddy current vector rotates one full revolution clockwise in one rotating cycle.

2.2.3.8 Probe with a Cup-Shaped Magnetic Core

The purpose to use a cup-shaped core is to make up for the limitation of the absolute coil. Structures of the cup-shaped core probe are as shown in Figs. 2.13 and 2.14. Figure 2.13 shows the vertical cross section of the probe, and Fig. 2.14 shows the horizontal cross section of the probe.

As shown in Figs. 2.13 and 2.14, the testing coil and the excitation coil of the cup-shaped core probe are both wounded on the cylinder in the middle of the magnetic core. The radius of the exciting coil could be enlarged to increase the linear range of the probe. When designing the probe, because the testing coil with a small radius has a higher sensitivity, the testing coil is wounded at the inside, and the exciting coil is wounded at the outside. Throughout the outside of the cup-shaped core, there is a shielding shell, and its function, on the one hand, is to reduce the magnetic leakage and, on the other hand, is shielding electromagnetic interference from outside, in order to improve the signal-to-noise ratio.

Fig. 2.13 Vertical cross section of the probe with a cup-shaped magnetic core

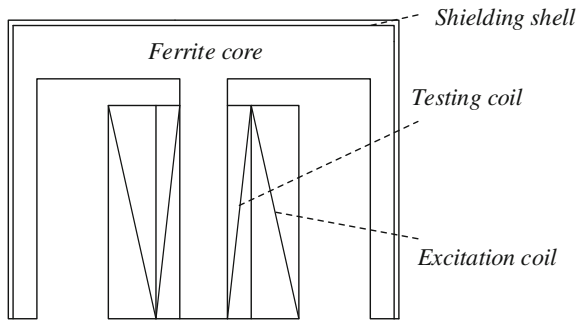
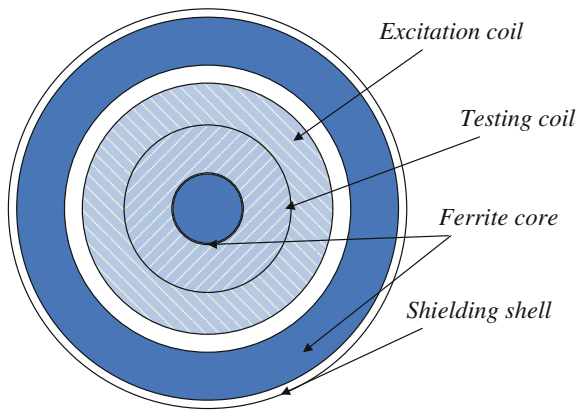


Fig. 2.14 Horizontal cross section of the probe with a cup-shaped magnetic core



With the cup-shaped core, the ability of the absolute coil to suppress the liftoff effect has been greatly improved, and meanwhile, it has a good shielding to other noise, especially the electromagnetic noise. The geometry of a cup-shaped core effectively concentrates the exciting magnetic field distribution and makes the tested object and the magnetic core together form a closed magnetic circuit.

The eddy currents induced by the cup-shaped core probe in the tested object have distributions of concentric rings. According to geometric principles, an arbitrary straight line through the center of a circle is perpendicular to the arc intersecting the line. Therefore, when using the cup-shaped core probe to detect cracks with arbitrary directions, if a crack defect is located directly below the probe, the crack is perpendicular to the eddy current rings in the tested object, so with the probe, the defect will be more effectively detected. If the excitation coil and the testing coil are wound evenly around the cylinder at the middle of the magnetic core, because of the central symmetric characteristic of the entire probe, no matter at what angle will the probe rotate, the performance of the probe will not be affected by the directivity. Using the cup-shaped core also helps to avoid errors due to deviation from the axis of the coil.

When the cup-shaped core probe is placed at the surface of the tested object without any defect, its output is a constant voltage, called the inherent voltage. With the cup-shaped core probe, when a defect is detected, the output voltage becomes larger, but the voltage increment is small compared to the inherent voltage. If we take the inherent voltage as the background noise, then the signal-to-noise ratio of the system is low. In order to eliminate the background noise and other interferences, another cup-shaped core probe with the same structure is placed in defect-free region of the tested object as a reference, and the output signals of the two probes are subtracted. In testing, the reference probe is fixed, and the testing probe is moved at the surface of the tested object.

With the cup-shaped core probe, cracks in different directions could be detected. At the same time, the liftoff noise suppression is also taken into account.

2.2.3.9 Cross-Winding Probe

In order to improve the signal-to-noise ratio, the inherent voltage should be removed, so it is desired to design probes with zero adjustment function; i.e., at defect-free parts of the tested object, the probe output is zero. In design, we can make the direction of the combined magnetic field at the point without any defect parallel to the testing coil, and then, the probe output is zero. When there is a defect in the tested object, the direction of the combined magnetic field will change, and then, there is flux interacting with the testing coil, so the probe will output a voltage reflecting the defect.

The purpose of the cross-winding probe is to design a probe with auto zero adjustment function and able to detect cracks along various directions. The structure of the cross-winding probe is as shown in Fig. 2.15.

With the cross-winding coil, two coils are wound on the cylindrical ferrite core, both perpendicular to each other, one as the excitation coil and the other as the testing coil. Both coils have the same numbers of turns and are both perpendicular to the surface of the tested object. The magnetic field of the excitation coil is parallel to the testing coil, and the eddy current magnetic field is opposite to the exciting magnetic field, but also parallel to the testing coil, and therefore, when

Fig. 2.15 The structure of the cross-winding probe

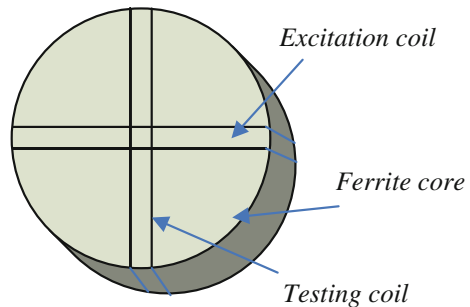
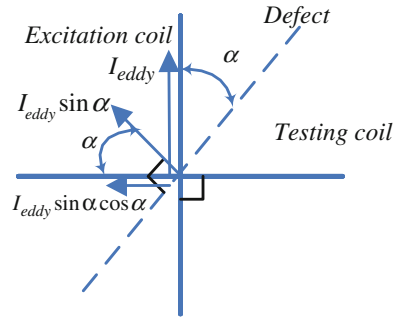


Fig. 2.16 Analysis of the cross-winding probe



there is no defect, the output of the cross-winding probe is 0. When the eddy current distribution is altered by the defects in the tested object, the magnitude and direction of the magnetic field generated by the eddy current will change so that defects are reflected in the probe output voltage. Diagram of the testing process of the cross-winding probe is as shown in Fig. 2.16.

Assuming the angle between the extension direction of the crack and the excitation coil is α , the eddy current of the excitation magnetic field is parallel to the excitation coil plane, as shown in Fig. 2.16. If the eddy current is decomposed into one component parallel to the crack and another component perpendicular to the crack, the eddy current component parallel to the crack is affected very little by the crack, basically causing no voltage change in the testing coil, so only the eddy current component $I_{eddy} \sin \alpha$ perpendicular to the crack is effective. In addition, the eddy current causing the change of the induced voltage in the testing coil is the component parallel to the testing coil. Therefore, if once again decomposing the part of the eddy current affected by the defects (eddy current component perpendicular to the crack), the probe output will depend on the component parallel to the testing coil after decomposition.

$$I_{eff} = I_{eddy} \sin \alpha \cos \alpha = 0.5 I_{eddy} \sin 2\alpha \tag{2.18}$$

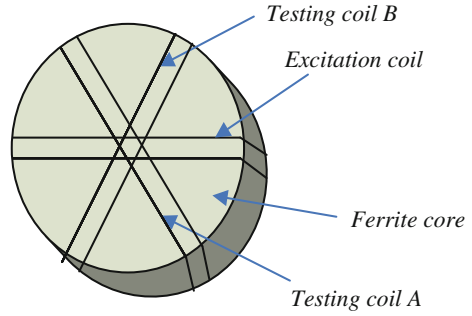
The above equation shows that the situation when the angle between the extension direction of the crack and the direction of the current in the excitation coil is $0-\pi$, it is the same as that when the angle is $\pi-2\pi$.

When $\alpha = 0$ or 0.5π , the extension direction of the crack is parallel to the excitation coil or the testing coil, and the probe output voltage is 0. With this configuration, the cross-winding coil probe cannot detect the cracks.

2.2.3.10 Star-Shaped Coil Probe

The star-shaped coil probe is an improvement based on the cross-winding coil probe. The purpose is to make up for the testing blind region of the cross-winding probe. The star-shaped coil is composed of two testing coils and an exciting coil,

Fig. 2.17 The structure of the star-shaped coil probe



and the three coils are all perpendicular to the surface of the tested object. The structure of the star-shaped coil probe is as shown in Fig. 2.17.

The three coils on the star-shaped coil probe split the circle equally; that is, the angle between any two coils is $\pi/3$. Similarly, let the angle between the crack and the excitation coil be α , because the eddy current direction is parallel to the current in the excitation coil; after decomposition of the eddy current, the eddy current component vertical to the crack $I_{\text{eddy}} \sin \alpha$ will generate voltage in the testing coil. Then, we decompose the eddy current component vector further into two components parallel to the two testing coils, respectively. Assuming I_1 is the component parallel to the excitation coil A, and I_2 is the component parallel to the excitation coil B, the process of decomposition is as in Fig. 2.18.

Then, it could be known that $\beta = \pi/2 - \pi/3 - \alpha = \pi/6 - \alpha$.

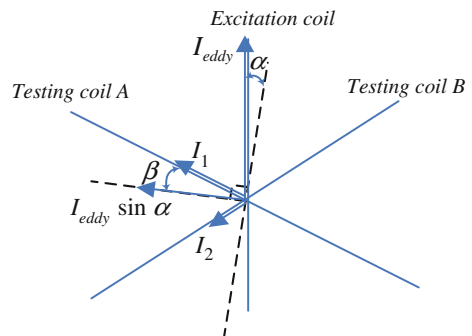
According to the law of sines,

$$I_1 = 2I_{\text{eddy}} \sin \alpha \sin\left(\frac{\pi}{6} + \alpha\right) \tag{2.19}$$

$$I_2 = 2I_{\text{eddy}} \sin \alpha \sin\left(\frac{\pi}{6} - \alpha\right) \tag{2.20}$$

When connecting two testing coils into one testing coil, they can be in series or differential. When the two testing coils are connected into the differential form,

Fig. 2.18 Analysis of the testing process of the star-shaped coil probe



because the two testing coils have the same numbers of turns and characteristics, therefore, it can be approximated that the output of the differential star-shaped coil probe $u = u_1 - u_2$ depends on the eddy current $I_1 - I_2 \propto I_{\text{eddy}} \sin^2 \alpha$. Therefore, when the extension of the crack is parallel to the excitation coil, output voltage of the differential star-shaped coil probe is zero; i.e., crack along this direction cannot be detected. In terms of the structure, the differential star-shaped coil probe is symmetric about the exciting coil. When there are no defects, the eddy current components along the directions parallel with the two testing coils are equal; therefore, differential output voltage is 0 when there are no defects; i.e., the differential star-shaped coil probe has the function of auto-zero adjustment. The differential design also cancels out the common interference factors to the two testing coils and improves the signal-to-noise ratio of the probe. Compared to the cross-winding probe, the differential star-shaped coil probe has increased performance.

When the two testing coils are connected in series, the output voltage of the probe is the sum of the induced voltages of the two testing coils. Similarly, the output of the star-shaped coil probes in series is $u' = u_1 + u_2$, which can be thought of as depending on $I_1 + I_2 \propto I_{\text{eddy}} \sin 2\alpha$. When detecting the defects in the tested object, the star-shaped coil probes in series have similar characteristics with the cross-winding probe, but the scale factor is different. Also, it is worth noting that when the probe is placed at a region free from defects, the probe output voltage is not 0, and the output signal is the sum of the induced voltages of the two coils, so the star-shaped coil probes in series do not have auto-zero adjustment. When testing cracks parallel or perpendicular to the excitation coil with the in series star-shaped coil probes, there is no signal output, so we cannot distinguish these two defects.

With the star-shaped coil probe, some improvements are made based on the cross-coil probe, and some of the shortcomings are made up for, but there are still testing blind spots.

2.2.3.11 The Horizontal–Vertical Coil Probe

The excitation coil placed horizontally on the surface of the tested object will generate in the tested object eddy current opposite to the excitation current in the coil. When the testing coil is perpendicular to the surface of the tested object, the excitation magnetic field and the magnetic field of the eddy current are both parallel to the testing coil. Therefore, when the probe is placed at the tested object where there is no defect, the horizontal–vertical coil probe output signal is 0, so it has the auto-zero adjustment function. The structure of the horizontal–vertical coil probe is as shown in Fig. 2.19.

During testing, if the probe is moved in the defect-free region, the eddy currents in the tested object have ring distributions, as shown in Fig. 2.20a. When the horizontal–vertical coil probe is above the crack, the crack will intersect with the

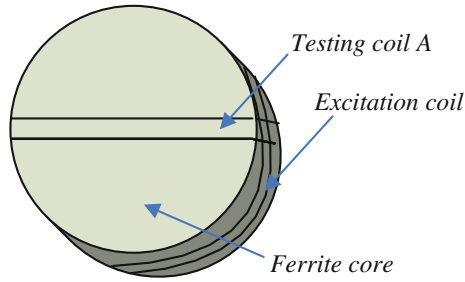


Fig. 2.19 The structure of the horizontal-vertical coil probe

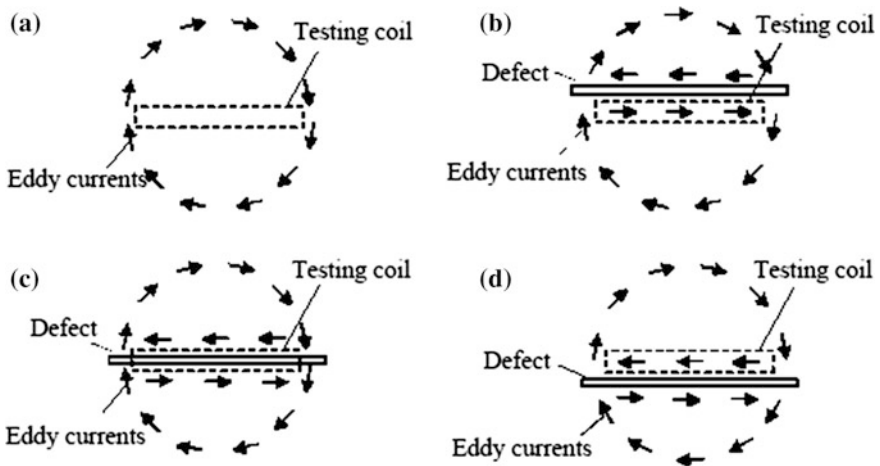


Fig. 2.20 The mechanism of the horizontal-vertical coil probe. **a** With no defect. **b** Testing coil on one side of the defect (positive output). **c** Testing coil on the central of the defect (0 output). **d** Testing coil on the other side of the defect (negative output)

eddy current ring. At the place of intersection with the defect, the conducting material can be seen as an open circuit, and along both sides of the crack, there will be eddy currents with opposite directions and equal magnitudes. These eddy currents, together with the original eddy current loops, will form two new loops. The mechanism of the horizontal-vertical coil probe is as shown in Fig. 2.20.

As in Fig. 2.20b, the eddy currents on both sides of the defect are in the opposite direction, but the magnetic field of eddy current on the circumference is parallel to the testing plane, so no voltage is induced in the testing coil. Moving the probe makes the testing coil approach the eddy current on one edge of the crack, although eddy currents on both edges have equal magnitudes; because the distances from the testing coils are different, voltage will be induced in the testing coil, and this voltage can be assumed positive. When the probe is moved such that the testing coil is just above the defect, as shown in Fig. 2.20c, the opposite eddy currents on the two

edges have equal distances from the testing coil, so the magnetic fields of the two eddy currents cancel each other out, and the probe output is 0. With the probe continuing to move, the situation as shown in Fig. 2.20d will emerge. As the distance to the eddy current of the lower part in Fig. 2.20d is smaller, the probe output voltage is negative. In the whole process of moving the probe to detect a crack, the probe output voltage will go from zero to a positive value and then from a peak positive voltage drop pass zero, until reaching the negative voltage peak. When the probe leaves the crack, its output voltage changes to 0 again.

When the crack is perpendicular to the testing coil, the magnetic field of the eddy current is parallel to the testing coil plane. Now, the horizontal–vertical coil probe output is zero, so we are unable to detect a crack perpendicular to the testing coil.

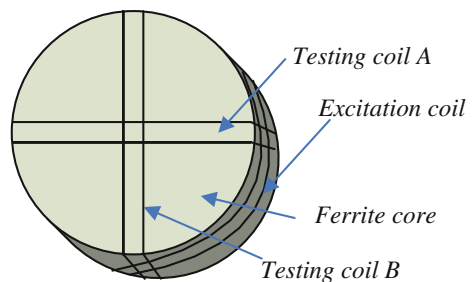
2.2.3.12 The Improved Horizontal–Vertical Coil Probe

Because the horizontal–vertical probe has testing blind region, i.e., with it we cannot detect cracks perpendicular to the testing coil. Another testing coil is needed to make up for this shortcoming. When the two testing coils are not parallel, the second testing coil can detect cracks perpendicular to the first testing coil, which makes up the testing blind region of the probe. In order to obtain a higher degree of sensitivity, for the improved probe, the two testing coils should be mutually perpendicular, so that for the cracks perpendicular to the first testing coil, the eddy current in the tested object will be parallel to the second testing coil, and thus, the crack is detected with a higher sensitivity. The structure of the improved horizontal–vertical coil probe is as shown in Fig. 2.21.

Figure 2.21 shows that the three coils are all wound on the ferrite magnetic core, and the testing coil A is perpendicular to the testing coil B, and both are perpendicular to the excitation coil. The exciting coil is placed horizontally. Similarly, we can know that, when there are no defects, the output of the improved horizontal–vertical coil probe is 0, so it has zero adjustment characteristic.

Given that when the defect is on both sides of the testing coil, the direction of the induced voltage will change, and the two testing coils are not connected as a whole. Instead, two channels are used to analyze the induced voltages in the two testing coils. In this way, in the testing device, two signal processing and A/D conversion channels are required to work simultaneously. The analysis of the two signals takes

Fig. 2.21 The structure of the improved horizontal–vertical coil probe



the logical OR; that is, when the recorded voltage on any of the channel exceeds a threshold, the testing device will output an alarm signal, so that cracks along each direction can be detected effectively.

2.2.4 The Reciprocity Rule in Probe Design

Applying the reciprocity rule in probe design reasonably is helpful to extend the ideas in probe development and design.

For the probe with isolated excitation coil and testing coil, if the functions of the excitation coil and the testing coil are swapped, i.e., inputting a pulse excitation in the original testing coil, and at the same time measuring the change of induction voltage in the original excitation coil, then making adjustments according to the specific situation of testing, functions similar with the original probe can be implemented. This law is called the reciprocity rule in probe design. Previously mentioned electrical differential probe and magnetic differential probe reflect this idea.

In order to detect cracks along each direction, several probes developed by the authors have been introduced earlier. For the cup-shaped magnetic core probe and the cross-winding coil probe, if the functions of excitation and testing are swapped, it is still the original probe. In particular, for the cross-winding probe, there will be no change in performance after the swap. For the cup-shaped magnetic core probe, considering the actual requirements on the testing coil, setting the exciting coil outside and the small radius testing coil inside is more helpful for improving linearity range and the testing sensitivity, although after the swap the new cup-shaped core probe can still achieve similar capabilities to the original probe, the testing sensitivity is reduced.

2.3 Circuits of the Pulsed Eddy Current Testing

Circuits of the pulsed eddy current testing are mainly composed of the excitation source, the probe, the analog signal processing unit, the microcontroller subsystem, and other components. There is also a power supply module for the entire device. Among them, the analog signal processing unit contains the amplifier, the envelope detector, the front-end and back-end filtering, and other function circuits; the microcontroller subsystem consists of the microcontroller (including the A/D converter), manual reset, sound and light alarm, quantification display, expanded memory, and serial communication circuits. The structure of the testing circuit is shown in Fig. 2.22.

Periodic pulse signal with adjustable frequency and duty cycle is generated by the excitation source and input into the exciting coil of the probe. On the rising and falling edges of the excitation signal, eddy currents are induced in the tested object, and the change of the magnetic field generated by the eddy current in the tested

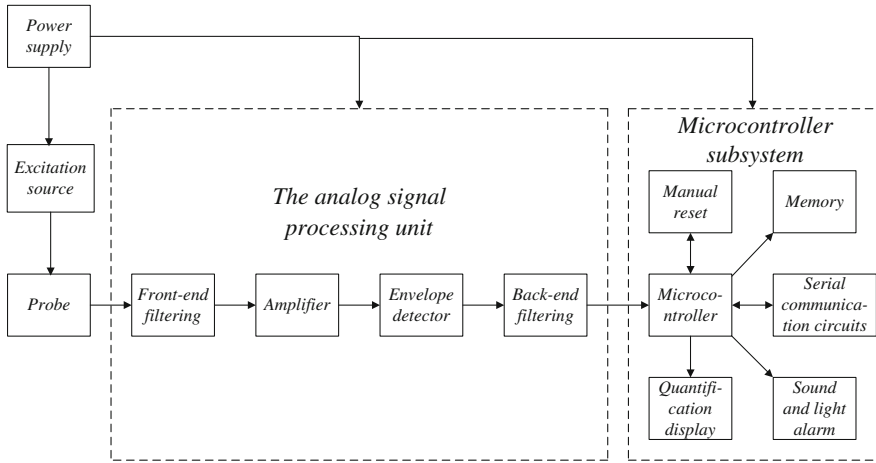


Fig. 2.22 Diagram of the structure of the pulsed eddy current testing circuit

object is detected by the testing coil of the probe. The defect signal detected by the probe is transmitted to the analog signal processing unit, through the processing including the amplification, waveform detection, and filtering and then obtaining signal suitable for analysis and processing on the microcontroller. Via the built-in A/D converter (ADC), the digitization of the measured analog signal is completed in the microcontroller. Then, appropriate judgment, analysis, calculation, and processing are done according to user requirements, and after the testing, the data stored in memory are transmitted to the PC via a serial port using asynchronous communication.

2.3.1 The Power Supply Module

There are three voltage levels for the portable pulsed eddy current testing device, namely +5, +3, and -5 V. The +5 V power supply provides power for microcontroller, signal source, and other digital IC, the -5 V power supply works as the reverse voltage of the operational amplifier, and the +3 V power supply is for the external flash memory. Among them, the -5 and +3 V power supplies can be built on top of the +5 V power supply. Therefore, we should first design a stable +5 V power supply.

The instrument is powered with four normal dry batteries, but during working, the battery voltage will decrease gradually, and therefore, the battery cannot be used directly as a stable DC power supply. Meanwhile, the power supply module should also have a large output current to provide enough power, particularly instantaneous pulse output power. The TPS60110 power chip from Texas Instruments is adopted, in accord with the characteristic of the battery that the voltage gradually decreases.

The input voltage range required for the chip to work normally is 2.7–5.4 V, and in this range, the chip can output stable +5 V DC voltage, and the maximum output current is up to 300 mA. The power source circuit of the pulsed eddy current testing instrument is shown in Fig. 2.23.

In Fig. 2.23, in circuit design, attention should be paid that pin 3 is the enable terminal, and it must be connected to the power supply to make it a high voltage level, and then, the circuit will work properly; that is, the pin must not be suspended. The output of the power source is type Π filtering circuit, to restrain the superposed high-frequency ripple in the DC voltage output of the power supply. The entire circuit only uses a few external capacitors, so the structure of the circuit is simple.

The -5 V power supply is converted by the +5 V DC voltage using the converter chip MAX764. The conversion circuit is shown in Fig. 2.24.

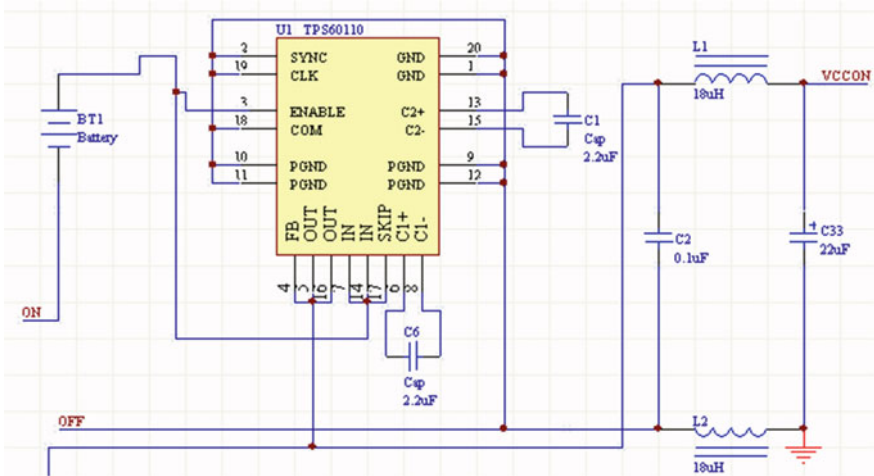


Fig. 2.23 The +5 V power source circuit with TPS60110

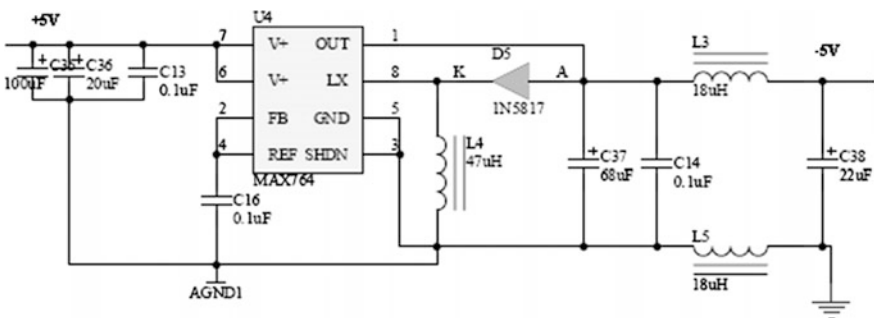


Fig. 2.24 The -5 V power source module

The +3 V power supply also uses the +5 V DC voltage as input, with three terminal regulator chip AS117-3.0. In layout, the power sources for the respective purposes are placed close to corresponding chips and separated from the other levels, in order to reduce interference between them.

2.3.2 The Excitation Source

A periodic repetitive pulse is used as the excitation signal for the pulsed eddy current testing instrument. In experiments, in order to test the effects of pulse parameters on the testing performance, a pulse generating circuit with adjustable repetition frequency and duty cycle is designed. A 555 timer is used to generate the pulse with continuously adjustable duty cycle. The design of the excitation signal generating circuit is shown in Fig. 2.25.

The duty cycle of the output pulse of the excitation source can be adjusted over a wide range; the diodes D_1 and D_2 provide charging and discharging channels for the capacitor C_1 , respectively. Potentiometers P_1 and P_2 control the charging and discharging cycles of the output pulse, respectively. The charging circuit is composed of R_1 , D_2 , input resistance R_{P2} of the potentiometer P_2 , and capacitance C_1 and the discharging circuit is composed of R_2 , D_1 , input resistance R_{P1} of the potentiometer P_1 , and capacitance C_1 . The charging cycle determines the time duration T_H of the high-level voltage of the output pulse, while the discharging cycle is the time duration T_L of the low-level voltage of the pulse, and the sum of them $T = T_H + T_L$ is just the pulse cycle. When $R_1 = R_2 = 1\text{ k}\Omega$, and the total resistance of the potentiometer P_1 and P_2 is $1\text{ M}\Omega$, by adjusting the potentiometer, the ratio of the charging cycle and the discharging cycle of the timer, i.e., the ratio of the high-level voltage duration and the low-level voltage duration, changes between 10,000:1 and 1:10,000. In addition, the duty cycle of the output excitation signal is as follows:

$$\text{Duty} = \frac{T_H}{T_H + T_L} \times 100\% \tag{2.21}$$

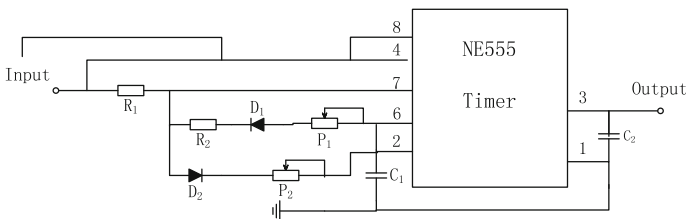


Fig. 2.25 Excitation source circuit

In the excitation source circuit, duty cycle of the pulse can be adjusted continuously between 0.01 and 99.99%. Pin 7 of the NE555 is discharging pin, and pin 2 is trigger pin. When the voltage on pin 2 is lower than 1/3 of the input voltage, it is seen as that the trigger signal emerges, and the timer output voltage is high level. Pin 6 is the threshold pin. When voltage of pin 6 is higher than 2/3 of the input voltage, it is seen as that the signal exceeds the threshold, and then, it is needed that voltage of pin 2 is no lower than 1/3 of the input voltage, and the timer output voltage is low level.

Therefore, the time duration of high-level output of the timer is as follows:

$$T_H = RC_1 \ln \frac{u_{cc} - 0.6 - u_1}{u_{cc} - 0.6 - u_2} \quad (2.22)$$

in which 0.6 V is voltage drop of the diode, u_{cc} is the input voltage, $u_1 = u_{cc}/3$ is the low triggering threshold, $u_2 = 2u_{cc}/3$ is the high triggering threshold, R is the equivalent resistance in the charging circuit, and $R = R_1 + R_{P2}$. Similarly, the time duration of the low level is as follows:

$$T_L = (R_2 + R_{P2})C_1 \ln \frac{u_{cc} - 0.6 - u_1}{u_{cc} - 0.6 - u_2} \quad (2.23)$$

and then the repetition period of the pulse is

$$T = T_L + T_H = (R_1 + R_2 + R_{P1} + R_{P2})C_1 \ln \frac{u_{cc} - 0.6 - u_1}{u_{cc} - 0.6 - u_2} \quad (2.24)$$

and the duty cycle is as follows:

$$\text{Duty} = \frac{R_1 + R_{P2}}{R_1 + R_2 + R_{P1} + R_{P2}} \quad (2.25)$$

2.3.3 The Analog Signal Processing Module

The probe output signal is generated by the change of the electromagnetic field caused by a defect. This signal is often weak, has poor anti-interference ability, and includes noises. So before entering the probe signal into the A/D converter and the microcontroller, the analog signal should be processed accordingly. The noise should be removed, and the signal must be amplified to improve the anti-interference ability and the signal-to-noise ratio. Then, the probe output signal passes through the A/D convertor and changes into the kind of signal suitable for processing in the microcontroller. The analog signal processing module includes several sections such as the front-end filtering, isolation–amplification, envelope detection, and the back-end filtering.

When analyzing and processing the probe output signal, although in the probe design noise suppression measures have been taken, signal processing circuit is still needed for further processing. The probe output signal contains high-frequency noise, influencing measurement of the waveform. Therefore, it is required to filter the signal first. Some noises are generated with the signal at the same time, and others are superimposed in the transferring process. The process of eliminating or reducing the noise and extracting the useful signal, depending on the different characteristics of the signal and the noise, is just filtering.

The response of the pulsed eddy current testing has a very wide spectrum, but mainly the middle frequency and low frequency parts of the spectrum are analyzed. The front-end filter is designed as a low-pass filter. For implementation, a circuit composed of the RC circuit and the operational amplifier is used as the active RC low-pass filter.

Because the active filter circuit is applied, the probe output signal will also be enhanced while removing the high-frequency noise. However, the probe output signal is often weak and needs further amplification to enhance the useful signal and improve the resistance of the signal to noises introduced in the later stages of the circuit. The so-called isolation primarily refers to making the working status of the current circuit not affected by change of load in the subsequent circuit. Because a voltage follower is used in the filter circuit, the main function of the amplification circuit is to amplify the signal, but it also plays the role of isolating the previous and later circuits. The optical isolation is often used as the circuit isolation, but the magnitude of the eddy current transducer signal is normally from dozens of millivolts to hundreds of millivolts; that is, the signal is small and not suitable for optical isolation.

The portable pulsed eddy current testing instrument determines whether there is any defect in the tested object based on the peak value of the probe output signal, so it is necessary to extract the peak value of the probe output signal. An envelope detector module is added to the testing device. The principle of envelope detection is to obtain the envelope of the signal waveform through the RC charging-discharging.

2.3.4 The Microcontroller Subsystem

The microcontroller subsystem mainly accomplishes functions such as A/D conversion, threshold setting, alarming, data storage, serial port communication, and quantified display of the inspection data.

For the microcontroller chip, a high-performance microcontroller ADuC812 from ADI (Analog Device Inc) company is selected. It is a fully integrated 12-bit data acquisition system, and the chip contains a high-performance 8-channel ADC with self-calibration, 2-channel 12-bit DAC, and a programmable 8-bit MCU.

The serial port circuit of the pulsed eddy current testing instrument has two functions: the first is downloading and online debugging the microcontroller

program, and the second is transferring the data in the memory of the testing device to the PC. The selected chip ADuC812 has online programming function, provided by the Development Kit of QuickStart development system, which contains the support of ADuC812. Under this system, the microcontroller system can be debugged directly, and after debugging, the program can be downloaded to ADuC812.

At the three cases of power up, power down, and power off, the reset circuit of ADuC812 has the corresponding functions. When the power supply voltage of the microcontroller is less than 2.5 V, it is required to keep the RESET pin high; when the power supply voltage is higher than 2.5 V, the RESET pin should remain low voltage level for at least 10 ms; the power-on reset circuit should be able to work under 1.2 V or even lower voltages. In this book, the active low reset chip max705 capable of manual resetting is used. When the MCU is powered on, the system is reset; the program runs from the starting position. During operation, the reset switch can be pressed manually to implement the system reset.

With the reset circuit, in addition to ensuring normal operation of the microcontroller, the designed manual resetting function can be used to implement alarm threshold setting of the device. If the selected alarm threshold is set in the microcontroller program in advance, the scope of application of the testing device could be limited to only detecting defects of a certain material; that is, when using it to test other materials, phenomena like false alarms or missed defects are possible. Therefore, when using the testing device under different testing conditions on tested objects with different materials, appropriate alarm thresholds should be set depending on the specific tested object.

The steps of operation include first placing the probe at the region of the tested object without any defect and pressing the manual reset button to reset the microcontroller. In the initial phase of the program, the threshold is selected and set by the device first, i.e., starting the ADC continuous sampling and comparing the acquired data in the microcontroller, selecting the maximum value, and setting the sum of the maximum value and an additional margin as the alarm threshold of defect detection. With such a design, on the one hand, the device can be used to test different materials so that the range of application is widened; on the other hand, the respective testing threshold values can also be set according to different testing conditions, such as changes of the liftoff height and changes of the environmental temperature. As described earlier, when there is liftoff at the probe, the amplitude of the output signal will be reduced. If the device maintains the preset threshold value, missed tests will emerge. Therefore, when the probe is used at a liftoff height different from the original one, by pressing the reset switch, the alarm threshold under the new testing conditions is set.

The oscillator circuit and the clock circuit of the microcontroller decide together the timing of the microcontroller. According to the difference of the hardware circuits, ADuC812 can use the on-chip clock oscillator, or the external clock source. To make the circuit as simple as possible, the on-chip clock oscillator is used, so that it is only required that the crystal oscillator be connected in parallel between the XTAL1 and XTAL2 pins, and two capacitors be connected between the two pins and the ground. The capacitor value is generally between 10 and 60 pF.

Whether using the on-chip clock oscillator, or the external clock source, the clock working range of ADuC812 should be selected in the range of 400 kHz–16 MHz. Although the kernel of ADuC812 is static, i.e., its operating frequency can be as low as DC, the maximum sampling rate of the ADC is 200kSps, so when the clock frequency is lower than 400 kHz, the ADC will not work properly. In addition, choice of the crystal oscillator also affects transmitting rate of the serial port communication. In order to guarantee the transmitting rate of the serial port, the crystal oscillator frequency of the microcontroller should not be too low.

Four tricolor LEDs placed side-by-side are used as the defect display of the testing device, and they divide the detected signal amplitude from the 0 to 2.5 V into eight uniform levels. If connecting different pins of the light-emitting diodes, we can choose to make them emit red or green light. In testing, the amplitude of the signal can be judged based on the location and color corresponding to the diode. Arranged from left to right, if the LED on the left is lit, it indicates that the voltage is small; when the same diode emits red light, the indicated voltage level is higher than that when emitting the green light.

After acquiring the data with the ADC of the microcontroller, the MCU program will analyze and judge the samples, divide them into proper ranks according to their values, output the number of this rank through ports P33, P34, and P35, and connect the output high level to the pin of the corresponding diode through a decoder 74LS138. In this way, on the one hand, the circuit is simplified, saving resources of the microcontroller; on the other hand, this also decreases the volume and reduces the power consumption.

The function of the alarm circuit is that when a defect is detected, an alarm signal is raised. A sound and light alarm is used; that is, when a defect is found, the microcontroller will output a high voltage level and light the alarm LED and drive the buzzer to emit the sound at the same time. In order to enhance the load-carrying capacity of the port of the microcontroller, a pull-up resistor is set at the port, and two reversers are used to enhance the signal.

References

1. Auld, B.A., Moulder, J.C.: Review of advances in quantitative eddy current nondestructive evaluation. *J. Nondestr. Eval.* **18**(1), 3–36 (1999)
2. Fenghe, Y., Jiang, T., Sun, Y.: Analysis of the characteristics of pulsed eddy current fields. *Instrum. Tech. Sens.* (5), 38–39 (2003) (in Chinese)
3. Binfeng, Y., Feilu, L.: The pulsed eddy current non-destructive testing device based on the integrated Hall sensors. *Meas. Tech.* (10), 8–9 (2004) (in Chinese)
4. Bieber, J.A., Shaligram, S.K., Rose, J.H., Moulder, J.C.: Time-gating of pulsed eddy current signals for defect characterization and discrimination in aircraft lap-joints. *Rev. Prog. QNDE* 1915–1921 (1997)
5. Sophian, A., Tian, G.Y., Taylor, D., Rudlin, J.: A feature extraction technique based on principal component analysis for pulsed eddy current NDT. *NDT E Int.* **36**(1), 37–41 (2003)
6. Tian, G.Y., Sophian, A.: Defect classification using a new feature for pulsed eddy current sensors. *NDT E Int.* **38**(1), 77–82 (2005)

7. Deqiang, Z., Tian, G., Wang, H., Wang, P.: Evaluation of applied stress using pulsed eddy current technology. *Chin. J. Sci. Instrum.* **31**(7), 1588–1593 (2010) (in Chinese)
8. Abidin, I.Z., Tian, G.Y., Wilson, J., Yang, S., Almond, D.: Quantitative evaluation of angular defects by pulsed eddy current thermography. *NDT E Int.* **43**(7), 537–546 (2010)

Chapter 3

The Remote-Field Eddy Current Testing

3.1 Outline

The remote-field eddy current (RFEC) testing is a special eddy current testing technology that utilizes the characteristics of the remote-field region of the eddy current to detect the defects and was applied in the inner inspection of small caliber pipeline first. A typical RFEC testing device is depicted in Fig. 3.1, which includes a coaxial low-frequency AC excitation coil and another coaxial detection coil placed 2–3 times of pipeline diameters away, and some necessary mechanical fixation and propulsion mechanism.

The RFEC is a unique phenomenon existing in ferromagnetic pipelines. A coaxial low-frequency AC excitation coil is placed in the pipeline, and the magnetic energy generated by this coil propagates along the two opposite axial directions, each with two different coupling paths, and the analysis of these two energy-coupling paths is the key to the understanding of this RFEC phenomenon.

The directly coupled energy attenuates exponentially by the strong permeability of the ferromagnetic pipeline wall. The other energy-coupling and propagation path describes that the magnetic field excites circumferential eddy current, and the magnetic energy diffuses to outside of the pipeline and propagates along the pipeline. The magnetic energy generates eddy current in the pipe wall again, thus penetrates the pipe wall, and arrives at the detection coil. This path is called the indirect energy-coupling path.

Near the excitation coil in the pipeline, the directly coupled energy dominates, but because the directly coupled energy decays faster than the indirectly coupled energy outside the pipe wall, with the increasing distance from the excitation coil, the indirectly coupled energy gradually becomes dominant. Therefore, both of the two sides of the excitation coil are divided into two regions: the region where the directly coupled energy dominates is known as the near-field region, and the region where the indirectly coupled energy dominates is the remote-field region. The position of the boundary of the two regions is determined by the parameters such as

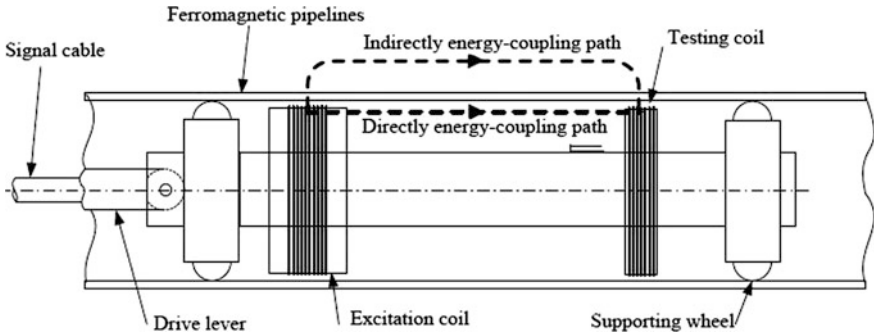


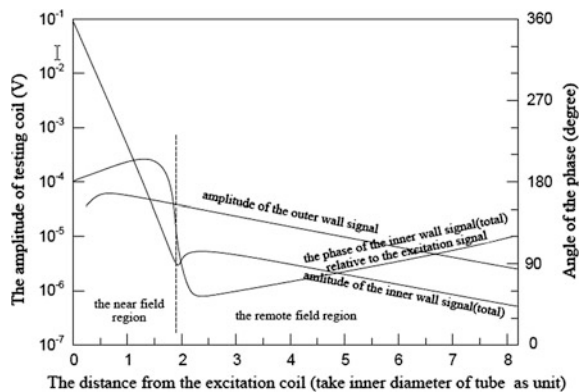
Fig. 3.1 Typical RFEC probe

the thickness of the wall, the permeability, the electrical conductivity, and the excitation frequency, and this position is usually two diameters away from the excitation coil. Sometimes, a transition region is divided between the near field and the remote field.

In Fig. 3.2 are the curves of variations of the amplitude and phase of the detected signal with the distance from the excitation coil. In the near-field region, the amplitude of the detected signal attenuates exponentially, while in the remote-field region, the inner wall signal and the outer wall signal attenuate exponentially with the same level, and this attenuation is not as fast as in the near-field region. The phase of the detected signal jumps in the transition region and varies linearly with the axial distance from the detection coil.

The magnetic energy in the remote field mainly comes from the indirect coupling. The magnetic energy starts from the excitation coil, penetrates the pipe wall twice, and carries the structural information of the pipe wall, and this information is just the foundation of the RFEC testing. If other parameters are kept constant, the magnetic field strength at the inner diameter is closely related to the thickness of the pipe wall, and the logarithm of the amplitude and the phase have linear relationships with the

Fig. 3.2 The variations of the amplitude and phase of the detected signal in the receiving coil with the distance from the excitation coil



pipe wall thickness. When cracking or other defects emerge in the pipe wall, this situation is equivalent to that the local thickness of the pipe wall changes, so the amplitude and phase of the magnetic field near the inner surface of the pipe wall will change, and this change could be detected.

Compared with traditional eddy current testing technology, the RFEC testing is not restricted by the skin depth of the eddy current, and the defects on the inner and outer surfaces of the pipe wall could be detected with the same sensibility.

The RFEC phenomenon was discovered in the fifties of the last century. At the development department of the Shell Company, this inspection technique was applied to the testing of oil-bearing pipes with diameters of 170–203 mm and wall thickness of 9.5–12.7 mm [1]. The testing frequency was 60 Hz, and the same solenoidal coils were used as the excitation and receiving coils. The detected signal was the result of circumferential averaging. This technique was mainly used to detect the variation of the pipe wall thickness. The application of the RFEC testing was very slow in the following more than 20 years because this technique was too specialized, the development of the electronic technology fell behind, and the electromagnetic analyzing methods were limited.

In 1978, detailed experiments of the RFEC phenomenon were done at the Shell Company, and the curves of variations of the amplitude and phase shift with the axial position were obtained, and simple explanations of the RFEC were proposed based on the curves [2]. In 1984, T.R. Schmidt, the pioneer of the RFEC technique, proposed the hypothesis of the energy coupling in the RFEC phenomenon [3]. At the same time, a semiempirical model was established for quantitative analysis of the RFEC phenomenon. In 1986, the American Gas Association and Nanjing University of Aeronautics and Astronautics cooperated to study the RFEC phenomenon using numerical methods, showing the electromagnetic field distribution in the RFEC, and found the phenomenon of “potential valley” and “phase knot” [4]. In 1987, Atherton D.L. of Canada confirmed the hypothesis of Schmidt by experiments. All these work strengthened the research on the mechanism of the RFEC.

In the late 1980s and early 1990s, the RFEC attracted the attention of many scholars in the field of nondestructive testing, and they studied the RFEC by experiments and numerical calculations [5–7]. Some scholars tried to simulate the RFEC in 3D, but with the limitation of the capability of the computers, the simulation results were not acceptable. At the aspect of application, in the late 1980s, some commercial products for the testing of small caliber pipelines began to appear, but the original structure of the 1950s and 1960s was still used for the probes. The testing signal was weak, the length of the probe was big, and the required excitation power was high. Except in the USA, the RFEC technique was used in Canada for the testing of nuclear reactor pressure pipes, and some gas companies in Japan applied the RFEC to the on-site testing of gas pipelines.

At present, in the field of numerical simulation of the RFEC, with the rapid development of the computers, the main focus has shifted from the 2D axisymmetric model in the 1980s to the 3D model and improved algorithm made the simulation programs simplified. With this new development, the work to study the characteristics of 3D defects has begun.

Nowadays, the researches focus on the testing of the unpiggable pipe [8], crack detection in raised-head fastener holes of aircraft [9], the inspection of prestressed concrete pressure pipe [10], and development of new sensors [11].

3.2 The Mathematical Model of the RFEC in the Pipeline

The mathematical model is the basis to carry out theoretical analysis and finite element simulation. In this section, the mathematical model for a FEM analysis of the RFEC in the pipeline is derived from the Maxwell's equations, to guide the modeling and analysis of the RFEC.

3.2.1 Basic Equations

Maxwell's equations are used to describe macroscopic electromagnetic phenomena. They are the basis of electromagnetic theory and the starting point to derive the mathematical model of the RFEC.

The Maxwell's equations are

$$\begin{cases} \nabla \times H = J + \frac{\partial D}{\partial t} \\ \nabla \times E = -\frac{\partial B}{\partial t} \\ \nabla \cdot D = \rho \\ \nabla \cdot B = 0 \end{cases} \quad (3.1)$$

in which H is the magnetic field strength, B is the magnetic flux density, D is the electric displacement vector, E is the electric field strength, J is the excitation electric current density, and ρ is the volumetric electric current density. Their relations are decided by the characteristics of the media. In isotropic media, the following relations hold

$$\begin{aligned} D &= \varepsilon E \\ B &= \mu H \\ J &= \sigma E \end{aligned} \quad (3.2)$$

in which ε is the electric permittivity, μ is the magnetic permeability, and σ is the electric conductivity.

Because the RFEC is a kind of low-frequency electromagnetic phenomenon, and we are mainly concerned with its steady-state characteristics, so the following assumptions are made,

1. The electric current density J and the field variables E , D , B , H vary in a sinusoidal fashion, and the harmonic components are ignored,
2. The influences of the moving velocity of the probe on the magnetic field and eddy current are neglected,
3. All the parameters in the model are isotropic and constant;
4. The magnetic hysteresis effect is ignored,
5. The displacement current is ignored, i.e., $\frac{\partial D}{\partial t} = 0$.

Based on the above assumptions, the phasor notations of the Maxwell's Eqs. (3.1) are obtained,

$$\begin{cases} \nabla \times \dot{H} = \dot{J}_c + \dot{J}_e \\ \nabla \times \dot{E} = -j\omega\dot{B} \\ \nabla \times \dot{D} = \rho \\ \nabla \times \dot{B} = 0 \end{cases} \quad (3.3)$$

together with the phasor notations of the constitutive Eqs. (3.2),

$$\begin{aligned} \dot{D} &= \varepsilon\dot{E} \\ \dot{B} &= \mu\dot{H} \\ \dot{J}_e &= \sigma\dot{E} \end{aligned} \quad (3.4)$$

in which \dot{J}_c is the density of the applied excitation electric current, \dot{J}_e is the density of the eddy current.

To simplify the system of equations for the later numerical calculation, the magnetic vector potential \dot{A} is defined as

$$\nabla \times \dot{A} = \dot{B} \quad (3.5)$$

To guarantee the uniqueness of \dot{A} , it is stipulated that

$$\nabla \times \dot{A} = 0 \quad (3.6)$$

which is called the Coulomb gauge. Substituting (3.5) into (3.3),

$$\nabla \times \dot{E} = -j\omega(\nabla \times \dot{A}) = \nabla \times (-j\omega\dot{A}) \quad (3.7)$$

i.e.,

$$\nabla \times (\dot{E} + j\omega\dot{A}) = 0 \quad (3.8)$$

According to its irrotational characteristic, scalar electric potential function $\dot{\phi}$ is

$$\dot{E} + j\omega\dot{A} = -\nabla\dot{\phi} \quad (3.9)$$

so,

$$\dot{E} = -(\nabla\dot{\phi} + j\omega\dot{A}) \quad (3.10)$$

Substituting (3.4), (3.5), and (3.10) into (3.3), we can get

$$\nabla \times \left[\frac{1}{\mu} (\nabla \times \dot{A}) \right] = \dot{J}_c - \sigma(\nabla\dot{\phi} + j\omega\dot{A}) \quad (3.11)$$

Because the material is isotropic, μ is a constant, and according to the Coulomb gauge (3.6) and the following vector identity,

$$\nabla \times \nabla \times F = \nabla(\nabla \cdot F) - \nabla^2 F$$

it is derived that

$$\nabla^2 \dot{A} = -\mu \dot{J}_c + \mu \sigma(\nabla\dot{\phi} + j\omega\dot{A}) \quad (3.12)$$

From Maxwell's Eq. (3.1),

$$\nabla \times J = -\frac{\partial \rho}{\partial t} \quad (3.13)$$

Substituting (3.10) into the above equation,

$$-\nabla \cdot \sigma(\nabla\dot{\phi} + j\omega\dot{A}) = -\frac{\partial \rho}{\partial t}$$

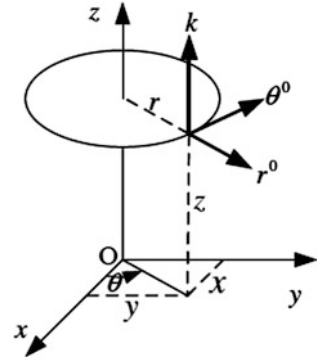
Ignoring the displacement current, we have $\frac{\partial \rho}{\partial t} = 0$, and σ is isotropic and constant; then,

$$\nabla \cdot (\nabla\dot{\phi} + j\omega\dot{A}) = 0 \quad (3.14)$$

Under the given boundary conditions, from Eqs. (3.12) and (3.14), \dot{A} and $\dot{\phi}$ could be solved; then,

$$\begin{aligned} \dot{B} &= \nabla \times \dot{A} \\ \dot{J}_e &= -\sigma(\nabla\dot{\phi} + j\omega\dot{A}) \end{aligned}$$

Fig. 3.3 The cylindrical coordinate system



When no defects exist, the RFEC model of the pipeline is axisymmetric, so the magnetic vector potential \dot{A} has only circumferential component \dot{A}_θ , and $\frac{\partial \dot{A}_\theta}{\partial \theta} = 0$; then, Eqs. (3.12) and (3.14) could be simplified in the cylindrical coordinates as (depicted in Fig. 3.3),

$$\frac{\partial^2 \dot{A}_\theta}{\partial r^2} + \frac{1}{r} \frac{\partial \dot{A}_\theta}{\partial r} + \frac{\partial^2 \dot{A}_\theta}{\partial z^2} - \frac{\dot{A}_\theta}{r^2} = -\mu J_{c\theta} + \mu\sigma \left(j\omega \dot{A}_\theta + \frac{1}{r} \frac{\partial \dot{\phi}}{\partial \theta} \right) \quad (3.15)$$

$$\frac{\partial}{\partial \theta} \left(\frac{1}{r} \frac{\partial \dot{\phi}}{\partial \theta} \right) = 0 \quad (3.16)$$

It is assumed that electric current source only exists in the excitation coil as $J_{c\theta}$ in the RFEC, and there is no voltage source, so $\frac{\partial \dot{\phi}}{\partial \theta} = 0$. Then, Eq. (3.16) is satisfied naturally, and Eq. (3.15) could be simplified further to

$$\frac{\partial^2 \dot{A}_\theta}{\partial r^2} + \frac{1}{r} \frac{\partial \dot{A}_\theta}{\partial r} + \frac{\partial^2 \dot{A}_\theta}{\partial z^2} - \frac{\dot{A}_\theta}{r^2} = -\mu J_{c\theta} + j\omega\mu\sigma \dot{A}_\theta \quad (3.17)$$

Under the given boundary conditions, \dot{A}_θ could be solved from Eq. (3.17), then the field variables could be derived,

$$\begin{aligned} \dot{B}_r &= -\frac{\partial \dot{A}_\theta}{\partial z} \\ \dot{B}_z &= \frac{\dot{A}_\theta}{r} + \frac{\partial \dot{A}_\theta}{\partial r} \\ \dot{J}_{e\theta} &= -j\omega\sigma \dot{A}_\theta \end{aligned} \quad (3.18)$$

3.2.2 The Propagation of the AC Magnetic Field in the Ferromagnetic Pipe Wall

In the RFEC, the electromagnetic field starts from the excitation coil, penetrates the ferromagnetic pipe wall to the outside air, and travels back into the pipe. This process is the key for a better understanding of the RFEC phenomenon. In this section, based on the above basic equations, the principle of axial propagation of the magnetic field in the pipe wall is further analyzed.

In the RFEC model, there exists no excitation current in the pipe wall; that is, $\dot{J}_c = 0$. Then, Eq. (3.17) becomes

$$\frac{\partial^2 \dot{A}_\theta}{\partial r^2} + \frac{1}{r} \frac{\partial \dot{A}_\theta}{\partial r} + \frac{\partial^2 \dot{A}_\theta}{\partial z^2} - \frac{\dot{A}_\theta}{r^2} = j\omega\mu\sigma \dot{A}_\theta \quad (3.19)$$

Except the transition region, the magnetic field lines are basically axial in the pipe wall. Because in the axial-symmetric model, the magnetic field lines are in fact the contour lines of $|r\dot{A}_\theta|$, we have $\frac{\partial \dot{A}_\theta}{\partial r} \gg \frac{\partial \dot{A}_\theta}{\partial z}$; then, the item $\frac{\partial^2 \dot{A}_\theta}{\partial z^2}$ in the above equation could be ignored and reduced to the one-dimensional case,

$$\frac{\partial^2 \dot{A}_\theta}{\partial r^2} + \frac{1}{r} \frac{\partial \dot{A}_\theta}{\partial r} - \frac{\dot{A}_\theta}{r^2} = j\omega\mu\sigma \dot{A}_\theta \quad (3.20)$$

When $r \rightarrow \infty$, we have $\frac{1}{r} \frac{\partial \dot{A}_\theta}{\partial r} \rightarrow 0$ and $\frac{\dot{A}_\theta}{r^2} \rightarrow 0$; then, the above equation becomes

$$\frac{\partial^2 \dot{A}_\theta}{\partial r^2} = j\omega\mu\sigma \dot{A}_\theta \quad (3.21)$$

which is the diffusion equation of one-dimensional electromagnetic field in a good conductor and has an analytic solution as

$$\dot{A}_\theta = \dot{A}_1 e^{-\sqrt{j\omega\mu\sigma}r} + \dot{A}_2 e^{-\sqrt{j\omega\mu\sigma}r} \quad (3.22)$$

in which coefficients \dot{A}_1 and \dot{A}_2 are decided by the excitations applied on the boundaries of the conductor. If the conductor occupies a half space, then $\dot{A}_2 = 0$, so

$$\dot{A}_\theta = \dot{A}_1 e^{-\sqrt{j\omega\mu\sigma}r} = \dot{A}_1 e^{-(1+j)\sqrt{\omega\mu\sigma/2}r} \quad (3.23)$$

Writing \dot{A}_1 as $A_1 \sin(\omega t + \psi_1)$, Eq. (3.23) in the time domain is

$$A_\theta(t) = A_1 e^{-\sqrt{\omega\mu\sigma/2}r} \sin(\omega t - \sqrt{\omega\mu\sigma/2}r + \alpha_1) \quad (3.24)$$

The skin depth is defined as $d = \sqrt{\frac{2}{\omega\mu\sigma}}$; then, the above equation becomes

$$A_\theta(r) = A_1 e^{-\frac{r}{d}} \sin\left(\omega t - \frac{r}{d} + \alpha_1\right) \tag{3.25}$$

which states that whenever the distance r increases one skin depth d , the amplitude of \dot{A}_θ decreases to 36.8 %, and the phase falls behind one rad.

Equation (3.20) is solved with the finite element method, and the obtained numerical solution is compared with the analytical solution as shown in Fig. 3.4. The parameter $d = 0.056$, so it could be seen that when $r \gg d$, the solution of Eq. (3.20) is very close to the analytical solution of Eq. (3.21).

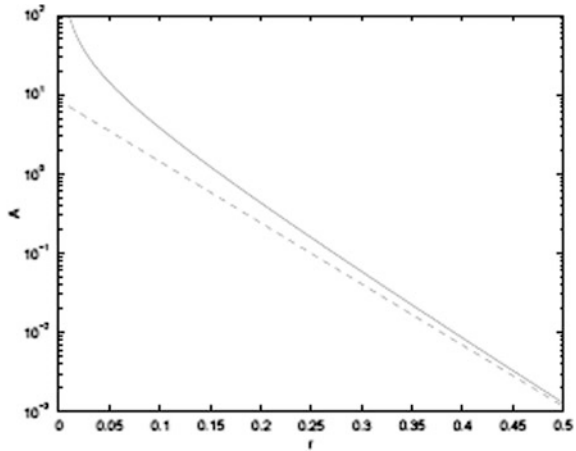
For the understanding of the results, assume that when $r \gg d$, the solution of (3.20) could be expressed approximately using $A_1 e^{-\frac{r}{d}\sqrt{J}}$; then,

$$\left| \frac{\partial^2 \dot{A}_\theta}{\partial r^2} \right| = \frac{1}{d} \left| \frac{\partial \dot{A}_\theta}{\partial r} \right| = \left| \frac{\dot{A}_\theta}{d^2} \right|$$

Because $r \gg d$, we have $\left| \frac{1}{r} \frac{\partial \dot{A}_\theta}{\partial r} \right| \ll \left| \frac{\partial^2 \dot{A}_\theta}{\partial r^2} \right|$ and $\left| \frac{\dot{A}_\theta}{r^2} \right| \ll \left| \frac{\partial^2 \dot{A}_\theta}{\partial r^2} \right|$; then, $\frac{1}{r} \frac{\partial \dot{A}_\theta}{\partial r}$ and $\frac{\dot{A}_\theta}{r^2}$ could be ignored, so (3.20) changes into (3.21).

In a practical RFEC model, the skin depth d is smaller than the thickness of the pipe wall and is generally of the magnitude of 1/5 to 1/3 of the thickness, and the radius of the pipe is much bigger than the skin depth, so the propagation characteristic of the magnetic field along the radial direction in the pipe wall in the near and remote fields of the RFEC could be described approximately with one-dimensional skin depth equation.

Fig. 3.4 Numerical solution (solid line) compared with the analytical solution (dashed line)



3.2.3 The Voltage Signal of the Receiving Coil

According to the electromagnetic induction principle, the electromotive force of one single receiving coil is

$$e = -\frac{d\Phi}{dt} \quad (3.26)$$

Using the phasor notation,

$$\dot{e} = -j\omega\dot{\Phi} \quad (3.27)$$

then,

$$\dot{\Phi} = \iiint_S \dot{B}dS = \iiint_S (\nabla \times \dot{A})dS = \oint_C \dot{A}dl$$

1. If the receiving coil is coaxial with the pipeline and the model is axisymmetric, then \dot{A} only has circumferential component \dot{A}_θ and is perpendicular to r , then the magnetic flux of the coil with radius r is

$$\dot{\Phi} = \oint_C \dot{A}dl = \int_0^{2\pi} \dot{A}_\theta d\theta = 2\pi r \dot{A}_\theta$$

in which \dot{A}_θ is the circumferential component of the magnetic vector potential on the wire of the coil. Substituting this into Eq. (3.26), then the induced EMF of the single-turn receiving coil with a radius of r in the sinusoidal AC electromagnetic field is

$$\dot{e} = -j2\pi wr \dot{A}_\theta$$

Applying the above equation to the multiturn receiving coil, the induced potential of the multiturn coil could be obtained.

Because the MVP value at every turn of the multiturn coil is unknown, the value of \dot{A}_θ at the radius of r_c , i.e., $\dot{A}_{c\theta}$, is used as the average of the MVPs of all the coils to solve for the induced potential,

$$\dot{e} = -j2\pi wr \dot{A}_{c\theta}$$

in which W is the number of turns of the receiving coil. It could be seen that the amplitude of the induced voltage \dot{E} of the coaxial receiving coil is proportional to the amplitude of \dot{A}_θ on the wires of the coil inside the pipeline, and the phase delay is 90° .

- (2) If multiple induction coils are placed circumferentially, each single induction coil is no longer axisymmetric, and the area of the coil is small, so it is proper to analyze with the following equation:

$$\dot{\Phi} = \iint_S \dot{B}_c dS$$

in which S is the cross-sectional area of the coil, and \dot{B}_c is the magnetic flux density in some point inside the coil.

If the receiving coil is parallel with the axial direction of the pipeline, we have

$$\dot{e} = -j\omega \dot{B}_{cz} S$$

If the receiving coil is perpendicular to the axial direction of the pipeline, then

$$\dot{e} = -j\omega \dot{B}_{cr} S$$

So when analyzing the non-axisymmetric model, the main work is to check the distribution of \dot{B} near the inside diameter and compare \dot{B}_r with \dot{B}_z to find a beneficial direction for the receiving coil.

3.3 The FEM Modeling of the RFEC in the Pipeline

In this section, the finite element method is introduced briefly, together with the FEM software package ANSYS, and several methods for the electromagnetic field simulation in ANSYS. Then, the method of building the RFEC model and some points in need of special attention are described, including the full RFEC FEM model, the local analyzing method to simplify the complexity in the simulation of the defects, and the 2D and 3D local defect model.

3.3.1 Introduction to the FEM and ANSYS

The numerical simulation of the physical phenomena is in fact the process of solving their mathematical models with given initial conditions or boundary conditions. The mathematical models of most of the physical phenomena are partial differential equations without analytic solutions. The methods for numerically solving the PDEs include the finite difference method, the finite element method, the integration equation method. Of these methods, the FEM is more suitable for problems with irregular boundaries and mixed kinds of media. The FEM is relatively mature, and there are many successful general FEM software packages such as ANSYS.

The FEM is the process of solving the boundary value problem numerically. The principle involves presenting the whole continuous region with many subregions. In the subregions, the unknown functions are expressed with simple interpolation functions with unknown coefficients. Therefore, the original boundary value problem with an infinite number of degrees of freedom is transformed into a problem with a finite number of degrees of freedom; the solution of the whole system is approximated with a finite number of unknown coefficients. Then, Ritz variation or Galerkin method are used to get a set of algebraic equations, and the solution of the boundary value problem is obtained by solving the system of algebraic equations.

A significant advantage of the FEM is that when processing problems with complicated shapes or when the boundary condition contains complex medium, it is not subject to the restrictions of the shapes of the field boundaries, and the second and third kinds of boundaries and the interfaces between different media do not need special processing, thus very suitable for solving electromagnetic field problems with irregular shape and mixed media.

The FEM is easy to implement on a computer, a computer program could be written to do the operations such as element meshing, overall assembling, and algebraic solving. Although the programs are usually complicated and lengthy, every stage is easy to be standardized into a general subprogram, and the precision of the calculation is good. There are many mature general-purpose finite element software packages, and a more detailed introduction will be given in the later section.

When solving engineering electromagnetic field problems, the steps could be divided approximately as the following:

1. The discretization of the continuous field, i.e., dividing the continuous field into finite number of elements. This is the first and the most important step in the finite element analysis. Different strategies of discretization will affect the consumption of computer memory, the time length of the calculation and the accuracy, especially when using general-purpose FEM software packages. For field on a 2D plane, the shape of the element can be triangular or quadrilateral. For field in the 3D space, the shape can be tetrahedron, rectangle or hexahedron, etc. In the same solution area, elements with different shapes could be used together.
2. The choice of a proper interpolation function, i.e., choosing the interpolation function that can approximately describe the unknown solution in an element. Usually, a first-order (linear) or second-order (quadratic) interpolation function is used, in order to obtain good computational performance and accuracy.
3. Building a system of finite element equations describing the characteristics of the whole solution region. In general, the process is based on the principle that at the nodes where some elements are connected, because the nodes are shared by the elements, the field variables of the elements connected at these nodes are required to be the same.

4. Solving the system of equations using the direct method or iterative method. The boundary conditions of the problem should be considered first, and then, the system of equations is solved, so unknown values of the field variables are obtained. Finally, through interpolation of these solved values, the values at an arbitrary field point can be calculated.

Reviewing the development history of the RFEC, it can be seen that the finite element analysis plays a very important role, mainly reflected in the following aspects:

1. The research on the RFEC mechanism. Exploring the internal mechanism of the RFEC and its characteristics, in order to better use it for nondestructive testing. In the 1980s, the RFEC technology underwent a rapid development owing to the application of the finite element method.
2. Defect response signal analysis and the research on the defect quantification method.

The numerical simulation by the finite element method can serve as a “test bed” generating defect signals to provide data for the research on the defect signal analysis and defect quantification.

If we only rely on building many samples and doing experiments to obtain the data for defect analysis, the process will be very time-consuming, and large sums of money must be spent. Moreover, some of the samples are difficult to build or test in the laboratory.

3. The optimal design of the RFEC probe. Conducting various numerical simulations of the probe by finite element method, to evaluate the advantages and disadvantages of various schemes, and choose the best scheme for further experimental study.

The study in this text mainly involves the first two aspects.

The finite element method, as a general numerical calculation method, already has a mature calculation model, and each stage in the calculation process is easy to be standardized, so it is not difficult to build a general calculation program to be used in various fields. In the past several decades, FEM software packages were developed in many countries, including ALGOR, ANSYS, ABAQUS, MARK, and NASTRAN. Of these packages, ANSYS is a mature and powerful general-purpose FEM analysis software package used widely in the fields such as structural mechanics, electromagnetics, and heat analysis.

When using ANSYS for electromagnetic field simulation, the steps of the finite element analysis are similar to those of a general finite element analysis. Since ANSYS is a general finite element analysis software, it will hide the details of the finite element analysis. The function of the ANSYS software is implemented by various processors, including the preprocessor, the solver, and two postprocessors. The main function of the preprocessor is to help build the finite element model. The finite element model could be obtained by meshing the directly built or imported solid model and could also be generated directly. In the solver, the boundary condition and the load are set for the model, and a proper method is selected to

solve the problem. This stage is the main part of the finite element analysis. After obtaining the solution, the postprocessor is needed to further process the results. The results could be viewed or exported to other software.

The following steps are commonly necessary when using ANSYS for a simulation,

1. Building the solid model and setting the parameters,
2. Generating the meshes to obtain the finite element model,
3. Setting the boundary conditions,
4. Applying the excitation and solving the problem, and
5. Post-processing the results, or exporting the results to other software.

When using ANSYS to solve 2D or 3D static, harmonic, and transient low-frequency magnetic field problems, the scalar potential, vector potential, and the edge-based methods could be applied. The scalar potential and the vector potential methods are both nodal methods, and the degrees of freedom are on the nodes, and the degrees of freedom of the edge-based method are on the edges of the elements. When the two-dimensional magnetic field analysis is carried out, only the vector potential method can be used, and the main degree of freedom is AZ. These three methods can all be used for 3D static, harmonic, and transient analysis, but each has advantages and disadvantages and are suitable for different problems. In the scalar potential method, there is only one degree of freedom, which is suitable for most of the three-dimensional static magnetic field analysis and cannot be used when there exist eddy currents. The main degrees of freedom of the vector potential method include three components AX, AY, and AZ of the vector potential. For voltage loading and circuit coupling analysis, the three degrees of freedom of current, voltage drop, and voltage can be introduced. When the interfaces between the different magnetic materials are contained in the calculation area, because the normal component of the magnetic vector potential is particularly large, decreased accuracy, and even error will be resulted. The scalar and vector potential methods can be used in the same model, but it is necessary to note that they must be connected in the same medium by the INTER115 elements. The edge-based method has a good ability to solve the three-dimensional low-frequency electromagnetic field problem and has a higher accuracy than the vector potential method, especially when iron regions exist in the model. However, when the model does not contain any iron region or velocity effect and circuit coupling exist, the edge element method cannot be used.

In this chapter, we use the vector potential method to simulate the two-dimensional remote-field eddy current model. The results are output to a text file, and then MATLAB is used to do further processing. A local analysis method is used to reduce the size of the model for 3D analysis. In order to set the boundary conditions easily, the vector potential method is used for analysis. Since the relative permeability of the pipeline is not large, the decreased accuracy of the vector potential method can be accepted.

3.3.2 Building the Remote-Field Eddy Current Model

In the process of actual testing, the remote-field eddy current inspector is moving in the pipeline with a certain velocity, because the distributions of the defects in the pipeline are not uniform, this testing process is transient, and the numerical simulation is difficult. In the early stage of the study when the main focus is in the analysis of the RFEC phenomenon and the defect response, it is not required to simulate the exact testing signal. The model could be simplified, that is, the inspector is static and the velocity effect is not considered, and the transient process and the high-frequency harmonic components are not considered. The problem is dealt with as a low-frequency harmonic electromagnetic field problem, and only the stationary response is analyzed.

When the defect analysis is conducted for the RFEC, it is found that when the same model includes the excitation coil and the defects in the remote-field region, the scale of the model will become very large, and the process of meshing and problem solving will consume much computer resources, and the local adjustment of the defects requires reprocessing of the whole model, and the work load will be huge. Because the interference of the defects to the magnetic field is limited in a small region, when the defect changes it is not required to recalculate the whole model, so a two-step local analysis method is taken: first, the complete RFEC model including the excitation coil is simulated to obtain the basic magnetic field distribution of the RFEC, and then, the local model of the remote-field region containing the defect is established. For the sake of distinction, the RFEC model with the excitation coil is called the complete RFEC model, and the model only containing the remote-field defect region is called the local RFEC defect model.

The complete RFEC model is a two-dimensional axisymmetric non-defect pipeline model containing the excitation coil, which is mainly used to simulate the basic magnetic field distribution of the RFEC, and to analyze the influencing factors.

The classical RFEC testing apparatus is shown in Fig. 3.5. When the defect in the pipeline is not considered, the model is axisymmetric, and the cross section

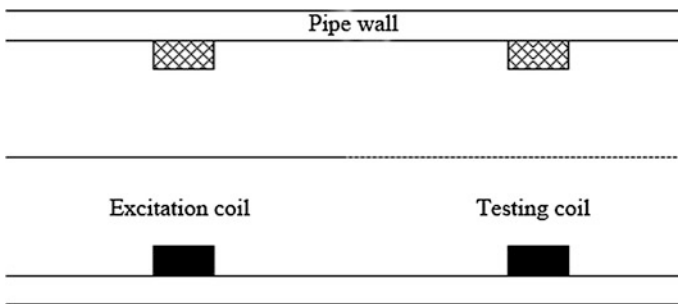


Fig. 3.5 The diagram of the remote-field eddy current model

containing the axis is taken, as shown in Fig. 3.5. The dimensions and physical parameters of the model are as follows:

1. The pipeline: OD is 100 mm, ID is 80 mm, $\mu_r = 70$, $\sigma = 7 \times 10^6$ S/m
2. The excitation coil: OD is 80 mm, ID is 60 mm, the width is 20 mm, $\mu_r = 1$, $\sigma = 3.33 \times 10^7$ S/m, 100 turns, and the excitation source is sinusoidal with a voltage of 12 V and a frequency of 30 Hz
3. Air: $\mu_r = 1$.

The RFEC problem is an open-domain problem, and the finite element model must be bounded, so it is necessary to expand the model boundary in the finite element analysis to handle the open-domain problem approximately, but this will lead to a sharp increase in the size of the model. We are mostly concerned about the magnetic field distribution in the remote field, which is determined by the magnetic field in the air outside the pipe. In order to get a more accurate solution, we need to expand the model to reduce the error caused by the model boundary. The model's solution region is shown in the ABCD region of Fig. 3.6, and the boundaries AD, BC, and CD are far from the excitation source, usually 10–20 times of the outer diameter is taken. When there is no defect in the pipe wall, considering the symmetry of the model, only the A'BCD' region is considered.

In the actual testing, the final detection signal is the voltage of the receiving coil. The amplitude and phase of this voltage can be expressed by the magnetic field at the receiving coil, so the receiving coil is not needed in the simulation model. This method has an additional benefit, because the nature of the defect detection is detecting the changes of the magnetic field, so any sensor with the ability to detect the magnetic field changes can be used. In addition to the induction coil, Hall components are also acceptable. Analysis of the magnetic field changes at the defect is more general and universal than analysis of the receiving coil. Therefore, we do not consider the receiving coil in the RFEC model.

The basic idea of finite element analysis is to approximate the solution in the local area in an element with a simple interpolation function, which is the main source of error. In order to reduce the error caused by the interpolation function

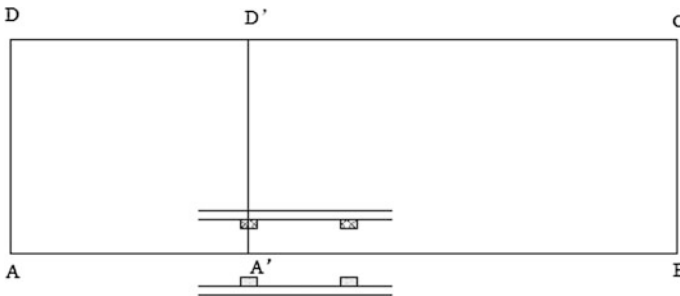


Fig. 3.6 The solution region of the RFEC model

approximation, we should choose the interpolation function, which is close to the solution of the actual problem. However, the choices of interpolation function in ANSYS and other general finite element analysis software are limited, and typical choices include a linear interpolation function and the quadratic interpolation function. On the other hand, the size of the element could be reduced, so that the solution in the local area of the element can be better approximated with the selected interpolation function. Therefore, in order to get accurate results, it is necessary to mesh the model properly according to the distribution of the solution to reduce the error caused by the simple interpolation function approximation. The approximate estimation of the error can provide reference for the meshing of the model.

The magnetic field in the RFEC phenomenon presents exponential decay of different rates, and the attenuation along the radial direction is the fastest. The amplitude of the magnetic vector potential is approximately expressed as

$$|\dot{A}_\theta| = A_0 e^{-r/d} \tag{3.28}$$

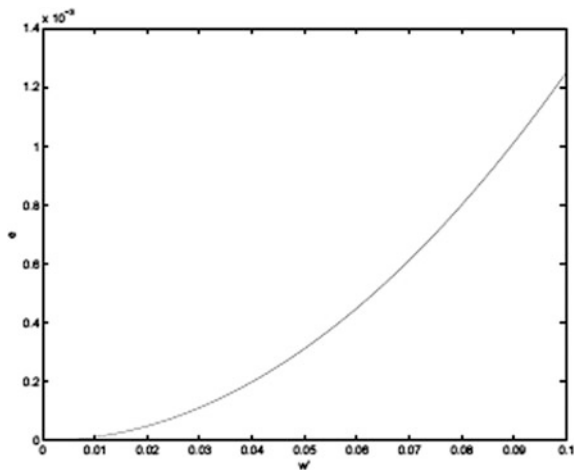
in which d is the skin depth.

Assuming the radial dimension of the meshes in the pipe wall is w , and let $r' = r/d$ and $w' = w/d$. For simplicity, the interpolation function in the FEM calculation is a linear function; then, the relative error using the linear interpolation function is

$$e = \frac{\frac{1}{2}(A_0 e^{-r'} + A_0 e^{-r'-w'}) - A_0 e^{-r'-w'/2}}{A_0 e^{-r'-w'/2}} = \frac{1}{2}(e^{-w'/2} + e^{w'/2}) - 1 \tag{3.29}$$

Figure 3.7 shows the change of the relative error with the size of the element when using linear interpolation function, when the radial direction of the element in

Fig. 3.7 The change of relative error with the size of the meshing using the linear interpolation functions



the pipe wall is $1/10$ of the skin depth d , the relative error is limited within 0.1% . The distribution of the magnetic field in other regions is also basically exponential, only the attenuation rate is smaller, and the size of the element could be bigger.

Meshing is a very important stage in the finite element analysis. The quality of the meshing directly decides the correctness, the accuracy, and the calculation time of the simulation. The normally accepted rule when meshing is that the meshes are denser where the magnetic field changes rapidly, and sparser where the magnetic field is uniform; and the meshes are denser where the magnetic field is strong, and sparser where the magnetic field is weak. Near the interface between two different media, denser meshes are also needed.

In order to better control the size of the mesh, it is needed to further divide the geometric model, such as the outer air is divided into several layers, the inner layer is denser, and the outer layer is sparser. In order to speed up the process of meshing, regular meshing should be used in the regular region, such as the coil, pipe, remote-field region, and so on, and the automatic meshing is adopted in the irregular region.

In the process of meshing for the RFEC model, there are some guidelines to follow:

1. No matter in the remote-field or near-field region, the magnetic field in the pipe wall changes very quickly in the radial direction, showing a fast exponential attenuation, so the radial meshing must be very dense and far less than the skin depth;
2. In the near-field and transition region, the magnetic field in the pipe wall and in the air inside the pipe changes very quickly along the axial direction, and it also needs denser meshes;
3. The magnetic field changes slowly in the air outside the pipe, so the mesh could be sparser, but at the region near the pipe surface, the mesh should be denser to ensure smooth transition;
4. In the remote-field region, the magnetic field in the wall and in the air inside the pipe changes slowly in the axial direction, the axial size of the mesh element can be slightly larger, so the mesh element is rectangular in the axial direction.

After the meshing process, it is necessary to set the type of the elements to be PLANE53, and the axial symmetry parameter should be added.

Figure 3.8 is the result of meshing for the complete model (for the convenience of display, the meshing sizes are all increased), and Fig. 3.9 is the amplification of the meshing results near the source of the excitation.

There exist three types of boundary conditions in the electromagnetic problems, i.e., the Dirichlet boundary condition, the Neumann boundary condition, and their combination. In Fig. 3.6 showing the finite element model of RFEC, the boundaries of $A'B$, BC and CD' have the Dirichlet boundary conditions, the $A'D'$ boundary has the Neumann boundary condition. In ANSYS, the default boundary condition is the Neumann boundary condition, i.e., the flux lines are perpendicular to the boundary, and this needs no specific settings. It is only necessary to set the nodal DOF AZ to 0

Fig. 3.8 The meshing results of the complete RFEC model

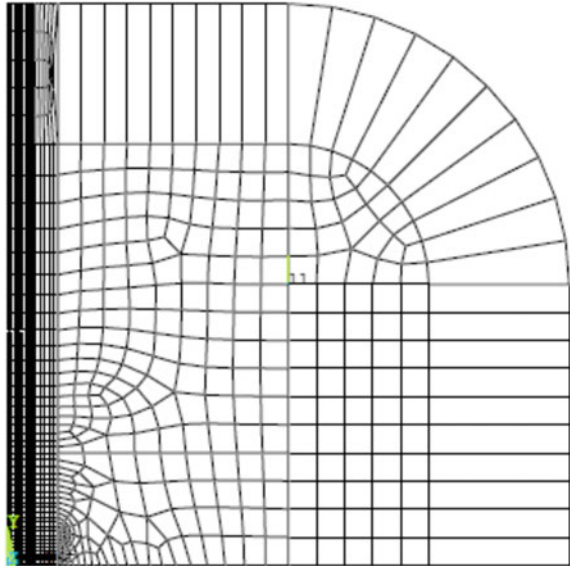
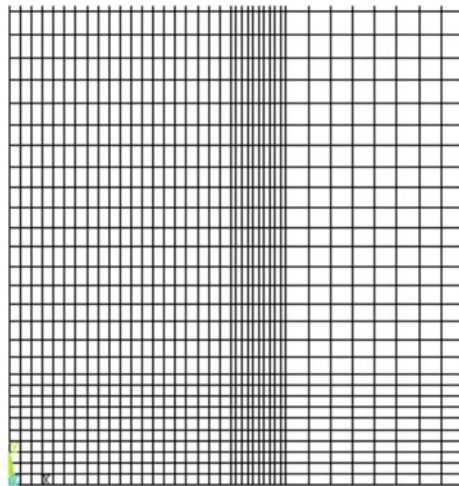


Fig. 3.9 The meshing results near the excitation coil



at the $A'B$, BC and CD' boundaries, so that the Dirichlet boundary conditions are satisfied.

In the above model and boundary setting, the BC and CD boundaries are approximated as infinity boundaries. Because the magnetic field distribution in the remote field is very important, the error caused by the approximation cannot be ignored, especially for the approximate treatment of the pipe wall and its surfaces. In order to minimize the error caused by the boundary approximation, the approach

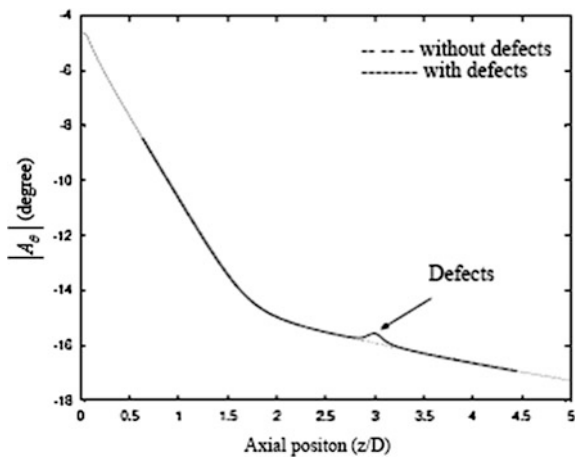
should be close to the actual situation, and the boundary conditions in ANSYS should be applied to handle this problem.

The excitation coil in the model is realized by setting the real constants of the elements in ANSYS, and the currents of these elements are coupled together to specify that all the elements in the coil share the same current.

The RFEC problem is an open-domain problem. In order to get an acceptable solution, the model size will be expanded to more than ten times, and the size of the model is very large. The range of change of the magnetic field in the model is large. According to the different used frequency, the difference is ten orders of magnitude, and the vast majority of energy is concentrated near the excitation source, and the part of interest is in the remote field where the magnetic field is very weak. The small error near the excitation source can give a great influence to the signal of the defect area. Because the field strength changes quickly with an exponential attenuation, especially in the pipe wall the magnetic field changes faster in the radial direction, the mesh must be dense to ensure certain accuracy. Thus, the complete RFEC model has a large scale. The defects are usually non-symmetric and must be solved by the three-dimensional model. The 3D model is obtained by rotating the two-dimensional model, and the scale of the model can be increased by two orders of magnitude, and the number of elements is in the order of a million.

In the simulation of the defect signal with a fully circumferential two-dimensional complete RFEC model, the magnetic field changes caused by the defects are localized; that is, they are limited within a region near the defects, and the influence to the magnetic field is small and can be ignored. Figure 3.10 shows a comparison of the amplitudes of \dot{A}_θ with and without defects. From the figure, except in a small region near the defects, the distributions of the magnetic field for these two cases coincide, which suggests that the disturbance of the defects to the magnetic field is limited in a small region.

Fig. 3.10 The variations of $|\dot{A}_\theta|$ with axial position for the two cases of with and without defects



Therefore, the simulation results of the 2D complete RFEC model can be used as the approximate boundary conditions, and only the defects in the local area are simulated to obtain the defect response signal. This procedure is called the local analysis method. The specific steps are as follows:

1. Building the two-dimensional complete non-defect pipeline axis-symmetric model including the excitation source, as shown in Fig. 3.11 with the external dashed box. The distribution of the magnetic field \dot{A}_θ is simulated and
2. Selecting the defect region and building two-dimensional or three-dimensional model, as shown in Fig. 3.11 with the internal dashed box. The boundary conditions of the model are obtained by the calculation of \dot{A}_θ with the 2D complete model, and the local model is simulated to obtain a more detailed and accurate defect signal distribution.

Because the simulation of the 3D complete RFEC model cannot be conducted, only the fully circumferential defects are considered with the 2D complete and local models, to validate the correctness and effectiveness of the local analysis method.

First, the 2D complete RFEC model containing the defect is built, and the defect response signal is obtained. Then, local analysis method is applied to the same defect to obtain the response signal, as shown in Fig. 3.12. The signals from the two methods almost coincide, and the mean square error is 0.03° , so the defect signal obtained by the local analysis method is credible.

For the defects with the same radial depths and axial lengths, the bigger are their circumferential dimensions, the more influences they will have for the magnetic field. Since local analysis method can be used for the simulation of the full circumferential defects, it can also be used for three-dimensional simulation of the non-axisymmetric defects with smaller circumferential sizes.

Fig. 3.11 The diagrams of the complete and local defect models

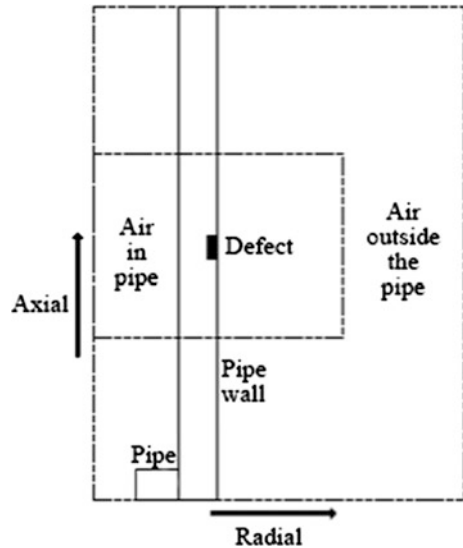


Fig. 3.12 The comparison of the results from the complete and local model

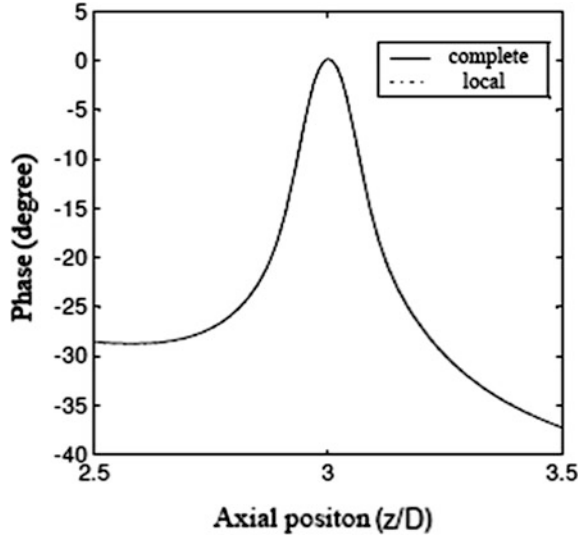


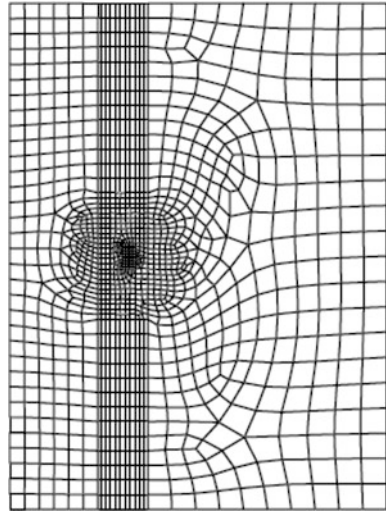
Table 3.1 Comparison of the scales of the models using the direct and local analysis methods

Models		Number of elements	Number of nodes
Direct analysis methods	Complete model with defects	7026	21,984
Local analysis methods	Complete model without defects	5436	16,412
	Local model with defects	1889	5768

Table 3.1 lists the number of elements and nodes of the three models. Although the total sizes of the two models in the local analysis method are larger than those of the direct method, the local method is not advantageous in terms of the computation complexity in the simulation of the 2D defect model. However, usually different sets of parameters are adopted for multiple runs of simulations, when using the local analysis method, we only need to modify and simulate the local defect model and do not need to repeat the simulation of the complete model, so the local analysis method in the two-dimensional defect simulation has its advantages. In simulation of three-dimensional model, the advantages of local analysis method are more obvious. As can be shown from Table 3.1, the local model is one order of magnitude smaller than the complete model, and the local analysis method is both correct and effective.

A two-dimensional local defect model with a full circumferential defect is shown in Fig. 3.11 with the internal dashed box, and its radial width is 3 times the radius of the pipe and the axial length is 2–4 times the radius of the pipe, according to the size of the defect.

Fig. 3.13 The meshing result of the 2D local defect model



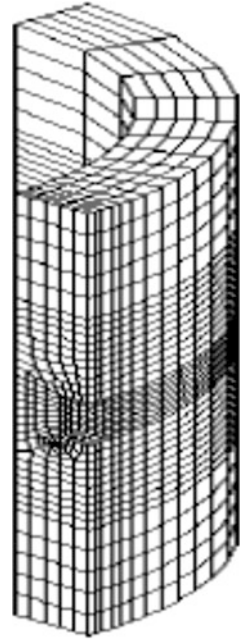
The existence of the defect leads to the distortion of the nearby magnetic field, and therefore, the mesh should be dense near the defect. At the interface of the pipeline and the air, the axial component \dot{B}_z of the magnetic field \dot{B} is parallel to the interface, and a big jump emerges, so a thin layer of air is added in the air of the interface, and dense and regular meshing is adopted, which can reduce the calculation error and improve the accuracy when obtaining the distribution of the magnetic flux density near the inner wall surface by interpolation. Figure 3.13 is the result of the actual meshing.

The boundary conditions of the local 2D model are very simple, i.e., Dirichlet boundary conditions are satisfied on the four edges. On the axis $\dot{A}_\theta = 0$ is set, and on the other three edges \dot{A}_θ are set with corresponding values from the simulation of the non-defect 2D complete model.

Because there is no excitation coil in the model, the load is not necessary, and the same method as used in the complete model is adopted.

The 3D local finite element model with defects is obtained by rotating the already meshed 2D local model. Since the whole model is symmetric about the plane containing the center of the defect and the axis of the pipeline, only one-half of the model is analyzed. At the same time, for a defect with a relatively small circumferential dimension, its influence to the distribution of the magnetic field along the circumferential direction is limited in a certain range, so that a certain region on one side of the defect could be selected for analysis, to further reduce the model size. With the existence of the non-symmetric defects, the magnetic field near the defects will change in the circumferential direction, and the nearer to the defects the bigger the magnetic field will change. So the closer the elements are to the defect, the smaller their circumferential dimensions should be. In ANSYS, it can be realized by controlling the scaling of the rotation trajectory. The actual finite

Fig. 3.14 3D local defect model



element model is shown in Fig. 3.14 (for the convenience of display, there is no air part, and the sizes of the elements are increased).

In the simulation of 3D electromagnetic field, the nodal scalar and vector potential method or the edge-based method can be selected. Because of the existence of the eddy current, the scalar method cannot be used alone in the three-dimensional simulation of the RFEC. Due to the use of local analysis method for three-dimensional simulation, the part of the model where the scalar potential method can be used (air) is not large, so the combination of vector potential and scalar potential methods is not advantageous and will instead make the problem more complicated, so it is not used. Therefore, the three-dimensional RFEC local defect model can be simulated by using vector potential method and edge-based method.

When applying the vector potential method, the SOLID97 elements are used, and the boundary conditions on the outer surface of the model were defined as Dirichlet boundary conditions. The 3 DOFs \dot{A}_x , \dot{A}_y and \dot{A}_z of the boundary nodes can be obtained according to the following formula from the \dot{A}_θ obtained with the two-dimensional complete simulation model,

$$\dot{A}_x(x, y, z) = \frac{y}{\sqrt{x^2 + y^2}} \dot{A}_\theta(r, \theta, z)$$

$$\dot{A}_y(x, y, z) = \frac{-x}{\sqrt{x^2 + y^2}} \dot{A}_\theta(r, \theta, z) \quad (3.30)$$

$$\dot{A}_z(x, y, z) = 0$$

The elements in the wall of the pipe have the DOF of $\dot{\phi}$. Since there is no externally applied excitation source in the pipe wall, so on the nodes at the outer boundaries this DOF is set to 0.

When using the edge-based method, the SOLID117 element is selected. This type of element has a DOF of AZ at the center nodes on the edges indicating the integral of \dot{A} on this edge,

$$AZ = \int \dot{A} dl \quad (3.31)$$

Based on the distribution of \dot{A}_θ obtained from the simulation of 2D complete model, from (3.30) \dot{A}_l and \dot{A}_r on the two ends of this edge and \dot{A}_m at the center point could be calculated. The integral of \dot{A} on this edge could be approximately expressed with the 3-point formula:

$$AZ = \int \dot{A} dl = \frac{1}{4} (\dot{A}_l + 2\dot{A}_m + \dot{A}_r) \cdot l \quad (3.32)$$

For the one-quarter model in Fig. 3.14, the axial cross section is not penetrated with flux lines, so the AZ DOFs of all the elements on this face can be directly set to 0. The elements in the pipe wall also have $\dot{\phi}$ DOF. Because there is no externally applied excitation source in the pipe wall, the boundary conditions at the nodes of the outer surface of the pipe wall are set as $\dot{\phi} = 0$.

3.4 2D FEM Simulation of RFEC in Pipeline

The complete defect-free two-dimensional RFEC model is established in ANSYS. The simulated distribution of magnetic field lines is as shown in Fig. 3.15, and it could be seen that the magnetic field energy is mostly concentrated at the near-field zone near the coil, and the magnetic field at the remote field in the pipe and outside the pipe is very weak.

The figure of magnetic flux lines of the axisymmetric model is in fact the contour plot of $|r\dot{A}_\theta|$. Because $|r\dot{A}_\theta|$ changes greatly and rapidly for the RFEC phenomenon, the general magnetic flux lines cannot describe accurately the distribution of the weak magnetic field in the remote region. So contour plot of $\log(|r\dot{A}_\theta|)$ is used as the equivalent magnetic flux line plot. As shown in Fig. 3.16, the variation

Fig. 3.15 The distribution of magnetic flux lines for the RFEC

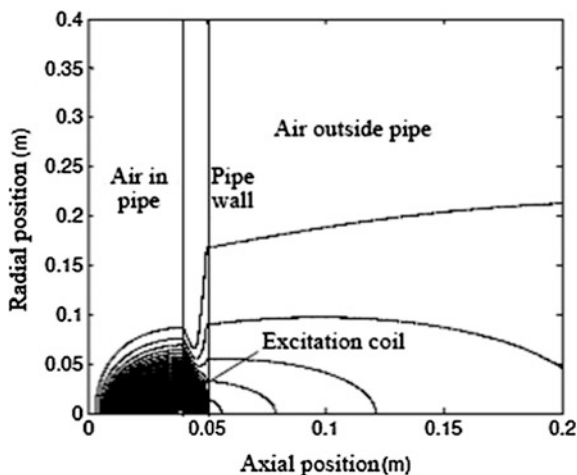
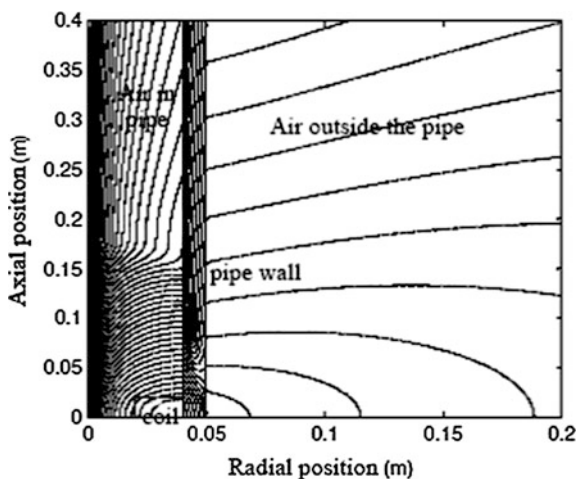


Fig. 3.16 The logarithmic flux lines of the RFEC



of the magnetic field of the whole model can now be displayed more clearly. The thing to note is that the meaning of the distance between the flux lines has changed, compared with the normal flux lines. These newly defined flux lines are called the logarithmic flux lines.

From Fig. 3.15, the distribution of the magnetic field could be observed. The magnetic field is the strongest in the near-field region, followed by the air outside the pipeline, and the magnetic field in the remote field in the pipe is the weakest. The magnetic field in pipe wall and in the remote-field region inside the pipe is basically along the axial direction. From Fig. 3.16, it can be seen that the exponential attenuation rate of the magnetic field is different in different regions, and the attenuation is the fastest along the radial direction of the pipe wall, followed by the axial direction

in the near-field region, and the slowest attenuation is in the air outside the pipeline. Within 0.5 times of the diameter is the near-field region, and the distribution of the magnetic field is similar to what is generated by a coil in the free space. Near the distance of 1 diameter is a transitional zone, and the logarithmic flux lines show the circuitous phenomenon, which is the “potential valley” phenomenon, and its local amplification is as shown in Fig. 3.17a. Figure 3.17b is the equal-phase plot of \dot{A}_θ for the same region, from which it can be seen that in the pipe wall and the equal-phase lines form the shape of a stair, that is, the “phase knot” phenomenon. Outside the 1.5 times of diameter of the pipe, the magnetic field in the pipeline is basically along the axial direction, and this begins the remote-field area.

Figure 3.18 shows the variations of the amplitude and the phase of \dot{A}_θ with the axial position, which is the characteristic curve of the RFEC phenomenon. In the near-field region, the amplitude of the vector magnetic potential has fast exponential

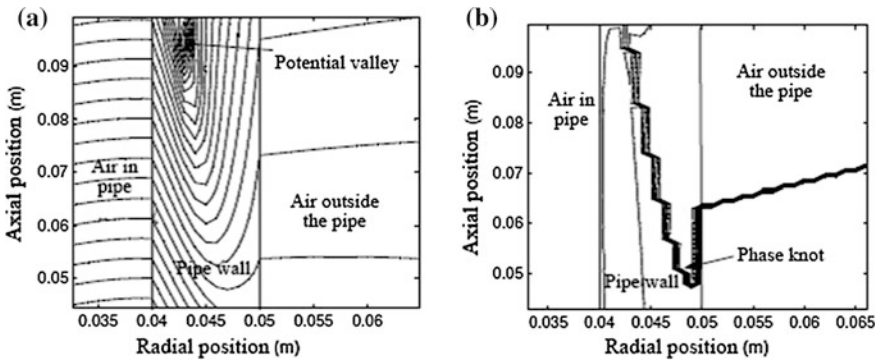
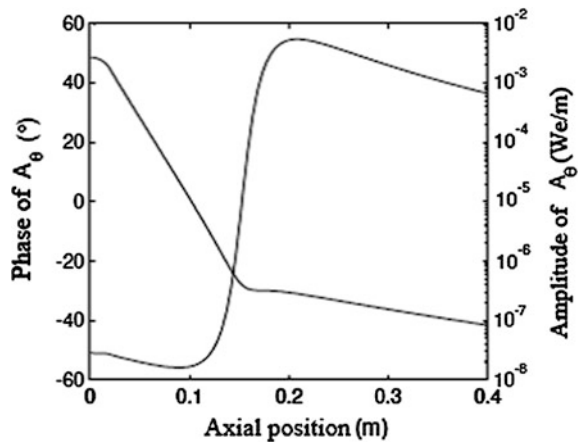


Fig. 3.17 The potential valley and the phase knot. a Potential valley; b phase knot

Fig. 3.18 Variation of \dot{A}_θ with the axial position at the inner surface of the pipe wall



decay, while in the remote-field region, it is also exponentially decaying, but the variation is relatively slow. Phase angle of the magnetic vector potential in the near-field region almost does not change, while in the transition region a significant jump appeared, and in the remote-field region the variation is again slow.

Figure 3.19 shows the variations of the amplitude and phase of the two components \dot{B}_r and \dot{B}_z of the magnetic induction intensity \dot{B} with the axial position near the inner wall surface of the pipe (5 mm inside). The axial component \dot{B}_z is two orders of magnitude larger than the radial component \dot{B}_r . The magnetic flux density is basically in the axial direction at the inner surface. Therefore, the detection coil of the three-dimensional probe is also parallel to the pipe axis, for the detection of the change of the axial component \dot{B}_z of \dot{B} .

Figure 3.20 is the radial distribution of the amplitude and phase of \dot{A}_θ in the wall at different axial positions. $z = 0$ m is the near-field region, $z = 0.1$ m is the

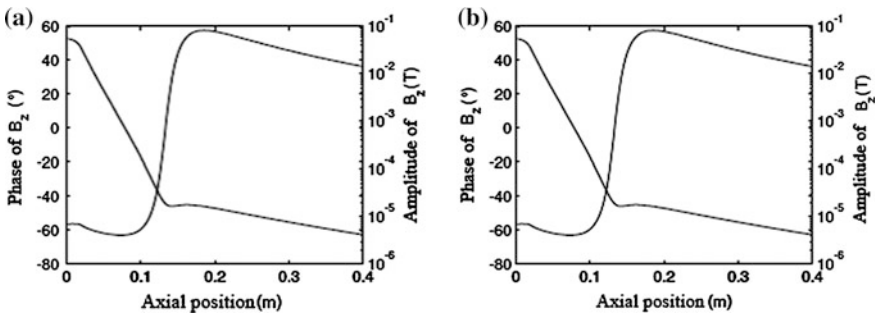


Fig. 3.19 The variation of \dot{B} with the axial position near the inner surface of the pipeline. **a** Axial component \dot{B}_z ; **b** radial component \dot{B}_r .

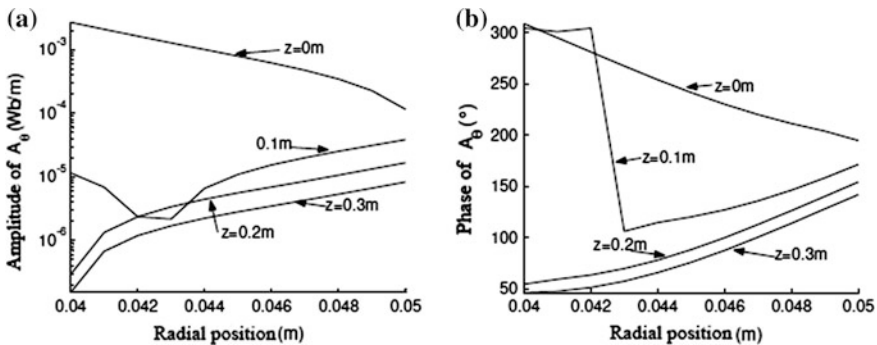


Fig. 3.20 The variation of \dot{A}_θ inside the pipe wall with the radial position at different axial positions. **a** Amplitude \dot{B}_z ; **b** phase \dot{B}_r .

transitional region, and $z = 0.2$ m and $z = 0.3$ m are the remote-field regions. In the near-field and remote-field region, the amplitude of \dot{A}_θ shows exponential variation in the radial direction, and the phase is changing linearly with the same rate and this can be estimated by using one-dimensional skin effect equation. In the wall of the near-field region, from inside to outside the amplitude of \dot{A}_θ attenuates and its phase lags, and the amplitude is big at the two sides and little in the middle, which is just the phenomenon of “potential valley” observed from Fig. 3.17a. The phase jumps, i.e., the “phase knot” phenomenon from Fig. 3.17b. At the outer surface of the pipe wall, the amplitude and phase changes of \dot{A}_θ are caused by the magnetic field propagating outside the pipe along the axial direction.

3.4.1 Electromagnetic Decomposition Analysis

In order to further understand the mechanism of the RFEC phenomenon and compare the effects of the magnetic and electric conducting capabilities of the pipe, electromagnetic decomposition analysis is conducted for the RFEC model. In the time-varying electromagnetic fields, the electric and magnetic fields are transformed reciprocally and cannot be separated. In the process of analysis, we always try to weaken the influence of electric field or magnetic field in the model and compare it with that of the RFEC phenomenon to observe the effect of electric field (eddy current) or magnetic field on the formation of the special RFEC phenomenon.

Based on the complete RFEC model, the material properties of the pipeline are set to the four cases in Table 3.2, and the simulation results are shown in Fig. 3.21. The plot on the left is the logarithmic flux lines, and the right is the variations of phase and amplitude of \dot{A}_θ at the inner surface of the pipe wall with the axial position. The four cases are described as follows:

1. Figure 3.21a is simulation result for $\mu_r = 1$ and $\sigma = 0$, i.e., the isolated coil in the free air without remote-field-effect or phase changes.
2. Figure 3.21b is simulation result for $\mu_r = 1$ and $\sigma = 7 \times 10^6$ S/m. There is no remote-field phenomenon; the distribution of the magnetic field is almost the

Table 3.2 Parameter settings for the pipe wall

		Relative permeability μ_r	Electrical conductivity (S/m)	Similar material
Non-ferromagnetic	Non-conductive	1	0	Air
	Electric conduction	1	7×10^6	Copper
Ferromagnetic	Non-conductive	70	0	Tombarthite
	Electric conduction	70	7×10^6	Steel

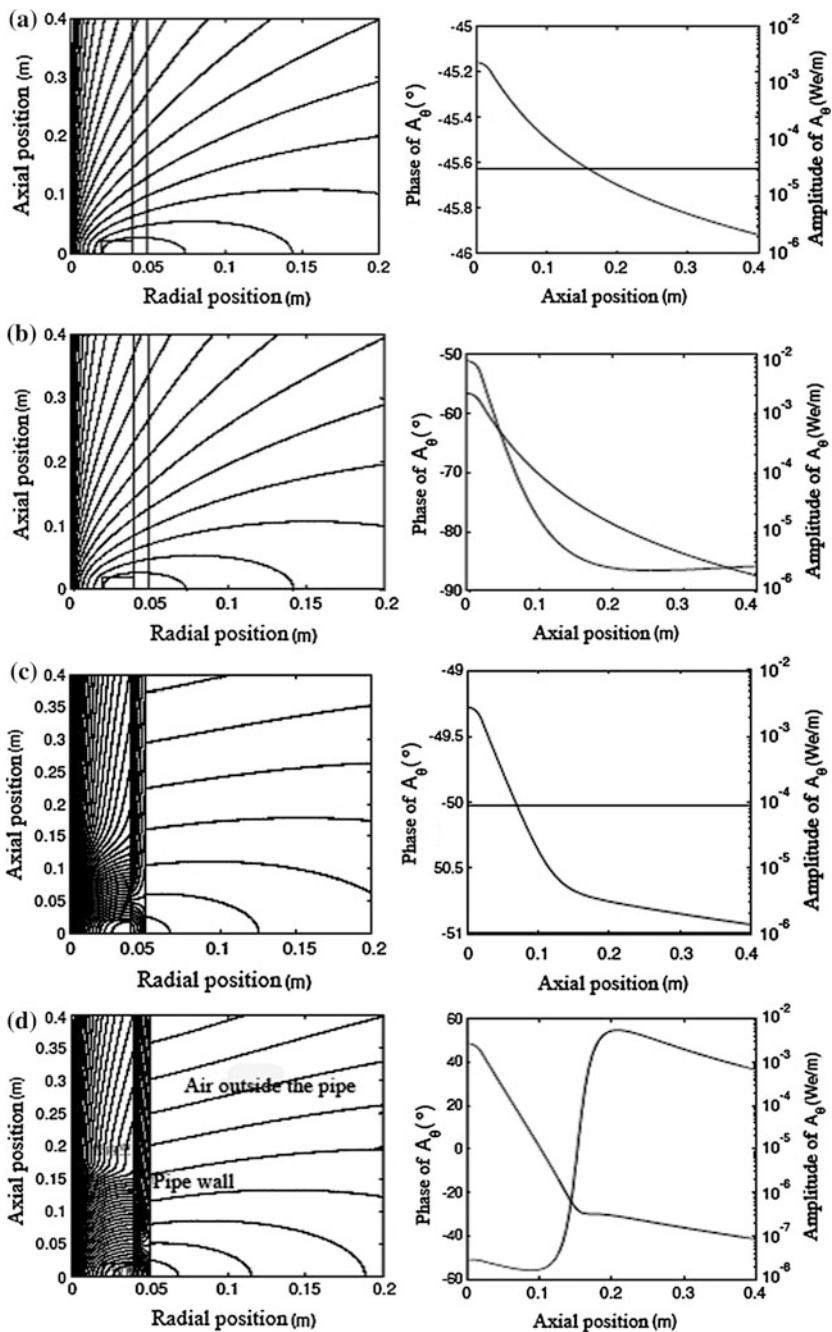


Fig. 3.21 Electromagnetic decomposition analysis. **a** Weak magnetic conductivity and non-electric conductivity. **b** Weak magnetic and electric conductivity. **c** Strong magnetic conductivity and non-electric conductivity. **d** Strong magnetic and electric conductivity

same as that of the coil in the free air. The phase change caused by the eddy current exists.

3. Figure 3.21c is simulation result for $\mu_r = 70$ and $\sigma = 0$. The remote-field phenomenon exists, and the distribution of the magnetic field is almost the same as the normal RFEC. The near-field and remote-field regions could be distinguished. Since there is no eddy current, no phase change exists.
4. Figure 3.21d is simulation result for $\mu_r = 70$ and $\sigma = 7 \times 10^6$ S/m, i.e., the previously analyzed RFEC phenomenon. The near-field and remote-field regions could be distinguished clearly. There also exists the phase change caused by the eddy current.

From the comparison of the above four cases,

1. The distributions of magnetic field of Fig. 3.21a, b are similar, and those of Fig. 3.21c, d are similar, indicating that the magnetic conductivity is essential for the distribution of magnetic field of the whole region. The distribution of the magnetic field in the RFEC phenomenon is mainly decided by the strong magnetic conductivity of the ferromagnetic pipeline.
2. There is no phase change for the magnetic fields in Fig. 3.21a, c, while there are phase changes caused by the eddy currents in Fig. 3.21b, d. This indicates that the eddy current induced by the magnetic field in the pipeline is the main reason for the magnetic field phase change in RFEC, but the law of phase change is not uniform, which is derived from that the induced eddy current (by the varying magnetic field) is not uniform.
3. Comparing Fig. 3.21c, d, the distributions of the magnetic field are very close, but in the transition region of Fig. 3.21c, there is no the potential valley phenomenon as in Fig. 3.21d. The magnetic fields in their remote region both penetrate twice the pipe wall returning to the inside of the pipe and carrying the structural information of the pipe wall and both could be used to inspect full thickness pipe wall defects. But because the former does not have phase change caused by the eddy current, only the amplitude could be used as the detected signal, the inspection performance is no better than the RFEC, and it lacks the ability to detect axial cracking. As a comparison, with the RFEC we could detect the influences of the defect on the distribution of the magnetic field and also the influences on the eddy current.

In short, the magnetic field distribution of the RFEC is mainly determined by the magnetic field conductivity of the pipe wall, while the phase characteristics of the magnetic field are caused by the electrical conductivity of the pipe wall and, at the same time, influenced by the magnetic field conductivity of the wall.

3.4.2 *The Evaluation Model of the Magnetic Field at the Inner Pipeline Surface*

The variation of the magnetic field at the inner wall surface of the pipe is the most important feature of the magnetic field distribution in the RFEC. If an approximate mathematical model could be built, it will be helpful to estimate the magnetic field distribution of the RFEC. In the logarithmic plot of \dot{A}_θ , its amplitude curve is basically two line sections, the turning point is the intersection of the two segments, the amplitude variation curve of \dot{A}_θ is obtained by the superposition of two exponentially decaying curves. The phase curve also contains two sections of straight lines, with a long transition region, and the turning point coincides with that of the amplitude curve.

Then, it is estimated that \dot{A}_θ has the following form in the time domain,

$$\dot{A}_\theta = A_1 e^{-\frac{\sigma}{d_{11}} - j\frac{\sigma}{d_{12}} + j\alpha_1} + A_2 e^{-\frac{\sigma}{d_{21}} - j\frac{\sigma}{d_{22}} + j\alpha_2} \quad (3.33)$$

in which the first item $A_1 e^{-\frac{\sigma}{d_{11}} - j\frac{\sigma}{d_{12}} + j\alpha_1}$ is the directly coupling part, $A_1 e^{j\alpha_1}$ is the initial value of \dot{A}_θ of the directly coupling magnetic field at the excitation coil, d_{11} is the attenuation rate of the amplitude of \dot{A}_θ along the axial direction, when the axial position increases a distance of d_{11} the decay of the amplitude of the magnetic field is 36.8 %. d_{12} is the lag rate of the phase of \dot{A}_θ along the axial direction, when the axial position increases a distance of d_{12} , lag of the phase is 1 radian. The second item $A_2 e^{-\frac{\sigma}{d_{21}} - j\frac{\sigma}{d_{22}} + j\alpha_2}$ is an indirect coupling part, and $A_2 e^{-j\alpha_2}$, d_{21} and d_{22} have similar meanings indicating the initial value and the law of changing of the indirectly coupled magnetic field.

Then, LMS fitting is conducted for the four sections of straight lines of the two curves,

$$\begin{aligned} A_1 &= 0.0060 \text{ Wb/m} \\ d_{11} &= 0.0159 \text{ m} \\ d_{12} &= 0.7824 \text{ m} \\ \alpha_1 &= -0.08781 \\ A_2 &= 1.06 \times 10^{-6} \text{ Wb/m} \\ d_{21} &= 0.1556 \text{ m} \\ d_{22} &= 0.5593 \text{ m} \\ \alpha_2 &= 1.341 \end{aligned}$$

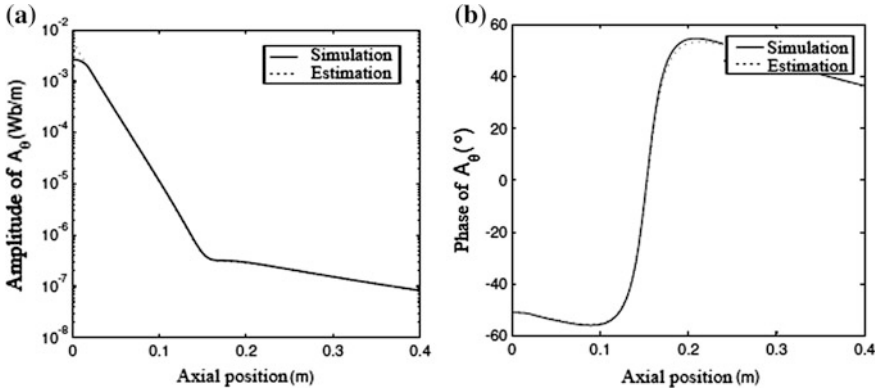


Fig. 3.22 Comparison of the simulation results and the estimation model. **a** Amplitude; **b** phase

that is,

$$\dot{A}_\theta = 0.0060e^{-\frac{\sigma}{0.0159} - j\frac{\omega}{0.7824} + 0.0878j} + 1.06 \times 10^{-6}e^{-\frac{\sigma}{0.1556} - j\frac{\omega}{0.5393} - 1.341j} \quad (3.34)$$

Figure 3.22 is the comparison of the estimation model and the real simulation results, which are very close, thus proving the validity of the estimation model.

From the fitting results,

1. Different from the propagation of the electromagnetic field in a good conductor, d_{11} and d_{12} in Eq. 3.33 have different values, and d_{21} and d_{22} are not the same either, i.e., the changing rates of the amplitude and the phase are different. From the previous electromagnetic decomposition analysis, there exists the remote-field phenomenon even in non-conducting ferromagnetic pipeline, i.e., the magnetic field energy could be decomposed into direct and indirect coupling energy, indicating that the main factor deciding the distribution of the magnetic field in the RFEC is the strong magnetic conductivity in the pipe wall, and it is not so related to the electrical conductivity. Only in conductive pipeline, there is a phase change of the magnetic field, indicating the main factor deciding the phase distribution is the electrical conductive energy of the pipe wall. Because the main factors deciding the amplitude and the phase are different, they may have different attenuation rates.
2. $A_1 \gg A_2$ and $\alpha_1 \ll \alpha_2$, mainly because the indirectly coupled magnetic field penetrates twice the pipe wall. With the influence of the eddy current in the pipe wall, the amplitude attenuates and the phase lags, and the amounts of the attenuation and the lag are related to the thickness of the pipe wall and the skin depth.
3. $d_{11} \ll d_{22}$, indicating that the direct coupling magnetic field attenuates much faster than the indirectly coupled energy, and this is decided by the strong magnetic field conductivity of the pipeline. The directly coupled magnetic field attenuates rapidly in the pipeline with the influence of the pipe wall, and the pipe

wall does not influence the propagation of the indirectly coupled magnetic field outside the pipeline along the axial direction, so its attenuation is relatively slow.

4. d_{21} and d_{21} are close. Because they are influenced by the eddy currents in the pipe wall, with the limitation of the skin depth effect, eddy currents with different radial depth will have different influences. While the indirectly coupled magnetic field is not restricted by the skin depth effect, and the eddy currents with different radial depths will have similar influences, so d_{21} is slightly larger than d_{21} .

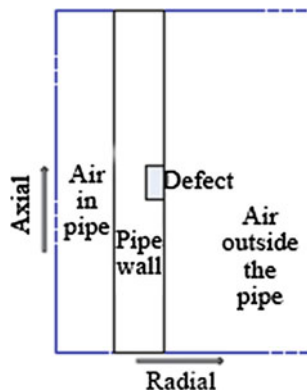
The coefficients A_1 , d_{11} , d_{12} , ∂_1 , A_2 , d_{21} , d_{22} , and ∂_2 in the estimation model are related to the physical parameters in the RFEC model, such as the magnetic permeability and electrical conductivity, the diameter and thickness of the pipeline, and the amplitude of the excitation source. From the analysis of these factors, an estimation model for these coefficients could be built, and finally obtaining an estimation model for the magnetic field at the inner wall surface from the physical parameters of the RFEC model.

3.4.3 Analysis of the Full Circumferential Defect

The pipe with a full circumferential groove or a crack is axisymmetric, which can be simulated with a two-dimensional axisymmetric model, greatly reducing the complexity of the model. Although the full circumferential defects are practically nonexistent, this simplified model can be used to analyze the influences of the circumferential and radial dimensions of the defect on the response signal, serving as an approximate analysis means when it is difficult to conduct a FEM analysis of 3D non-axisymmetric defect. This was also accepted at the early stage of finite element analysis of the RFEC phenomenon.

In order to reduce the complexity of the model and simplify the process of simulation of the full circumferential defect, the local analysis method is used, and Fig. 3.23 is a diagram of the local 2D model of the groove defect at the outer

Fig. 3.23 The 2D local model of the full circumferential defect



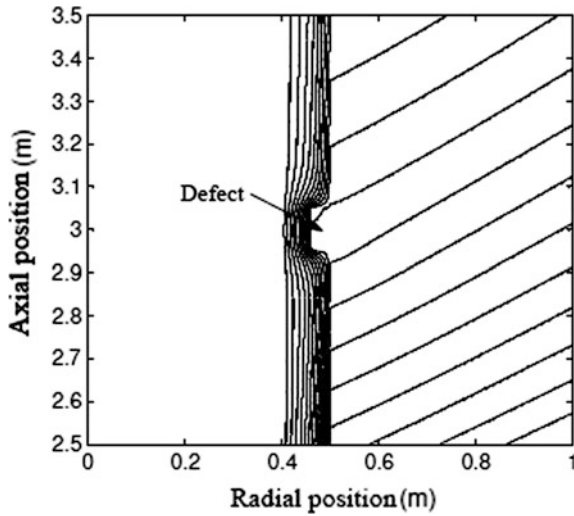


Fig. 3.24 The distributions of the flux lines from the full circumferential defect at the outer surface of the pipeline

surface of the pipe wall. The restrictions of \dot{A}_θ applied on the four boundaries are from the simulation of the complete pipeline RFEC model with the default parameters.

Figure 3.24 is the distribution of the flux lines when there exists a groove defect at the outer surface of the pipeline, 3 times the diameters of the pipeline away from the excitation source. The axial width of the groove is 10 mm, and the radial depth is 4 mm (40 % thickness). The defect only disturbs the magnetic field in a small local region. Figure 3.25 is the phase and amplitude curves of \dot{A}_θ at the inner wall surface of the pipe, and at the location of the defect (0.3 m), there is a very large peak.

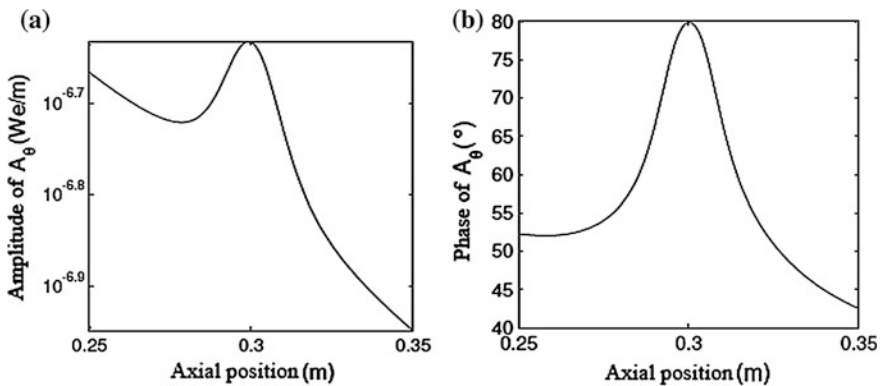


Fig. 3.25 Distribution of \dot{A}_θ at the inner pipe wall surface with the full circumferential defect. **a** Amplitude; **b** phase

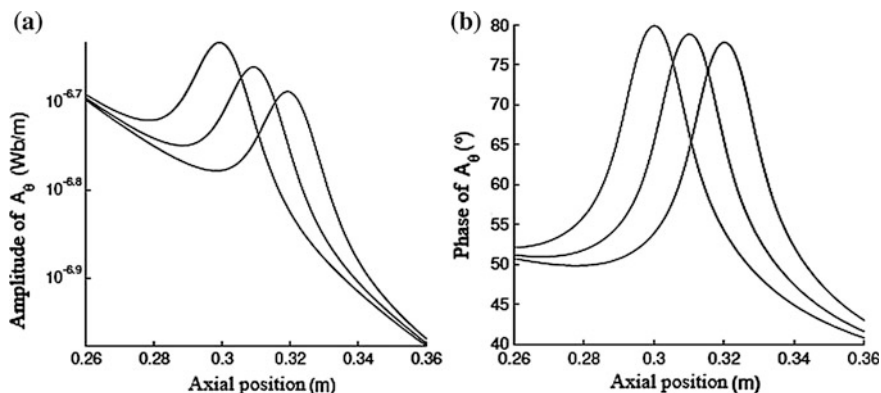


Fig. 3.26 The distribution of \dot{A}_0 at the inner pipe wall surface with defects at different locations. **a** Amplitude; **b** phase

The magnetic field distribution obtained by the above model is equivalent to the detection signal when the excitation coil is fixed and only the detection coil is moving. In the actual testing, the excitation coil and the detection coil are moving in the pipeline with the same speed, and the distance between them is fixed. Figure 3.26 shows the distributions of the magnetic fields from the same one defect at three different axial positions in the remote region (i.e., the distances from the excitation coil are different). They have the same shapes and can be transformed mutually with translational operations. The variation of the signal of the same part of the defect with the position is in accord with the case without any defect, so the change of the signal from the variation of the position has nothing to do with whether or not a defect exists. Using this characteristic, the magnetic field distribution obtained by the simulation can be used to obtain the actual testing information.

Assuming that without any defect, the vector magnetic potentials at the distances z_1 and z_2 from the excitation coil are \dot{A}_{01} and \dot{A}_{02} , respectively, and some defect generates vector magnetic potential \dot{A}_1 at the distance z_1 from the excitation coil; then, it could be obtained that the vector magnetic potential \dot{A}_2 at the distance z_2 from the excitation coil is

$$\dot{A}_2 = \frac{\dot{A}_{02}}{\dot{A}_{01}} \dot{A}_1$$

So the corresponding testing signal could be obtained from the distribution of the magnetic field of the defect,

$$\dot{A}_t(z) = \frac{\dot{A}_0(z = z_t)}{\dot{A}_0(z)} \dot{A}_f(z)$$

in which $\dot{A}_t(z)$ is the real testing signal, $\dot{A}_0(z)$ is the distribution of the magnetic field without any defect, and $\dot{A}_f(z)$ is the distribution of the magnetic field with a defect, and z_t is the position of the receiving coil. By the above transformation, the magnetic field distribution obtained from the simulation of the above model could be converted into the defect signal in the actual testing, and Fig. 3.27 shows the testing signal corresponding to the magnetic field distribution in Fig. 3.25. In the analysis of this chapter, we use this method to transform the magnetic field distribution with the defect into the defect signal.

Figure 3.28 shows the distribution of the flux lines generated by the groove defect at the inner surface of the pipe wall with the same position and the same dimensions. Compared with distribution of flux lines of the outer surface defect in Fig. 3.24, it can be seen that only the flux lines near the defect are different, and the other lines are almost the same.

Figure 3.29 shows the testing signals of the groove defect at the inner and outer surfaces of the pipe wall. The solid line is the outer surface defect, and the dashed line is the inner surface defect. It could be seen that when using the amplitude as the testing signal, the peak value of the signal of the inner surface defect is bigger, and the outer surface defect signal is wider. When using the phase as the testing signal, the inner and outer defects almost show the same characteristics. It is found that the RFEC testing method has the same sensitivity to the defects at the inner and outer surfaces of the pipeline, so only the outer surface defect will be considered in the following study of the full circumferential defect signal.

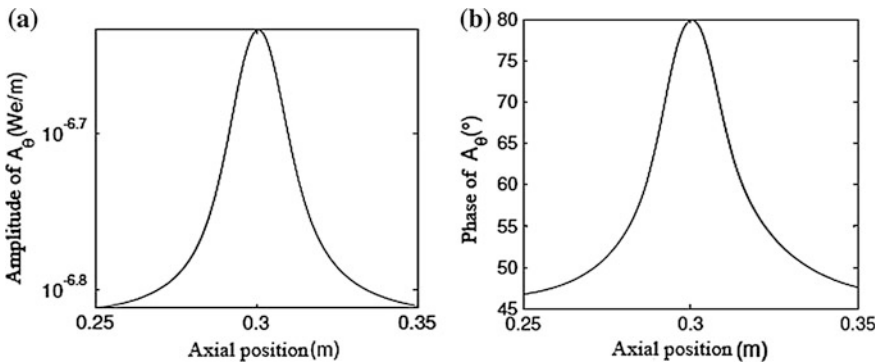


Fig. 3.27 The full circumferential defect signal. a Amplitude; b phase

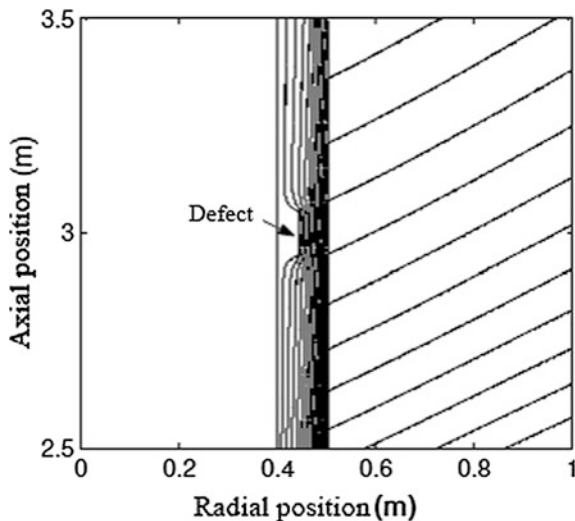


Fig. 3.28 The distribution of the flux lines of the full circumferential defect at the outer surface of the pipe wall

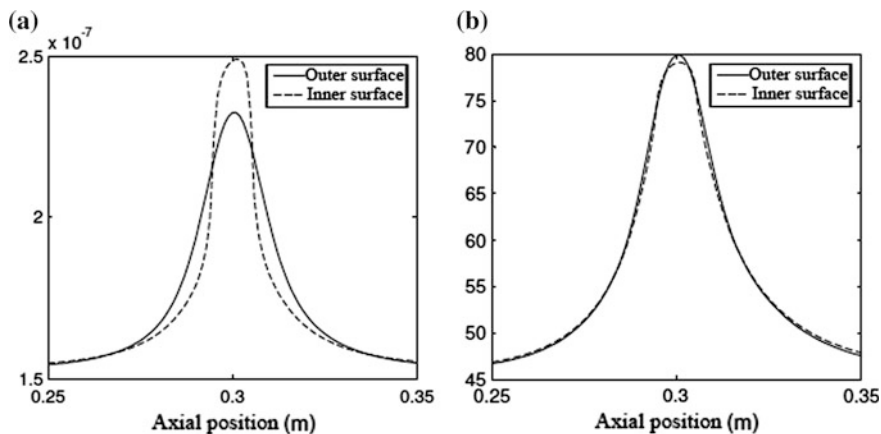


Fig. 3.29 Comparison of the signals of inner and outer surface defects. **a** Amplitude; **b** phase

3.4.4 Relation of the Defect Signal with the Dimensions of the Defect

Figure 3.30 shows the testing signal of the full circumferential defects of different radial depths (with axial width 0.005 m), and it can be seen from the figure that the amplitude signal at the defect is approximately exponential with the defect depth, while the phase signal has a linear relationship with the defect depth. The peak

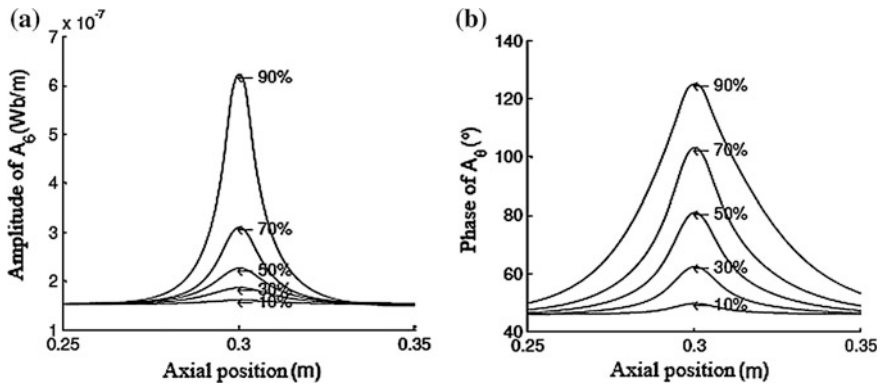


Fig. 3.30 Comparison of defect signals of different radial depths. **a** Amplitude; **b** phase

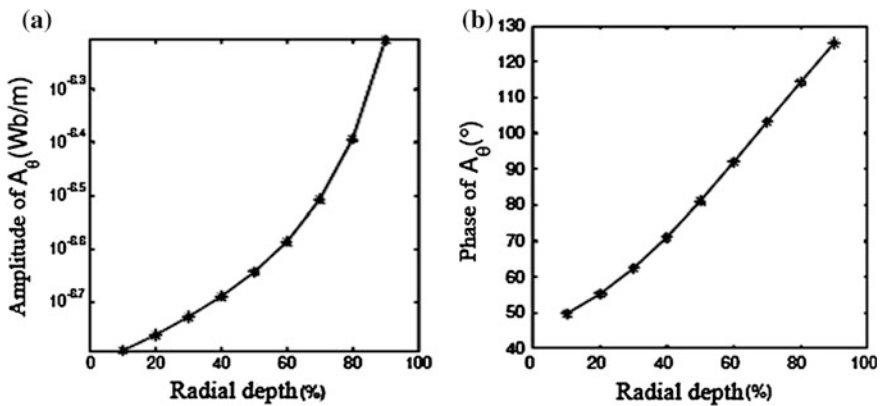


Fig. 3.31 Relation of peak value of defect signal with radial depth. **a** Amplitude; **b** phase

value of the defect signal is used as the characteristic feature of the signal. The relationships between the amplitude and the phase, and the defect depth are shown in Fig. 3.31. Therefore, the use of phase as the testing signal is better for quantifying the depth of the defect. When the depth is 10 % pipe wall thickness (i.e., 1 mm), the amplitude and phase signals cannot be detected, so this depth is the limit of detectable defect depth.

Figure 3.32 shows the testing signals of the full circumferential defects with the same radial depth (5 mm, 50 % pipe wall thickness) and different axial widths. When the axial size is very small, such as 0.1 mm, equivalent to a circumferential crack, there are still detectable amplitude and phase signals, indicating that the RFEC has the capability to detect the circumferential crack.

Figure 3.33 is the relationship between the peak value of the defect signal and the axial width, and the amplitude signal is approximately linear with the axial

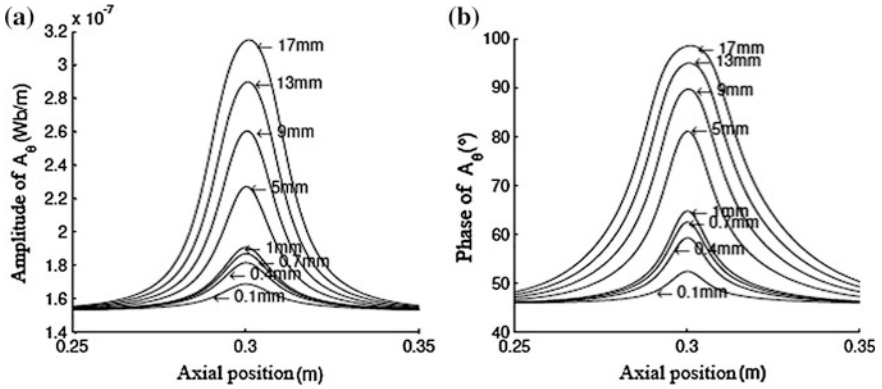


Fig. 3.32 Comparison of defect signals of different axial widths. a Amplitude; b phase

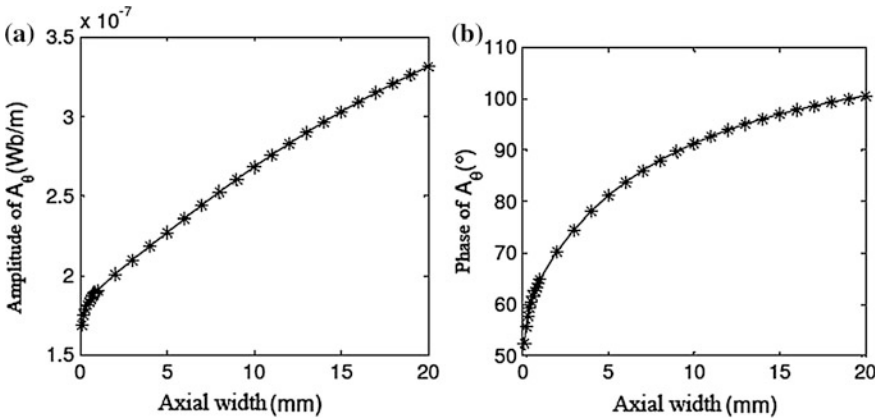


Fig. 3.33 Relation of defect signal peak value with axial width. a Amplitude; b phase

width. While for the phase signal, the peak value increases slowly with the increasing axial width and gradually approaches one certain max value.

Generally speaking, the width of the defect signal is mainly determined by the width of the defect, and under the ideal situation, if the defect is wide enough, the width of the defect signal should be equal to the width of the defect. However, the actual defect width is limited, so the integral of the defect signal along the axial direction is selected as the characteristic variable, which contains the information of both signal amplitude and width. Figure 3.34 is the relationship between the integral of the defect signal and the axial width, when the defect width is big (larger than 0.5 mm), the integrals of the amplitude and phase signals have obvious linear relationships with the axial width, so they could be used as the characteristic variables for quantification of the axial width of the defect.

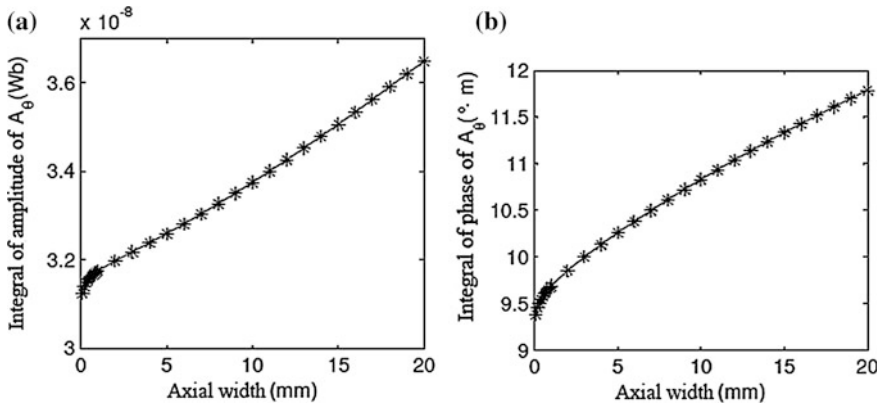


Fig. 3.34 Relation of defect signal peak value with axial width. **a** Amplitude; **b** phase

Based on the above analysis of the relationship between the defect signal and the radial depth and axial width, the amplitude and phase signals can both be used in the full circumferential defect detection, and groove and crack defects with depths bigger than 1 mm (that is, 10 % pipe wall thickness) could be detected. When conducting axial and radial sizing of the defects, the use of peak value of the phase signal and the integral along the axial direction as the characteristic variables can be more convenient.

3.5 3D FEM Simulation of the RFEC in the Pipeline

The real defects in the pipe wall are generally not full circumferential. In order to obtain the defect response signal in accord with the reality, a 3D finite element model is necessary to simulate the RFEC. The full three-dimensional model of the RFEC is large, and it is difficult to carry out defect analysis on a normal PC, so the local analysis method is used for the simulation to reduce the size of the 3D model.

3.5.1 Signal of the Groove Defect

In the actual pipeline inspection, the shapes of the defects are arbitrary, but the shapes can be divided into three categories: the groove defects along the circumferential direction (i.e., circumferential defects), the groove defects parallel to the pipeline center axis (i.e., axial defects), and round hole shape pitting defects (i.e., radial defects). The circumferential defects are similar to the full circumferential defects already analyzed with the two-dimensional axisymmetric model, so they will not be analyzed in details any more. Axial defects seldom emerge in the

actual pipeline, so they will not be analyzed in detail, either. The stress corrosion cracking of natural gas pipeline is mainly in the axial direction and is close to the axial groove defect. Therefore, the main focus is on analyzing the characteristics of the axial defect signals.

When testing non-axisymmetric defects, to obtain the circumferential position of the defect, 3D sensors must be used, composed of many axial direction coils placed at equal circumferential distances at the inner surface of the pipe wall. As the testing signal, the induced voltage of the coil is determined by the axial component \dot{B}_z of the magnetic induction intensity \dot{B} in the region near the coil. In the remote-field region of the RFEC, the magnetic field near the inner wall of the pipe is mainly in the axial direction. The radial and circumferential components of the magnetic induction intensity are small, and the amplitude and phase of \dot{B} are very close to the axial component \dot{B}_z . So in the following analysis, the distribution of \dot{B} is mainly investigated and used as the basis of the defect signal.

Assuming that at the distance of 3 times of radius to the excitation coil, there is an axial groove defect with a length of 10 mm, width of 2 mm, and depth of 4 mm. The distribution of the magnetic induction intensity near the inner surface of the pipe wall (5 mm inside) is as in Fig. 3.35, and the scale of the region is that the circumferential extents are 45° on both sides. Along the axial direction, the lengths are 50 mm on both sides. Because the amplitude and phase are large at the side of the excitation source, for the convenience of observation of the distribution of the magnetic field, the axial position is reversed in the plot, and the right side is near the excitation source. The amplitude distribution of \dot{B} in Fig. 3.35a is relatively uniform, and the amplitude variation caused by the defect is basically not seen. The phase distribution in Fig. 3.35b shows very obvious defect characteristics, and at the location of the defect, there is a very high peak, and there are two less obvious valleys on both sides in the axial direction.

Figure 3.36 shows the eddy current vector plot near the axial groove defect (only one-half of the defect is drawn), and the magnitude of the eddy current in the defect

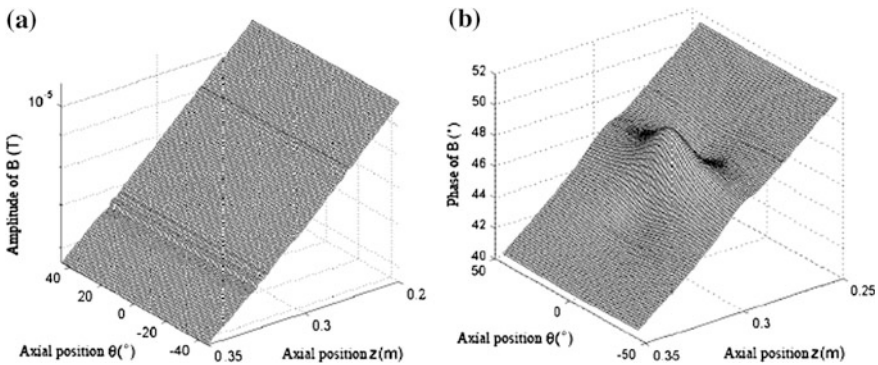
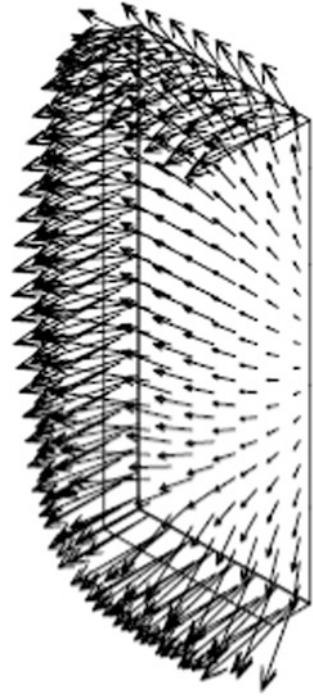


Fig. 3.35 Distribution of \dot{B} of the axial defect. **a** Amplitude; **b** phase

Fig. 3.36 Vector plot of the eddy current around the defect



(left in the figure) is close to that at the two sides along the axial direction (upper and lower sides in the figure) and their directions are the same. Therefore, the eddy currents on both sides of the circumferential direction flow around the inner edges of the defect and the magnitude is not influenced. The magnetic induction intensity distribution is not the defect response signal of the inspection, but can be converted into the actual testing signal using the same method as the analysis of the simulation results of the two-dimensional model. The defect signal detected by the receiving coil at the position z_t is

$$\dot{B}_t(z) = \frac{\dot{B}_0(z = z_t)}{\dot{B}_0(z)} \dot{B}_f(z)$$

in which $\dot{B}_0(z)$ is the distribution without any defect, \dot{B}_f is the distribution with a defect, and \dot{B}_t is the real testing signal. From this, the real defect detection signal could be obtained, as shown in Fig. 3.37. Because the part of the variation of the magnetic field with the axial position is removed, the testing signal in Fig. 3.37 could better show the defect signal than the distribution of the magnetic field in Fig. 3.35.

The amplitude and phase signals in Fig. 3.37 have basically similar characteristics, and the phase signal is more obvious, so it is more appropriate to use phase as the testing signal.

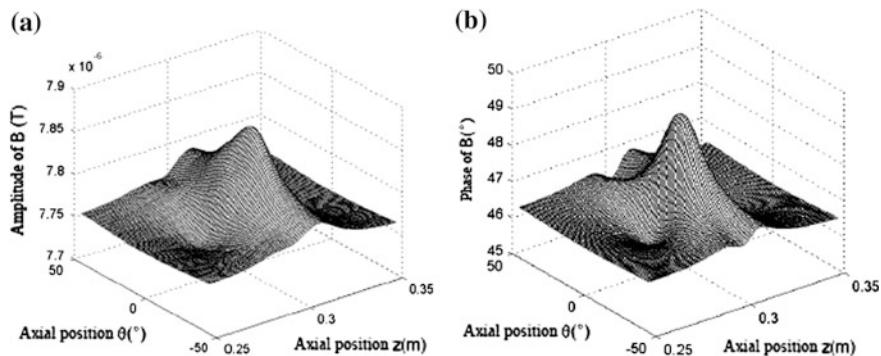


Fig. 3.37 The testing signal of the axial defect

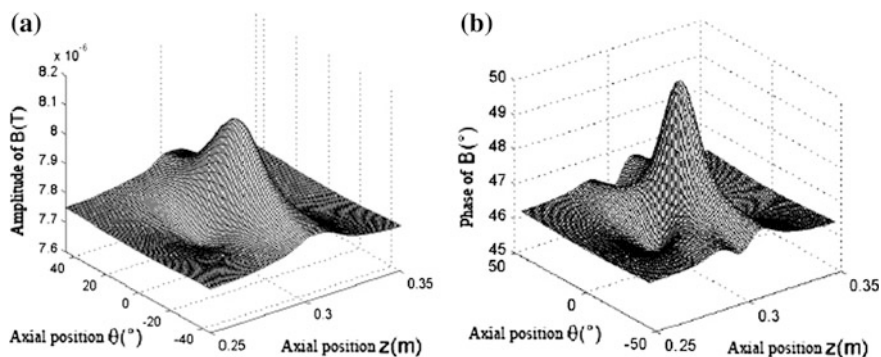


Fig. 3.38 The testing signal of the circumferential defect. a Amplitude; b phase

Figure 3.38 is defect signal of a circumferential groove, with a circumferential length of 10 mm, an axial width of 2 mm, and a radial depth of 4 mm. The shape of the signal is very similar to that of the axial flaw, but the peak values of the amplitude and phase signals are bigger.

Figure 3.39 shows the signal of radial groove defect, with a radial depth of 9 mm, axial length of 3 mm, and circumferential width of 3 mm. The shape of the signal is very similar to the previous two cases, only that the peak of the phase signal is a little steeper.

The above three defects with different directions have different shapes, but their volumes are similar ($80, 80$ and 81 mm^3 , respectively), from their signal plots it is difficult to differentiate these three defects, and the reason may be that the size differences are small. Figure 3.40 shows the comparison of the signals of the three defects after expanding their dimensions to twice of the original dimensions, as shown in Table 3.3. Their signals are obviously enhanced compared with those of the previous smaller defects, and the differences among the signals of the three defects are also increased. It is still difficult to differentiate them from the shapes of

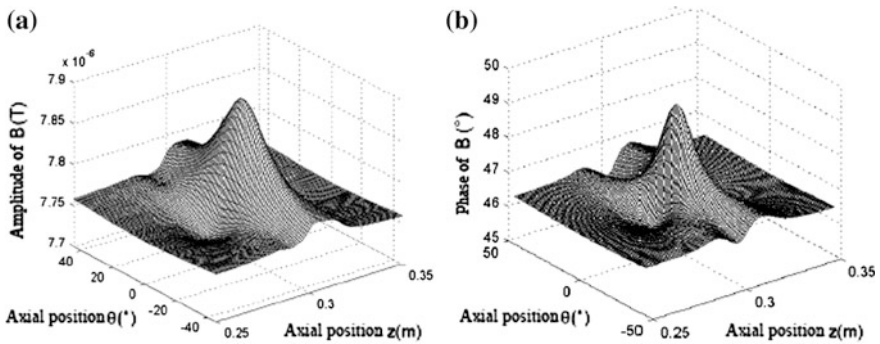


Fig. 3.39 Testing signal of the radial defect. **a** Amplitude; **b** phase

the signals, which indicates that the RFEC testing is not sensitive to the shape of the defect. It will be difficult to know the shape of the defect in the inspection process.

Since the actual testing signal changes along the axis of the pipeline, comparing the differences among the three defects with different directions along the axis is more meaningful, in Figs. 3.41 and 3.42, the testing signals at the centers of the three defects with different directions are compared. From the figures, the signal peak value of the circumferential defect is the maximum, especially the amplitude signal. When the defect is small, the amplitude signals of the axial and radial defects are close, and the phase signals are barely distinguishable. With the increasing differences of the dimensions of the defects, the signal differences are revealed. The signal of the axial flaw is wider in the axial direction, and the peak value of the signal of the radial defect is larger, this trend of variation is in accord with the intuition. When the defect is large, the width of the signal along the axial direction is close, but the increase of the axial dimension of the defect has little influence to the width of the signal. Therefore, the RFEC testing method is the most sensitive to the axial defect and has the highest sensitivity. In addition, with the increase of the size of the defect, the degrees of depression at both sides of the signal peak are reduced.

The amplitude and phase signals of the magnetic field can be affected by the pipe wall structure when the magnetic field penetrates through the pipe wall from outside to the inside at the remote-field region. If there are some defects in the pipe wall, equivalently the wall thicknesses decrease, so the weakening and lagging effects of the eddy currents on the magnetic field will be decreased, then the amplitude and phase signals are increased. From the skin effect equation, the influence of eddy current on the amplitude and phase of the magnetic field is related to the distance of the magnetic field through the eddy current and not related to the value of the eddy current. So the amplitude and phase information of the magnetic field penetrating directly through the defect is closely related to the defect depth. For the RFEC, the amplitude and phase changes of the magnetic field penetrating through the pipe wall at the defect are used to implement defect detection. However, the magnetic field near the inner surface at the defect does not only contain the component carrying

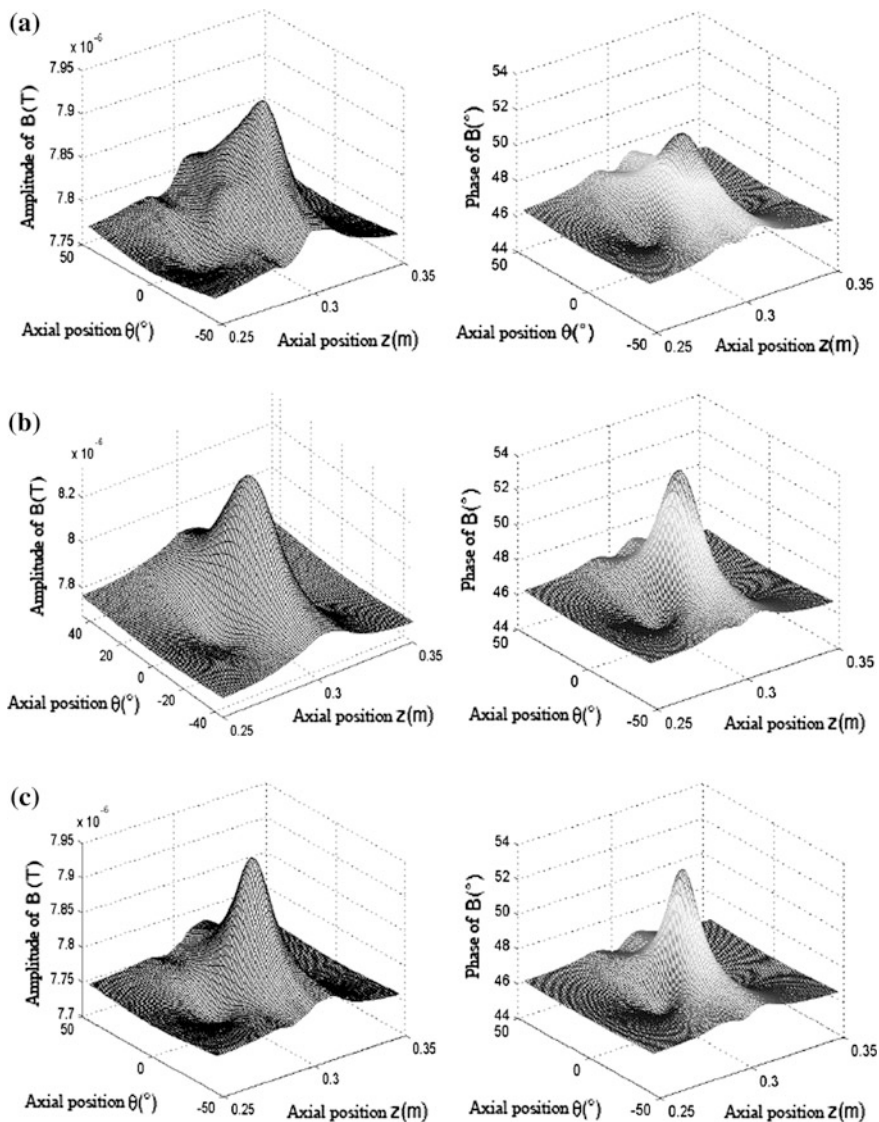


Fig. 3.40 Signals of axial grooves with different widths. **a** Axial defect; **b** circumferential defect; **c** radial defect

the defect information, and it also includes the part of magnetic field without any defect information. The measured total magnetic field is the superposition of the two parts.

When the defect is relatively small, the part of the magnetic field with defect information is relatively weak, and the contribution to the magnetic field in the pipe at the defect position is small, so the defect information is not fully expressed.

Table 3.3 Dimensions of three groove defects

Defect types	Axial dimension (mm)	Circumferential dimension (mm)	Radial dimension (mm)	Volume (mm ³)
Axial defect	20	2	4	160
Circumferential defect	2	20	4	160
Radial defect	4	4	9	144

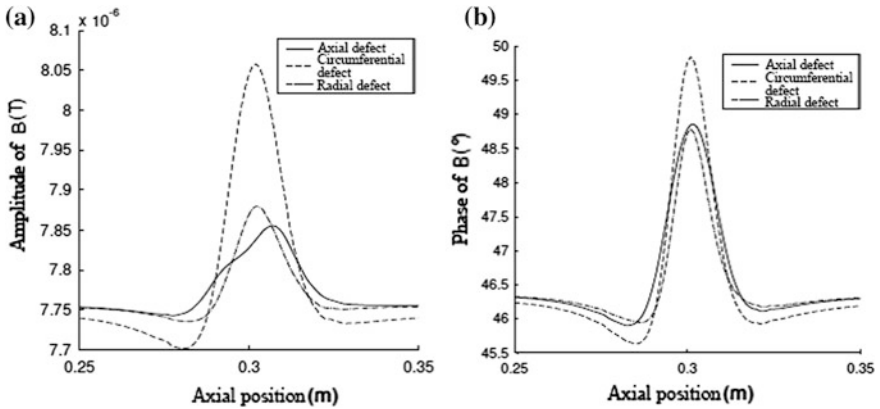


Fig. 3.41 Comparison of signals of three small defects with different directions. **a** Amplitude; **b** phase

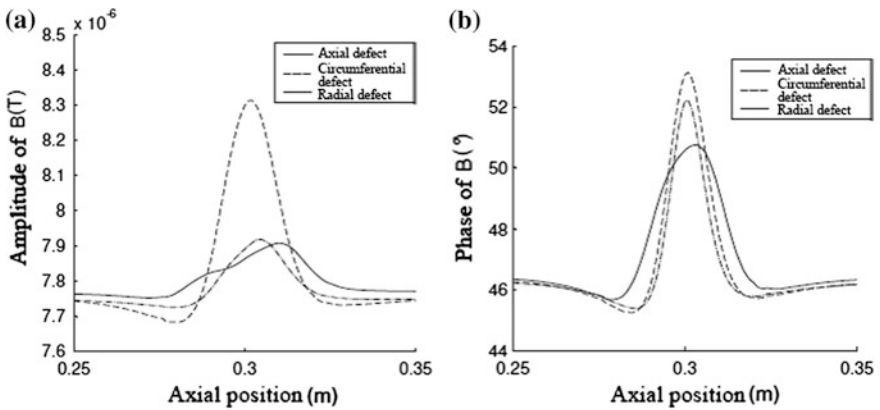


Fig. 3.42 Comparison of signals of three large defects with different directions. **a** Amplitude; **b** phase

So the defect depth is barely reflected in the information provided by the above three small defects with different orientations. The main reason of the change in the distribution of magnetic field near the defect is that the defect changes the magnetic circuit in the pipe wall, and the magnetic field lines flow around inside of the defect. The larger is the cross section of the defect the more the magnetic circuit will be altered, so the signal of the circumferential defect is the most obvious.

According to the bound wave theory, the propagation direction of the magnetic energy is perpendicular to the flux lines. Around the defect (i.e., both sides in the axial direction and both sides in the circumferential direction), the direction of the flux lines changes, and flow around the corner of the defect, resulting in a change of the path when the magnetic field penetrates through the pipe wall at this location. The path is longer than the case without any defect, and the magnetic field attenuates more under the influence of the eddy current, and the phase lag is also bigger. When the defect size is relatively small and the energy of direct penetrating through the defect is not dominant, the characteristics of this part of the magnetic field are expressed, that is, depressed parts appearing around the locations of peak values in the signals of the above three kinds of defects. Because the magnetic field in the pipe wall is mainly axial, this change in the axial direction is more obvious, and in the above plot, the depressed parts of the axial direction are more obvious. This phenomenon is not found in the full circumferential defect signal, because the magnetic field in the inner region of the defect is completely dominated by the part of direct penetrating through the defect.

3.5.2 Relationship Between Axial Defect Signal and Defect Size

Figure 3.43 shows the signals of grooves with an axial length of 10 mm, radial depth of 4 mm and different circumferential widths. The selected widths are 2, 6, and 10 mm. Comparing the three defects with different widths, it is easy to find that the shapes of the signals are basically the same, and the peak values of the amplitude and phase signals change greatly with the defect widths. The larger is the width, the higher are the peak values.

Figure 3.44 shows the signals of the cracks with smaller circumferential sizes. The widths are 0.2, 0.6, and 1 mm. Their signal characteristics are similar to those of the above groove defects, but the magnitude is much smaller. The effective signal of the crack with a width of 0.2 mm is very small. The effective phase signal is only 1° , and the effective amplitude signal is in the order of 10^{-8} T. Although the effective signal can be observed in the simulation, it is relatively weak and approaches the limit of crack detection.

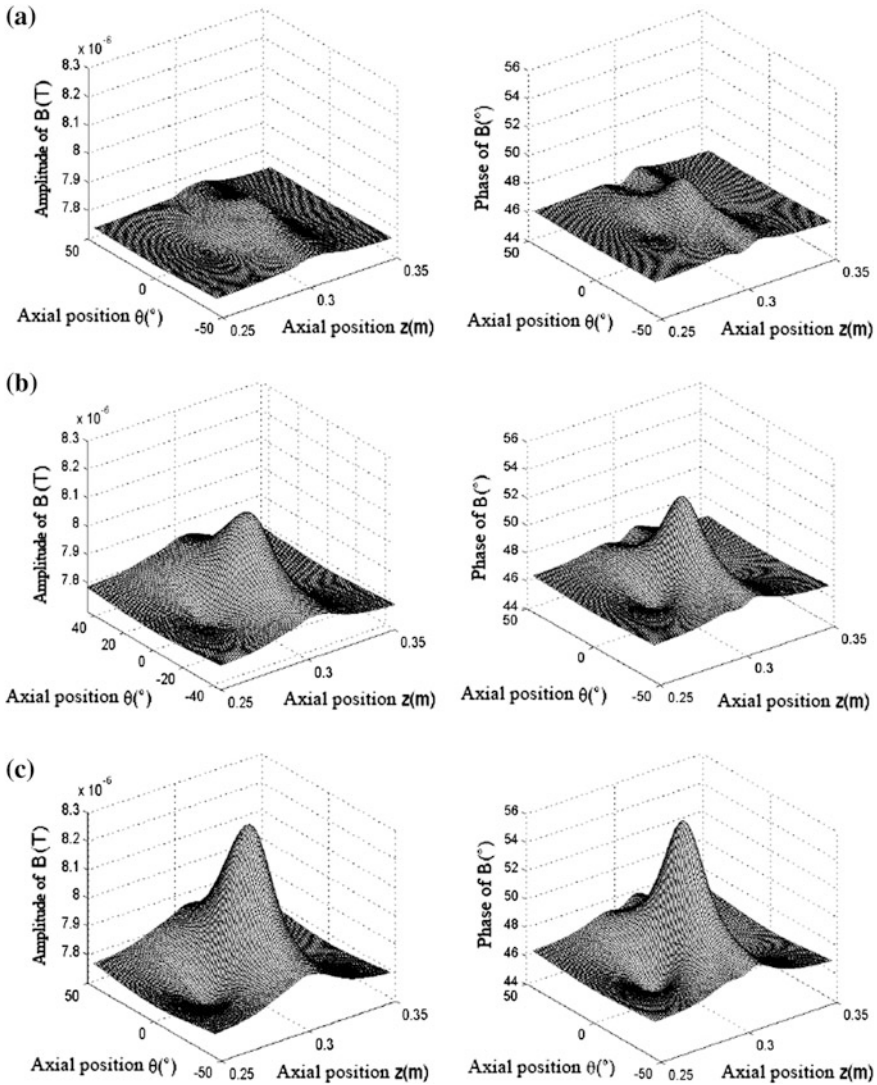


Fig. 3.43 The signals of axial grooves with different widths. a 2 mm width; b 6 mm width. c 10 mm width

Figure 3.45 shows the curves of variations of the peak values of the amplitude and phase signals of the axial flaw with the widths of the defects. The peak value of the phase signal is linear with the defect width, and in accord with the fitted straight line. The peak value of the amplitude curve is exponential with the width of the defect (logarithmic coordinates are used in the figure), which is in accord with the fitted logarithmic curve. Therefore, the peak values of the amplitude and phase

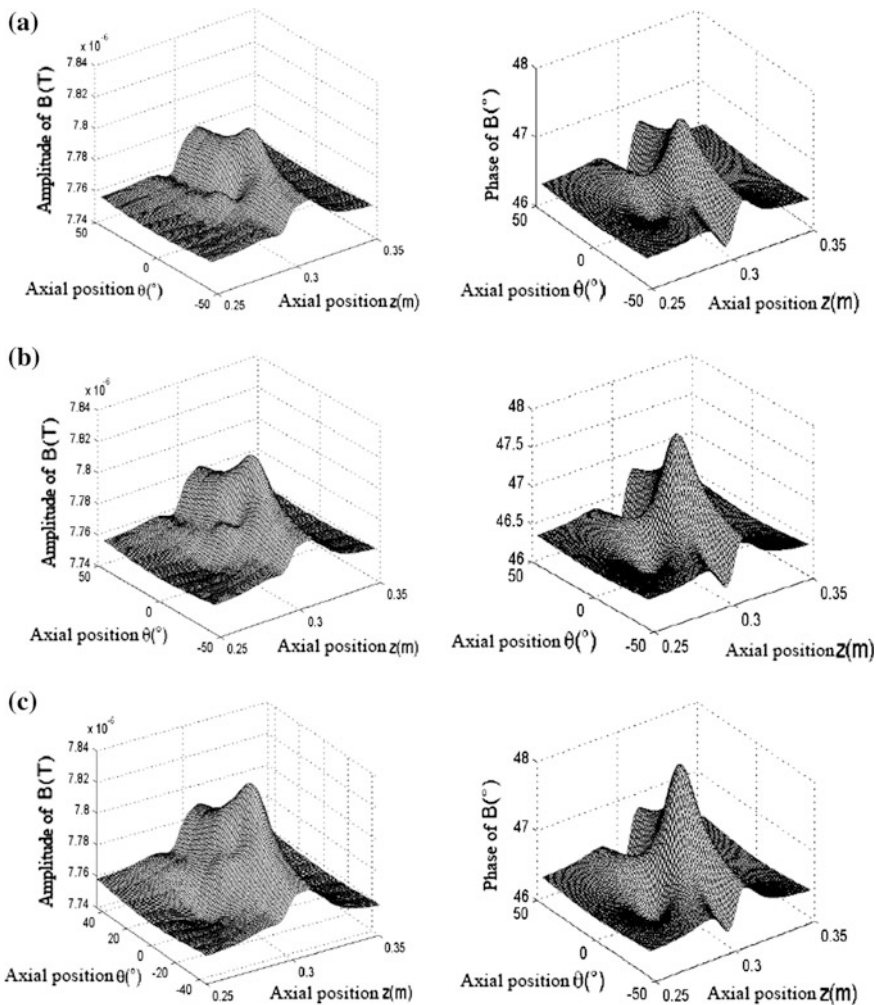


Fig. 3.44 The signals of axial cracks with different widths. **a** 0.2 mm width; **b** 0.6 mm width; **c** 1 mm width

signals can be used as the basis for the quantification of the circumferential width of the small size axial defect.

Figure 3.46 shows signals of groove defects with an axial length of 10 mm, circumferential width of 2 mm, and different radial depths. The depths are 1, 5, and 9 mm. When the defect depth is only 1 mm, its amplitude and phase signals are very weak, and the shape of the signal is not like that of the deeper defect. It can be considered that the detection limit of the depth of an axial crack is 1 mm (10 % wall

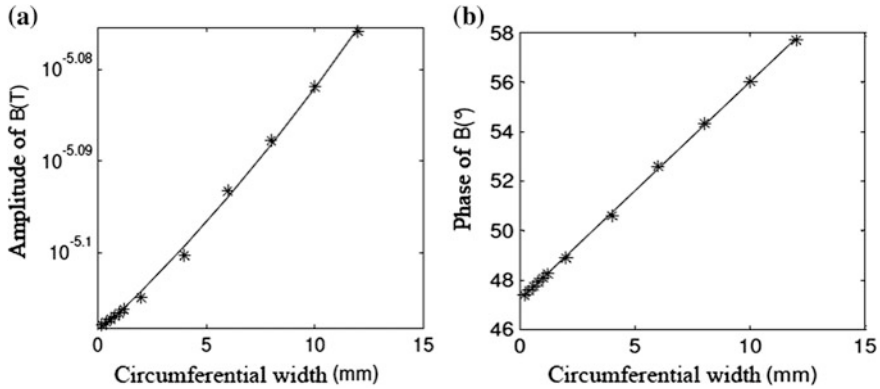


Fig. 3.45 The relationship between the signal peak value of axial defects and circumferential widths. **a** Amplitude; **b** phase

thickness). When the defect depth is 9 mm, two independent peaks appear in the amplitude signal, and there is a valley between the two peaks, with a peculiar shape. In Fig. 3.47 is the curve of variation of axial defect signal with axial direction. The whole process of the two peaks appearing gradually with the increasing defect depth is shown. With the increase of the depth of defect, the amplitude signal is gradually increased, and when the depth is more than half of the wall thickness (5 mm), the original single peak is divided to two peaks, and with the further increase of the depth of the defect, the peak values increase with the two peaks further splitting, and the valley between the two peaks is even lower. While the shapes of the phase signals of different depths are basically unchanged, and with the increase of the depth of the defect, the peak value increases quickly, and the signal width is also increased.

Figure 3.48 shows the curves of variations of peak values of the amplitude and phase signals with the depth of the axial defect. Fig. 3.48a shows the fitted exponential curve. The peak value of the amplitude signal is exponential with the depth of the defect. Fig. 3.48b shows the fitted quadratic power function curve, which indicates that the peak value of the phase signal changes quadratically with the defect depth and is linear with the square of the depth of the defect.

Figure 3.49 shows the signal of the groove defect with a circumferential width of 2 mm, radial depth of 4 mm, and different axial lengths. The lengths are 10, 20, and 30 mm. Similar to Fig. 3.48, the change of the amplitude signal is large. When the length of the defect is large enough, two peaks appear in the amplitude signal and between them is a valley. With the increase of the length of the defect, the peaks are gradually separated. While the shape of the phase signal is basically unchanged.

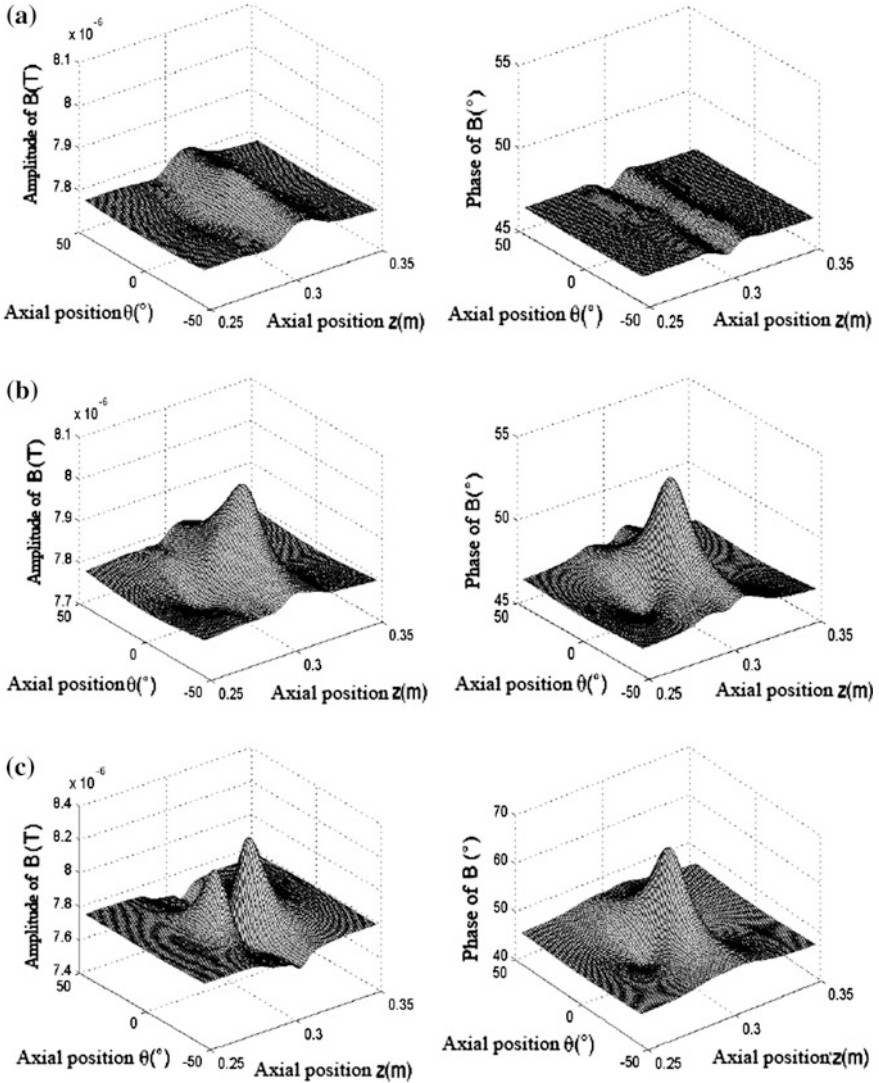


Fig. 3.46 Axial defect signals with different depths. **a** 1 mm depth; **b** 5 mm depth; and **c** 9 mm depth

Figure 3.50 shows the curve of variations of the peak values of the amplitude and phase signals of the axial defect with the length of the defect. Because the shape of the amplitude signal changes much, its peak value is not obviously related with the defect length. The peak value of the phase signal increases with the defect length, and this increase is slower and slower, approaching to one certain maximum. This result is consistent with that of the full circumferential defect.

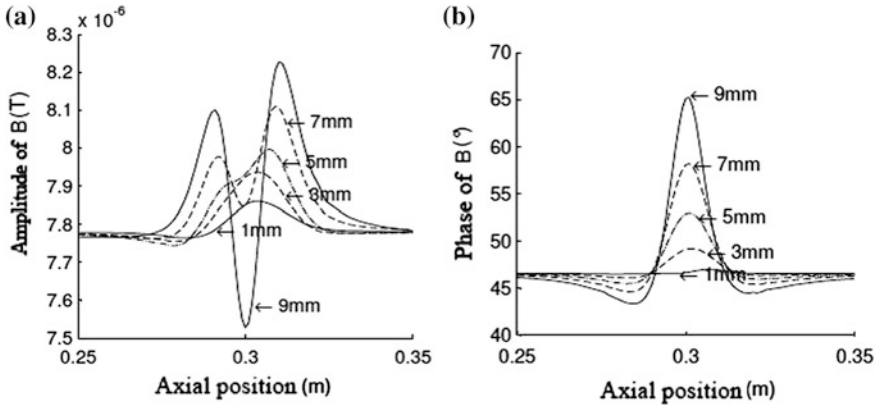


Fig. 3.47 Variations of defect signals of different depths with the axial position. **a** Amplitude; **b** phase

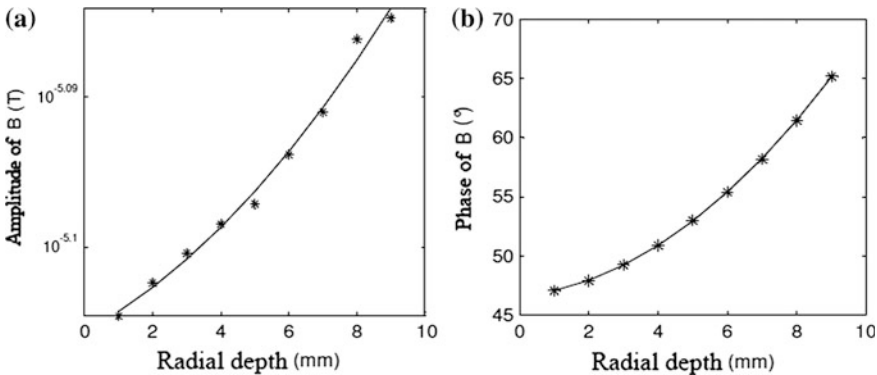


Fig. 3.48 Relationship between the signal peak value of axial defects and radial depth. **a** Amplitude; **b** phase

From the analysis of the relationship between the signal characteristics of the axial defect and the circumferential width, the radial depth, and the axial length, the phase signal of the defect is stable with the dimensions of the defect, and the peak value is proportional to the circumferential width of the small defect and proportional to the square of the radial depth, approaching a maximum with the increasing defect length. While the change of the amplitude signal is more complex, when the defect is deep or long, there will be two peaks, and there is a valley between the two peaks. Moreover, the RFEC has the ability to detect the axial crack.

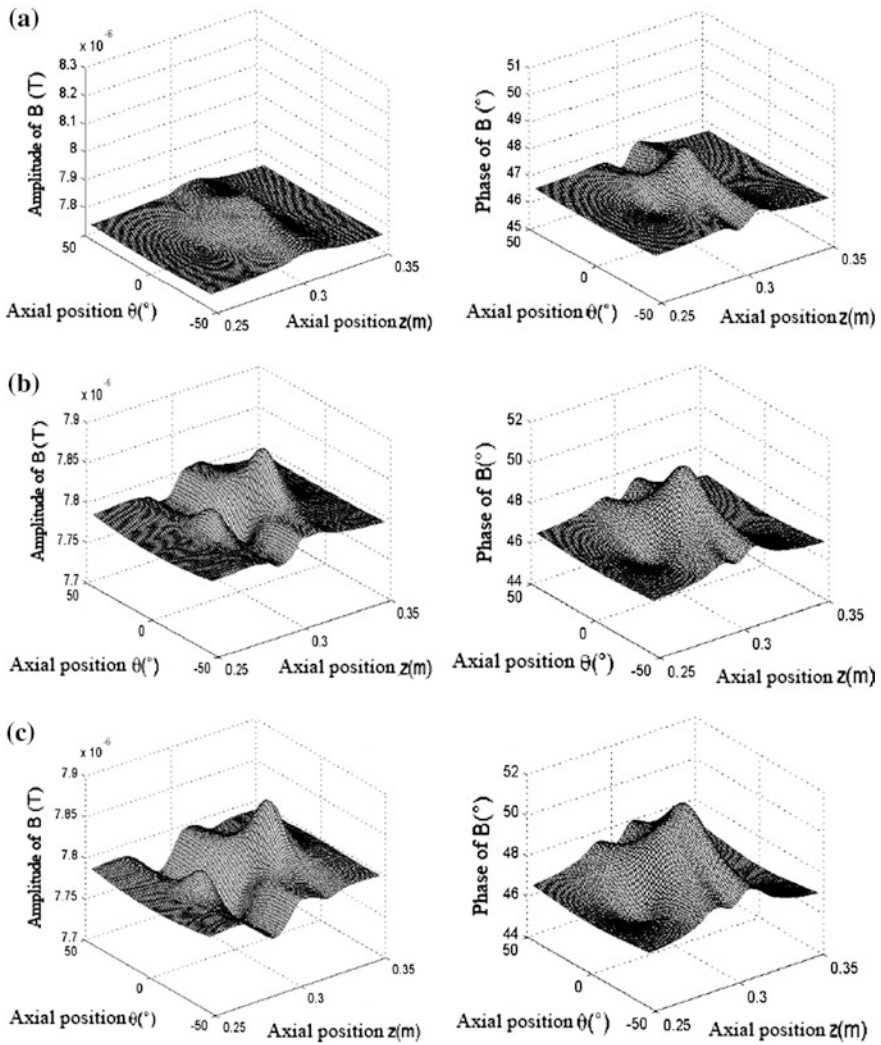


Fig. 3.49 Signals of axial defects with different lengths. **a** 10 mm length; **b** 20 mm length; and **c** 30 mm length

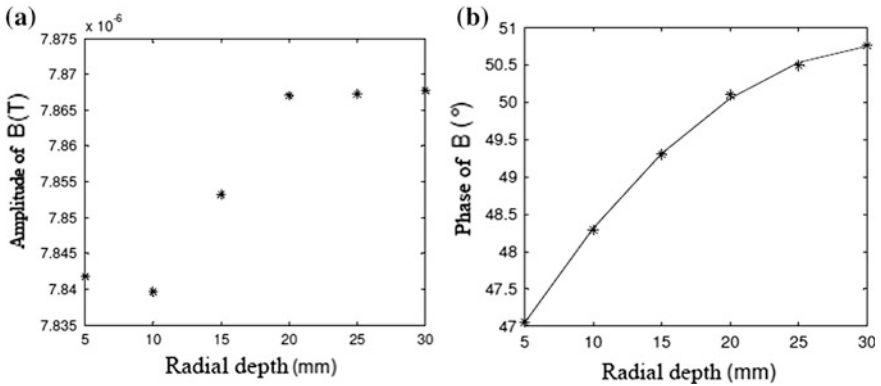


Fig. 3.50 Distributions of \dot{B} for the axial defects. **a** Amplitude; **b** phase

References

- Schmidt, T.R.: The casing inspection tool - an instrument for the in-situ detection of external casing corrosion in oil wells. *Corrosion* **7**, 81–85 (1961)
- Schmidt, T.R.: Remote field eddy current inspection technique. **42**(2), 225–230 (1984)
- Schmidt, T.R.: The remote field eddy current inspection technique. *Mater. Eval.* **2**, 225–230 (1984)
- Lord, W., et al.: Finite element study of the remote field eddy current phenomenon. *IEEE Trans. Magn.* **24**(1), 435–438 (1987)
- Hoshikawa, H., et al.: Characteristics of remote-field eddy current technique. *Mater Eval.* **47**(1), 93–97 (1989)
- Sun, Y.-S.: Finite-element study of diffusion energy flow in low-frequency eddy current fields. *Mater. Eval.* **47**(1), 87–92 (1989)
- Atherton, D.L., Sullivan, S.: Remote-field through-wall electromagnetic inspection technique for pressure tubes. *Mater. Eval.* **44**(13), 1544–1550 (1986)
- Teitsma, A.: Remote field eddy current inspection of unpiggable pipelines. Final report, GTI project 30801—02 (2004)
- Sun, Y.S., Roach, D., Zhu, H.: New advances in detecting cracks in raised-head fastener holes using rotational remote field eddy current technique. In: ASNT Fall Conference, Columbus, OH (2005)
- Atherton, D.L., Morton, K.L.: Inspection of prestressed concrete pressure pipe. *Rev. Prog. QNDE* **19**, 709–1715 (2000)
- Yusa, N., Demachi, K., Chen, Z.M.: An RFEC probe with a superconductor shield. *Rev. Prog. QNDE* **23**, 405–412 (2004)

Chapter 4

Low-Frequency Eddy Current Testing

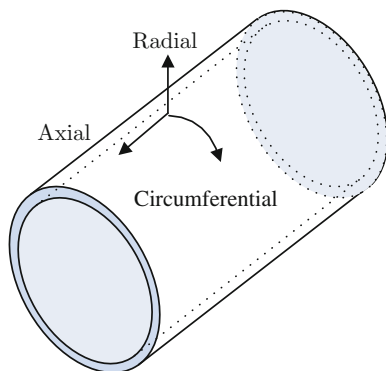
4.1 Introduction

Eddy current testing is a nondestructive testing method based on electromagnetic induction principle. The metal conductor is placed in an alternating magnetic field, and the eddy current will be induced. Hughes used the induced current method to detect the different metals and alloys, explained the feasibility of using the eddy current to detect defects of the conductive material in 1879. However, after that for a long period of time, the eddy current testing technology has developed slowly because there were not effective methods to suppress the interference factors. The first thickness testing instrument based on eddy current method was born in 1926. Forster proposed impedance analysis method in the 1950s which promoted eddy current testing technology quickly [1]. From the 1970s, there appeared many detection methods, such as multifrequency eddy current, far-field eddy current, and pulsed eddy current successively in the field of eddy current testing. They have improved the impedance analysis method from different aspects.

Most of the traditional eddy current testing is the eddy current nondestructive testing. The application of eddy current distance measurement is less. Recently, studies on the deformation of pipe by eddy current distance testing principle were developed. The pipeline deformation testing tool based on eddy current distance testing places a number of coil probes along the circumferential direction of the pipeline (Fig. 4.1). The deformation of the pipe can be analyzed by the measurement results of all the distance testing probes. Coil probe with its complex circuit unit is called eddy current displacement sensor.

At present, the main research direction of the eddy current displacement sensor is to increase the linear range and improve the accuracy of the measurement. The geometry of the eddy current displacement sensor coil was optimized by Darko Vyroubal and Draien Zele via lots of experiments. It was found that the measurement range of the small cross section of the uniform circular windings has far testing distance [2]. And then, Vyroubal [3] proposed a new eddy current

Fig. 4.1 Definition of axial, circumferential, and radial direction of pipe wall



displacement sensor model based on weak coupling transformer which simplified the calculation of sensor probe impedance. Tsutomu Mizuno proposed that the general copper wire of probe can be coated by a thin layer of iron film and a thin layer of nickel film, which can improve the quality factor, sensitivity, and linear range of the eddy current displacement sensor [4].

The research of common eddy current displacement sensor has been mature [5–11]. However, these results may be not applicable to the deformation detection of oil and gas pipelines. The diameters of oil and gas pipelines are generally from 500 to 1500 mm [12]. In the process of detecting the deformation of the pipeline, the inner inspector should be smoothly passed through the deformation region of the pipeline. So the safe distance between the eddy current displacement sensor and the pipe wall is at least 10 % of the diameter of the pipe. However, the measuring distance of existing eddy current displacement sensor is generally less than 10 mm. So the eddy current distance testing is rarely applied to the detection of oil and gas pipeline deformation.

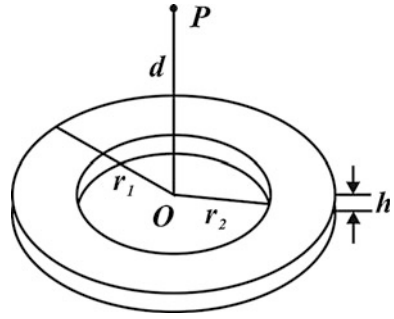
According to the different excitation frequencies, the eddy current testing method can be classified into high-frequency eddy current testing and low-frequency eddy current detection method. The high-frequency eddy current testing has higher resolution. However, it can only detect near-surface defects because of the skin effect. The electromagnetic field amplitude of high-frequency eddy current testing will attenuate, and the transmission distance is short. The transmission distance of low-frequency eddy current is longer. So the frequency of non-contact detection of oil and gas pipeline deformation will be about 100 Hz [13].

4.2 Finite Element Simulation of Eddy Current Coils

4.2.1 The Finite Element Modal of Coils

The electromagnetic analysis software Maxwell by ANSOFT company is used to simulate the eddy current coils. Figure 4.2 shows the three-dimensional simulation

Fig. 4.2 The schematic diagram of the probe coil



model. The coil material is copper, and the other areas are set as air. The excitation current is applied in the cross section of the model. The current frequency is 100 Hz, and the percentage error is set as 0.1. The magnetic flux along the coil central line OP is simulated, and thus, the testing resolution at each position can be obtained [14].

The thickness of the coil is h . The external diameter is r_1 . The inner diameter is r_2 . The distance from point O to point P is d . If the tested pipe is placed on point P, the greater the amplitude and its gradient of magnetic field excited by the coil, the higher the testing resolution.

To calculate the resistance of the coil, we consider the equivalent radius r of the coil is $(r_1 + r_2)/2$, the cross section of the coil wire is S , the electrical resistivity is ρ , the number N of coil turns is $(r_1 - r_2)h/S$, the length L of the wire is $2\pi rN$, so the coil resistance is:

$$R = \frac{\rho L}{S} = \frac{2\pi\rho r h(r_1 - r_2)}{S^2} \tag{4.1}$$

The factors affecting the coil resistance are the equivalent radius r , and the thickness and the difference between internal and external diameter of the coil because the cross section and the electrical resistivity of the coil wire remain constant in these simulations. Let the number A of excitation ampere-turns on the coil is NI , so the voltage, current, and active power on the coil are obtained in formulas (4.2), (4.3), and (4.4).

$$U_R = RI = \frac{2\pi\rho r h(r_1 - r_2)}{S^2} \cdot \frac{A}{N} = \frac{2\pi\rho r}{S} A \tag{4.2}$$

$$I = \frac{A}{N} = \frac{S}{h(r_1 - r_2)} A \tag{4.3}$$

$$P = U_R I = \frac{2\pi\rho r}{h(r_1 - r_2)} A^2 \tag{4.4}$$

Simulations can be conducted under the condition which excitation voltage, excitation current and excitation power remain constant, respectively. To keep excitation voltage as a constant, rA should be constant. To keep excitation current as a constant, $A/(h(r_1 - r_2))$ should be constant. To keep excitation power as a constant, $rA^2/(h(r_1 - r_2))$ should be constant. The above three simulation conditions were used to simulate and research the influence of difference between coil inner and outer diameter, thickness, and equivalent radius on detecting resolution.

4.2.2 Result of Probe Coil Finite Element Simulation

4.2.2.1 The Influence of Difference Between Inner and Outer Diameter on Detecting Resolution

Magnetic induction intensity on the central line OP of coil with the change of distance d was simulated under the condition which excitation voltage, equivalent radius, and thickness of probe coil remain constants. In the simulation, equivalent radius r is 100 mm, thickness h is 10 mm, and rA is kept 0.05 A m as a constant. When $r_1 - r_2$ is 180, 100, and 20 mm, respectively, simulation results are shown in Fig. 4.3.

In Fig. 4.3, horizontal axis is the distance d between specimen and probe. Vertical axis is the magnetic induction intensity detected. From Fig. 4.3, we can see when the difference between coil inner and outer diameter increases, the magnetic induction intensity generated by the coil probe is increased near the probe, and the magnetic induction intensity is decreased far away from the probe. Since the curve is nonlinear, it is divided into two sections to analyze the variation of the magnetic

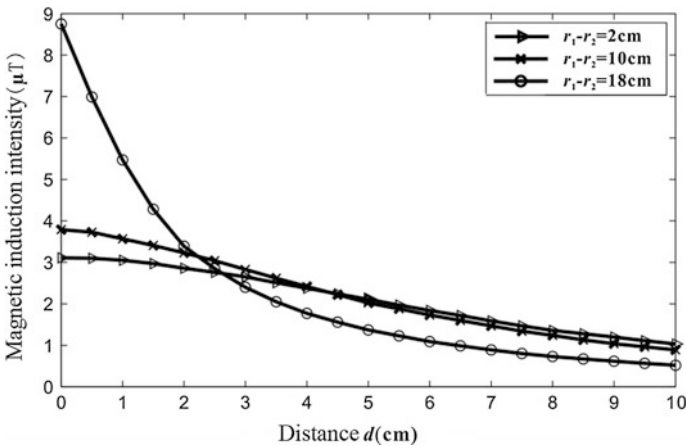


Fig. 4.3 The influence of difference between outer and inner coil diameter on magnetic induction intensity (voltage as a constant)

Table 4.1 Magnetic induction intensity change rate with difference between inner and outer diameter (voltage as a constant)

The difference between inner and outer diameter $r_1 - r_2$ (cm)	Average magnetic induction intensity change rate at distance d 0–5 cm ($\mu\text{T}/\text{cm}$)	Average magnetic induction intensity change rate at distance d 5–10 cm ($\mu\text{T}/\text{cm}$)
18	1.476	0.170
10	0.354	0.226
2	0.2	0.216

induction intensity, as shown in Table 4.1. We can know that the magnetic induction intensity in the near distance can be improved by increasing the difference between inner and outer diameter, but the change rate of the magnetic induction intensity in the far distance varies little. To sum up, in the case that the excitation voltage, the equivalent radius, and the thickness of the coil are constant, the magnetic induction intensity and its change rate in the near distance increase when the difference between inner and outer diameter of the coil increases, whereas the magnetic induction intensity in the far distance is less and its change rate varies little. That is to increase difference between the inner and outer diameter is beneficial to improve the resolution of the coil probe in the near distance, reduce the difference between the inner and the outer diameter is beneficial to improve the resolution of the coil probe in the far distance.

Magnetic induction intensity on the central line OP of coil with the change of difference between inner and outer diameter was simulated under the condition which excitation current, equivalent radius, and thickness of probe coil remain constants. In the simulation, equivalent radius r is 100 mm, thickness h is 10 mm, and $A/(h(r_1 - r_2))$ is kept 2500 A/m² as a constant. When $r_1 - r_2$ is 180, 100, and 20 mm, respectively, simulation results are shown in Fig. 4.4.

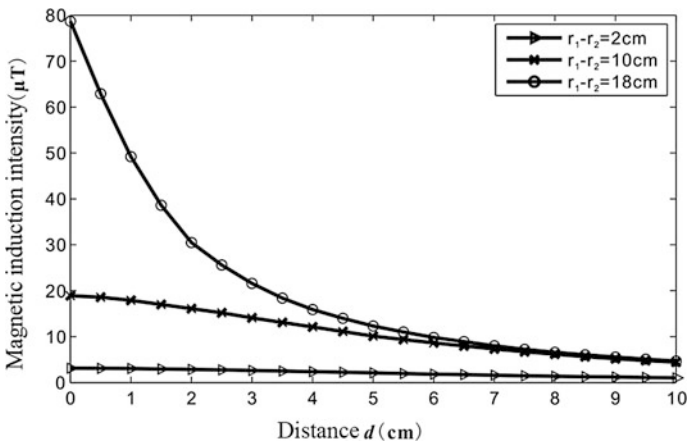


Fig. 4.4 The influence of difference between the outer and inner coil diameter on magnetic induction intensity (current as a constant)

By Fig. 4.4, when the difference between the inner and outer diameter of the coil increases, the magnetic induction intensity of the coil probe increases at any distance. From Table 4.2 we can see that increasing the difference between inner and outer diameter is beneficial to the increase in the magnetic induction intensity change rate at any distance. To sum up, in the condition that coil excitation current, equivalent radius, and thickness of the coil remain constants, when the difference between inner and outer diameters is increased, magnetic induction intensity and its change rate of the coil increase at any distance. That is to increase the difference between the inner and the outer diameters of the coil is conducive to improve the resolution of the coil probe in any distance.

Magnetic induction intensity on the central line OP of coil with the change of distance d was simulated under the condition which excitation power, equivalent radius, and thickness of probe coil remain constants. In the simulation, equivalent radius r is 100 mm, thickness h is 10 mm, and $rA^2/(h(r_1 - r_2))$ is kept $125 \text{ A}^2/\text{m}$ as a constant. When $r_1 - r_2$ is 180, 100, and 20 mm, respectively, simulation results are shown in Fig. 4.5.

Table 4.2 Magnetic induction intensity change rate with difference between inner and outer diameter (voltage as a constant)

The difference between inner and outer diameter $r_1 - r_2$ (cm)	Average magnetic induction intensity change rate at distance d 0–5 cm ($\mu\text{T}/\text{cm}$)	Average magnetic induction intensity change rate at distance d 5–10 cm ($\mu\text{T}/\text{cm}$)
18	13.28	1.526
10	1.76	1.128
2	0.2	0.216

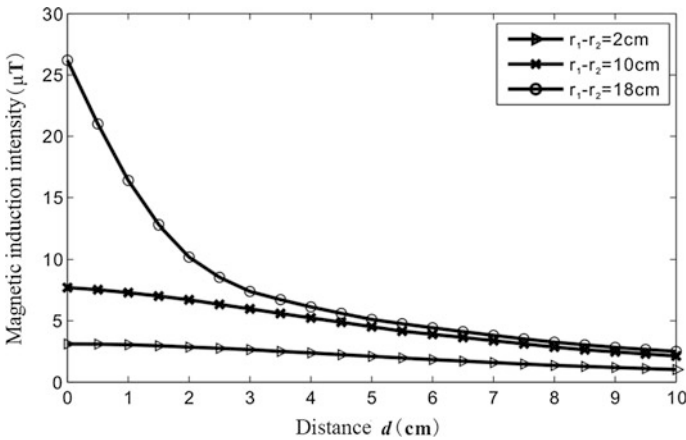


Fig. 4.5 The influence of difference between the outer and inner coil diameter on magnetic induction intensity (power as a constant)

Table 4.3 Magnetic induction intensity change rate with difference between inner and outer diameter (voltage as a constant)

The difference between inner and outer diameter $r_1 - r_2$ (cm)	Average magnetic induction intensity change rate at distance d 0–5 cm ($\mu\text{T}/\text{cm}$)	Average magnetic induction intensity change rate at distance d 5–10 cm ($\mu\text{T}/\text{cm}$)
18	1.84	0.522
10	0.638	0.478
2	0.2	0.216

By Fig. 4.5, when the difference between the inner and outer diameter of the coil increases, the magnetic induction intensity of the coil probe increases at any distance. From Table 4.3 we can see that increasing the difference between inner and outer diameter is beneficial to the increase in the magnetic induction intensity change rate at any distance. To sum up, in the condition that coil excitation power, equivalent radius, and thickness of the coil remain constants, when the difference between inner and outer diameters is increased, magnetic induction intensity and its change rate of the coil increase at any distance. That is to increase the difference between the inner and the outer diameters of the coil is conducive to improve the resolution of the coil probe in any distance.

4.2.2.2 The Influence of Thickness of Probe Coil on Detecting Resolution

Magnetic induction intensity on the central line OP of coil with the change of distance d was simulated under the condition which excitation voltage, equivalent radius, and difference between the inner and outer radius of probe coil remain constants. In the simulation, outer radius r_1 is 110 mm, inner radius r_2 is 90 mm, equivalent radius $r = 100$ mm, rA is kept 0.05 A m as a constant, and the thickness of the coil is varied. When the thickness h is 90, 50, and 10 mm, respectively, simulation results are shown in Fig. 4.6.

By Fig. 4.6, when the thickness of the coil increases, the magnetic induction intensity of the coil probe decreases at any distance. From Table 4.4, when the coil thickness is increased, the change rate of the magnetic induction intensity is not changed obviously in the near distance, and the change rate of the magnetic induction intensity is decreased in the far distance. So in the condition that coil excitation voltage, equivalent radius, and the difference between the inner radius and the outer radius of the coil remain constants, when the coil thickness is increased, the magnetic induction intensity of the coil decreases at any distance and its change rate also decreases in the far distance. That is to decrease the thickness of the coil is conducive to improve the resolution of the coil probe, especially in the far distance.

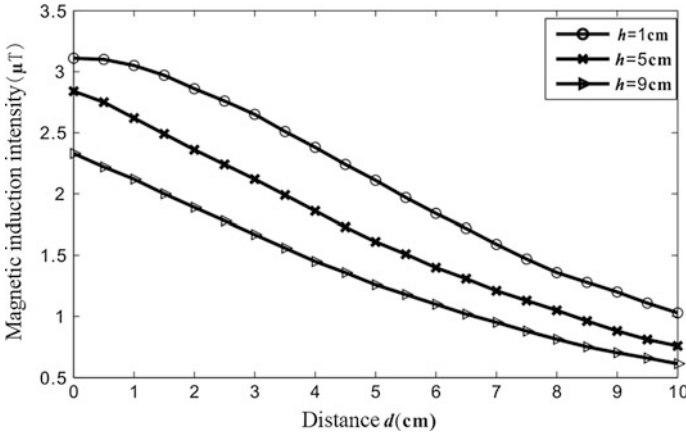


Fig. 4.6 The influence of coil thickness on magnetic induction intensity (voltage as a constant)

Table 4.4 Magnetic induction intensity change rate in different thickness of the coil (voltage as a constant)

Thickness h (cm)	Average magnetic induction intensity change rate at distance d 0–5 cm ($\mu T/cm$)	Average magnetic induction intensity change rate at distance d 5–10 cm ($\mu T/cm$)
9	0.214	0.129
5	0.246	0.170
1	0.2	0.216

Magnetic induction intensity on the central line OP of coil with the change of distance d was simulated under the condition which excitation current, equivalent radius, and difference between the inner and outer radius of probe coil remain constants. In the simulation, outer radius r_1 is 110 mm, inner radius r_2 is 90 mm, equivalent radius $r = 100$ mm, $A/(h(r_1 - r_2))$ is kept $2500 A/m^2$ as a constant, and the thickness of the coil is varied. When thickness h is 90, 50, and 10 mm, respectively, simulation results are shown in Fig. 4.7.

By Fig. 4.7, when the thickness of the coil increases, the magnetic induction intensity of the coil probe increases at any distance. From Table 4.5, we can see that increasing the coil thickness is beneficial for improving the change rate of magnetic induction intensity. So in the condition that coil excitation current, equivalent radius, and difference between the inner radius and the outer radius of the coil remain constants, when the coil thickness is increased, the magnetic induction intensity of the coil and its change rate increase at any distance. That is to increase the thickness of the coil is conducive to improve the resolution of the coil probe.

Magnetic induction intensity on the central line OP of coil with the change of distance d was simulated under the condition which excitation power, equivalent

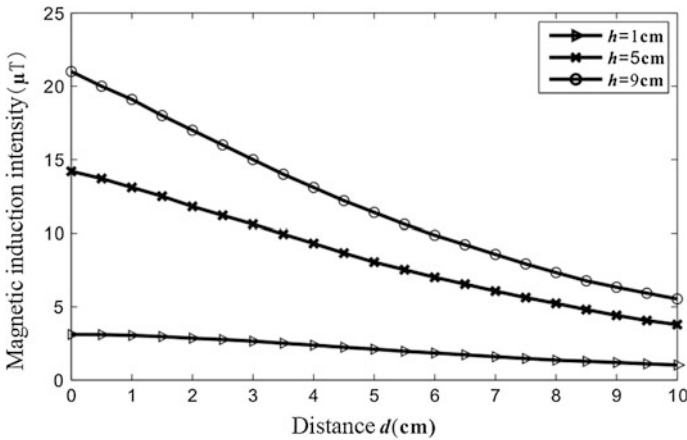


Fig. 4.7 The influence of coil thickness on magnetic induction intensity (current as a constant)

Table 4.5 Magnetic induction intensity change rate in different thickness of the coil (current as a constant)

Thickness h (cm)	Average magnetic induction intensity change rate at distance d 0–5 cm ($\mu T/cm$)	Average magnetic induction intensity change rate at distance d 5–10 cm ($\mu T/cm$)
9	1.92	1.174
5	1.232	0.85
1	0.2	0.216

radius, and difference between the inner and outer radius of probe coil remain constants. In the simulation, outer radius r_1 is 110 mm, inner radius r_2 is 90 mm, equivalent radius $r = 100$ mm, $rA^2/(h(r_1 - r_2))$ is kept = $125 A^2/m$ as a constant, and the thickness of the coil is varied. When thickness h is 90, 50 and 10 mm, respectively, simulation results are shown in Fig. 4.8.

By Fig. 4.8, when the thickness of the coil increases, the magnetic induction intensity of the coil probe increases at any distance. From Table 4.6, we can see that increasing the coil thickness is beneficial for improving the change rate of magnetic induction intensity. So in the condition that coil excitation current, equivalent radius, and difference between the inner radius and the outer radius of the coil remain constants, when the coil thickness is increased, the magnetic induction intensity of the coil and its change rate increase at any distance. That is to increase the thickness of the coil is conducive to improve the resolution of the coil probe. However, the curves of $h = 90$ mm and $h = 50$ mm are similar. That means when the thickness of the coil increases to a certain extent, its influence is not effective any more.

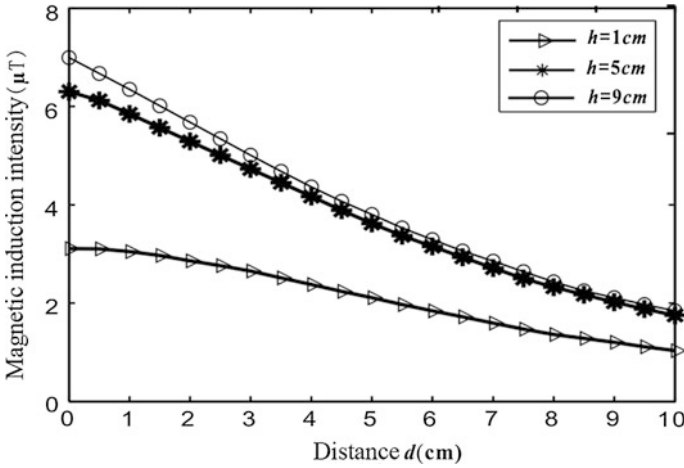


Fig. 4.8 The influence of coil thickness on magnetic induction intensity (power as a constant)

Table 4.6 Magnetic induction intensity change rate in different thickness of the coil (power as a constant)

Thickness h (cm)	Average magnetic induction intensity change rate at distance d 0–5 cm ($\mu\text{T}/\text{cm}$)	Average magnetic induction intensity change rate at distance d 5–10 cm ($\mu\text{T}/\text{cm}$)
9	0.638	0.392
5	0.536	0.374
1	0.2	0.216

4.2.2.3 The Influence of Equivalent Radius of Probe Coil on Detecting Resolution

Magnetic induction intensity on the central line OP of coil with the change of distance d was simulated under the condition which excitation voltage, thickness, and difference between the inner and outer radius of probe coil remain constants. In the simulation, $r_1 - r_2$ is 20 mm, $h = 10$ mm, d is 100 mm, and rA is kept 0.05 A m as a constant. The change of the magnetic induction intensity and its change rate with the increase of the equivalent radius of the coil are shown in Figs. 4.9 and 4.10, respectively.

Figure 4.9 shows the fitting curve of the magnetic induction intensity varies with the equivalent radius at distance d as 100 mm. We can see when the equivalent radius is 70 mm, the magnetic induction intensity achieves its maximum. Figure 4.10 shows the fitting curve of the change rate of magnetic induction intensity varies with the equivalent radius at distance d as 100 mm. We can see when the equivalent radius is 50 mm, the change rate of magnetic induction intensity achieves its maximum. After many simulations, the following conclusions

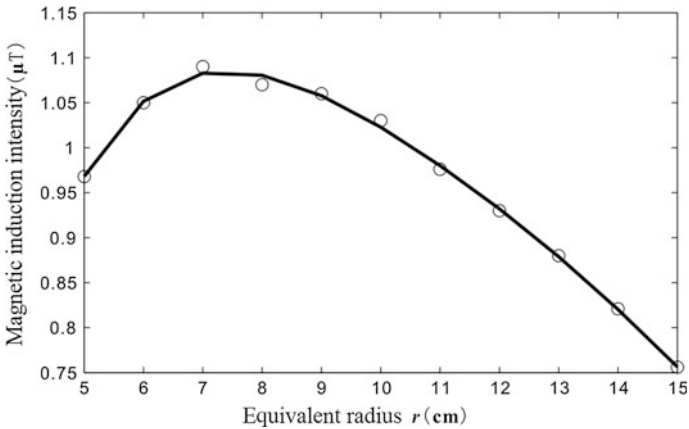


Fig. 4.9 Fitting curve of the magnetic induction intensity with the change of the equivalent radius of the coil (voltage as a constant)

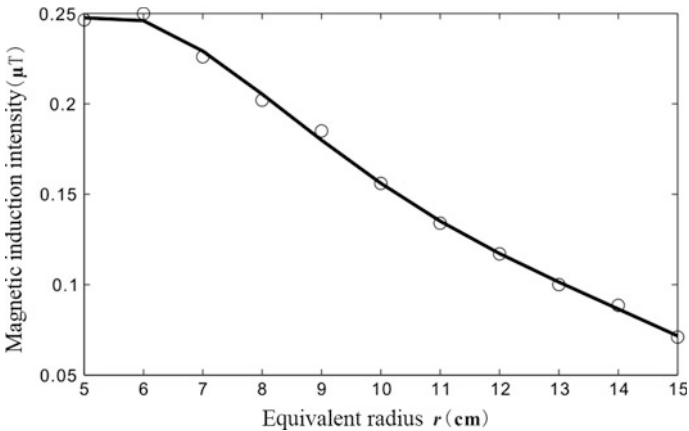


Fig. 4.10 Fitting curve of the change rate of magnetic induction intensity with the change of the equivalent radius of the coil (voltage as a constant)

can be drawn: When r is $0.7d$, the magnetic induction intensity achieves its maximum; when r is $0.5d$, the change rate of magnetic induction intensity achieves its maximum. So in order to make the coil resolution highest in the d distance under the condition that the excitation voltage, the difference between the inner radius and outer radius, and the thickness of the coil remain constants, the equivalent radius of the coil should be $0.5d - 0.7d$.

Magnetic induction intensity on the central line OP of coil with the change of distance d was simulated under the condition which excitation current, thickness, and the difference between the inner and outer radius of probe coil remain constants. In the simulation, $r_1 - r_2$ is 20 mm, $h = 10$ mm, d is 100 mm, and

$A/(h(r_1 - r_2))$ is kept 2500 A/m^2 as a constant. The change of the magnetic induction intensity and its change rate with the increase of the equivalent radius of the coil are shown in Figs. 4.11 and 4.12, respectively.

Figure 4.11 shows the fitting curve of the magnetic induction intensity varies with the equivalent radius at distance d as 100 mm. We can see when the equivalent radius is about 140 mm, the magnetic induction intensity achieves its maximum. Figure 4.12 shows the fitting curve of the change rate of magnetic induction intensity varies with the equivalent radius at distance d as 100 mm. We can see when the equivalent radius is about 80 mm, the change rate of magnetic induction

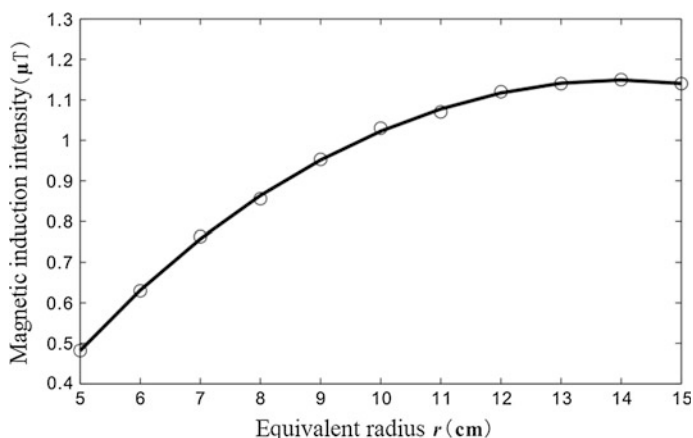


Fig. 4.11 Fitting curve of the magnetic induction intensity with the change of the equivalent radius of the coil (current as a constant)

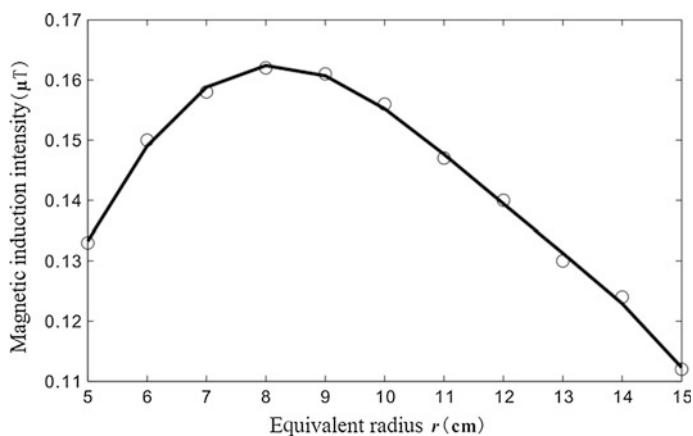


Fig. 4.12 Fitting curve of the change rate of magnetic induction intensity with the change of the equivalent radius of the coil (current as a constant)

intensity achieves its maximum. After many simulations, the following conclusions can be drawn: When r is $1.4d$, the magnetic induction intensity achieves its maximum; when r is $0.8d$, the change rate of magnetic induction intensity achieves its maximum. So in order to make the coil resolution highest in the d distance under the condition that the excitation current, the difference between the inner radius and outer radius, the thickness of the coil remain constants, the equivalent radius of the coil should be $0.8d - 1.4d$.

Magnetic induction intensity on the central line OP of coil with the change of distance d was simulated under the condition which excitation power, thickness, the difference between the inner and outer radius of probe coil remain constants. In the simulation, $r_1 - r_2$ is 20 mm, $h = 10$ mm, d is 100 mm, and $rA^2/(h(r_1 - r_2))$ is kept $125 \text{ A}^2/\text{m}$ as a constant. The change of the magnetic induction intensity and its change rate with the increase of the equivalent radius of the coil are shown in Figs. 4.13 and 4.14, respectively.

Figure 4.13 shows the fitting curve of the magnetic induction intensity varies with the equivalent radius at distance d as 100 mm. We can see when the equivalent radius is about 100 mm, the magnetic induction intensity achieves its maximum. Figure 4.14 shows the fitting curve of the change rate of magnetic induction intensity varies with the equivalent radius at distance d as 100 mm. We can see when the equivalent radius is about 70 mm, the change rate of magnetic induction intensity achieves its maximum. After many simulations, the following conclusions can be drawn: When r is equal to d , the magnetic induction intensity achieves its maximum; when r is $0.7d$, the change rate of magnetic induction intensity achieves its maximum. So in order to make the coil resolution highest in the d distance under the condition that the excitation power, the difference between the inner radius and the outer radius, the thickness of the coil remain constants, and the equivalent radius of the coil should be $0.7d - 1d$.

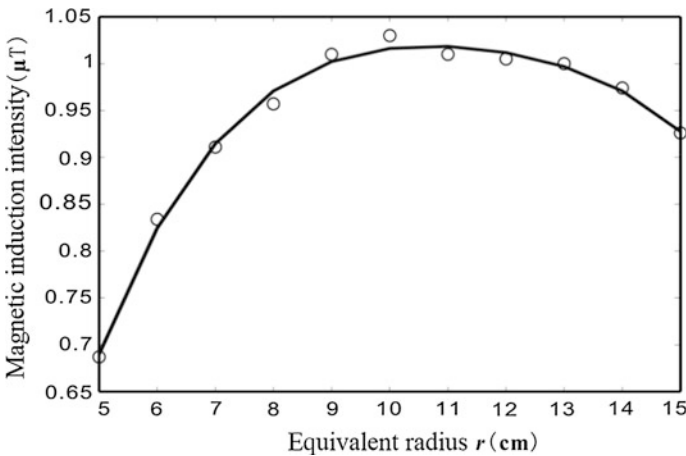


Fig. 4.13 Fitting curve of the magnetic induction intensity with the change of the equivalent radius of the coil (power as a constant)

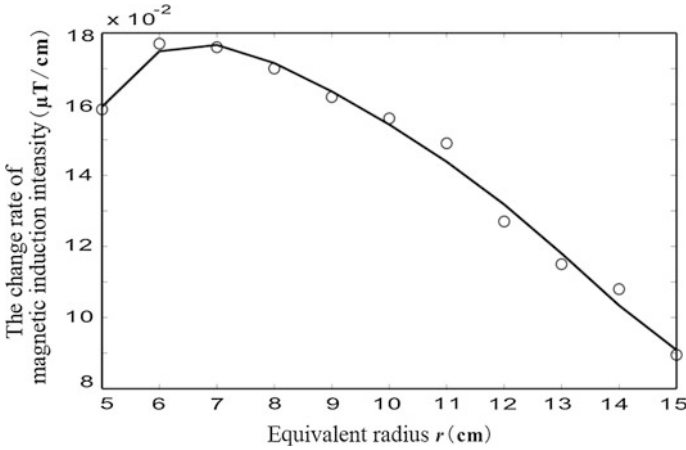


Fig. 4.14 Fitting curve of the change rate of magnetic induction intensity with the change of the equivalent radius of the coil (power as a constant)

4.2.3 Theoretical Analysis of Probe Coil Model

In this section, we will analyze the influence of the difference between the inner radius and the outer radius, thickness and equivalent radius of the coil on the magnetic induction intensity, and its change rate of the coil probe, which is based on the theory of electromagnetic field.

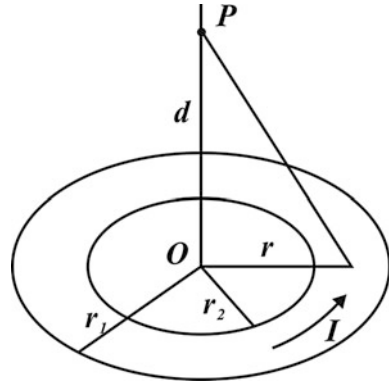
4.2.3.1 The Influence of Difference Between the Inner Radius and the Outer Radius of Probe Coil on Magnetic Field Yielded by the Probe

The influence of the difference between the inner radius and the outer radius on the magnetic field of the coil probe is analyzed, and the theoretical model shown in Fig. 4.15 can be established.

In Fig. 4.15, the thickness of the coil is ignored. We can assume the coil as a planar coil. The outer radius is r_1 . The inner radius is r_2 . The equivalent radius is r . The coil is applied with the excitation current I and the magnetic induction intensity and its change rate with distance d from the point P to the center O of the coil are analyzed.

The excitation voltage of the coil is kept constant. That means rA is constant. Because the equivalent radius r is unchanged, and the excitation ampere-turns is excitation current I in Fig. 4.15, I remains unchanged. Current density J is $I/(r_1 - r_2)$. By electromagnetic theory, the magnetic induction intensity on point P can be obtained by integrating.

Fig. 4.15 The theoretical model for the influence of the difference between the inner radius and the outer radius on the magnetic field of the coil probe



$$B = \frac{\mu_0 I}{2(r_1 - r_2)} \left[\ln \left(\frac{r_1 + \sqrt{r_1^2 + d^2}}{r_2 + \sqrt{r_2^2 + d^2}} \right) + \frac{r_2}{\sqrt{r_2^2 + d^2}} - \frac{r_1}{\sqrt{r_1^2 + d^2}} \right] \quad (4.5)$$

Keep the equivalent radius r , excitation current I , and distance d as constants. Making $r_1 = r + x$ and $r_2 = r - x$, formula (4.6) can be obtained.

$$B = \frac{\mu_0 I}{4x} \left[\ln \left(\frac{r + x + \sqrt{(r + x)^2 + d^2}}{r - x + \sqrt{(r - x)^2 + d^2}} \right) + \frac{r - x}{\sqrt{(r - x)^2 + d^2}} - \frac{r + x}{\sqrt{(r + x)^2 + d^2}} \right] \quad (4.6)$$

Formula (4.6) is the relationship between the magnetic induction intensity B and the difference x of the inner radius and the outer radius under the condition of constant excitation voltage on the probe.

Assume the equivalent radius r as 0.1 m and the excitation current I as 0.5 A. When x is 0.01, 0.05, and 0.09 m, respectively, the curve of magnetic induction intensity B versus the distance d is shown in Fig. 4.16.

The simulation results shown in Fig. 4.16 are in agreement with the theoretical analysis in Fig. 4.3.

The excitation current of the probe coil is kept constant. That means $I/(h(r_1 - r_2))$ is constant. Because the thickness h is unchanged, and the excitation ampere-turns is excitation current I in Fig. 4.15, I remains unchanged. Current density J is $I/(r_1 - r_2)$. By electromagnetic theory, the magnetic induction intensity on point P can be obtained by integrating.

$$B = \frac{\mu_0 J}{2} \left[\ln \left(\frac{r_1 + \sqrt{r_1^2 + d^2}}{r_2 + \sqrt{r_2^2 + d^2}} \right) + \frac{r_2}{\sqrt{r_2^2 + d^2}} - \frac{r_1}{\sqrt{r_1^2 + d^2}} \right] \quad (4.7)$$

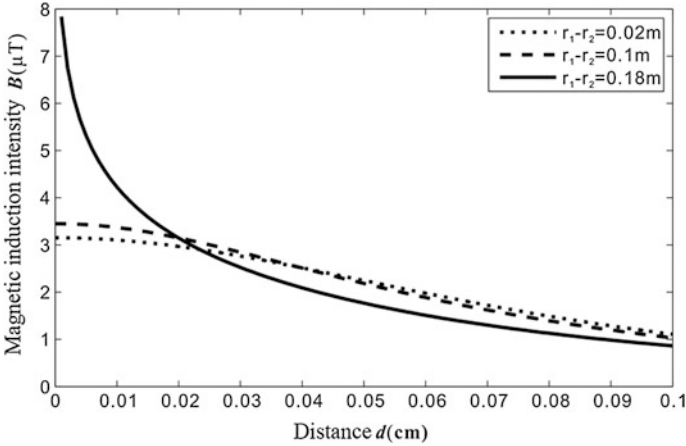


Fig. 4.16 The theoretical curve for the influence of the difference between the inner radius and the outer radius on the magnetic induction intensity (voltage as a constant)

Keep the equivalent radius r , current density J , and distance d as constants. Making $r_1 = r + x$ and $r_2 = r - x$, formula (4.8) can be obtained.

$$B = \frac{\mu_0 J}{2} \left[\ln \left(\frac{r+x+\sqrt{(r+x)^2+d^2}}{r-x+\sqrt{(r-x)^2+d^2}} \right) + \frac{r-x}{\sqrt{(r-x)^2+d^2}} - \frac{r+x}{\sqrt{(r+x)^2+d^2}} \right] \quad (4.8)$$

Formula (4.8) is the relationship between the magnetic induction intensity B and the difference x of the inner radius and the outer radius under the condition of constant excitation current on the probe.

Assume the equivalent radius r as 0.1 m and the excitation current density J as 25 A/m. When x is 0.01, 0.05, and 0.09 m, respectively, the curve of magnetic induction intensity B versus the distance d is shown in Fig. 4.17.

The simulation results shown in Fig. 4.17 are in agreement with the theoretical analysis in Fig. 4.4.

The excitation power of the probe coil is kept constant. That means $rA^2/(h(r_1 - r_2))$ is constant. Because the equivalent radius r and the thickness h of the coil are unchanged, and the excitation ampere-turns is excitation current I in Fig. 4.15, $I^2/(r_1 - r_2)$ remains unchanged. Assuming M as $I^2/(r_1 - r_2)$, current density is:

$$J = \sqrt{\frac{M}{r_1 - r_2}} \quad (4.9)$$

By electromagnetic theory, the magnetic induction intensity on the point P can be obtained by integrating.

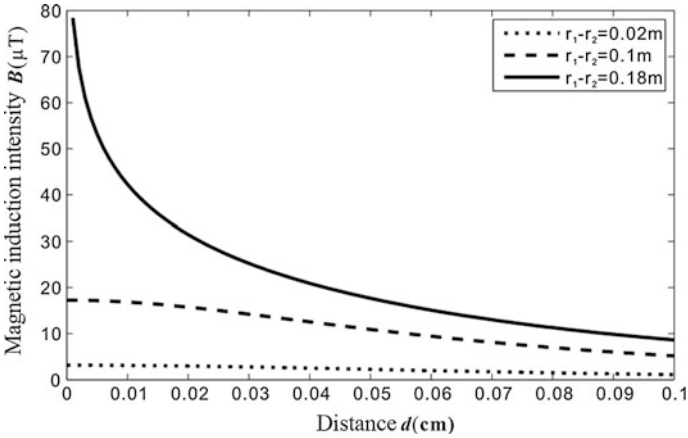


Fig. 4.17 The theoretical curve for the influence of the difference between the inner radius and the outer radius on the magnetic induction intensity (current as a constant)

$$B = \frac{\mu_0 \sqrt{M}}{2\sqrt{r_1 - r_2}} \left[\ln \left(\frac{r_1 + \sqrt{r_1^2 + d^2}}{r_2 + \sqrt{r_2^2 + d^2}} \right) + \frac{r_2}{\sqrt{r_2^2 + d^2}} - \frac{r_1}{\sqrt{r_1^2 + d^2}} \right] \quad (4.10)$$

Keep the equivalent radius r , distance d , and M as constants. Making $r_1 = r + x$ and $r_2 = r - x$, formula (4.11) can be obtained.

$$B = \frac{\mu_0 \sqrt{M}}{2\sqrt{2x}} \left[\ln \left(\frac{r + x + \sqrt{(r + x)^2 + d^2}}{r - x + \sqrt{(r - x)^2 + d^2}} \right) + \frac{r - x}{\sqrt{(r - x)^2 + d^2}} - \frac{r + x}{\sqrt{(r + x)^2 + d^2}} \right] \quad (4.11)$$

Formula (4.11) is the relationship between the magnetic induction intensity B and the difference x of the inner radius and the outer radius under the condition of constant excitation power on the probe.

Assume the equivalent radius r as 0.1 m and M as 12.5 A²/m. When x is 0.01, 0.05, and 0.09 m, respectively, the curve of magnetic induction intensity B versus the distance d is shown in Fig. 4.18.

The simulation results shown in Fig. 4.18 are in agreement with the theoretical analysis in Fig. 4.5.

4.2.3.2 The Influence of the Thickness of Probe Coil on Magnetic Field Yielded by the Probe

The influence of the thickness of the coil on the magnetic field of the coil probe is analyzed, and the theoretical model shown in Fig. 4.19 can be established.

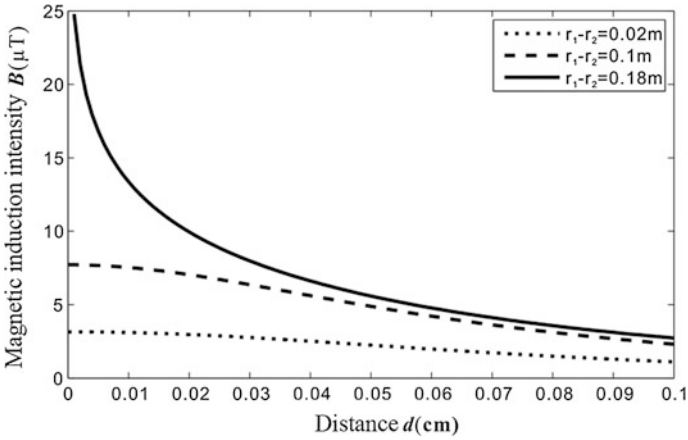
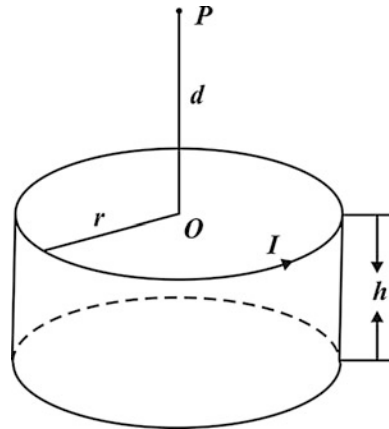


Fig. 4.18 The theoretical curve for the influence of the difference between the inner radius and the outer radius on the magnetic induction intensity (power as a constant)

Fig. 4.19 The theoretical model for the influence of the thickness of the coil on the magnetic field of the coil probe



In Fig. 4.19, the difference between the inner radius and the outer radius of the coil is ignored. We can assume the coil as a cylinder. The thickness of the coil is h . The equivalent radius is r . The coil is applied with the excitation current I and the magnetic induction intensity and its change rate with distance d from the point P to the center O of the coil are analyzed.

The excitation voltage of the coil is kept constant. That means rA is constant. Because the equivalent radius r is unchanged, and the excitation ampere-turns is excitation current I shown in Fig. 4.19, I remains unchanged. Current density J is I/h . By electromagnetic theory, the magnetic induction intensity on point P can be obtained by integrating.

$$B = \frac{\mu_0 I}{2h} \left(\frac{d+h}{\sqrt{r^2+(d+h)^2}} - \frac{d}{\sqrt{r^2+d^2}} \right) \tag{4.12}$$

Formula (4.12) is the relationship between the magnetic induction intensity B and the thickness h of the coil under the condition of constant excitation voltage on the probe.

Assume the equivalent radius r as 0.1 m and the excitation current I as 0.5 A. When h is 0.01, 0.05, and 0.09 m, respectively, the curve of magnetic induction intensity B versus the distance d is shown in Fig. 4.20.

The simulation results shown in Fig. 4.20 are in agreement with the theoretical analysis in Fig. 4.6.

The excitation current of the coil is kept constant. That means $A/(h(r_1 - r_2))$ is constant. Because the difference between the inner radius and the outer radius is unchanged, and the excitation ampere-turns is excitation current I in Fig. 4.19, current density J is I/h and it remains unchanged. By electromagnetic theory, the magnetic induction intensity on point P can be obtained by integrating.

$$B = \frac{\mu_0 J}{2} \left(\frac{d+h}{\sqrt{r^2+(d+h)^2}} - \frac{d}{\sqrt{r^2+d^2}} \right) \tag{4.13}$$

Formula (4.13) is the relationship between the magnetic induction intensity B and the thickness h of the coil under the condition of constant excitation current on the probe.

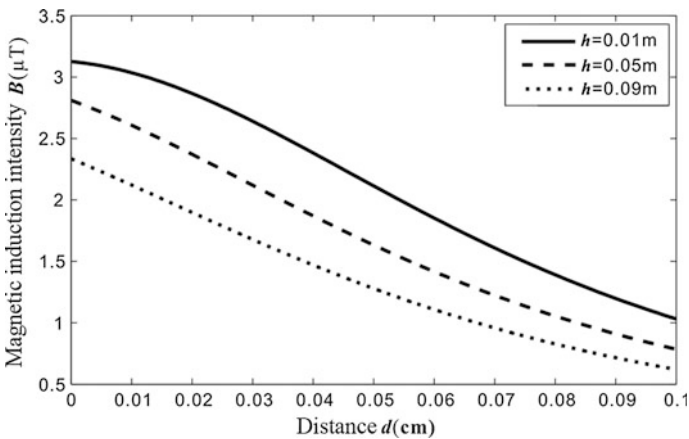


Fig. 4.20 The theoretical curve for the influence of the thickness of the coil on the magnetic induction intensity (voltage as a constant)

Assume the equivalent radius r as 0.1 m and current density J as 50 A/m. When h is 0.01, 0.05, and 0.09 m, respectively, the curve of magnetic induction intensity B versus the distance d is shown in Fig. 4.21.

The simulation results shown in Fig. 4.21 are in agreement with the theoretical analysis in Fig. 4.7.

The excitation power of the coil is kept constant. That means $rA^2/(h(r_1 - r_2))$ is constant. Because the equivalent radius and the difference between the inner radius and the outer radius are unchanged, and the excitation ampere-turns is excitation current I in Fig. 4.19, I^2/h remains unchanged. Assuming M is I^2/h , the current density is:

$$J = \sqrt{\frac{M}{h}} \quad (4.14)$$

By electromagnetic theory, the magnetic induction intensity on the point P can be obtained by integrating.

$$B = \frac{\mu_0 \sqrt{M}}{2\sqrt{h}} \left(\frac{d+h}{\sqrt{r^2 + (d+h)^2}} - \frac{d}{\sqrt{r^2 + d^2}} \right) \quad (4.15)$$

Formula (4.15) is the relationship between the magnetic induction intensity B and the thickness h of the coil under the condition of constant excitation power on the probe.

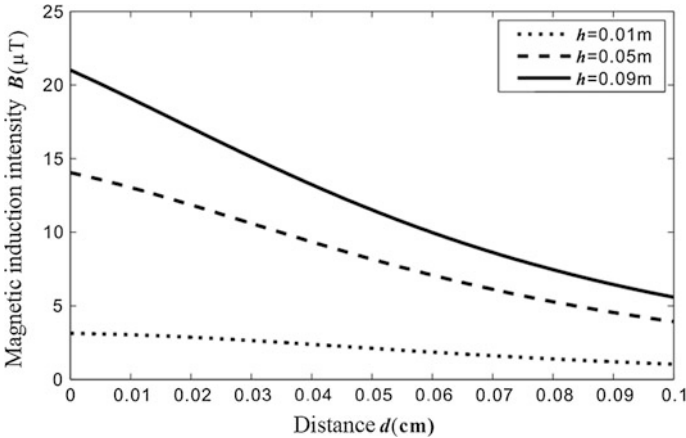


Fig. 4.21 The theoretical curve for the influence of the thickness of the coil on the magnetic induction intensity (current as a constant)

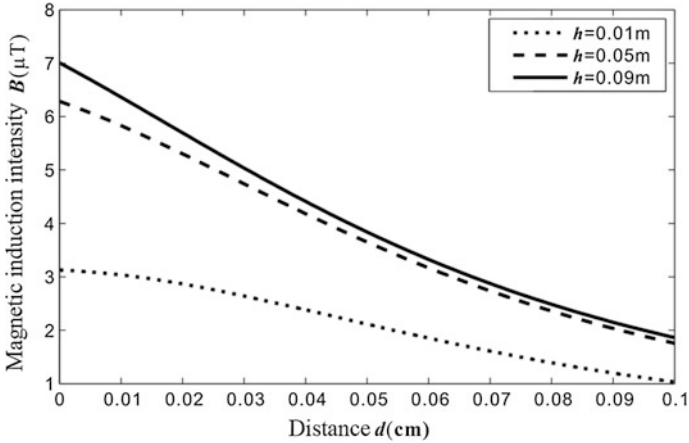


Fig. 4.22 The theoretical curve for the influence of the thickness of the coil on the magnetic induction intensity (power as a constant)

Assuming the equivalent radius r as 0.1 m, M is $25 A^2/m$. When h is 0.01, 0.05, and 0.09 m. respectively, the curve of magnetic induction intensity B versus the distance d is shown in Fig. 4.22.

The simulation results shown in Fig. 4.22 are in agreement with the theoretical analysis in Fig. 4.8.

4.2.3.3 The Influence of the Equivalent Radius of Probe Coil on Magnetic Field Yielded by the Probe

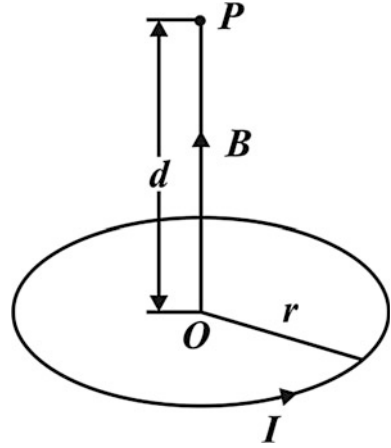
The influence of the equivalent radius on the magnetic field of the coil probe is analyzed, and the theoretical model shown in Fig. 4.23 can be established.

In Fig. 4.22, the difference between the inner radius and the outer radius, and the thickness of the coil are ignored. We can assume the coil as a single-turn coil. The equivalent radius is r . The coil is applied with the excitation current I and the magnetic induction intensity and its change rate with distance d from the point P to the center O of the coil are analyzed.

The excitation voltage of the coil is kept constant. That means rA is constant. However, the excitation ampere-turns A is excitation current I in Fig. 4.23, rI remains unchanged. Let $V = rI$, $I = V/r$. By electromagnetic theory, the magnetic induction intensity on point P can be obtained.

$$B = \frac{\mu_0 Vr}{2(r^2 + d^2)^{3/2}} \tag{4.16}$$

Fig. 4.23 The theoretical model for the influence of the equivalent radius on the magnetic field of the coil probe



The change rate of magnetic induction intensity on point P is

$$\frac{dB}{dr} = \frac{\mu_0 V}{2} \left[\frac{1}{(r^2 + d^2)^{3/2}} - \frac{3r^2}{(r^2 + d^2)^{5/2}} \right] \quad (4.17)$$

When r is $0.707d$, the magnetic induction intensity on point P achieves its maximum; when r is $0.5d$, the change rate of the magnetic induction intensity on point P achieves its maximum, which is in agreement with the simulation results.

The excitation current of the coil is kept constant. That means $Al/(h(r_1 - r_2))$ is constant. Because the difference between the inner radius and the outer radius, and the thickness are unchanged, and the excitation ampere-turns is excitation current I in Fig. 4.23, current density J remains unchanged. By electromagnetic theory, the magnetic induction intensity on point P can be obtained.

$$B = \frac{\mu_0 I r^2}{2(r^2 + d^2)^{3/2}} \quad (4.18)$$

The change rate of magnetic induction intensity on point P is

$$\frac{dB}{dr} = \frac{\mu_0 I}{2} \left[\frac{2r}{(r^2 + d^2)^{3/2}} - \frac{3r^3}{(r^2 + d^2)^{5/2}} \right] \quad (4.19)$$

When r is $1.414d$, the magnetic induction intensity on point P achieves its maximum; when r is $0.816d$, the change rate of the magnetic induction intensity on point P achieves its maximum, which is in agreement with the simulation results.

The excitation power of the coil is kept constant. That means $rA^2/(h(r_1 - r_2))$ is constant. Because the difference between the inner radius and the outer radius, and the thickness are unchanged, and the excitation ampere-turns is excitation current I in Fig. 4.23, rI^2 remains unchanged. Let $M = rI^2$, so the current I is

$$I = \sqrt{\frac{M}{r}} \quad (4.20)$$

By electromagnetic theory, the magnetic induction intensity on the point P can be obtained.

$$B = \frac{\mu_0 \sqrt{M} r^{3/2}}{2(r^2 + d^2)^{3/2}} \quad (4.21)$$

The change rate of magnetic induction intensity on the point P is

$$\frac{dB}{dr} = \frac{\mu_0 \sqrt{M}}{2} \left[\frac{3\sqrt{r}}{2(r^2 + d^2)^{3/2}} - \frac{3r^{5/2}}{(r^2 + d^2)^{5/2}} \right] \quad (4.22)$$

When r is equal to d , the magnetic induction intensity on point P achieves its maximum; when r is $0.655d$, the change rate of the magnetic induction intensity on point P achieves its maximum, which is in agreement with the simulation results.

It should be noted that in different simulation conditions, the conclusion may be different. For example, under the condition that the excitation voltage of the coil probe is constant, the thickness of the probe is reduced to improve the detection resolution; under the condition of keeping the excitation current of the coil probe, increasing the thickness of the coil probe is beneficial to improve the detection resolution. The reason for this is that simulation wire cross section S and resistivity ρ will remain unchanged, thereby increasing the thickness of the probe coil means increasing the coil resistance. Under the condition of constant voltage excitation, resistance increasing means current decreasing. Thus to reduce the power which is not conducive to improve the detecting resolution; under the condition of keeping the same excitation current, the increase of resistance means that the voltage increases and the power increases, so it is advantageous to improve the detection resolution.

In practice, there are few situations that the excitation voltage or the excitation current of the coil probe remains constant. Most of the cases are the excitation voltage, and current will have an upper limit. Therefore, the simulation results obtained under the condition of keeping the excitation power of the probe are more practical.

4.3 Pipe Deformation Detecting System Based on Low-Frequency Eddy Current

The block diagram of low-frequency eddy current detection system for pipe deformation is shown in Fig. 4.24. The system is composed of coil probes, a digital AC unbalanced electric bridge, and a signal processing and display module [15].

4.3.1 Systematic Design

The frequency of the eddy current probe is 100 Hz. The pipeline deformation detector can detect 1 mm tiny deformation of the wall, and the minimum diameter of the detector is 80 % of the pipe diameter. The distribution of the probes in the pipe is shown in Fig. 4.25.

The diameter of oil and gas pipeline is d . The radius of the detector in Fig. 4.25 is $0.3d$. The probes are arranged on the detector along the circumferential direction, and the circumferential resolution of each probe is 45° . Thus, the diameter of the probe is $0.23d$, and the distance between the probe and the pipe wall is $0.223d$. There is a rule that the diameter of the coil probe is approximately equal to the detection distance of the probe.

If there are 12 coil probes along the circumference of the detector, the circumferential resolution of each coil probe is raised to 30° , but the diameter of each coil probe is reduced to $0.155d$, and the radial detecting sensitivity is reduced. If there are 6 coil probes along the circumference of the detector, the diameter of each coil probe is raised to $0.3d$ and the radial detecting sensitivity is increased to some degree. However, the circumferential resolution of each coil probe is decreased to 60° . So the circumferential resolution is contradictory to the radial detecting sensitivity. Eight coil probes on the detector can be determined.

In summary, the diameter of oil and gas pipeline is d . The radius of the detector is $0.6d$. There are 8 coil probes along the circumference of the detector.

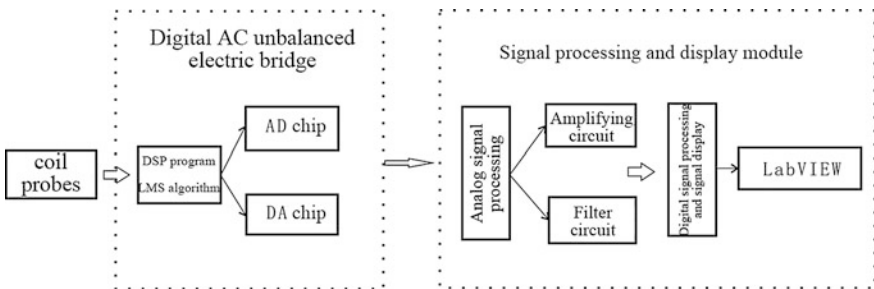
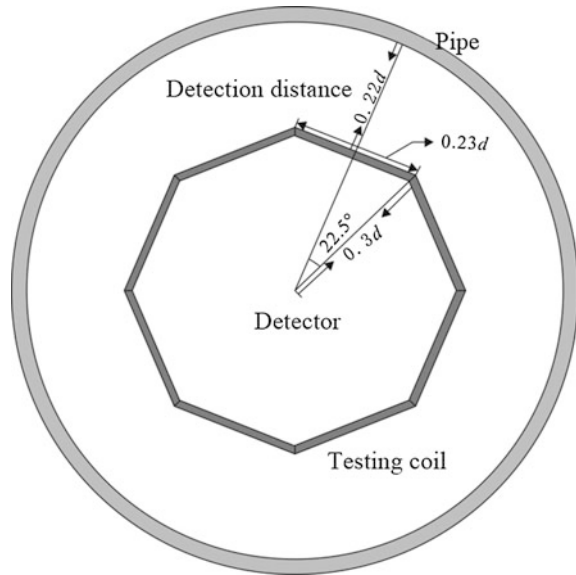


Fig. 4.24 The block diagram of pipe deformation detection system

Fig. 4.25 The distribution of eddy current probes



The diameter of the probe is $0.23d$, and its circumferential resolution is 45° . In the detection process, the excitation signal of 100 Hz is used to detect tiny deformation of 1 mm at the detecting distance as the diameter of the probe.

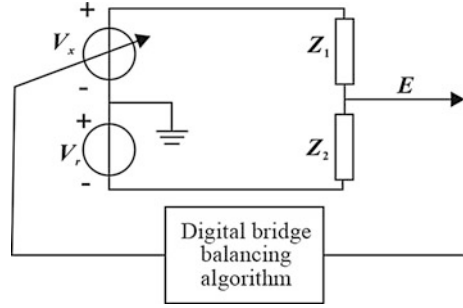
4.3.2 Digital Alternating Current Bridge Measuring Circuit

In order to improve the detection resolution of eddy current displacement sensor, the compensation coil is used on the center of the pipeline, which is not used to detect deformation. It is used as compensation coil to the 8 circumferential detecting probes, respectively, which can reduce the environmental noise and temperature influence.

Compensation coil probe requires the use of AC unbalanced bridge circuit as the measurement circuit. Unbalanced bridge is used to measure the output voltage of the bridge. To reduce the measurement error and to improve the accuracy of the measurement, the bridge should be accurately balanced before measurement. Traditional analog AC bridge circuit is composed of two same probes and two same resistance with high precision resistor as four bridge arm of the bridge, whose balance accuracy is low. It is difficult to adjust and has poor reliability. It cannot adapt to the requirements of the automatic measurement.

However, the digital AC bridge has the advantages such as high accuracy, high reliability, and suitable for automatic measurement. Therefore, the mean square least (LMS) algorithm is used to measure the output voltage of the bridge as

Fig. 4.26 The principle diagram of the digital alternating current bridge



measurement circuit of eddy current probe, so as to effectively reduce the output voltage of the bridge and to increase the detection resolution of the probe.

Figure 4.26 is the principle diagram of the digital alternating current bridge. V_r and V_x are same sinusoidal voltage sources whose frequencies are ω_0 . However, their amplitudes and phases are different. V_r is reference voltage source whose amplitude is A and phase is 0° . Its amplitude and phase remain constant. The amplitude and phase of V_x are changeable. V_r and V_x can be expressed as:

$$V_r = A \sin(\omega_0 t) \quad (4.23)$$

$$V_x = B \sin(\omega_0 t + \phi) \quad (4.24)$$

In Eq. (4.24), the B and ϕ can be used to adjust the balance of the bridge. The other two bridge arms are two detection coils Z_1 and Z_2 . Due to the structure parameters of two detecting coil are similar, Z_1 is nearly equal to Z_2 . So when the bridge is balanced, V_r is nearly equal to V_x .

V_x can be expressed as the sum of the cophase components and the orthogonal components, that is,

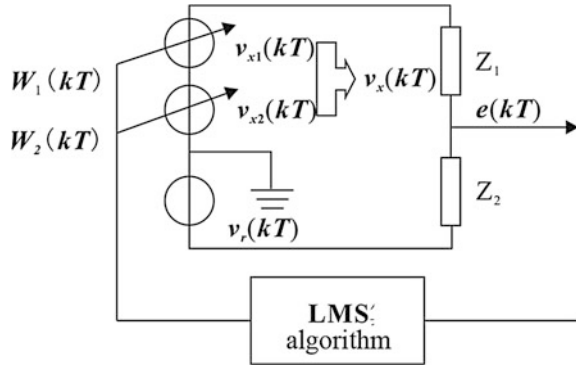
$$V_x = V_{x1} + V_{x2} = W_1 A \sin \omega_0 t + W_2 A \cos \omega_0 t \quad (4.25)$$

In Eq. (4.24), V_{x1} and V_{x2} are the cophase components and orthogonal components, respectively. W_1 and W_2 are the weight coefficients of the cophase components and the orthogonal components, respectively. In order to balance the bridge, the W_1 and W_2 can be modified by any initial values, and the output voltage E of the bridge is the minimum.

$$E = \frac{V_x Z_2 - V_r Z_1}{Z_1 + Z_2} \quad (4.26)$$

LMS algorithm can realize the automatic balance of digital bridge, as shown in Fig. 4.27. The output voltage E is sampled. The sampling period is T . The sampling frequency is $1/T$. At the k th sampling, the output voltage E can be expressed as the instantaneous output voltage $e(kT)$. The instantaneous voltage $v_x(kT)$ is composed

Fig. 4.27 LMS algorithm for digital AC bridge



of cophase components $v_{x1}(kT)$ and orthogonal component $v_{x2}(kT)$, and their weight coefficients are $W_1(kT)$ and $W_2(kT)$, respectively. At each sampling interval, the weight coefficients $W_1(kT)$ and $W_2(kT)$ are adjusted in the fastest direction of $e^2(kT)$ descending, which makes the RMS of output voltage reach the minimum.

At the k th sampling, the weight coefficients are:

$$W_1((k + 1)T) = W_1(kT) - \mu e(kT)A \sin(\omega_0 kT) \tag{4.27}$$

$$W_2((k + 1)T) = W_2(kT) - \mu e(kT)A \cos(\omega_0 kT) \tag{4.28}$$

In the equation, μ is step size, which is a very small constant.

The instantaneous reference voltage source v_r can be expressed as:

$$v_r(kT) = A \sin(\omega_0 kT) \tag{4.29}$$

The instantaneous variable voltage source v_x can be expressed as:

$$v_x(kT) = v_{x1}(kT) + v_{x2}(kT) \tag{4.30}$$

In Eq. (4.30), the cophase component is:

$$v_{x1}(kT) = W_1(kT) \cdot A \sin(\omega_0 kT) \tag{4.31}$$

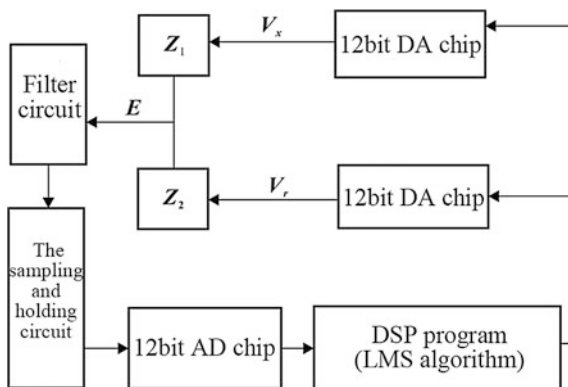
In Eq. (4.30), the orthogonal component is:

$$v_{x2}(kT) = W_2(kT) \cdot A \cos(\omega_0 kT) \tag{4.32}$$

where k is 0, 1, 2 ...

The step size mentioned in Eqs. (4.27) and (4.28) is also known as the convergence factor and is slightly greater than zero. μ controls the convergence and stability of the LMS algorithm. When μ gets bigger, the stability of the algorithm

Fig. 4.28 The block diagram of automatic balance of the digital AC bridge



gets faster, but the stability gets poorer. When μ is small, the algorithm has slow convergence speed and good stability.

In practical applications, the two detection coils and the two digital AC power supplies form the 4 bridge arms. Figure 4.28 shows the block diagram of automatic balance of the digital AC bridge, which uses DSP chip to achieve the control of the digital bridge. First of all, using a 12-bit DA chip to generate a sinusoidal voltages V_r and V_x , with two detection coils Z_1 and Z_2 together constitutes the AC bridge. The bridge output signal E is converted into digital signal through the filter circuit, the sampling and holding circuit, and the 12-bit AD convertor. The output voltage V_x can be changed by LMS algorithm, so the automatic balance of digital AC bridge is realized.

Z_2 and Z_1 are two similar structural parameters in AC bridge measurement circuit. When the bridge balance is balanced, V_r is equal to V_x . So W_1 is set to 1, W_2 is set to 0 as the initial values which can make the bridge to reach equilibrium faster. In addition, the bridge balance is not the final goal in the digital alternating current measurement circuit which is applied in the eddy current detection. It is only a means to realize the following measurement. So the feedback loop should be disconnected when the bridge is balanced. And then, weight coefficients W_1 and W_2 values are fixed, so that W_1 and W_2 will not be changed in the subsequent measurement. The changes in the detection will be measured accurately. The whole process of the algorithm is shown in Fig. 4.29.

In order to control the feedback loop, the program adds a feedback variable to the digital AC bridge. The value of the feedback variable is set to “false” before the program proceeds, while the bridge is not automatically balanced, and the weight coefficients W_1 and W_2 are the initial values. The value of the feedback variable is changed to “true” in the process of operation. The bridge is beginning to balance automatically, and the weight coefficient W_1 and W_2 are beginning to change. After the bridge reaching its equilibrium, the feedback variable set to “false” again, the weight coefficient W_1 and W_2 are fixed, and the detection is proceeded afterward. Output voltage e (kT) is shown after amplifying and filtering, and the amplitude of

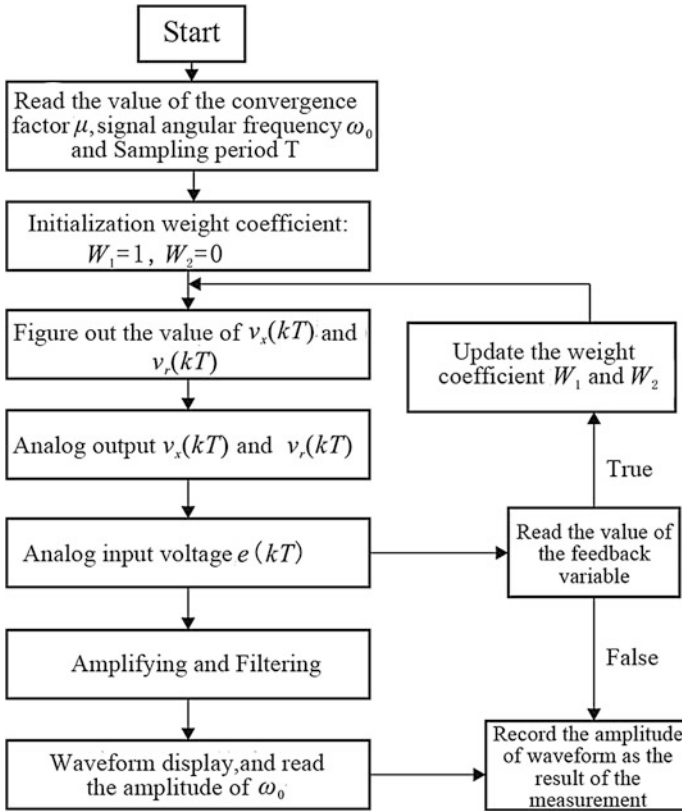


Fig. 4.29 LMS algorithm flowchart of digital bridge

the ω_0 component of the waveform is read. If the value of the feedback variable is “true,” it can be judged whether the bridge is balanced by the amplitude. If the value of the feedback variable is “false,” the amplitude of the waveform is measured, read, and recorded.

4.3.3 Signal Processing and Display Module

Digital AC output signal of unbalanced bridge is often very weak and is accompanied by noise, so it is necessary to signal processing. First, analog signal method is used, including signal amplification, filtering, and other means to process the bridge output signal, after reading through the AD chip, and then LabVIEW software is used to process the digital signal, and finally the detection results are displayed on the software interface.

The output voltage magnitude of digital AC unbalanced bridge is from millivolts to tens of microvolts. After amplifying and gathering, the detection sensitivity can be greatly improved.

The digital AC output voltage of the bridge also includes the noise signal, and the amplifier circuit will amplify noise, too, so the filter circuit is essential. The active low-pass filter is composed of RC circuit and operational amplifier.

The output signal of the digital AC unbalanced bridge is converted into a digital signal by 12 bit AD acquisition card after it is amplified and filtered in the analog circuit. In order to improve the detection sensitivity, the LabVIEW visual programming method is adopted; the amplitude of the useful signal is extracted by using digital signal processing method; the noise of other frequency is filtered out, and the detection results are displayed.

The back panel of the program is shown in Fig. 4.30. The core is constructed by two functions of the FFT spectrum and extracting the single-frequency information. The program can display the initial signal waveform, its FFT spectrum, the amplitude of 100 Hz component, and 100 Hz component waveform. The program interface is shown in Fig. 4.31.

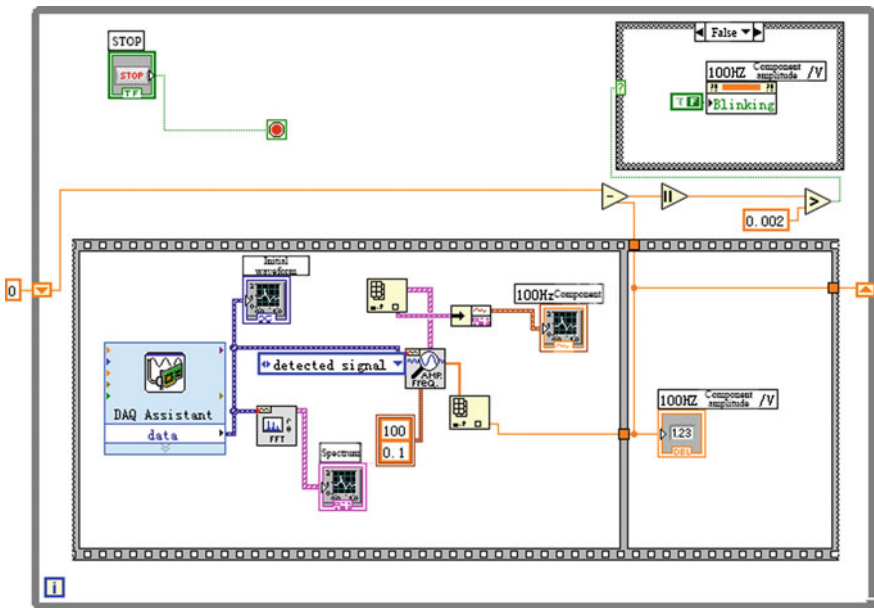


Fig. 4.30 The back panel of the program

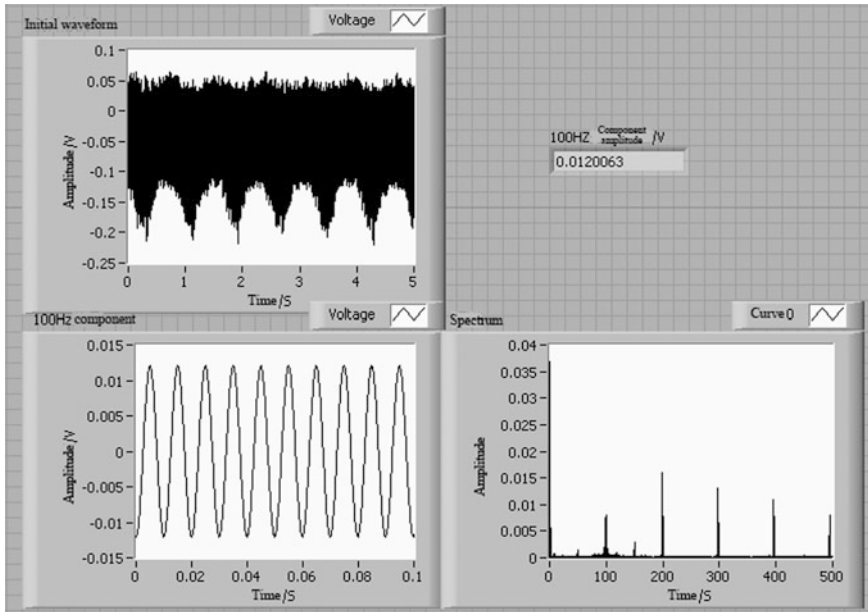


Fig. 4.31 The program interface

References

1. United States Nondestructive Testing Manual (Electromagnetic Volume). World Publishing Corporation (1999)
2. Vyroubal, D., Zele, D.: Experimental optimization of the probe for eddy-current displacement transducer. *IEEE Trans. Instrum. Meas.* **45**(6), 995–1000 (1993)
3. Vyroubal, D.: Impedance of the eddy-current displacement probe: the transformer model. *IEEE Trans. Instrum. Meas.* **53**(2), 384–391 (2004)
4. Mizuno, T., Enoki, S.: Extending the linearity range of eddy-current displacement sensor with magnetoplated wire. *IEEE Trans. Magn.* **43**(2), 543–548 (2007)
5. Fichte, L.O., Clemens, M.: A method combining boundary integral equation and separation method applied to plane eddy current problems. *IEEE Trans. Mag.* **2**, 568–571 (2007)
6. Cui, J., Ding, F., Li, Y.: A novel eddy current angle sensor for electrohydraulic rotary valves. *Meas. Sci. Technol.* **19**(1), 1–4 (2008)
7. Arpaia, P., Daponte, P., Grimaldi, D.: ANN-based error reduction for experimentally modeled sensors. *IEEE Trans. Instrum. Meas.* **51**(1), 23–30 (2002)
8. Goldshtein, A.E., Kalganov, S.A.: Measuring displacement of local conductive objects using traveling magnetic field. *Electr. Power Eng.* **5**, 315–316 (2005)
9. Nakane, H., Sohara, Y., Omori, S.: Measuring the thickness of a thin film conductor using solenoid coils. *IEEE Trans. Instrum. Meas.* **40**(2), 429–432 (1991)
10. Yating, Y., Pingan, D.: Optimization of an eddy current sensor using finite element method. In: *Proceedings of the 2007 IEEE International Conference on Mechatronics and Automation*, vol. 8, pp. 3795–3800 (2007)
11. Reghem, P., Destobbeleer, E., Derrey, T.: Precision of an eddy current sensor with magnetic circuit losses. In: *20th International Conference on Industrial Electronics, Control and Instrumentation*, vol. 3, pp. 915–919 (1994)

12. Bowler, J., Sabbagh, H., Sabbagh, D.: The reduced impedance function for cup-core eddy-current probes. *IEEE Trans. Magn.* **25**(3), 2646–2649 (1989)
13. Chen, X.: *Oil and Gas Pipeline Deformation Low-Frequency Eddy Current Testing Method*. Tsinghua University, Beijing (2010). (in Chinese)
14. Songling, H., Chen, X., Peng, X., et al.: Finite element simulation and analysis for oil and gas pipeline deformation eddy current testing coil probe. *J. Tsinghua Univ. (Sci. Technol.)* **51**(3), 390–394 (2011). (in Chinese)
15. Chen, X., Huang, S., Zhao, W., et al.: Oil and gas pipeline deformation low-frequency eddy current testing method. *Elect. Meas. Instrum.* **47**(6), 10–13 (2010). (in Chinese)

Chapter 5

Metal Magnetic Memory Testing

5.1 Introduction

The mechanical stress is directly related to the spontaneous magnetization and the residual magnetic field of the ferromagnetic material. Residual stresses and stress concentration in the component of structures impinge on the mechanical properties, erosion-resistance, dimensional precision, and cause fatigue failure. They also impact magnetic characteristics of ferromagnetic materials. The effects of stress on ferromagnetic magnetization have been studied at least since 1961 [1]. The effects of stress on static features of magnetization and hysteresis curves, e.g., susceptibility, coercivity, power loss, remanence, under uniaxial or biaxial even stresses were studied [2–10]. The effect of stress on hysteresis has also been modeled both by a microscopic model which distinguishes magnetization directions within domains and by a model which considers only macroscopic variables for polycrystalline materials without examining behavior inside individual domains [11]. Naturally, such studies require the coapplication of magnetic fields.

The domain structures and magnetic properties of polycrystalline ferromagnetic materials under stresses, especially uneven stresses, without coapplied field, have not been studied. For the first time, spontaneous magnetization phenomena in production were noticed in the 1970s by Mr. Zhong [12]. He found that demagnetized ferromagnetic materials were intensely magnetized by cutting or operation. He named the first “magnetization by machining” and the second “magnetization through operation.” The same phenomena were observed in Russia at the beginning of 1980s when strong magnetization was detected in the areas of boiler pipe destruction. Russian researcher Doubov called this phenomenon as metal magnetic memory (MMM) [13]. He investigated the level and distribution of residual magnetization and accordingly considered the scattering magnetic field on the surface of the tested equipment as a result of the influence of magnetoelastic and magnetomechanical effects. In the formation of MMM, the influence of magnetic field of the Earth was overestimated. A simple two-domain model was created to illustrate

stress-induced bulk moments by Garshelis [14]. The condition under which stress alone can establish net magnetic moments in the absence of applied field was discussed. However, there were no test data for the model validation.

Welding always brings concentration of stress into the zone of heat action. Y-sloping-shape welding format is widely used. It generates stress in joints inevitably because of restricted state by the welding seam. These stress concentrations aroused by welding-produce abnormality of magnetic field on the surface of welded objects inevitably [15–17]. The distribution of stress is also researched by MMM and the magnetic field distributions of the specimen before and after annealing are compared [18, 19]. Active defects can be detected by MMM method, too [20, 21]. Defects of metallurgical and production operation will induce stress concentration under the action of operating loads. These defects in engineering components can be detected using MMM [22].

5.2 The Relationship Between Metal Magnetic Memory and Geomagnetic Field

Metal magnetic memory testing belongs to weak magnetic field detection. It is necessary to study the influence of geomagnetic field on metal magnetic memory phenomenon and the detection process because the geomagnetic field is a vector field and the intensity of the field in the vertical direction is zero. Secondly, the geomagnetic field is not a constant field. It changes with different latitude, height, and even in different geographical environment. Based on the variable vector character of the geomagnetic field, is the external performance of the metal magnetic memory phenomenon random? So the reliability of the metal magnetic memory testing technology is also concerned.

5.2.1 *The Influence of Geomagnetic Field to Metal Magnetic Memory Testing*

Residual stress caused by butt welding of steel pipe was researched. To rule out other factors that may cause the magnetic field distortion, such as material, structure, different heat treatment process is adopted for two steel pipes made of the same process. One was untreated, and the other was treated by low-temperature annealing. The magnetic field distribution near the surface of the steel pipes before and after low-temperature annealing was measured.

The specimen (Fig. 5.1) is a pipe made of low alloy steel 16MnR, with a circular flux-shielded metal arc-welding seam. The width of the welding seam is 20 mm.

Chemical compositions and mechanical properties of 16MnR are presented in Tables 5.1 and 5.2.

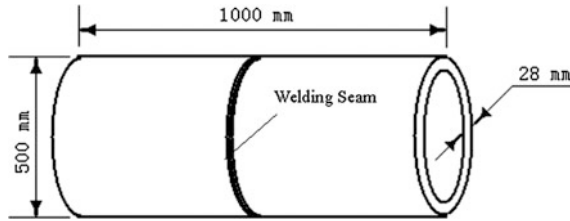


Fig. 5.1 The pipe specimen with welding seam

Table 5.1 Chemical composition (%)

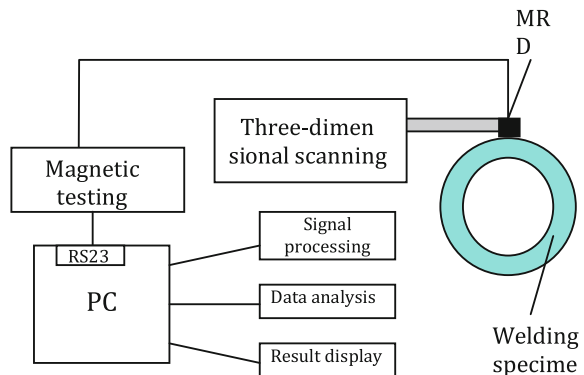
Steel No.	C	Mn	Si	S	P
16MnR	≤0.20	1.20–1.60	0.20–0.55	<0.030	<0.035

Table 5.2 Mechanical properties

Steel No.	Wall thickness (mm)	Tensile experiment			Impact experiment		Band experiment 180° <i>d</i> is buckling diameter; <i>a</i> is wall thickness
		Tensile strength σ_b (MPa)	Yielding strength σ_s (MPa)	Extending rate δ (%)	Temperature (°C)	V impact power (transverse) (J)	
16MnR	16–36	490–620	325	21	20	31	$d = 3a$

Figure 5.2 shows the testing system for a weak magnetic field, which is based on Honeywell’s HMC-1001. The magnetic probe in the system is a magnetic resistance device (MRD), which has sensitivity of 10^{-8} T. The magnetic testing system module has the probe driving, amplifying, and filtering of the magnetic signals, A/D transforming, and RS232 communicating functions. Three-dimensional magnetic

Fig. 5.2 A weak magnetic field testing system



field signals on the surface of the specimen are received by a platform made of non-ferromagnetic aluminum alloy. The magnetic field distribution can be observed on computer screen real-time. Magnetic field values can be stored in computer automatically and used for following analysis and data processing.

To evaluate the magnetic phenomena generated by welding, three-dimensional magnetic field measurements were taken before and after annealing. The specimen was placed with testing line upperwards and aligned with the geomagnetic field. The specimen-testing line was perpendicular to the seam. Testing liftoff (the distance between the probe and the tube surface) was 8 mm. 101 points were measured along the specimen length with a central point (marked with zero on abscissa axis on the figures) on the seam. Three-dimensional magnetic field component distributions of the specimen before and after annealing are presented in Figs. 5.3, 5.4, and 5.5, respectively.

A low-temperature annealing (far below the Curie point 768 °C) was processed to release the residual stress. The specimen was heated to 600 °C and kept it for 5 h by heating carpet and then cooled at a rate of 50 °C/h at room temperature. This annealing can release most of the stresses aroused by welding and does not change the chemical compositions of the specimen. Thus, the magnetic field on the surface of the specimen after annealing reflects the status of stress removal.

Fig. 5.3 Magnetic field distribution of axial direction

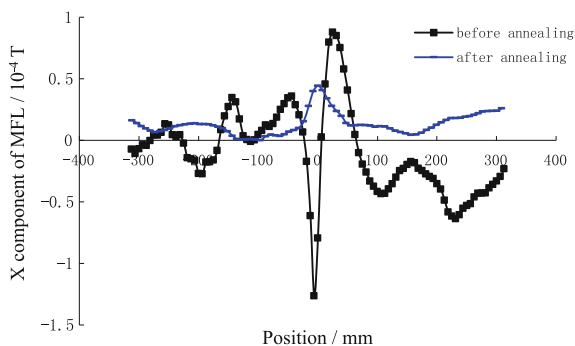


Fig. 5.4 Magnetic field distribution of circular direction

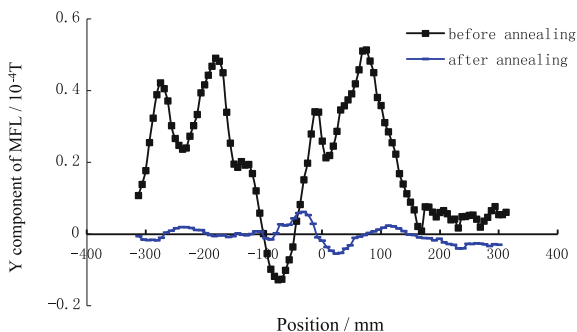
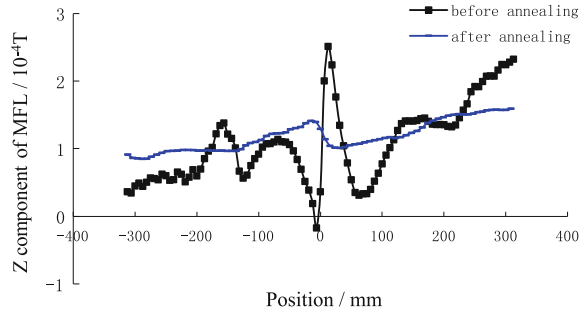


Fig. 5.5 Magnetic field distribution of normal direction



From the magnetic field curves before annealing in Figs. 5.3, 5.4, and 5.5, one can see that the area near the welding seam has the largest amplitude and fluctuation of the axial (X direction) and normal (Z direction) components of magnetic field. The amplitude of the circular (Y direction) component of magnetic field before annealing is the smallest and approaches the magnitude of the geomagnetic field.

From the magnetic field curves after annealing, an obvious decline of magnetic field after stress-removal annealing is seen. The amplitude of axial component of magnetic field decreases to the level of geomagnetic field after annealing and the circular component decreases to a minimum. The Z component of magnetic field decreases to some degree after annealing. Comparing the corresponding curves in Figs. 5.3, 5.4, and 5.5, it is obvious that stress concentration produces magnetic abnormality on the surface of ferromagnetic materials. The relationship between stress and magnetic field distribution is of interest.

After the magnetic testing and before annealing in Sect. 2.3, small hole stress testing method was adopted to get the stress distribution near the welding seam. Holes were drilled near the welding seam and along the axial direction of the pipe, so the residual stresses near the holes were relaxed by material discontinuity. Then, the strain was measured with a strain-meter and corresponding stresses were calculated from the measured strains.

Residual stresses perpendicular to the welding seam were given by hole drilling method. Eleven points were measured: five points on each side of the weld seam, and one point was located directly on the seam. The distance between the tested points is 10 mm. The main values of residual stress in circular and axial directions are presented in Figs. 5.6 and 5.7, respectively. Abscissa shows the distance from the welding seam, and y -axis shows the values of residual stress. σ_y represents the main stress parallel to the welding seam. σ_x represents the main stress parallel to the specimen axis.

Figure 5.8 gives the contrast of normalized axial stress and normalized X and Z components of magnetic field. One can see that the variation of X and Z components of magnetic field have mutative trend according to that of stress in the specimen. The tensile stress along the welding seam increases the X and Z components of magnetic field, and the compressive stress decreases them.

Fig. 5.6 Residual stresses in circular direction

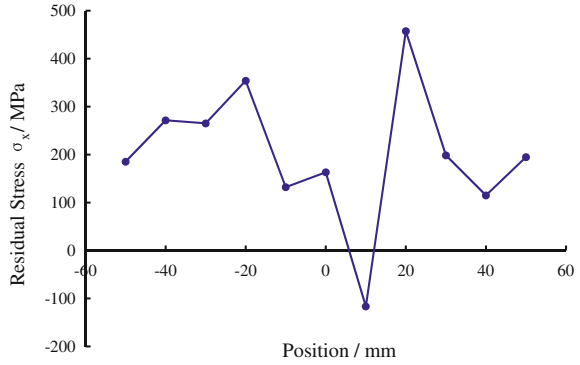


Fig. 5.7 Residual stresses in axial direction

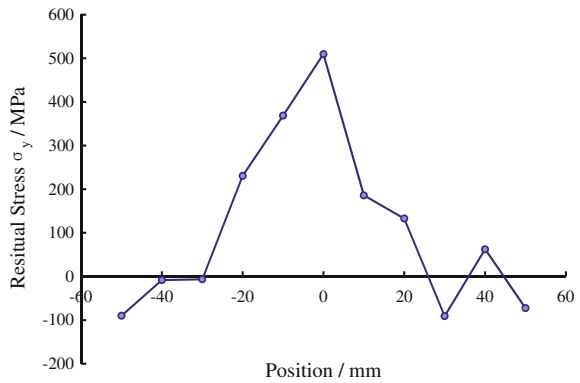
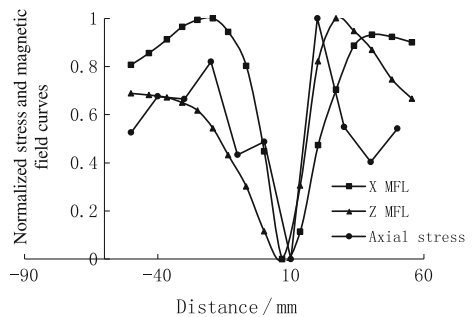


Fig. 5.8 The normalized residual stress and magnetic curve



Stress can change the directions of domains and manifest itself as local magnetic characteristics anomaly, which will form magnetic flux leakage above the surface of ferromagnetic materials. If there is stress in ferromagnetic materials, the direction of spontaneous magnetization is determined by the minimum of magnetocrystalline and stress energies. If the stress distribution is uneven in ferromagnetic crystal, stress energy will vary along with stress. As a result, the direction of spontaneous

magnetization will change, too. These changes induce the appearance of magnetic poles and demagnetizing fields inside ferromagnetic materials. To compensate this demagnetization increase, the structures of domains have to change to some degree. From comparison of the curves before and after annealing in Figs. 5.3, 5.4, and 5.5, one can see that stress in ferromagnetic materials decreases to a low level after annealing and induces changes in the direction of domains. Some directions of domains even change to the reversal.

Tensile stress causes the magnetization of domains to align with the stress, and compressive stress results in the magnetization of domains perpendicular to the stress. If there is no stress direction change (tensile or compressive), only the variation of stress amplitude, only 1800 domain walls will appear and the walls exist on the position of the smallest stress. If there is some change in stress direction, 900 domain walls will be created on the position of stress direction change. Combining the two instances above, the accordant mutative trend of X and Z components of magnetic field and axial stress in the specimen can be explained.

Residual stress in welding specimen affects the direction of ferromagnetic material domains and thus varies the magnetic field on the surface of specimen. Magnetic abnormality on the surface of inspected ferromagnetic material could be used for residual stress inspection. The normal component of magnetic field correlates the most with internal stress. The distribution of stress can therefore be derived from the distribution of normal components of magnetic field on the surface of tested ferromagnetic material.

The above study only presented plane stresses near the surface. In fact, the stress is multiaxial and the effects of stress are far more complex. The relationship between the general vector of three-dimensional stress and that of magnetic field is more significant for stress inspection. However, it is difficult to get exact values of normal stresses inside ferromagnetic materials. Further work should be concentrated on determining the quantitative relationship between magnetic and stress vectors.

5.2.2 The Influence of Geomagnetic Field to Metal Magnetic Memory Generation

The distributions of two-dimensional stress and corresponding three-dimensional magnetic field are tested in Sect. 5.2.1. In the section, the relationship between residual stress and magnetic field abnormality on the surface of ferromagnetic materials was also discussed. However, these experiments were processed under the circumstance of geomagnetic field. So the action of geomagnetic field was still not resolved in the formation of stress-induced magnetic field abnormality.

Therefore, residual stress specimens were produced by tight matching of round rings and pegs in geomagnetic field or in shielding geomagnetic field as contrast.

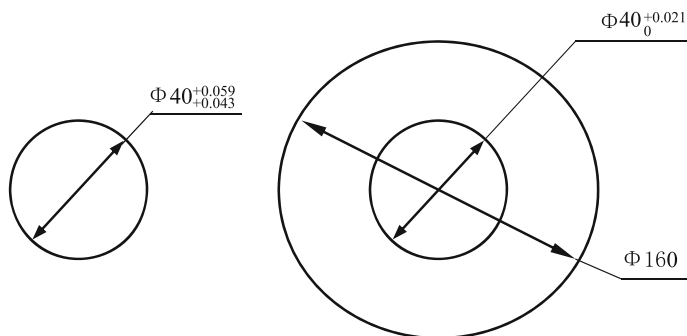


Fig. 5.9 The dimensions of ring and peg specimen

The influence of geomagnetic field was studied in the formation of stress-induced magnetic field abnormality above the surface of inspected ferromagnetic material.

The initial specimens, made of mild steel, are pairs of round rings and pegs. The ring is a circular board with a round hole on its center. The peg is a short column, which has a tight matching with the hole of the ring. Figure 5.9 shows the dimensions of the specimen. The external diameter of the ring is 160 mm, and the internal diameter of it is 40 mm, which has a tolerance of $0 \sim +0.021$ mm. The external diameter of peg is 40 mm, which has a tolerance of $+0.043 \sim +0.059$ mm. The thickness of all the specimens is 6 mm.

The rings and pegs have strong remanence (exceeding one Gauss on certain place) because of residual stress produced by manufacturing. So the rings and pegs were annealed to reduce residual stress and remanence by heating them at $800\text{ }^{\circ}\text{C}$ (just exceeding Curie point) for one hour, then allowing them to cool naturally in the furnace. After that, their remanence decreased to less than 0.02 Gauss under shielded environment.

Chemical composition of the mild steel specimen is presented in Table 5.3.

The peg and the ring should be assembled together to form a specimen which has residual stress. To determine the influence of geomagnetic field on the formation of residual magnetization induced by stress, the pegs were pressed into the rings by hydraulic pressure machine in the environment of geomagnetic field and in the environment of geomagnetic field removal. Figure 5.10 illustrates the schematic hydraulic equipment and a specimen is pressed on the condition of geomagnetic field removal. The maximum pressure of the hydraulic pressure machine is 15 t.

Three aluminum columns block the specimen from contacting to ferromagnetic components of the hydraulic pressure machine, which can avoid the magnetization of specimens by the remanence of ferromagnetic components. A cylinder made of

Table 5.3 Chemical composition (%)

Steel No.	C	Mn	Si	S	P
20	≤ 0.20	1.20–1.60	0.20–0.55	< 0.030	< 0.035

78Ni Permalloy was used to shield environment geomagnetic field. The diameter of the cylinder is 200 mm and the height of it is 400 mm. Two specimens were made in the magnetic field-shielding cylinder. Other two specimens were made under geomagnetic field environment for contrast.

Figure 5.11 shows a weak magnetic field testing system, which is based on Honeywell’s HMC-1001. The magnetic probe in the system is a magnetic resistance device (MRD), whose sensitivity is 10^{-8} T. The magnetic testing system module carries out the probe driving, amplifying and filtering of the magnetic signals, A/D transforming, and RS232 communicating functions. Those magnetic field signals on the surface of specimen are gotten using the scanning of a three-dimensional platform. The scanning platform is produced by aluminum alloy to avoid disturbance to tested magnetic field. The imaging of magnetic field distribution can be presented in computer screen real-time. Magnetic field values can be stored in computer automatically and used for following analysis and data processing.

To evaluate the influence of geomagnetic field on the formation of stress-induced magnetization, two contrast specimen series were made using the equipment shown in Fig. 5.10. Specimen series one was made in the magnetic field-shielding cylinder and specimen series two was made under geomagnetic field environment. And then magnetic field abnormality testing was processed as shown in Fig. 5.11. The specimen was placed horizontally and tested in magnetic field-shielding cylinder. Testing liftoff (the distance between probe and the

Fig. 5.10 A sketch map of the hydraulic pressure system

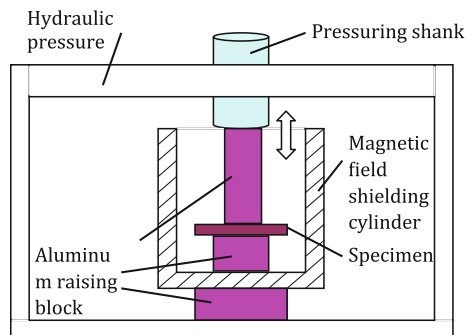


Fig. 5.11 A sketch map of the experiment testing system

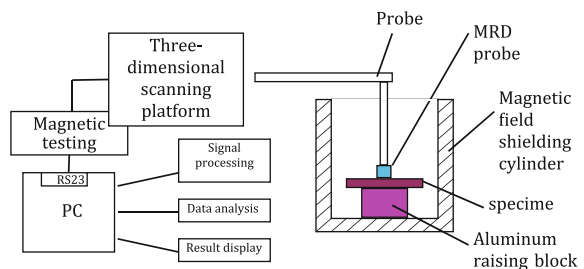
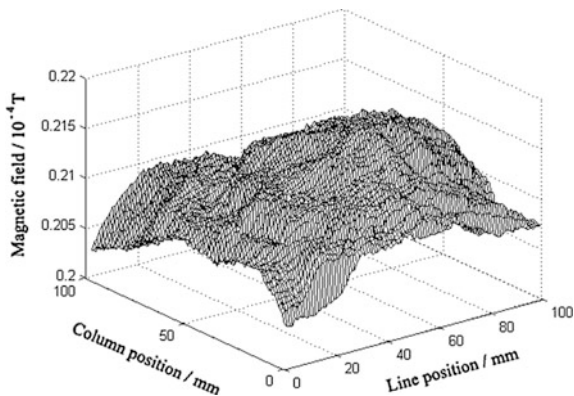


Fig. 5.12 Magnetic field distribution of one of specimen series one

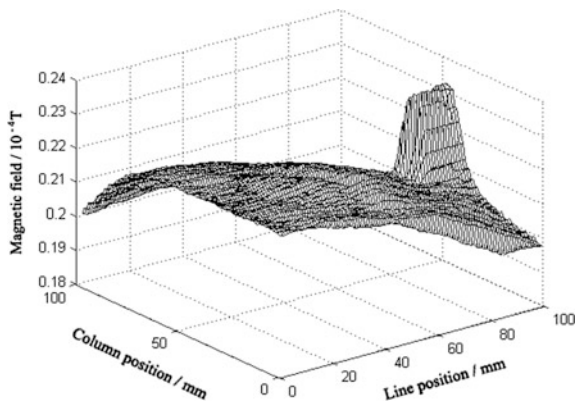


specimen surface) was 8 mm. Testing area was a square zone of 100 x 100 mm. The center point of the testing area was the center of the specimen. Figures 5.12 and 5.13 show the magnetic field distributions of one of specimen series one, one of series two, respectively. The labels of horizontal coordinates are the distances between the measured points to the left bottom corner of the testing area. The label of vertical coordinates shows the amplitudes of the magnetic field.

To contrast the tested magnetic fields of specimens series one and series two, corresponding central line and column are plotted in Figs. 5.14 and 5.15.

Residual stress in tightly assembled specimen affects the direction of ferro-magnetic material domains and thus varies the magnetic field above the surface of specimen. From the magnetic field distribution in Fig. 5.12, one can see that the area near the center has larger amplitudes of magnetic field. But the fluctuation of magnetic field amplitudes is very less, about 3.4 %. The result indicates that the area of specimen-matching zone has slightly larger stress. There is a slight abnormality on the right of Fig. 5.13. This abnormality maybe caused by local stress concentration. And the fluctuation of magnetic field amplitudes in Fig. 5.13 is also very less.

Fig. 5.13 Magnetic field distribution of one of specimen series two



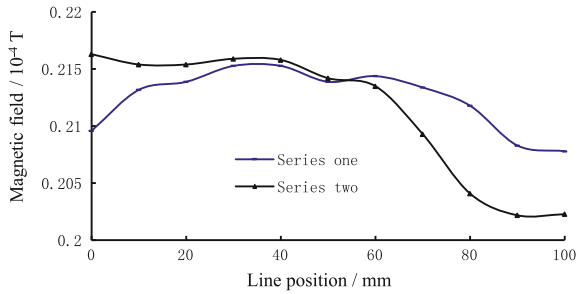


Fig. 5.14 Contrast of central column magnetic field distribution between Figs. 5.12 and 5.13

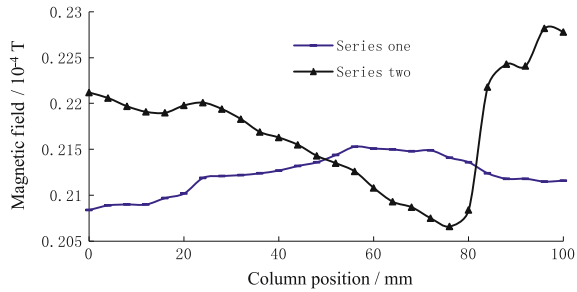


Fig. 5.15 Contrast of central line magnetic field distribution between Figs. 5.12 and 5.13

From the contrast curves in Figs. 5.14 and 5.15, one can see that specimen series one and series two have approximately equal amplitude of magnetic field. The mean magnetic field of them is about 0.21 gauss. The experimental error is less than 1.5 % from the changes of mean magnetic field intensity of the same specimen series. The mean amplitude of magnetic field in Fig. 5.12 is 0.85 % larger than that of in Fig. 5.13. So considering experimental error, it is obvious that stress-induced magnetic field abnormality above the surface of ferromagnetic materials is independent of geomagnetic field.

5.2.3 Stress Distribution Detection by Metal Magnetic Memory Testing Method

Large stress in the component of structures will affect the mechanical properties, erosion-resistance, fatigue ability, and dimension precision greatly. Researching on the distribution of residual stress in components, the value of stress and eliminating the damages induced by stress have become the focus. Welding always brings concentration of stress into the zone of heat action. Y-sloping-shape welding format is largely used in projects and this welding format produces stress in the jointed

component inevitably because of restricted state by the welding seam. The stress distribution of a specimen with a Y-sloping-shape welding seam was tested using metal magnetic memory testing method. To validate the result, the same specimen was tested by small hole method. The stress distribution of the magnetic testing was identical with that of small hole stress testing method.

The specimen tested is a No. 20 steel plate, which has a Y-shape-sloping manual arc-welding seam on it. To eliminate the shape influence of the fortified seam on the magnetic field, the higher part of the seam is planed until the seam is the same height with the motherboard. The thickness of the specimen is 10 mm. The mean width w of the seam is about 8 mm and the depth of it is about 7 mm.

The specimen is placed horizontally in geomagnetic field and then the normal components of the magnetic flux leakage (MFL) are inspected with a constant liftoff h of 10 mm. The MFL signals are amplified and filtered, and after that, A/D transform and sampling are performed. Finally, the digital MFL signals corresponding to those sampling points are transferred to PC for further processing by RS232. For geomagnetic field can be considered a uniform field in the inspecting area, the MFL signals will reveal the residual stress in the specimen. Figure 5.16 shows the testing method, and the crossed points in the testing plane are MFL sampling positions.

Figure 5.17 shows the metal magnetic testing system. The magnetic probe in the system is a magnetic resistance device (MRD), and the magnetic testing system module carries out the probe driving, amplifying and filtering of the MFL signals,

Fig. 5.16 The sketch map of the MFL stress testing method

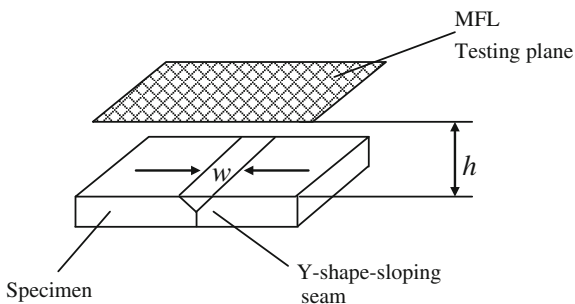
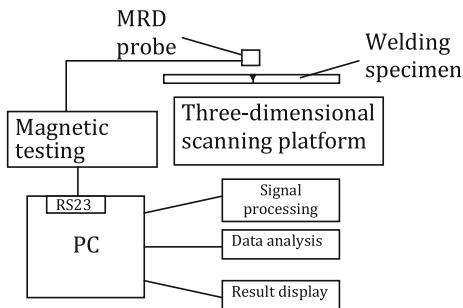


Fig. 5.17 A stress testing system by metal magnetic memory testing method



A/D transforming, and RS232 communicating functions. Those MFL signals over the specimen with 10 mm as liftoff are gotten by the scanning of a three-dimensional platform. The scanning platform is produced by aluminum alloy to avoid the influence on the distribution of spatial geomagnetic field. The welding seam of the specimen is placed horizontally along the direction of north–south on the platform.

The normal components of the magnetic field were inspected using the above method. Figure 5.18 shows the distribution of the MFL amplitudes. X coordinates show the positions away from the welding seam. Y coordinates show the positions along the welding seam direction. Vertical coordinates show the normal components of MFL amplitudes at different positions.

From Fig. 5.18, we can see that the amplitudes of MFL are not influenced by Y coordinates; they only varies according to X coordinates. To see the relationship between the normal components of MFL and X direction position more clearly, a curve intercepted from Fig. 5.18 is shown in Fig. 5.19. Its horizontal coordinates are the positions away from one side of the welding seam.

Small hole stress testing method was adopted to get the stress distribution near the welding seam. Figure 5.20 gives the result. L is the distance from the stress testing position to the welding seam. σ_y represents the main stress parallel to the welding seam. Comparing Fig. 5.19 with Fig. 5.20, we can see that the normal

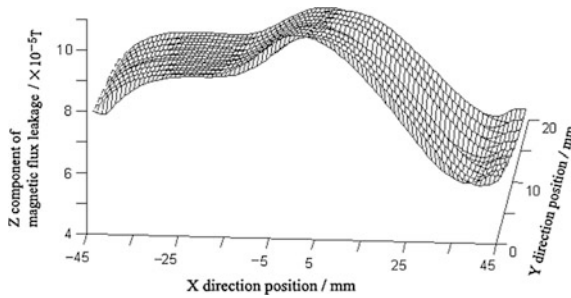


Fig. 5.18 The spatial distribution of normal components of MFL above 10 mm from the specimen

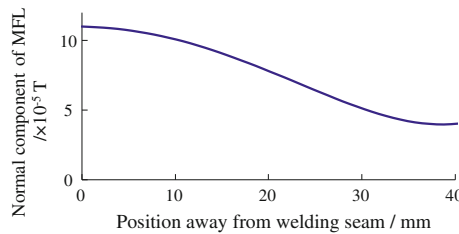


Fig. 5.19 One-dimensional distribution of normal components of MFL above 10 mm from the specimen

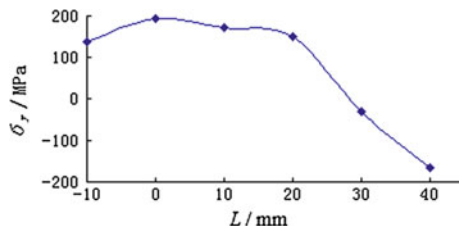


Fig. 5.20 The stress distribution from small hole drilling testing method

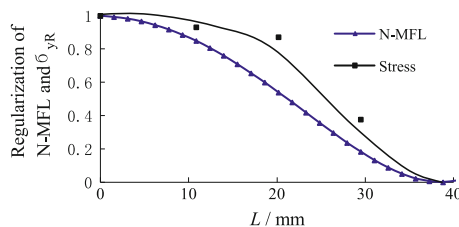


Fig. 5.21 Regularization of the normal components of MFL and the stresses versus the distances away from the welding seam

components of MFL have accordant mutative trend to those of stress in the specimen. The tensile stress along the welding seam largens the normal components of MFL, and the compressive stress lessens them.

Figure 5.21 gives the regularization curves of the magnetic signals and the stresses. N-MFL represents the regularization value of normal components of MFL, and σ_{yR} represents the regularization value of main stress along the welding seam direction. L shows the distance away from the welding seam. The two curves in Fig. 5.21 show very similar mutative trends and this is important for determining the stress distribution from MFL distribution.

In multicrystal ferromagnetic materials, if there is no magnetizing field and interior stresses, the probability of the directions of domains will be the same along all directions. So there is no magnetic flux leakage above the materials. The stresses in ferromagnetic materials will change the directions of domains and show as local magnetic characteristics anomaly, which will form magnetic flux leakage above the ferromagnetic materials. Tensile stress leads that the easy axes of domain trends to parallel to the stress and compressive stress results in the easy axes of domain perpendicular to the stress. In the experiment above, the tensile stress along the Y -axis direction conduces to the easy axes of domain parallel to it. The compressive stress along the Y -axis direction turns the easy axes of domain perpendicular to it. The magnitudes and directions of the stresses change according to stress concentration and lead to different magnetic flux leakage above the ferromagnetic materials. Thus, the accordant mutative trend of the normal components of MFL and Y -axis direction stress in the specimen can be explained successfully.

References

1. Dunaev, F.N.: Magnetic texture of ferromagnets subjected to external stresses. *Izvestiya Akademii Nauk SSSR, Seriya Fizicheskaya*. **25**(12), 1502 (1961)
2. Langman, R.: The effect of stress on the magnetization of mild steel at moderate field strengths. *IEEE Trans. Magn.* **21**(4), 1314 (1985)
3. Schneider, C.S., Cannell, P.Y., Watts, K.T.: Magnetoelasticity for large stresses. *IEEE Trans. Magn.* **28**(5), 2626 (1992)
4. Sablik, M.J., Riley, L.A., Burkhardt, G.L., Kwun, H., Cannell, P.Y., Watts, K.T., Langman, R. A.: Micromagnetic model for biaxial stress effects on magnetic properties. *J. Magn. Magn. Mater.* **132**, 131 (1994)
5. Hauser, H.: Energetic model of ferromagnetic hysteresis 2: magnetization calculations of (110) [001] FeSi sheets by statistic domain behavior. *J. Appl. Phys.* **77**(6), 2625 (1995)
6. Sablik, M.J.: A model for asymmetry in magnetic property behavior under tensile and compressive stress in steel. *IEEE Trans. Magn.* **33**(5), 3958 (1997)
7. Makar, J.M., Tanner, B.K.: The effect of stresses approaching and exceeding the yield point on the magnetic properties of high strength pearlitic steels. *NDT & E Int.* **31**(2), 117 (1998)
8. Mao, W., Atherton, D.L.: Effect of compressive stress on the reversible and irreversible differential magnetic susceptibility of a steel cube. *J. Magn. Magn. Mater.* **214**, 69 (2000)
9. Makar, J.M., Tanner, B.K.: The effect of plastic deformation and residual stress on the permeability and magnetostriction of steels. *J. Magn. Magn. Mater.* **222**, 291 (2000)
10. Chen, Y.H., Jiles, D.C.: The magnetomechanical effect under torsional stress in a cobalt ferrite composite. *IEEE Trans. Magn.* **37**(4), 3069 (2001)
11. Hauser, H.: Energetic model of ferromagnetic hysteresis. *J. Appl. Phys.* **77**(5), 2584 (1994)
12. Zhong, W.: The demagnetization for a rotor of 23 MW gas turbine. *J. Test. Eval.* **3**, 25 (1984)
13. Doubov, A.: Proceedings of ChSNDT 7th conference on NDT and international research symposium, p 181. Shantou, China, Oct 1999
14. Garshelis, I.J.: Conditions for stress induced bulk moments. *J. Appl. Phys.* **50**(3), 1680 (1979)
15. Luming, L., Songling, H., Xiaofeng, W., et al.: Magnetic field abnormality caused by welding residual stress. *J. Magn. Magn. Mater.* **261**(3), 385–391 (2003)
16. Luming, L., Songling, H., Xiaofeng, W., et al.: Stress induced magnetic field abnormality. *Trans. Nonferrous Met. Soc. China* **13**(1), 6–9 (2003)
17. Huang, S.L., Li, L.M., Shi, K.R., et al.: Magnetic field properties caused by stress concentration. *J. Cent. S. Univ. Technol.* **11**(1), 23–26 (2004)
18. Li, L.M., Huang, S.L., Wang, L.F., et al.: Research on magnetic testing method of stress distribution. *Trans. Nonferrous Met. Soc. China* **12**(3), 388–391 (2002)
19. Huang, S.L., Li, L.M., Wang, X.F.: Magnetic evaluation method for stress annealing of ferromagnetic materials. *Mater. Technol.* **20**(1), 5–6 (2005)
20. Huang, S.L., Li, L.M., Wang, X.F., et al.: Novel NDT test method for stress concentrations and fatigue cracks. *Mater. Technol.* **18**(3), 149–150 (2003)
21. Leng, J., Liu, Y., Zhou, G., et al.: Metal magnetic memory signal response to plastic deformation of low carbon steel. *NDT & E Int.* **55**(4), 42–46 (2013)
22. Dubov, A.A.: Detection of metallurgical and production defects in engineering components using metal magnetic memory. *Metallurgist* **59**(5), 164–167 (2015)

Chapter 6

Magnetic Flux Leakage Testing

6.1 Introduction

As early as 1868, the British Naval Architects Association began to use magnetic flux leakage technology and found defects on steel pipe through the compass. In 1918, it was found that powder was absorbed near defects due to the changes in surface magnetic field; thus, magnetic particle detection method was invented. After continuous development, the magnetic flux leakage testing technology not only can detect the defects, but also can analyze the characteristics of the defects [1, 2].

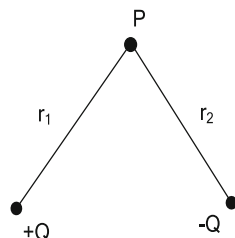
In the theoretical analysis of magnetic leakage field, it can be divided into analytical method and numerical method. In 1966, Zatsepin and Shcherbinin were the first to put forward the analytical equation of the magnetic flux leakage field of infinite long rectangular crack, as shown in Fig. 6.1 [3]. Based on the theoretical model, the magnetic flux leakage field can be generated by a dipole with two opposite polars. Taking the hole defect in the two-dimensional space as an example, the two magnetic poles are assigned to the two sides of the defect. The magnetic charge densities of the two poles are $-Q$ and $+Q$, respectively. So, the magnetic flux leakage of the defect in point $P(x, y)$ is given as follows:

$$\vec{B} = \vec{B}_1 + \vec{B}_2 = \frac{-Q}{4\pi\mu_0 r_1^3} \vec{r}_1 + \frac{Q}{4\pi\mu_0 r_2^3} \vec{r}_2 \quad (6.1)$$

Among them, μ_0 is the vacuum permeability. The holes, pits, and other defects on the surface of the workpiece can be simulated by the equivalent point dipole model. For the crack defect, it should be equivalent to the rectangular groove, whose length is infinite, and then, the equivalent surface dipole model is used to simulate the crack.

Using the dipole model, the authors calculated the magnetic leakage field of infinite long cracks in the surface [3]. After that, the magnetic field distribution of the finite length cracks in the surface was calculated by Shcherbinin and Pashagin [4].

Fig. 6.1 Magnetic dipole model



However, they did not connect the strength of the magnetic leakage field to the strength of the magnetizing field and the permeability. They used two-dimensional models. The main progress of the analytical method of magnetic leakage field analysis was completed by Edwards and Palmer in 1986 [5]. They perfected the magnetic dipole model. The shape parameters of the defect, the magnetizing field strength, the permeability, and the magnetic flux leakage of the material were firstly connected.

The limitation of Edwards and Palmer's model was that the permeability of the material was supposed as a linear parameter in the derivation process. So there were some errors between the theoretical results and the experimental results.

Therefore, numerical calculation method is usually adopted. The numerical calculation method overcomes the limitation of the magnetic dipole model. In the numerical calculation method of magnetic leakage field, the finite element method is used most widely. Lord and Hwang first introduced the finite element method to the calculation of the magnetic leakage field in 1975. They studied the effects of different shapes, different dip angles, and the depth and width of crack on the magnetic leakage field. It was pointed out that the numerical calculation was the only feasible method for solving the problem of magnetic leakage field in the nonlinear and complex shape defects [6]. The results of Lord and Hwang showed that the peak-valley values of the magnetic leakage field were approximately linear proportional to the increase of the depth of the defect. In 1986, the researches of Hwang and Lord were tested by Foster, and the results of Lord and Hwang were modified [7]. In 1980s and 1990s, Atherton [8, 9] and Bruder [10] et al. did a lot of work in the numerical calculation of the magnetic leakage field. Atherton calculated the defects of the pipe wall and obtained a two-dimensional distribution model of the magnetic leakage field. Altschuler Eduardo proposed the detection model of nonlinear crack defect in steel pipe in 1995. He concluded that the induction intensity of the magnetic leakage was approximately linear with the increase of the crack depth [11].

In view of the characteristics of the inverse problem of magnetic flux leakage detection, the existing methods can be classified as follows:

The direct method is to obtain the solution of the inverse problem by solving the Green equation. However, it is difficult to solve the Green equation. Because of the solving difficulty in direct method, the indirect method to solve the defect parameters is proposed. These methods can be divided into three categories: mapping method, iterative method, and signal classification method (Fig. 6.2).

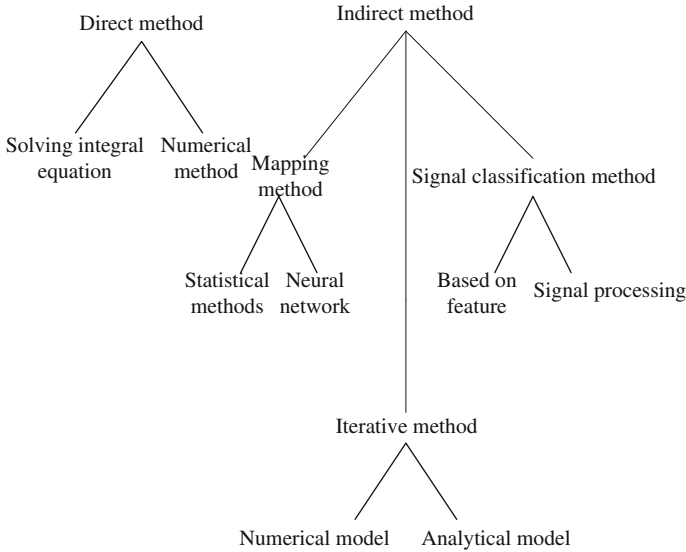


Fig. 6.2 Classification of defect quantification method

At present, the theory and implementation techniques of the simulation matching algorithm based on statistical methods have been more matured. However, the statistical method does not have the ability of adaptive processing, and it requires a large amount of test or simulation data. The statistical process is more complex. The paper [12] used neural network to calculate the magnetic leakage field, and the nonlinear approximation was used to establish the network model, and the learning algorithm was given. The drawback of the mapping method is that it relies on the consistency and accuracy of statistical samples or training samples seriously, and it is difficult to extend the ability to quantify the actual defects.

The iterative method is widely used in solving the inverse problem of electromagnetic field [13]. The essence of this method is to solve the inverse problem by feedback in the way of solving the positive problem. However, it is time-consuming for iterative calculation. Dr. Ramuhalli gave a two-dimensional finite element neural network to strike a balance between efficiency and accuracy [14]. Dr. Cui developed it to a three-dimensional finite element neural network and made it more available [15].

6.2 Magnetic Flux Leakage Testing Principle

The principle of magnetic flux leakage testing is shown in Fig. 6.3.

Magnetic flux leakage testing method is based on the high-permeability characteristics of ferromagnetic materials. When ferromagnetic materials are magnetizing by the external magnetic field, if the ferromagnetic material is continuous,

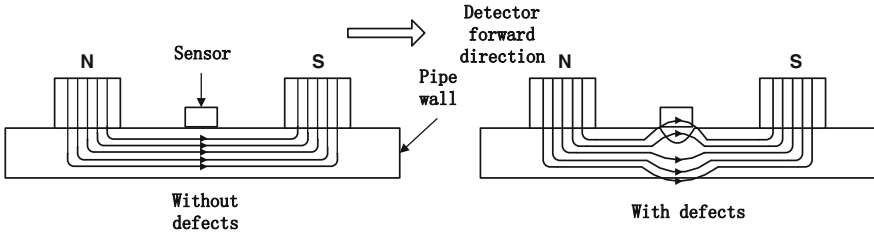


Fig. 6.3 The principle of magnetic flux leakage testing

uniform, the magnetic field will be constrained in the interior of the materials mostly. When there are defects in the material, due to the small permeability of the defect, large magnetic resistance, the magnetic lines will change way. Part of the magnetic flux from the defect will diffuse and form magnetic flux leakage above the surface of the workpiece.

Here, magnetic field strength of ferromagnetic material determines the strength of the magnetic flux leakage of defects directly. Under external magnetizing field, the relationship between the magnetic induction intensity \vec{B} and the magnetizing field strength \vec{H} of ferromagnetic materials is given as:

$$\vec{B} = \mu\vec{H} \tag{6.2}$$

Since the permeability of the material changes with the magnetizing field intensity \vec{H} , the relationship between \vec{B} and \vec{H} is also not linear, and the magnetization curve is nonlinear.

The phenomenon of magnetic leakage field is demonstrated by an example of the surface defect in a steel plate. Figure 6.4 is a section of the steel plate, and the magnetic properties of the steel plate are shown in Fig. 6.5.

The section area of the defect is S_a . The section area of the steel plate is S . So the remaining section of the defect area is $S - S_a$. If the magnetizing field H is uniform, the magnetic induction strength without defects is B_1 . So the working point on the $B-H$ curve was Q, and the corresponding permeability on curve one is point P.

Fig. 6.4 The sketch map of steel plate with a defect

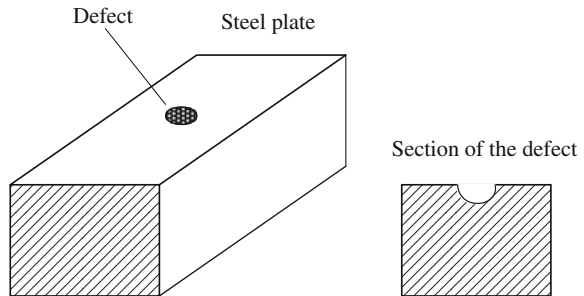
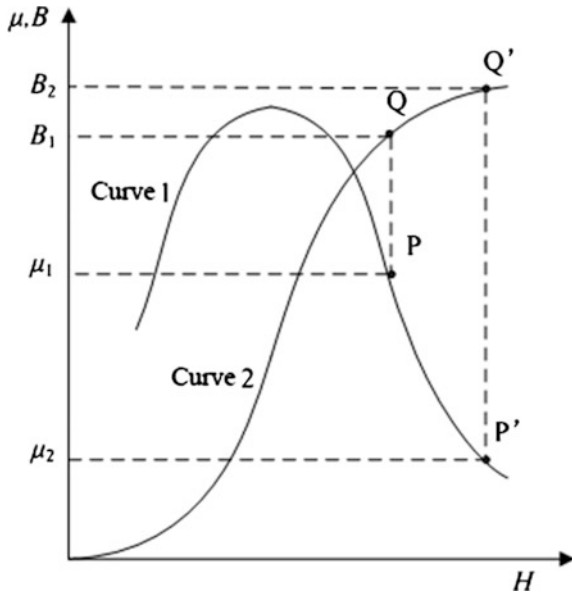


Fig. 6.5 The magnetic properties of the steel plate



Due to the existence of defects, the magnetic induction intensity in the remaining section increases, so the working point moves from Q to Q' in the magnetization curve. However, the corresponding permeability on Q' point changes smaller with the changing of working point from P to P' on the curve two. That is to say, due to the existence of defects, the magnetic induction strength increases on the reduced cross section, and the permeability of defects is smaller, so a part of magnetic flux will leak into the surrounding to form defect magnetic flux leakage field.

6.3 The Influence Factors of Magnetic Flux Leakage Testing

Magnetic leakage fields of defects will be affected by many factors; these factors include: the magnetizing magnitude, remanence, electrical conductivity, magnetic permeability, magnetic coupling loop, the distance between the magnetic poles, the moving speed of the detector, internal stress, and lift off of the probe.

When the tested material is magnetized, the magnetic leakage field can be generated at the defect, which depends on the magnetizing amplitude. If the magnetization is not enough, then the remaining thickness of the material is still possible to carry all the magnetic flux. So no magnetic flux leakage to the surface of the material can be measured. The tested material should be magnetized nearly saturated.

The applied magnetic field strength will affect the detection and quantification, so the influence of the external magnetic field strength will also affect the detection and quantification. The main factors affecting the detection and quantification are the following [16–18].

6.3.1 The Thickness of Material

The greater the thickness of the material is, the stronger the external magnetic field is required to reach saturation magnetization. In the case of constant external magnetic field, the change of the thickness is proportional to the magnetic field intensity and the magnetic induction intensity.

6.3.2 The Component of Material

Because of the change of carbon content, alloy component, and impurities, the magnetic permeability of the material is changed, and the magnetization of the material is affected. By using a strong external magnetic field, the influence can be eliminated by saturation magnetization. At this time, the change of the magnetic permeability will lead to inconsistency of the leakage magnetic signal. So it is difficult to effectively evaluate and analyze the testing signal.

6.3.3 The Coupling Loop

In a magnetizing system, steel brushes are used to couple the magnetic flux to the measured material. The coupling efficiency between the magnetizer and the measured material will have a certain effect on the magnetic induction intensity in the material. Short steel brush can provide higher coupling efficiency and higher magnetic induction strength, but longer steel brush can improve the pass-through ability of the inner inspector of pipes. If the applied magnetic field strength is only slightly higher than the saturation level, then the reducing coupling efficiency may decrease the magnetization of the material under saturation.

6.3.4 The Space Between Magnetic Poles

The shorter distance between the magnetizing poles can produce a higher magnetization, but this will lead to a decrease in the uniformity of the magnetic field.

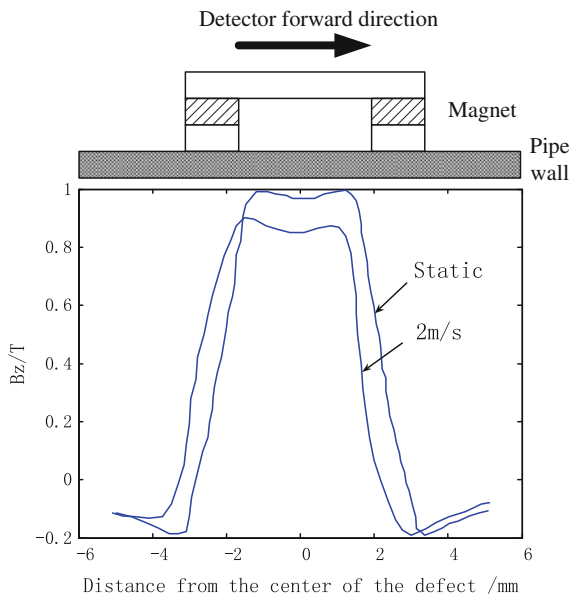
A longer distance between the poles can provide a relatively uniform magnetic field, but it will reduce the magnetization effect because the magnetic reluctance between the tested material will increase with the increase of the magnetic pole spacing, so stronger magnets are needed to make the material to reach saturation. Therefore, it is necessary to select the appropriate magnetic pole spacing aiming at the properties and the thickness of the material.

6.3.5 The Speed of Inspector

Because the tested material is a magnetic and electrical conductor, the normal component of the magnetizing field in detector will generate eddy current in the tested material and thus form a reverse magnetic field when the inspector scans. The eddy current will hinder the magnetic flux to penetrate into the tested material and induce the change of the magnetic field distribution. Through the finite element analysis, the influence of the inspector speed on the axial magnetic induction in the pipe wall is shown in Fig. 6.6.

In the static case, the axial component of the magnetic induction intensity of the pipe wall is symmetrically distributed between the two poles. The amplitude of the magnetic induction intensity decreased by about 10 % when the speed of the detector was 2 m/s. Therefore, in the design of the magnetizer, it is also necessary to take into account the actual scanning speed of the detector to ensure that the magnetic induction intensity of the material can be reached saturation at the design speed of the detector.

Fig. 6.6 The influence of the inspector speed on the axial magnetic induction in the pipe wall



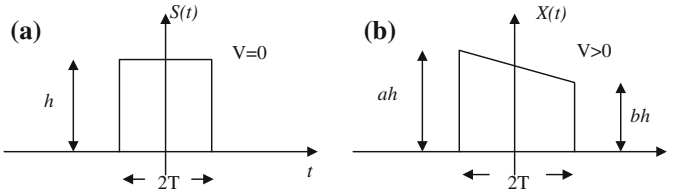


Fig. 6.7 A speed compensation filter model. **a** The speed is 0; **b** the speed is more than 0

Magnetic leakage signal is a one-dimensional time series, so it can be reconstructed by using one-dimensional Fourier transformation, and then the effect of speed is eliminated. By comparing the same defect waveform of magnetic leakage field in static case with the one in dynamic case, a speed compensation filter model can be built, as shown in Fig. 6.7.

Figure 6.7a represents the magnetic leakage signal waveform of a stationary magnetizing field. Figure 6.7b represents the magnetic leakage signal waveform under a constant scanning speed. The approximate expression is a trapezoid. The gradient filter is constructed by using the frequency domain identification method in system identification.

$$H(\omega) = \frac{X(\omega)}{S(\omega)} = \frac{a+b}{2} - \frac{a+b}{2\omega T} + j\frac{a-b}{2} \cos(\omega T) \quad (6.3)$$

Among them, $H(\omega)$ is the ratio of the Fourier transformation of the function $X(t)$ and $S(t)$. a and b are the functions of the speed.

The method to determine a_i and b_i is given below:

- calculate the Fourier transformations of magnetic leakage field signals under velocity V_i and stationary state
- obtain the transfer function $H(\omega)$ by (6.3)
- determine a_i and b_i under the speed by $H(\omega)$ and (6.3)
- least squares fitting the transfer functions of the testing data and the assumed model data, let the sum of squared errors the least.

6.3.6 The Remanence

Remanence refers to the residual magnetic field in the material which has been tested by magnetic flux leakage detection in the past. The remanence will affect the current level of magnetization, especially when the magnetizing level is low or moderate.

The remanence will reduce the magnetic induction intensity of the material being tested, thus affecting the detection and quantification of defects. Ferromaterial in

magnetizing will show a hysteresis effect. That is, after the magnetic field is removed, the material will remain within a certain magnetic induction intensity. When the material is magnetized again, the magnetization process will start from the remanence; thus, a new magnetization curve is produced. The magnetization curve is not only nonlinear, but also different from the magnetization each time.

6.3.7 The Internal Stress

The internal stress of materials will affect its magnetic conductivity and magnetic induction intensity of the materials and defects. The magnetic field distribution will distort and the testing results will be seriously affected. Permanent or plastic deformation of the material can change the permeability and also affect magnetic flux leakage testing.

At the lower magnetizing level, the influence of stress on the magnetic induction intensity of the material is very serious, as shown in Fig. 6.8. If the material is magnetized to saturation, the variation of stress can be ignored.

This conclusion should be used for the detection of corrosion. The high level of magnetization should be used, so that the magnetization of the material can reach a moderate level of saturation, so as to effectively reduce the influence of material component change, the magnetic pole spacing, the detection speed, and the internal stress on the magnetization and magnetic flux leakage.

6.3.8 The Lift off of Probe

When the probe is scanning on the surface of the material, the surface roughness of the material, such as the weld seams, defects, will cause the change of the lift off of

Fig. 6.8 The influence of stress on the magnetic induction intensity

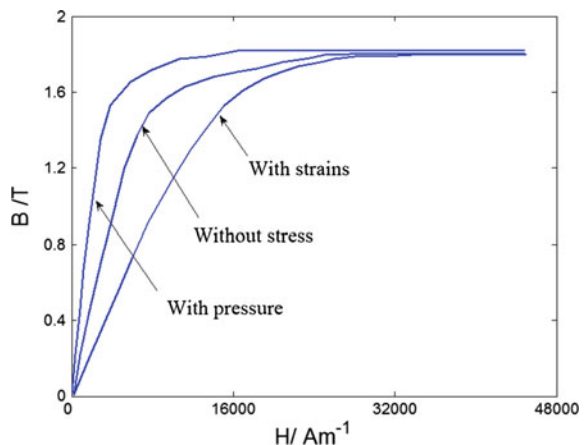
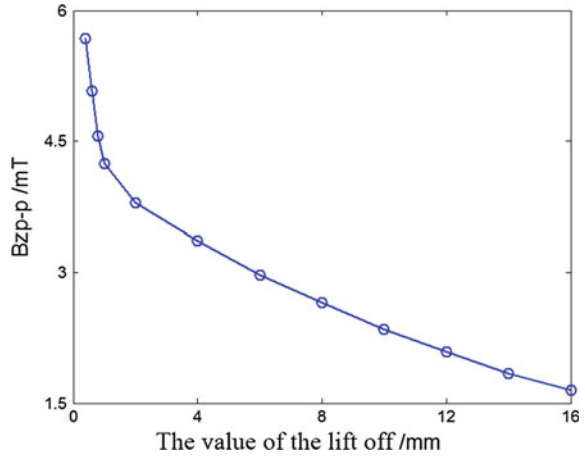


Fig. 6.9 The relationship between the value of the lift off and the peak–valley value B_{zp-p} of the magnetic flux leakage



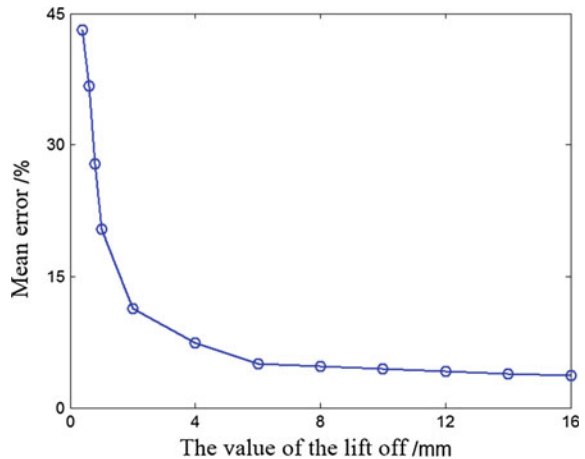
probes. Changes of lift off of the probe induce fluctuations of output signal. It can be seen as an interference signal and it will adversely affect the results of the testing, so it should be suppressed.

In order to study the lift off effect of the probe on the magnetic flux leakage testing for corrosion defects, a typical corrosion defect was simulated. Figure 6.9 shows the relationship between the value of the lift off and the peak–valley value B_{zp-p} of the magnetic flux leakage.

From Fig. 6.9, the peak–valley value of magnetic flux leakage decreases rapidly with the increase of the lift off value of the probe. Therefore, in order to improve the detection sensitivity, the value should be small. However, if the detection sensitivity of the probe meets the requirement of need, the selection of the lift off value should be to minimize the detection error.

In the case of the above model, the simulation results that the average error is caused by the probe fluctuation of 0.5 mm are shown in Fig. 6.10.

Fig. 6.10 The errors caused by the probe fluctuation of 0.5 mm



From Fig. 6.10, it can be seen that the fluctuation error caused by the increase of the lift off value decreases rapidly. Therefore, in order to reduce the negative effect caused by the fluctuation of the lift off value, we should select a larger lift off value under the permission of the detection sensitivity.

In magnetic flux leakage detection system, the testing signal of the detector consists of two parts: the magnetic leakage field caused by corrosion defects and the air-coupled magnetic field. Therefore, in the surface of the tested material with a corrosion defect, the probe measures an air-coupled magnetic field superimposed on the magnetic leakage field of the defect. Because the analysis and quantification of the defects are mainly dependent on the magnetic leakage field, the non-defect signal including the air-coupled magnetic field is equivalent to the noise. Changes in lift off will produce two effects. First, the magnetic leakage field detected by the detector decreases with the increase of the lift off value. On the other hand, the higher the lift off value of the probe is, the higher the air-coupled magnetic field is. Thus, the ratio of the magnetic flux leakage density and the air-coupled magnetic induction intensity is decreased. In addition, the magnetic flux leakage produced by small corrosion defects is weak, so the weak signal will be more difficult to identify when the lift off value increases. With the increase of the lift off value, the sensitivity of the probe to small corrosion defects can be significantly decreased.

Increasing the distance between the poles can be helpful to reduce the air-coupled magnetic field, but at the same time, the magnetic field strength of the material will be reduced. The test shows that when the internal magnetic field reaches saturation, the magnetic leakage field of the defect will not decrease distinctly under the condition of moderate increase of the magnetic pole spacing. And this can cause the reduction of air-coupled magnetic induction intensity, and the signal-to-noise ratio of the measured signal is improved. Of course, if the magnetic pole spacing is too large, it may lead to unsaturation of the magnetic induction intensity inside the material. Therefore, in the design of magnetic circuit, the distance between two magnetic poles should be increased as large as possible in ensuring that the magnetic induction strength of the material is sufficient to achieve saturation. Figure 6.11 shows the relationship between the signal-to-noise ratio R of the lift off value in the condition of different magnetic pole spacings and the same defect. The simulation parameters are the defect depth is 7.3 mm, the length and the width of defect are both 10 mm, and the magnetic pole spacing is 1000, 1100, and 1200 mm, respectively.

From Fig. 6.11, the signal-to-noise ratio of the probe increases with the increasing of magnetic pole spacing under the same lift off of the probe.

In order to improve the signal-to-noise ratio, the length of the steel brush can be shortened. The decrease of the length of the steel brush can increase the magnetic induction intensity coupled by the measured material and reduce the magnetic leakage field of the steel brush. But at the same time, it will lead to a short distance from the probe to the back iron. That means the probe has been relatively shifted to the stronger place of air direct coupling magnetic field.

Figure 6.12 shows the value of the signal-to-noise ratio R of the same defect at different lengths of steel brushes and different lift offs of probes. The simulation

Fig. 6.11 The effect of different pole spacing

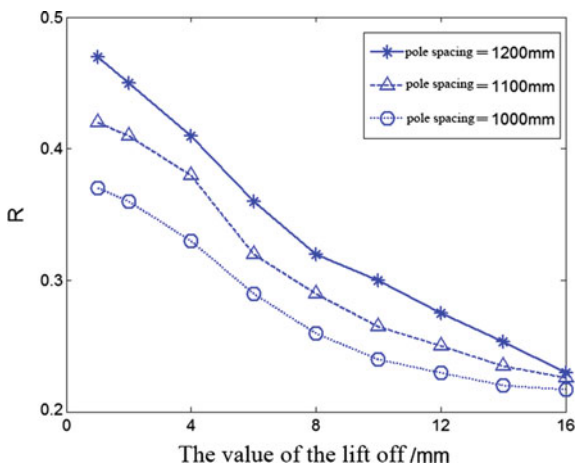
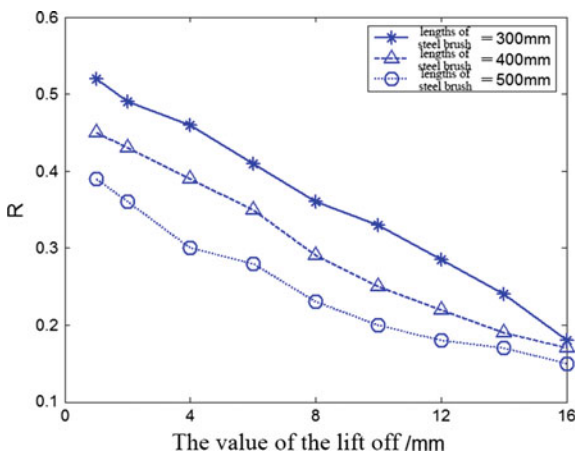


Fig. 6.12 The influence of lift off at different steel brushes



parameters are the defect depth is 7.3 mm, the length and the width of defect are both 10 mm, and the lengths of steel brushes are 300, 400, and 500 mm, respectively. In Fig. 6.12, it can be seen that the length of the steel brush can be reduced in a certain range, so that the signal-to-noise ratio can be increased.

6.4 Defect Quantification Method of Magnetic Flux Leakage Testing

The analysis and identification of the magnetic leakage signal after compensation is the key to the quantitative analysis method of the defect leakage magnetic testing. Defect appearance inversion from the magnetic flux leakage signal, including the

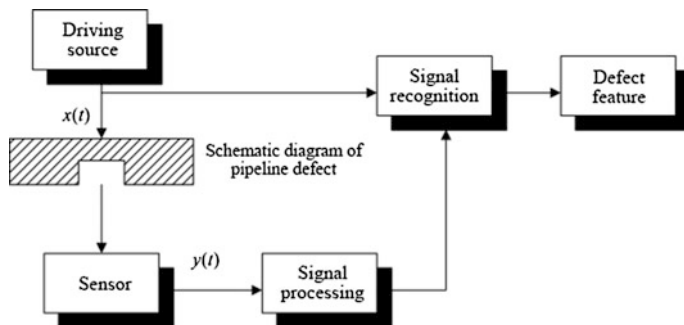


Fig. 6.13 Defect quantification process

distinction of defect types, the characteristics analysis, and the shape parameters of the defect quantitative analysis, can be attributed to a typical inverse problem of electromagnetic field, and the process is shown in Fig. 6.13.

6.4.1 Defect Quantification Method Based on Statistical Identification

Statistical recognition is a typical pattern-matching method, which is based on the standard signal library to establish the mapping relationship between the shape parameters and the characteristics of the magnetic flux leakage signal. According to the characteristics of the actual magnetic leakage testing signals, the size parameter of the defect is determined. At present, the statistical identification has been widely used in the quantitative analysis of the corrosion defect. Therefore, the statistical pattern recognition method based on principal component analysis, multivariate nonlinear regression, and subsection nonlinear discriminant analysis is conducted to identify the defect parameters based on the characteristics of multiple magnetic flux leakage signals.

Before the statistical identification of the defect magnetic leakage signals, it is necessary to preprocess the magnetic flux leakage signal, which includes the recognition of foreign body signals and the smooth interpolation of the waveforms. Common foreign bodies include welding, casing pipe, flange, three pass, and all kinds of valves. By analyzing the waveform characteristics of the signal, we can effectively distinguish these foreign bodies from the corrosion defects.

The casing pipe, the welding, and the flange are distributed in the entire circumference of the pipe and their magnetic leakage signals are more obvious. Their magnetic leakage signal waveforms are also distributed throughout the entire circumference; that is, it can be detected in the circumferential direction of the pipe. The axial span of the detection signal waveform of the welding and flange is smaller than that of the casing pipe. The waveform is relatively steep and the distribution

range is small. Three pass and the valve are fixed in the pipe's circumferential part, so only part of the probes can detect the corresponding magnetic leakage signal.

Because of the low sampling frequency of the defect magnetic leakage signal, the waveform obtained from the measurement of the defect leakage field can be a straight line connecting with the actual testing data. The result will be a broken line. There is a large difference between the actual signal and the testing waveform. It is likely to give a large error to the feature extraction of signal waveform. If the sampling frequency is increased, it will lead to the hardware design and software programming of detection system complex. Interpolation smoothing technique can be used to obtain smooth curve and waveform, thus provide effective means to signal sampling waveform replication of time domain. There are many interpolation methods, such as polynomial interpolation, Newton interpolation, piecewise linear interpolation, and spline interpolation. This book is based on the excellent properties of the three-spline function and the three-spline interpolation method is adopted.

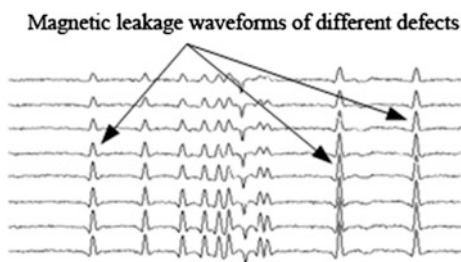
The three-spline interpolation method is to use the three-spline function to connect adjacent points to obtain the three-spline interpolation curve. Because the three-spline function has a high degree of smoothness (two-order) and approximation order (four-order), the resulting curve is very smooth.

The key to the qualitative and quantitative analyses of the magnetic flux leakage signal is the extraction of the signal characteristic quantity or the vector. The corrosion defect signal is an abnormal signal in the local space or time axis, as shown in Fig. 6.14.

For ease of analysis, the characteristics of the magnetic flux signal waveform are defined as follows:

- (1) Peak and valley values of signal waveforms Y_{p-p} . Many kinds of factors affect the magnitude of the magnetic leakage signal, so peak and valley values Y_{p-p} are used as the feature, which can eliminate the influence of the DC component of the magnetic leakage signal and improve the reliability of the detection, as shown in Fig. 6.15. In order to calculate Y_{p-p} , the maximum and minimum value of the defect signal should be found, and the absolute value of the difference between the adjacent pairs of extreme value can be obtained.
- (2) The signal's axial length L_X . The detector is sampled along the pipeline, and the threshold of detection signal is L_X , which can effectively reflect the axial

Fig. 6.14 Magnetic leakage waveforms of different defects



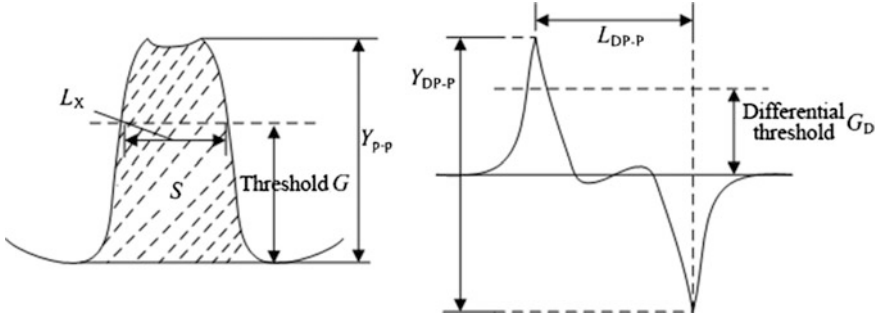


Fig. 6.15 The main characteristics of the axial component waveform of the defect magnetic leakage field

distribution of the defect. Combined with the peak and valley values, the shape of the defect can be roughly determined, which helps to quantitatively detect the defect length and the depth of the defect. For the signal interception threshold G , a fixed value can be set, or the threshold is set dynamically according to the signal characteristics.

- (3) The area of the signal waveform S . The area of the waveform is the area of the curve of a wave. The magnetic flux leakage signal of a single defect is composed of a peak and a valley, which is reflected by the short first-order central moment of the signal:

$$S = \sum_n^N \{x(t) - \min[x(t)]\} \tag{6.4}$$

- (4) The energy of the signal waveform E . The wave energy is equivalent to the two-order central moment of the signal, which reflects the discrete degree of the energy or signal of the magnetic signal fluctuations in a certain space. Using a formula for:

$$E = \sum_n^N \{x(t) - \min[x(t)]\}^2 \tag{6.5}$$

- (5) The peak and valley length of differential signal L_{DP-P} . After differential, the high-frequency part of the magnetic signal can be enhanced, and the variation rate of the magnetic leakage field is reflected by L_{DP-P} , the mechanism and finite element analysis. By the mechanism and finite element analysis results of the magnetic leakage field, we can see that the magnetic leakage field changes seriously at the length boundary of the defect, which can be used to measure the length of the defect.
- (6) The peak and valley value of the first-order differential signal Y_{DP-P} . The feature reflects the change of the highest point and the lowest point of the

magnetic leakage field. Since it reflects the depth of the defect, it can be used as an indicator of the depth of the defect.

- (7) The magnetic leakage field distribution of the defect has a space vector characteristic. Although the detection system is magnetized along the axial direction of the pipeline, the circumferential waveform of the magnetic field is composed of a plurality of signals. The width of the defect can be analyzed by the circumferential characteristic of the signal waveform. In addition, the evaluation of the width should be based on the number of probes that are covered by the circumferential magnetic leakage field distribution. So it is required to effectively intercept the magnetic leakage field size, in order to determine the number of the covered probes. After determining the maximum amplitude of the detected signal, the threshold value G_W is set to determine the number W_Z of covered probes. The signal length is L_Z with the threshold G_W . At the same time, the differential value of the circumferential signal and the corresponding threshold value G_{DW} of the probe can determine the number of probes covered by the differential signal. As a characteristic value of the width, it is denoted as W_{DZ} .

After defining the above characteristics, we can make use of the standard defect library, in which one dimension (length, width, and depth) of the defects change and other dimensions do not change. To screen out the characteristics of the magnetic leakage field signal which is most closely related to the defect size, and then carry out statistical identification.

The width and depth of the defect are related to several characteristics of magnetic flux leakage signals, and there is a nonlinear relationship between these characteristics, which constitutes a typical multivariate statistical analysis problem. To solve the problem, we can use multiple nonlinear regression method, principal component analysis method, linear pattern classifier, nonlinear discriminant function, and so on.

Using multiple nonlinear regression method to quantify the defect of magnetic flux leakage detection, it can be obtained from the following two aspects:

- (1) By variable substitution, the nonlinear relationship is transformed into a linear relationship. The scatter plot based on the theory, experience, and experimental data is used to decide the function type, and then the function is transformed into linear regression problem to be solved.
- (2) If the functional type of the actual problem is not easy to judge, a polynomial can be used to approximate it.

Assuming that there is a nonlinear relationship between the variable y (length, width, or depth of the defect) and x_1, x_2, \dots, x_p (the characteristics, which can determine the size of the defect, of the magnetic leakage field signal). Test sample size is n . The shape parameter datum obtained by the i th test is y_i . The corresponding variables are $x_{i1}, x_{i2}, \dots, x_{ip}$, and there is a nonlinear relationship between the y_i and the following polynomials:

$$x_{i1} + x_{i1}^2 + \cdots + x_{i1}^m, x_{i2} + x_{i2}^2 + \cdots + x_{i2}^n, \dots, x_{ip} + x_{ip}^2 + \cdots + x_{ip}^l \quad (6.6)$$

y_i can be expressed as:

$$y_i = \beta_0 + \beta_1 x_{i1} + \beta_2 x_{i2} + \cdots + \beta_p x_{ip} + \beta_{21} x_{i1}^2 + \beta_{22} x_{i2}^2 + \cdots + \beta_{2p} x_{ip}^2 \\ + \cdots + \beta_{m1} x_{i1}^m + \beta_{n2} x_{i2}^n + \cdots + \beta_{lp} x_{ip}^l \quad (6.7)$$

Substitution of the high order, let $x_{i1} = z_{i1}, x_{i2} = z_{i2}, \dots, x_{i1}^2 = z_{ip+1}, x_{i2}^2 = z_{ip+2}$. Multivariate polynomial regression can be used to solve the problem of multiple linear regression. The transformation form is given as:

$$y = a_0 + a_1 z_{i1} + a_2 z_{i2} + a_q z_{iq} + \varepsilon_i, \quad i = 1, 2, 3, n \quad (6.8)$$

In (6.8), $a_0, a_1, a_2, \dots, a_q$ are $q + 1$ parameters to be estimated, ε_i are random variables which are independent of each other and obey the same normal distribution. z_1, z_2, \dots, z_q are the value of the q independent transformed variables.

The next question is to find the parameter $a_0, a_1, a_2, \dots, a_q$ values of the variable z . Then reverse substitute to $\beta_0, \beta_1, \beta_2, \dots, \beta_{2p}, \dots, \beta_{m1}, \dots, \beta_{lp}$, so as to obtain the original form of the polynomial.

The least square estimation is used to calculate the value of the parameter a_i .

From the test sample data, the estimated values of $a_0, a_1, a_2, \dots, a_q$ can be obtained, and the estimated equation of the regression equation is derived.

$$\hat{y} = b_0 + b_1 z_{i1} + b_2 z_{i2} + \cdots + b_q z_{iq} \quad (6.9)$$

According to the principle of least square method, $b_0, b_1, b_2, \dots, b_q$ should make the sum of the deviation squares of all the observed values y_i and the regression values \hat{y}_i the minimum. That is to let the Q in (6.10) the minimum.

$$Q = \sum_{i=1}^n (y_i - \hat{y}_i)^2 = \sum [y_i - (b_0 + b_1 z_{i1} + b_2 z_{i2} + \cdots + b_q z_{iq})]^2 \quad (6.10)$$

Known sample data, Q is a non-negative quadric expression about $b_0, b_1, b_2, \dots, b_q$. So its minimum value must exist. According to the extremum principle, $b_0, b_1, b_2, \dots, b_q$ should be the solution of the following equation:

$$\begin{cases} \frac{\partial Q}{\partial b_0} = -2 \sum_{i=1}^n (y_i - \hat{y}_i) = 0 \\ \frac{\partial Q}{\partial b_j} = -2 \sum_{i=1}^n (y_i - \hat{y}_i) z_{ij} = 0 \end{cases} \quad (j = 1, 2, \dots, q) \quad (6.11)$$

6.4.2 Defect Quantification Method Based on Radial Basis Function Neural Network (RBFNN)

Although the statistical identification method of defects quantitative identification has better performance in practice, it is necessary to realize that the statistical method does not have the ability of adaptive processing, such as not having the ability to self-organizing, self-learning, and the ability to identify noises. And this method requires a large amount of test or simulation data. The statistical process is more complex. There is dependence on the sample.

In order to further improve the accuracy of detection, many scholars are committed to the introduction of a variety of new technologies to the quantitative analysis of defects. The neural network method is successfully applied to the processing of magnetic flux leakage signal and the reconstruction of magnetic field. However, the method of quantitative analysis of neural network, on the one hand, has the disadvantage of low computation speed and low recognition accuracy. On the other hand, it focuses on the inductive analysis of the existing detection results, so the adaptive ability of any defect is still insufficient.

Therefore, an iterative method based on radial basis function neural network is used to solve the problem of adaptive ability. Compared with ordinary neural network method, this method can improve the adaptability of different types of defects by using closed-loop structure. At the same time, it has the advantages of fast convergence speed, good anti-noise performance, and so on.

The process of solving the inverse problem with the iterative method is shown in Fig. 6.16. The essence of this method is to solve the inverse problem in the way of solving the positive problem. The positive problem can be solved by analytical and numerical methods.

Although the calculation process of the analytical method is simple and the calculation efficiency is high, but the complexity of the defects, the arbitrary, and the electromagnetic characteristics of the pipe wall material determine that the numerical method is more effective and accurate. At present, the common numerical method is the finite element method. However, the computational efficiency of the finite element method is not high, especially in the calculation of small defects. So the workload of the iterative calculation based on the finite element

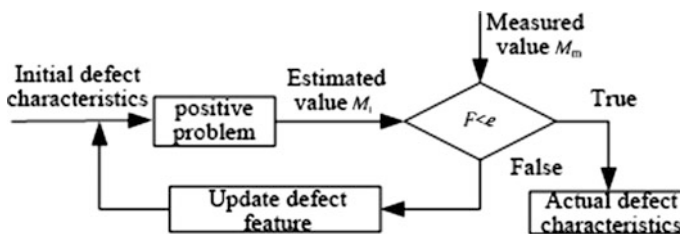


Fig. 6.16 Iterative method for solving inverse problem

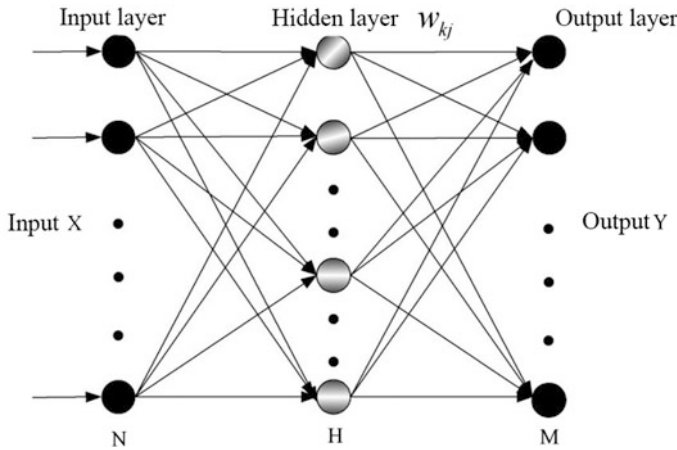


Fig. 6.17 The structure of radial basis function neural network

method is very large, especially in the use of the three-dimensional model, which limits its application in practice.

In order to overcome this difficulty, a radial basis function neural network (RBFNN) is used as the solution to the problem. The method combines the advantages of neural network and the iterative method, which can, on the one hand, improve the accuracy and adaptability by using the closed-loop iteration. On the other hand, it can improve the computational efficiency by using neural network.

As shown in Fig. 6.17, RBFNN is usually composed of three layers: input layer, hidden layer, and output layer. There is no connection among the nerve cells of each layer, and the information is transmitted between layers.

In Fig. 6.17, $X = (x_1, x_2, \dots, x_n)^T$ is the input vector, and $Y = (y_1, y_2, \dots, y_n)^T$ is the output vector. The input to output nonlinear mapping functions are usually the Gauss function, Multiquadric function, Duchon thin plate spline function, etc. Here, the most commonly used Gauss function is chosen as the radial basis function. At this time, RBFNN's input/output relationship is expressed as:

$$Y_l = F(X) = \sum_{j=1}^H w_{lj} \exp\left(-\frac{\|X - c_j\|^2}{2\sigma_j^2}\right), \quad l = 1, 2, \dots, M \quad (6.12)$$

where X is the input, $Y = (y_1, y_2, \dots, y_n)^T$ is the output, H is the number of basis function used, $\|\cdot\|$ means Euclid norm, c_j represents the center of the hidden layer of the j basis function unit, σ_j is the radius of the basis function, w_{lj} is the connection weights between the j basis functions and the output point l .

RBFNN training process can be seen as a set of given input and output data, in the multidimensional space to find a curve fitting or function approximation problem. The objective is to find the best fitting of the functional mapping

relationship between the input and output data in the statistical view. This process can be divided into three stages: First, a set of radial basis functions is defined, and the data of the input network are converted into the hidden layer. Secondly, the linear transformation between the hidden layer and the output layer is conducted. Finally, the unknown data are performed interpolation process through the network to obtain the corresponding solution.

Given data are $X = (x_1, x_2, \dots, x_n)^T$, and its corresponding output is $Y = (y_1, y_2, \dots, y_n)^T$. The objective is to obtain a function $f : X \rightarrow Y$, which satisfies the interpolation condition.

$$f(x_i) = y_i, \quad i = 1, 2, \dots, N \quad (6.13)$$

$f(\cdot)$ applies to all training data for RBFNN. Using the radial basis function method, $f(\cdot)$ can be expressed as:

$$f(x_i) = \sum_{j=1}^N w_j \phi_j(\|\bar{x} - c_j\|) \quad (6.14)$$

In the formula, $\{\phi_j(x)\}$, $j = 1, 2, \dots, N$ is a set of radial basis functions, $\{c_j\}$ is the centers of radial basis functions, and $\{w_j\}$ constitutes a group of weights.

The formula (6.14) is expressed by matrix as follows:

$$\begin{bmatrix} \phi_{11} & \phi_{12} & \cdots & \phi_{1N} \\ \phi_{21} & \phi_{22} & \cdots & \phi_{2N} \\ \vdots & \vdots & \ddots & \vdots \\ \phi_{N1} & \phi_{N2} & \cdots & \phi_{NN} \end{bmatrix} \begin{bmatrix} w_1 \\ w_2 \\ \vdots \\ w_N \end{bmatrix} = \begin{bmatrix} y_1 \\ y_2 \\ \vdots \\ y_N \end{bmatrix} \quad (6.15)$$

Among (6.15),

$$\phi_{ij} = \phi(\|x_i - c_j\|), \quad i = 1, 2, \dots, N, \quad j = 1, 2, \dots, N \quad (6.16)$$

So the formula (6.16) is equivalent to

$$\Phi W = Y \quad (6.17)$$

If the matrix Φ is non-singular, the inverse matrix Φ^{-1} exists.

$$W = \Phi^{-1} Y \quad (6.18)$$

The number of radial basis functions is limited by the number of training samples. If the number of training samples is too much, which is more than the

degree of freedom of the physical process. It will lead to deviation and appear over fitting, which lowers the performance of the neural network.

Using some previous information to reflect the mapping relationship between the input and output, adjusting the sample space, the ill-conditioned sample space is converted into a benign sample space, which can solve the problem of RBFNN over fitting. By adding the smoothness constraint, some prior information is embedded into the auxiliary non-negative functional, and the only and stable solution is obtained by limiting the scope of the solution.

The establishment of RBFNN is mainly divided into the following two steps:

Step 1: The choice of basis functions. Usually choosing basis functions based on experience or clustering algorithm. In this book, we use the K order algorithm. Its principle is to minimize the clustering performance, i.e., let the sum of the squares of the distance between the sample points to the center of the class minimum.

The steps of the K order mean algorithm here are given as:

- (1) Randomly select K data as clustering centers
- (2) According to the similarity distance formula, each of the data in the dataset is assigned to its nearest cluster
- (3) Calculate the new clustering center
- (4) If the clustering center does not change, the algorithm ends. Otherwise, jump to step (2).

After clustering the sample, we can calculate the radius σ_j of the basis function.

$$\sigma_j = \frac{1}{N_j} (X^P - c_j)^T (X^P - c_j) \quad (6.19)$$

Among them, N_j is the number of samples in the cluster, and X^P is the training sample.

Step 2: Training, i.e., determine the connection weights of the hidden layer to the output layer. The book will have an adaptive mechanism for the gradient descent method applied to the RBFNN parameter adjustment. The error function is defined as:

$$J(k) = \frac{1}{2} (Y(k) - y(W, k))^2 \quad (6.20)$$

where $J(k)$ is the error function, $Y(k)$ is the expected output, and $Y(W, k)$ represents the actual output of the network.

Therefore, an adaptive adjustment algorithm for the weighted matrix of the hidden layer to output layer is obtained:

$$W(k+1) = W(k) + \mu(k) \left(-\frac{\partial J(W)}{\partial W} \right) \Big|_{W=W(k)} + \alpha(k) (W(k) - W(k-1)) \quad (6.21)$$

The adjustment algorithm for the matrix of the hidden layer centers is:

$$C(k+1) = C(k) + \mu(k) \left(-\frac{\partial J(C)}{\partial C} \right) \Big|_{C=C(k)} + \alpha(k)(C(k) - C(k-1)) \quad (6.22)$$

The adjustment algorithm for the hidden layer radius matrix is given as:

$$\sigma(k+1) = \sigma(k) + \mu(k) \left(-\frac{\partial J(\sigma)}{\partial \sigma} \right) \Big|_{\sigma=\sigma(k)} + \alpha(k)(\sigma(k) - \sigma(k-1)) \quad (6.23)$$

Among them, $\mu(k)$ is the learning rate, $a(k)$ is the momentum term, which uses the results of previous adjustment to influence the amount of adjustment, thus speeding up the process of correction. When the previous adjustment was overshooted, the momentum term will be opposite to the error of the adjustment. The actual adjustment amount will be reduced and the oscillation will be avoided. While the previous adjustment amount is owed, the actual adjustment amount will increase. The role of $a(k)$ is to make the network changes tend to be stable, in order to facilitate the convergence of the network as soon as possible.

Calculation method for learning rate $\mu(k)$ is:

$$\text{When } \Delta J < 0, \mu(k) = \phi \mu(k-1), \quad \phi > 1 \quad (6.24)$$

$$\text{When } \Delta J > 0, \mu(k) = \beta \mu(k-1), \quad \beta < 1 \quad (6.25)$$

where ϕ and β are constants, $\Delta J = J(k) - J(k-1)$.

In the BP network, if the learning rate is too small, the network parameters will change slowly, and the convergence is also slow. If it is too large, it can accelerate the learning speed; however, it may lead to the continuous oscillation near the point of stability. So the learning rate is usually chosen a fixed value based on experience. When the change of total error is reduced ($\Delta J < 0$), the training error curve is flat. Then the learning rate should be multiplied by a constant, which is more than 1. So the step size increases, the number of iterations reduces, and falling into local minimum point is avoided. When the change of total error is increased ($\Delta J > 0$), which means that the training of the error curve changes sharply in the region, the learning rate should be multiplied by a number of less than 1. It is conducive to shorten the step size, so that the error decreases.

After the establishment of the RBFNN, the sample data are trained, which makes the error of the network forecast is lower than the predetermined threshold.

Combined with the training of the RBFNN, and then according to the iterative method shown in Fig. 6.16, we can get the algorithm flow of quantitative analysis of defects:

Randomly set a defect feature, which is called $x(0)$;

During the k th cycle, the input $x(k)$ is trained by the RBFNN, to get a prediction of the magnetic leakage field signal $y(k) = F(x(k))$;

Calculating the sum of error square:

$$E(k) = \frac{1}{2} \|d - y(k)\|^2 \quad (6.26)$$

Calculating the gradient value of $E(k)$ to $x(k)$, that is $\frac{\partial E(k)}{\partial x(k)}$;

Update x

$$x(k+1) = x(k) + \eta \left(-\frac{\partial E(k)}{\partial x(k)} \right) \quad (6.27)$$

where η is the learning rate of the iterative process.

If $E(k) \geq e$, go to the second step;

Until $E(k) < e$, exit from cycle.

Among them, the defect is characterized as x_i , the corresponding neural network calculation result is y_i , the expected output is d_i , and the sum of the error square is given as follows:

$$E = \frac{1}{2} \sum_{l=1}^M (d_l - y_l)^2 \quad (6.28)$$

There is:

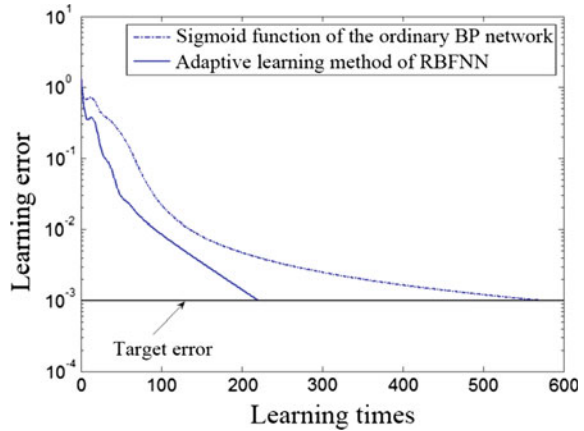
$$y_i = F(x_i) = \sum_{j=1}^H w_{ij} \exp \left(-\frac{\|x_i - c_j\|^2}{2\sigma_j^2} \right) \quad (6.29)$$

So, the gradient of E to x_i is given as:

$$\frac{\partial E(x)}{\partial x_i} = -\sum_{l=1}^M \left[(d_l - y_l) \left(-\frac{1}{\sigma_j^2} \sum_{j=1}^H w_{ij} (x_i - c_{ji}) \times \exp \left(-\frac{\|x - c_j\|^2}{2\sigma_j^2} \right) \right) \right], \quad i = 1, 2, \dots, N \quad (6.30)$$

Take the quantitative analysis of the circumferential width of the defect to verify the validity of the proposed method. In a three-dimensional finite element model of pipeline inspection, the depth of 30, 50, 80 % pipe wall thickness, the width of 1, 1.5, 2, 3, 3.5, 4, 4.5, 5, 5.5 times of the wall thickness, and the length of 1, 2, 3, 4, 5 times of the wall thickness of a total of 150 defects were calculated. Take 120 defect characteristics and simulation results data as a training sample to the RBFNN, the remaining 30 defect data were as a test set; that is, there is no duplication between the training samples and the test set. Other parameters required are: the diameter of the pipe is 1016 mm, the wall thickness of the pipe is 14.6 mm, and the lift off of the probe is 4 mm. And the defect width W is closely related to the circumferential width L_Z and the wave peak and valley value of the defect leakage field circumferential waveform Y_{ZP-P} . As a result, the W is used as the input of the

Fig. 6.18 Convergence of learning error of two neural networks



RBFNN, and the L_Z and Y_{ZP-P} are used as the output of the network to train the RBFNN. In Fig. 6.18, the change of the learning error of the BP based on the Sigmoid function and RBFNN is compared, and the target error is 0.001.

In Fig. 6.18, we can know that adaptive learning method of RBFNN achieves the target error after the 221st training and Sigmoid function of the ordinary BP network need to go through 572nd training to achieve the target error. The latter is significantly slower than the former.

6.4.3 Defect Quantification Method Based on Three-Dimensional Finite Element Neural Network

The iterative method based on radial basis function neural network used closed-loop structure to reduce the dependence of the statistical sample. However, it is still required to use uniform and standardized defect samples in the training process, so the dependence is not eliminated.

To solve this problem, a new iterative method based on 3D finite element method is proposed, which is embedding the finite element computation into the neural network structure, and the neural network is used as the normal problem-solving model in the iterative method.

6.4.3.1 Discretization Principle of Finite Element Method

The typical boundary value problem can be defined using the differential equation of the available area Ω and the boundary conditions of the surrounding area. The differential equations can be expressed as follows:

$$L\vec{\phi} = \vec{f} \quad (6.31)$$

where L represents a differential operator, \vec{f} represents an incentive or an imposed function, and $\vec{\phi}$ is the variable to be found.

Although the above boundary value problem can be solved by analytical method, only a few cases can be resolved. In order to overcome this difficulty, we can use the numerical method to solve the boundary value problem, and the most common method is the finite element method. The finite element method is a variational method, which means that the boundary value problem is represented by a variational expression (i.e., a functional). The minimum value of the function is corresponding to the control differential equation under the given boundary conditions. The approximate solution can be obtained by solving the minimum value of the function. Functional expressions correspond to the formula (6.31):

$$F(\tilde{\phi}) = \frac{1}{2} \langle L\tilde{\phi}, \tilde{\phi} \rangle - \frac{1}{2} \langle \tilde{\phi}, f \rangle - \frac{1}{2} \langle f, \tilde{\phi} \rangle \quad (6.32)$$

where $\tilde{\phi}$ represents the testing function. The solution of differential equation is obtained by solving the minimum value of the function to $\tilde{\phi}$. It is a very important step in finite element analysis to find out the testing function which can express or approximate the real solution in the whole solution domain. However, for many problems, this step is very difficult, especially for two- and three-dimensional problems. To overcome this difficulty, the entire region can be divided into several small subdomains (units), and the testing functions are defined in each subdomain. In the case of unit e , the following expressions $\tilde{\phi}^e$ can be obtained:

$$\tilde{\phi}^e = \sum_{j=1}^n N_j^e \phi_j^e = \{N^e\}^T \{\phi^e\} = \{\phi^e\}^T \{N^e\} \quad (6.33)$$

where $\tilde{\phi}^e$ represents the pending variables in the unit e , n represents the number of nodes in the unit e , $\tilde{\phi}_j^e$ represents value ϕ of node j in the unit, N_j^e is a basis function (also known as interpolation function or expansion function) that is associated with the node j in the unit e . The important feature of N_j^e is that it is not zero in the unit e , and it is zero outside the unit. Thus, the formula (6.32) can be expressed as follows:

$$F(\tilde{\phi}) = \sum_{e=1}^M F^e(\tilde{\phi}^e) \quad (6.34)$$

where $F^e(\tilde{\phi}^e)$ represents the functional value in unit e , M is the number of all the units in the solving region. According to formula (6.32), we can get:

$$F^e(\tilde{\phi}^e) = \frac{1}{2} \int_{\Omega^e} \tilde{\phi}^e L \tilde{\phi}^e d\Omega - \int_{\Omega^e} f \tilde{\phi}^e d\Omega \quad (6.35)$$

Substituting (6.33) into (6.35), we can get:

$$F^e(\tilde{\phi}^e) = \frac{1}{2} \{\phi^e\}^T \int_{\Omega^e} \{N^e\} L \{N^e\}^T d\Omega \{\phi^e\} - \{\phi^e\}^T \int_{\Omega^e} f \{N^e\} d\Omega \quad (6.36)$$

where $\{\dots\}^T$ represents the transpose matrix.

(6.36) can be written in matrix as:

$$F^e(\tilde{\phi}^e) = \frac{1}{2} \{\phi^e\}^T [K^e] \{\phi^e\} - \{\phi^e\}^T \{b^e\} \quad (6.37)$$

where $[K^e]$ is a $n \times n$ matrix, $\{b^e\}$ is a $n \times 1$ column vector. Their elements are:

$$\begin{aligned} K_{ij}^e &= \int_{\Omega^e} N_i^e L N_j^e d\Omega \\ b_i^e &= \int_{\Omega^e} f N_i^e d\Omega \end{aligned} \quad (6.38)$$

Since L is self adjoint, the element matrix $[K^e]$ is symmetric. Substituting (6.38) into (6.34), we can get:

$$F(\tilde{\phi}) = \sum_{e=1}^M \left(\frac{1}{2} \{\phi^e\}^T [K^e] \{\phi^e\} - \{\phi^e\}^T \{b^e\} \right) \quad (6.39)$$

By summing and computing, and then the use of the global encoding, (6.39) can be written as:

$$F = \frac{1}{2} \{\phi\}^T [K] \{\phi\} - \{\phi\}^T \{b\} \quad (6.40)$$

where $[K]$ is a $N \times N$ symmetric matrix, N is the number of unknown variables or nodes, $\{\phi\}$ is $N \times 1$ unknown vector whose elements are the expansion coefficients of unknown variables, $\{b\}$ is $N \times 1$ known vector. Let the partial derivative of F to ϕ_i is zero, get:

$$\frac{\partial F}{\partial \phi_i} = \frac{1}{2} \sum_{j=1}^N (K_{ij} + K_{ji}) \phi_j - b_i = 0 \quad i = 1, 2, 3, \dots, N \quad (6.41)$$

Because $[K]$ is symmetrical, the formula is changed to:

$$\frac{\partial F}{\partial \phi_i} = \sum_{j=1}^N K_{ij} \phi_j - b_i = 0 \quad i = 1, 2, 3, \dots, N \quad (6.42)$$

Or written in matrix form as:

$$[K]\{\phi\} = \{b\} \quad (6.43)$$

The boundary conditions for the problem are usually of two forms: One is the Dirichlet boundary conditions, i.e., given boundary value ϕ and the other is homogeneous Norman boundary condition, also called natural boundary condition; that is, the normal derivative of the boundary is zero. The first boundary conditions are necessary and must be imposed in the calculation. Second kinds of boundary conditions are usually met in the process of solving. In the finite element calculation, the boundary conditions can be satisfied by deleting rows and columns corresponding to the boundary nodes in the K matrix and the b vector.

6.4.3.2 Finite Element Neural Network

The discretization of the finite element method shows that the $[K]$ matrix and the $\{b\}$ vector are the keys to the solution, while the $[K]$ matrix can be decomposed into the neural network. This indicates the direction of establishing the finite element neural network.

Take a simple two-dimensional problem as an example:

$$-\nabla \cdot (\alpha \nabla \phi) + \beta \phi = f \quad (6.44)$$

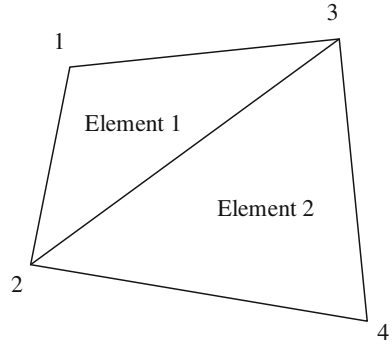
Its boundary condition is: on the boundary Γ_1 , $\phi = p$; on the boundary Γ_2 , $\alpha \nabla \phi \cdot \hat{n} + r \phi = q$. Where α, β are the coefficients related to the material properties. f is an external source. \hat{n} is the external normal vector. r, q, p are parameters related to the boundary.

Assuming that the solution region is divided into two units, a total of four nodes, as shown in Fig. 6.19, then the element matrix K^e and b^e can be expressed as:

$$\begin{aligned} K_{ij}^e &= \int_{\Omega^e} (\alpha \nabla N_i^e \cdot \nabla N_j^e + \beta N_i^e N_j^e) d\Omega \\ b_i^e &= \int_{\Omega^e} f N_i^e d\Omega \end{aligned} \quad (6.45)$$

The global matrix can be obtained by merging the two element matrices. So we need a set of integers for the unit encoding. Also, in order to identify the nodes at

Fig. 6.19 Grid partition for the solution area



the vertex of the unit, the other group of integers is required to give the node encoding. Because each element is associated with several nodes, a node, in addition to its position in the model, is also in the position of the corresponding element. This position can be used as integer encoding or part encoding. Global encoding shows the location of the node in the entire model.

In order to link these three kinds of encoding, an integer array or an array of contacts can be introduced. It is expressed as $n(i, e)$, where $i = 1, 2, 3$, $e = 1, 2, 3, \dots, M$. M represents the number of units. In an array of contacts, i means the local encoding of the node, e is the unit encoding, and $n(i, e)$ is the global encoding of the node. In this way, the array contains all the information about the unit and the node encoding.

As shown in Fig. 6.19, the array $n(i, e)$ can be set up in the solution area as shown in Table 6.1.

Using the connection information in Table 6.1, we can combine the unit matrix to establish the global matrix K . Taking node 2 as an example, because the node 2 is the second node of unit 1 and the third node of unit 2, respectively, the elements K_{22}^1 and K_{33}^2 in the unit matrix can be merged to obtain $K_{22} = K_{22}^1 + K_{33}^2$. For all four nodes to perform this operation, we can get:

$$K = \begin{pmatrix} K_{11}^1 & K_{12}^1 & K_{13}^1 & 0 \\ K_{21}^1 & K_{22}^1 + K_{33}^2 & K_{23}^1 + K_{32}^2 & K_{31}^2 \\ K_{31}^1 & K_{32}^1 + K_{23}^2 & K_{33}^1 + K_{22}^2 & K_{21}^2 \\ 0 & K_{13}^2 & K_{12}^2 & K_{11}^2 \end{pmatrix} \quad (6.46)$$

Table 6.1 Local and global encoding in the unit nodes

e	$n(1, e)$	$n(2, e)$	$n(3, e)$
1	1	2	3
2	4	3	2

The vector b can be obtained by the combination of the elements:

$$b = \begin{pmatrix} b_1^1 \\ b_2^1 + b_3^2 \\ b_3^1 + b_2^2 \\ b_1^2 \end{pmatrix} \tag{6.47}$$

In order to transform the finite element model into neural networks, it is necessary to decompose K_{ij}^e into two components: one component depends on the material properties α, β , the other is independent of the material. According to this idea, (6.45) can be transformed into:

$$K_{ij}^e = \int_{\Omega^e} (\alpha \nabla N_i^e \cdot \nabla N_j^e + \beta N_i^e N_j^e) d\Omega = \alpha S_{ij}^e + \beta T_{ij}^e \tag{6.48}$$

there into

$$S_{ij}^e = \int_{\Omega^e} \nabla N_i^e \cdot \nabla N_j^e d\Omega$$

$$T_{ij}^e = \int_{\Omega^e} N_i^e N_j^e d\Omega \tag{6.49}$$

On this basis, the finite element model can be transformed into a neural network, that is, the finite element neural network (FENN). Its structure is shown in Fig. 6.20.

By Fig. 6.20, the finite element neural network contains three layers: input layer, output layer, and hidden layer. The input layer consists of two sets of neurons.

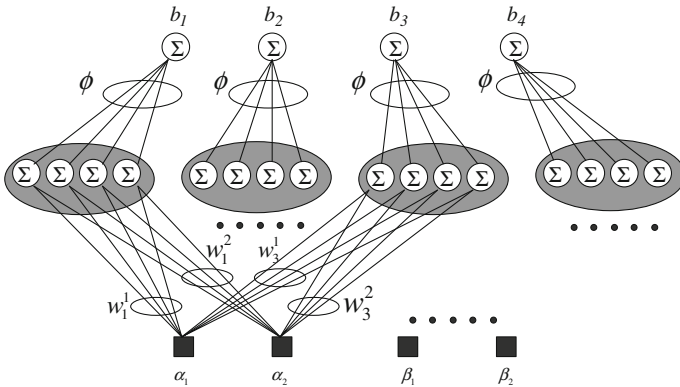


Fig. 6.20 The structure of the finite element neural network

One group of each unit uses α as the input, and the other group uses β as input. The hidden layer contains 16 neurons, and four of them constitute a group. Each neuron in the hidden layer acts as a collection point, and the output is the element K_{ij} of the global matrix K . Its expression is given as:

$$K_{ij} = \sum_{e=1}^2 (\alpha_e w_{ij}^e + \beta_e g_{ij}^e) \quad (6.50)$$

The output of the hidden layer neurons in each group is a row vector corresponding to a node in the K matrix. The weights between the input layer and the hidden layer are set as the corresponding values of S and T , and the relationship between w_{ij}^e , g_{ij}^e and T , S is: If i and j belong to one node, then $w_{ij}^e = S_{ij}^e$; otherwise, $w_{ij}^e = 0$. If i and j belong to one node, then $g_{ij}^e = T_{ij}^e$; otherwise, $g_{ij}^e = 0$.

Each of the hidden neurons is connected to an output neuron through a set of weights ϕ . Each element of ϕ corresponds to the node value ϕ_j . Each output neuron is also a collection point, and the output value is b_i :

$$b_i = \sum_{j=1}^4 K_{ij} \phi_j = \sum_{j=1}^4 \phi_j (\alpha_e w_{ij}^e + \beta_e g_{ij}^e) \quad (6.51)$$

By the above transformation, the finite element model of the solution can be transformed into the form of neural network. To get a solution to the unknown quantity, the boundary conditions must also be considered.

According to the variational principle of finite element method, the natural boundary conditions can be satisfied by adding an additional term $F_b(\phi)$ to the functional. It can be expressed as follows:

$$F_b(\phi) = \int_{\Gamma_2} \left(\frac{r}{2} \phi^2 - q\phi \right) d\Gamma \quad (6.52)$$

Here, the subscript b indicates the boundary. Assuming that M_s line segments are included in Γ_2 , then $F_b(\phi)$ can be expressed as a discrete form:

$$F_b(\phi) = \sum_{s=1}^{M_s} F_b^e(\phi^s) \quad (6.53)$$

where $F_b^e(\phi^s)$ represents the integral on the line s . The unknown function ϕ within each segment can be approximated as:

$$\phi^s = \sum_{j=1}^2 N_j^s \phi_j^s \quad (6.54)$$

where N is the basis function defined in the unit s , the expression is:

$$N_1^s = 1 - \xi, N_2^s = \xi \quad (6.55)$$

where ξ is the normalized distance between the node 1 and the node 2. In particular, in the node 1, $\xi = 0$. In the node 2, $\xi = 1$. Between the two nodes, it changes linearly. Then you can get:

$$\left\{ \frac{\partial F_b^s}{\partial \phi_j^s} \right\} = [K^s] \{ \phi^s \} - \{ b^s \} \quad (6.56)$$

Thereby,

$$\begin{aligned} K_{ij}^s &= \int_0^1 r N_i^s N_j^s l^s d\xi \quad i, j = 1, 2 \\ b_i^s &= \int_0^1 q N_i^s l^s d\xi \quad i = 1, 2 \\ \phi^s &= [\phi_1^s, \phi_2^s]^T \end{aligned} \quad (6.57)$$

If r and q are constant in each line segment, and they are expressed as r^s and q^s , respectively. So we can find the solution by using the analytic method:

$$\begin{aligned} K_{ij}^s &= r^s \frac{l^s}{6} (1 + \delta_{ij}) \\ b_i^s &= q^s \frac{l^s}{2} \end{aligned} \quad (6.58)$$

In order to take F_b into account the global equation, we can get:

$$\begin{aligned} \left\{ \frac{\partial F}{\partial \phi} \right\} &= \sum_{e=1}^M \left\{ \frac{\partial F^e}{\partial \phi^e} \right\} + \sum_{s=1}^{M_s} \left\{ \frac{\partial F_b^s}{\partial \phi^s} \right\} \\ &= \sum_{e=1}^M ([K^e] \{ \phi^e \} - \{ b^e \}) + \sum_{s=1}^{M_s} ([K^s] \{ \phi^s \} - \{ b^s \}) \\ &= \{ 0 \} \end{aligned} \quad (6.59)$$

The formula can be simplified to:

$$\frac{\partial F}{\partial \phi} = (K\phi - b) + (K^s \phi^s - b^s) = 0 \quad (6.60)$$

In order to expand the vector and matrix, it is clear that an array, linked to the global encoding of the line segment and the associated node, is needed. This array can be used $ns(i, s)$ ($i = 1, 2, 3, s = 1, 2, 3, \dots, M_s$) to express. It has a similar effect on the contact array $n(i, e)$ discussed earlier. Specifically, the value of $ns(i, s)$ represents the global encoding of the i node on the s line segment. Then, add every K_{ij}^s to $K_{ns(i,s), ns(j,s)}$ and add b_i^s to $b_{ns(i,s)}$. From the above derivation, we can see that $[K^s]$ and $\{b^s\}$ do not rely on the characteristics of the material, that is unrelated to α and β . This indicates that the natural boundary conditions can be used as the boundary of the hidden layer nodes and the corresponding output layer nodes of the bias input.

6.4.3.3 From One Dimension to Three Dimension

The method of constructing the finite element network and satisfying the boundary conditions is analyzed. However, the example is a two-dimensional problem. The actual quantifying problem of the magnetic flux leakage testing needs to use a three-dimensional model. Therefore, it is necessary to build up a three-dimensional finite element neural network to study the finite element neural network. For the finite element network, the key lies in the solution of w and g matrix, that is, the calculation of the weights between the input layer and the hidden layer. To obtain the elements of the two matrices, the value and the analytical expression of the interpolation function are needed. Taking one-dimensional problem as an example, the usual practice is to set the variable ϕ to make a linear change in each subdomain (that is each line), and thus getting the corresponding interpolation function

$$N_1^e(x) = \frac{x_2^e - x}{l^e}, N_2^e(x) = \frac{x - x_1^e}{l^e}, l^e = x_2^e - x_1^e \quad (6.61)$$

And the following are given as:

$$N_j^e(x_i^e) = \delta_{ij} = \begin{cases} 1, & i = j \\ 0, & i \neq j \end{cases} \quad (6.62)$$

For two-dimensional problems, the solution region is divided into n linear triangular elements, and then, the unknown function ϕ can be expressed as the form of $a + bx + cy$. The corresponding interpolation function can be obtained by solving the equations set up to the three vertices:

$$\begin{aligned} N_j^e(x, y) &= \frac{1}{2\Delta^e} (a_j^e + b_j^e x + c_j^e y), \quad j = 1, 2, 3 \\ a_1^e &= x_2^e y_3^e - y_2^e x_3^e; & b_1^e &= y_2^e - y_3^e; & c_1^e &= x_3^e - x_2^e; \\ a_2^e &= x_3^e y_1^e - y_3^e x_1^e; & b_2^e &= y_3^e - y_1^e; & c_2^e &= x_1^e - x_3^e; \\ a_3^e &= x_1^e y_2^e - y_1^e x_2^e; & b_3^e &= y_1^e - y_2^e; & c_3^e &= x_2^e - x_1^e; \end{aligned} \quad (6.63)$$

In (6.63),

$$\Delta^e = \frac{1}{2} \begin{vmatrix} 1 & x_1^e & y_1^e \\ 1 & x_2^e & y_2^e \\ 1 & x_3^e & y_3^e \end{vmatrix} = \frac{1}{2} (b_1^e c_2^e - b_2^e c_1^e) \tag{6.64}$$

So as to get the value of the interpolation function:

$$N_j^e(x_i^e, y_j^e) = \delta_{ij} = \begin{cases} 1, & i = j \\ 0, & i \neq j \end{cases} \tag{6.65}$$

where x_j^e and y_j^e ($j = 1, 2, 3$) represent the coordinates of the vertices.

For the three-dimensional problems, the solution region is divided into n linear tetrahedral elements, as shown in Fig. 6.21.

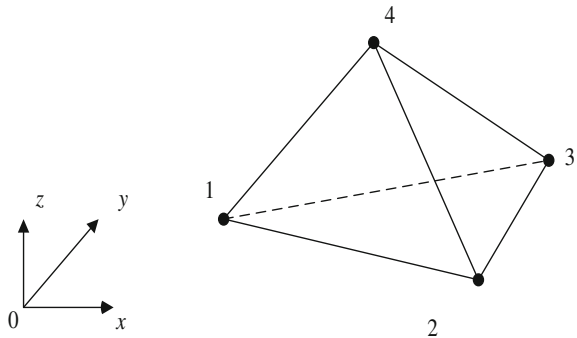
The unknown function ϕ within each region can be approximated as:

$$\phi^e(x, y, z) = a^e + b^e x + c^e y + d^e z \tag{6.66}$$

The four vertices of the unit are imposed on (6.66), and the equations are solved simultaneously. a^e, b^e, c^e, d^e can be obtained accordingly. If the value of ϕ on the j node is assigned as ϕ_j^e , we can get it:

$$\begin{aligned} \phi_1^e(x, y, z) &= a^e + b^e x_1^e + c^e y_1^e + d^e z_1^e \\ \phi_2^e(x, y, z) &= a^e + b^e x_2^e + c^e y_2^e + d^e z_2^e \\ \phi_3^e(x, y, z) &= a^e + b^e x_3^e + c^e y_3^e + d^e z_3^e \\ \phi_4^e(x, y, z) &= a^e + b^e x_4^e + c^e y_4^e + d^e z_4^e \end{aligned} \tag{6.67}$$

Fig. 6.21 The unit of linear tetrahedral element



From (6.67), we can obtain:

$$\begin{aligned}
 a^e &= \frac{1}{6V^e} \begin{vmatrix} \phi_1^e & \phi_2^e & \phi_3^e & \phi_4^e \\ x_1^e & x_2^e & x_3^e & x_4^e \\ y_1^e & y_2^e & y_3^e & y_4^e \\ z_1^e & z_2^e & z_3^e & z_4^e \end{vmatrix} = \frac{1}{6V^e} (a_1^e \phi_1^e + a_2^e \phi_2^e + a_3^e \phi_3^e + a_4^e \phi_4^e) \\
 b^e &= \frac{1}{6V^e} \begin{vmatrix} \phi_1^e & \phi_2^e & \phi_3^e & \phi_4^e \\ y_1^e & y_2^e & y_3^e & y_4^e \\ z_1^e & z_2^e & z_3^e & z_4^e \\ 1 & 1 & 1 & 1 \end{vmatrix} = \frac{1}{6V^e} (b_1^e \phi_1^e + b_2^e \phi_2^e + b_3^e \phi_3^e + b_4^e \phi_4^e) \\
 c^e &= \frac{1}{6V^e} \begin{vmatrix} \phi_1^e & \phi_2^e & \phi_3^e & \phi_4^e \\ x_1^e & x_2^e & x_3^e & x_4^e \\ z_1^e & z_2^e & z_3^e & z_4^e \\ 1 & 1 & 1 & 1 \end{vmatrix} = \frac{1}{6V^e} (c_1^e \phi_1^e + c_2^e \phi_2^e + c_3^e \phi_3^e + c_4^e \phi_4^e) \\
 d^e &= \frac{1}{6V^e} \begin{vmatrix} \phi_1^e & \phi_2^e & \phi_3^e & \phi_4^e \\ x_1^e & x_2^e & x_3^e & x_4^e \\ y_1^e & y_2^e & y_3^e & y_4^e \\ 1 & 1 & 1 & 1 \end{vmatrix} = \frac{1}{6V^e} (d_1^e \phi_1^e + d_2^e \phi_2^e + d_3^e \phi_3^e + d_4^e \phi_4^e)
 \end{aligned} \tag{6.68}$$

Thereby:

$$V^e = \frac{1}{6} \begin{vmatrix} 1 & 1 & 1 & 1 \\ x_1^e & x_2^e & x_3^e & x_4^e \\ y_1^e & y_2^e & y_3^e & y_4^e \\ z_1^e & z_2^e & z_3^e & z_4^e \end{vmatrix} = \text{Elementary volume} \tag{6.69}$$

If the expressions of a^e, b^e, c^e, d^e are replaced in (6.38), we can get:

$$\begin{aligned}
 \phi^e(x, y, z) &= \sum_{j=1}^4 N_j^e(x, y, z) \phi_j^e \\
 N_j^e(x, y, z) &= \frac{1}{6V^e} (a_j^e + b_j^e x + c_j^e y + d_j^e z) = \delta_{ij} \begin{cases} 1, & i = j \\ 0, & i \neq j \end{cases}
 \end{aligned} \tag{6.70}$$

By the expression and value of the above-mentioned interpolation function, the elements of w and g matrix of FENN can be obtained, and the construction of 3D FENN is realized.

A two-dimensional example of the FENN construction method is introduced in the front section. For a general case, the FENN construction can be set up according to the way shown in Fig. 6.22. It is assumed that the finite element mesh structure built in advance has M elements, N nodes, and the characteristic parameters of each

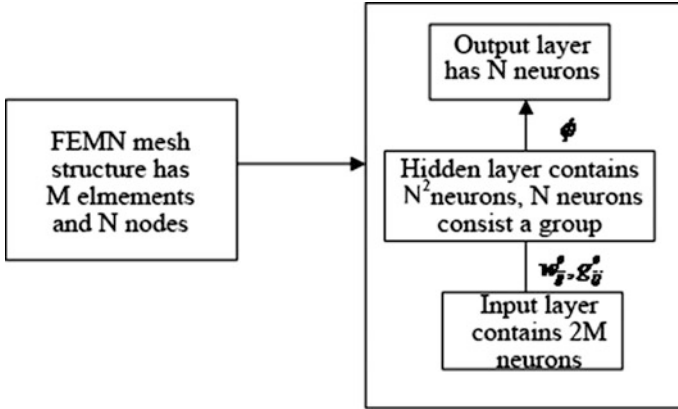


Fig. 6.22 The FENN construction method in general

element are α and β . Then the input layer of the neural network structure contains $2M$ neurons, namely M number of α and M number of β . They are then multiplied by the weight matrix element w_{ij}^e, g_{ij}^e as the input of the hidden layer. The hidden layer contains N^2 neurons, N neurons consist a group, and the output of each group is a row vector of K matrix. The output b_i of the hidden layer is then multiplied by the value ϕ of the corresponding node. The output layer has N neurons, representing the value b_i of the N nodes.

6.4.3.4 Solving Positive and Inverse Problems Using FENN

The essence of the FENN solution of the direct problem is seeking the weights ϕ of the FENN hidden layer to the output layer at the condition of material parameters and excitation source. Steps are as follows:

- (1) A finite element mesh is built, which includes M elements and N nodes. The material parameters α_i and β_i of each unit are added into the input neurons to calculate the output of each neuron. Any natural boundary conditions are used as the input of the hidden layer neuron. According to the Dirichlet boundary condition, some weights can be fixed. For all free weights, the initial values are randomly selected. Set the weight of t cycle as $\phi(t)$.
- (2) The output of the neural network in the t cycle is given as:

$$\hat{b}_i(t) = \sum_{j=1}^N K_{ij} \phi_j(t), \quad t = 1, 2, \dots, N \tag{6.71}$$

(3) to calculate the error of the output of the neural network:

$$E = \frac{1}{2} \|b - \hat{b}(t)\|^2 = \frac{1}{2} \sum_{i=1}^N (b - \hat{b}(t))^2 = \frac{1}{2} \sum_{i=1}^N E_i(t)^2 \quad (6.72)$$

(4) the gradient value of the error relative to the free hidden layer weight is calculated as:

$$\frac{\partial E(t)}{\partial \phi_j} = - \sum_{i=1}^N E_i(t) K_{ij} \quad (6.73)$$

(5) using gradient descent method to update the free weights:

$$\phi_j(t+1) = \phi_j(t) + \eta \left(- \frac{\partial E(t)}{\partial \phi_j} \right) \quad (6.74)$$

where η is the learning rate, which can be chosen as a suitable value according to the experience.

(6) repeat steps 2 to 5 until the output error is less than a predetermined threshold.

FENN can also be used to solve the inverse problem, that is, known the measured value ϕ and the external excitation source b , to solve the material parameters α and β . Specific algorithms are as follows:

- (1) randomly set the initial value of the material parameters α and β . $\alpha(t)$ and $\beta(t)$ represent material parameter values in the t cycle. The weights between the hidden layer and the output layer are fixed as ϕ .
- (2) in the t th cycle, the output of the network will be calculated by the input of $\alpha(t)$ and $\beta(t)$.

$$\hat{b}_i(t) = \sum_{j=1}^N K_{ij} \phi_j(t), \quad t = 1, 2, \dots, N \quad (6.75)$$

(3) to calculate the error of the output of the neural network:

$$E = \frac{1}{2} \|b - \hat{b}(t)\|^2 = \frac{1}{2} \sum_{i=1}^N (b - \hat{b}(t))^2 = \frac{1}{2} \sum_{i=1}^N E_i(t)^2 \quad (6.76)$$

(4) to calculate the gradient value of the error relative to $\alpha(t)$ and $\beta(t)$:

$$\begin{aligned}\frac{\partial E(t)}{\partial \alpha_e} &= - \sum_{i=1}^N E_i \left(\sum_{j=1}^N \phi_j w_{ij}^e \right) \\ \frac{\partial E(t)}{\partial \beta_e} &= - \sum_{i=1}^N E_i \left(\sum_{j=1}^N \phi_j g_{ij}^e \right)\end{aligned}\quad (6.77)$$

(5) using gradient descent method to update $\alpha(t)$ and $\beta(t)$:

$$\begin{aligned}\alpha_e(t+1) &= \alpha_e(t) + \eta \left(- \frac{\partial E(t)}{\partial \alpha_e} \right) \\ \beta_e(t+1) &= \beta_e(t) + \eta \left(- \frac{\partial E(t)}{\partial \beta_e} \right)\end{aligned}\quad (6.78)$$

(6) repeat steps 2 to 5 until convergence is reached; that is, the output error is less than a predetermined threshold.

The method of solving the positive and inverse problems with FENN is given above. In the problem of the quantitative detection of defects, the problem is that the shape parameters (i.e., the α and β) and the external magnetic field strength are known, and the distribution of the magnetic flux leakage (i.e., the weight ϕ) is solved. The inverse problem is that the external excitation source and the distribution of the magnetic leakage induction intensity are known, and the shape parameters of the defect are solved. Combined with the iterative method, the 3D-FENN is used as the positive problem model, and the iterative method based on 3D-FENN can be obtained.

This method has the characteristics of finite element calculation that is based on the Maxwell equation, considering the material nonlinearity, so it has high accuracy. And it has the characteristics of neural network, based on parallel computing, so the speed is fast. At the same time, it can also enhance the approximation ability by the feedback structure with iterative method.

References

1. Forster, F.: New findings in the filed of nondestructive magnetic leakage field inspection. *NDT Int.* **19**(2), 3–14 (1986)
2. Lord, W., Hwang, J.H.: Defect characterization for magnetic leakage fields. *Br. J. NDT* **19**(1), 14–18 (1977)
3. Zatsepin, N.N., Shcherbinin, V.E.: Calculation of the magnetostatic field of surface flaws. *Defektoskopiya* **5**, 50–59 (1966)
4. Shcherbinin, V.E., Pashagin, A.I.: Influence of the extension of a defect on the magnitude of its magnetic field. *Defektoskopiya* **8**, 74–79 (1972)

5. Edwards, C., Palmer, S.B.: The magnetic leakage field of surface-breaking cracks. *J. Phys. D (Appl. Phys.)* **19**(4), 657–673 (1986)
6. Hwang, J.H., Lord, W.: Finite element modeling of magnetic field/defect interactions. *J. Test. Eval.* **3**(1), 21–26 (1975)
7. Forster, F.: On the way from the “know-how” to “know-way” in the magnetic leakage field method of nondestructive testing. *Mater. Eval.* **43**, 1398–1402 (1985)
8. Atherton, D.L., Daly, M.G.: Finite element calculation of magnetic flux leakage detector signal. *NDT Int.* **20**(4), 235–238 (1987)
9. Mandal, K., Atherton, D.L.: Study of a racetrack-shaped defect in ferromagnetic steel by magnetic Barkhausen noise and flux leakage measurements. *J. Magn. Magn. Mater.* **212**(1), 231–239 (2000)
10. Bruder, B.: Magnetic leakage fields calculated by the method of finite differences. *NDT Int.* **18**(6), 353–360 (1985)
11. Altschuler, E.: Nonlinear model of flaw detection in steel pipes by magnetic flux leakage. *NDT & E Int.* **28**(1), 35–40 (1995)
12. Udpa, L., Udpa, S.S.: Application of neural networks to nondestructive evaluation. In: *First IEE International Conference on Artificial Neural Networks*, pp. 143–150 (1989)
13. Chen, J., Huang, S., Zhao, W.: Three-dimensional defect inversion from magnetic flux leakage signals using iterative neural network. *IET Sci. Meas. Technol.* **9**(4), 418–426 (2015)
14. Ramuhalli, P.: Neural network based iterative algorithms for solving electromagnetic NDE inverse problems. Ph.D Dissertation, Iowa State University, Iowa (2002)
15. Cui, W.: Study on the quantitative method of magnetic flux leakage detection for pipeline corrosion defects. Ph.D Dissertation, Tsinghua University, Beijing (2006) (in Chinese)
16. Jiang, Q.: Study on the defect quantification and application of magnetic flux leakage detection in pipeline. Ph.D Dissertation, Tianjin University, Tianjin (2002) (in Chinese)
17. Huang, S.: *The Theory and Application of Magnetic Internal Inspection for Defects of Oil and Gas Pipeline*. Machinery Industry Press, Beijing (2013) (in Chinese)
18. Huang, S.: *New Technology of Electromagnetic Nondestructive Testing*. Tsinghua University Press, Beijing (2014) (in Chinese)